# Geologic controls on fluid flow and seismic imaging of faults in carbonate rocks

## Insights from quantitative outcrop analysis and reflection seismic modeling

Vilde Dimmen

Thesis for the degree of Philosophiae Doctor (PhD)
University of Bergen, Norway
2023

UNIVERSITY OF BERGEN

# Geologic controls on fluid flow and seismic imaging of faults in carbonate rocks

## Insights from quantitative outcrop analysis and reflection seismic modeling

Vilde Dimmen

Thesis for the degree of Philosophiae Doctor (PhD)
at the University of Bergen

Date of defense: 16.06.2023

© Copyright Vilde Dimmen

The material in this publication is covered by the provisions of the Copyright Act.

Year: 2023

Title: Geologic controls on fluid flow and seismic imaging of faults in carbonate rocks

Name: Vilde Dimmen

Print: Skipnes Kommunikasjon / University of Bergen

# Scientific environment and funding

The research herein has been conducted at the Department of Earth Science, University of Bergen (Norway). The research was funded through a personal PhD grant for the candidate from VISTA - a basic research program in collaboration between The Norwegian Academy of Science and Letters, and Equinor (grant number 6272).

# Preface

This dissertation for the degree of philosophiae doctor (PhD) has been submitted to the Department of Earth Science, University of Bergen. The candidate enrolled in the PhD program and carried out the research within the Geodynamics and Basins Studies Group at the Department of Earth Science, University of Bergen. The work was supervised by Professor Atle Rotevatn, and co-supervised by Professor Isabelle Lecomte, and Professor Robert Gawthorpe (all from the University of Bergen).

This PhD thesis has an article-based format which is the most common format for a doctoral dissertation within natural sciences in Norway. Because of the different styles used by the journals in which the papers are published or submitted, the reference- and language style may vary throughout the thesis.

# Acknowledgements

I once said I would never do a PhD – now, there are so many people I must thank for helping me along the way and for following me on this journey. First and foremost, I want to thank my main supervisor, Atle, for always believing in me, and for being there every step of the way. I would never have started (or finished!) this without you and your (sometimes overly) optimistic attitude. You have been a great supervisor and given me the freedom and space to work on my own, while still providing guidance, support, and motivation. Thanks for also being a very good friend; I cherish all the fun memories and look forward to continuing working together.

My co-supervisor Isabelle Lecomte has been an inspiration and role model since the beginning. I am truly grateful for your patience and help with the seismic modeling and geophysical aspect of this thesis. Thanks to my co-authors, Casey Nixon, David Peacock, Cathy Hollis, Hilary Corlett, Rob Gawthorpe, and Wouter Gravendeel for discussions, feedback, and review of the papers. Special thanks to David for including me in your work and for fun and jokes in Malta, and to Hilary for the early mornings on Zoom and for inviting us over to Canada and guiding us around St. Johns'.

These years at GEO have been made extra special due to all the amazing people and friendships. In particular, I want to thank my very good friends and podcast co-hosts, Martin and Albina; thanks for being such great friends, for teaching me illustrator skills that I soon forget, and for always being 100% honest! Thanks to Izzy and Alice for being such good and inspirational friends, and to the rest of the "PhD girls' dinner", including Katrin, Natacha, Danielle, and Blækkan. Thanks to Jhon, Sebastian (and Anna), Tim, Edos, Fabian, Felix, Linn Merethe, Bjarte, Thomas, Xingguo, Helene, Åse, and all other PhD friends and colleagues for the good memories.

The past few months I got to spend some time in the administration at GEO, which has been a pleasant and rewarding distraction, and I am especially grateful for the warm welcome and friendships from Emilie, Karen, and Anders.

I also want to express my gratitude to all my friends and family outside of academia; thank you for cheering me on, on this somewhat incomprehensible journey, and for all the visits, trips, and conversations about anything but work.

My family has always been important to me, and I want to thank my parents and siblings for their love and support, and for providing both mental and physical space for rest throughout these years. I'm so lucky to have you all.

Finally, I want to thank Björn for being by my side through the many ups- and downs.

# Abstract

Exploration of the sub-surface has historically been driven largely by economic incentives through hydrocarbon exploration and other geological resources, but more recently the role of subsurface geology in the green shift has gained increasing focus. The subsurface is highly important for $CO_2$- and hydrogen storage, groundwater resources, geothermal energy and more, and crucial for all these applications are structures such as faults and fracture networks, and their control on subsurface fluid flow. The main focus of this thesis is to improve our understanding of the sub-surface through two overarching themes, (i) fault and fracture networks and their controls on fluid flow and fluid-rock interaction, and (ii) the seismic imaging of such faults and their fluid-rock reactive products in the subsurface.

Despite the consensus that structures exert strong control on fluid flow, few have attempted to quantify this relationship. In accordance with Theme (i) above, this thesis therefore starts by quantifying and visualizing the relationship between fluid flow and structural complexity (**Paper 1**). Using low-porosity cemented mounds as a record of paleo-fluid flow, node and branch topology is applied to characterize and visualize areas of structural complexity, quantitatively documenting their spatial correlation with focal areas for paleo-fluid flow.

In **Paper 2**, an overview of geologic controls on fluid flow in sedimentary rocks is given through a combination of literature review and analysis of outcrop examples, using iron oxide precipitates as a proxy for paleo-fluid flow. The paper documents fluid flow controls ranging from simple geological heterogeneities to more complex networks of structures, and documents and quantifies the topology of fracture networks and hybrid networks of depositional and structural conduits, and the relationship to paleo-fluid flow.

A key to mapping structural conduits in the subsurface is the imaging of faults using reflection seismic data. Addressing Theme (ii), **Paper 3** investigates the effect of small-scale faults (near or below seismic resolution) on seismic images using seismic modeling. The main outcome of this paper is the documentation of the effects that faults

that are borderline seismically resolvable, or that fall below seismic resolution, may have on seismic data. Notably, the paper illustrates how subtle reflector distortions may reflect discrete faults in the subsurface, which is an important new insight that may help improve and geologically-inform structural seismic interpretation.

In addition to imaging faults in the subsurface in their own right, also the products of fluid-rock interaction are of interest, and it is therefore important to understand their seismic signature. Using seismic modeling of fault-controlled dolomites in a limestone-dominated succession in the Gulf of Suez, **Paper 4** investigates the seismic imaging of a variety of massive and stratabound dolomite bodies under different geological and geophysical input parameters.  The main outcome of this paper is new insights to how fault-controlled hydrothermal dolomite bodies are imaged in seismic data; the paper documents that whereas the general presence and trends of dolomite occurrence in the subsurface is possible to infer from seismic data, the identification of individual stratabound dolomite bodies might not possible.

The findings from this thesis furthers the fundamental understanding of key geologic controls on fluid flow in the subsurface, and the imaging of potentially flow-controlling faults and their rock reactive products in reflection seismic data. The new insight presented in this thesis has a wide range of implications and applications, such as for locating economically significant ore deposits, in hydrocarbon seal risk assessment, groundwater management, contaminant transport and more.

# Samandrag

Utforsking av undergrunnen har historisk sett hovudsakleg vore drive av økonomiske insentiv gjennom leiting etter hydrokarbon og andre geologiske ressursar. I nyare tid, derimot, har geologiens rolle i det grøne skiftet fått aukande fokus. Undergrunnen er svært viktig for blant anna $CO_2$- og hydrogenlagring, grunnvassressursar og geotermisk energi, og avgjerande for alle disse bruksområda er strukturar som forkastingar og sprekkenettverk, og deira kontroll på væskestraum i undergrunnen. Hovudfokuset i denne avhandlinga er å forbetre forståinga av undergrunnen gjennom to overordna tema; (i) kontrollen forkastings- og sprekkenettverk har på væskestraum og reaksjonar mellom væsker og bergartar, og (ii) seismisk avbilding av slike forkastingar og deira væske-bergart reaksjonsprodukt i undergrunnen.

Sjølv om det er generell einigheit i at geologiske strukturer utøver sterk kontroll på væskestraum, har få forsøkt å kvantifisere dette forholdet. I samsvar med tema (i) ovanfor byrjar denne avhandlinga difor med å kvantifisere og visualisere forholdet mellom væskestraum og strukturell kompleksitet (**Artikkel 1**). Ved hjelp av sementerte haugar med lav porøsitet som bevis for paleo-væskestraum, nyttast topologi for å karakterisere og visualisere strukturell kompleksitet i lokaliserte område, og kvantitativt dokumentere deira korrelasjon med områder for lokalisert paleo-væskestraum.

**Artikkel 2** gir ei oversikt over geologiske kontrollar på væskestraum i sedimentære bergartar, basert på ein kombinasjon av litteraturanalyse og studie av eksempel frå felt der jernoksidutfelling blir brukt som bevis for paleo-væskestraum. Artikkelen dokumenterer eit vidt spenn av kontrollar på væskestraum og inkluderer alt frå enkle geologiske heterogeniteter til meir komplekse nettverk av strukturar, og dokumenterer og kvantifiserer topologien til både sprekkenettverk og hybridnettverk beståande av ein kombinasjon av sprekker og sedimentære avsetningsstrukturar som fungerer som leiarar for væskestraum.

Eit viktig verktøy for kartlegging av slike væskeleiande strukturar i undergrunnen er seismiske refleksjonsdata. I tråd med Tema (ii), undersøkjer **Artikkel 3** effekten av småskala forkastingar (nær eller under seismisk oppløysing) på seismiske bilde ved hjelp av seismisk modellering. Hovudmålet i denne artikkelen er å dokumentere effekten som forkastingar under- eller på grensa til seismisk oppløysing kan ha på seismiske data. For eksempel illustrerer artikkelen korleis subtile forandringar i ein refleksjon kan vere resultat av små forkastingar i undergrunnen, noko som er viktig ny innsikt og som mogleg kan bidra til å forbetre tolking av strukturar i seismikk.

I tillegg til avbilding av forkastingar i seg sjølv, er også produkta av væske-bergart interaksjon av interesse, og det er derfor viktig å også forstå deira seismiske signatur. Ved hjelp av seismisk modellering av forkastingskontrollerte dolomittar i ei kalksteinsdominert sone i Suezbukta, blir seismisk avbilding av både massive og stratigrafisk kontrollerte dolomittkroppar undersøkt med varierande geologiske og geofysiske parametrar i **Artikkel 4**. Resultata i denne artikkelen gir ny innsikt i korleis forkastingskontrollerte hydrotermale dolomittkroppar blir avbilda i seismiske data; artikkelen dokumenterer at dei generelle trendane og nærværet av dolomitt i undergrunnen er mogleg å slutte frå seismiske data, men identifisering av individuelle, stratigrafisk kontrollerte dolomittkroppar er ikkje stadfesta mogleg.

Funna frå denne avhandlinga fremjar den grunnleggande forståinga av sentrale geologiske kontrollar på væskestraum i undergrunnen, og avbilding av potensielt strøymingskontrollerande forkastingar og deira bergreaktive produkt i refleksjonsseismiske data. Den nye innsikta presentert i avhandlinga har eit breitt spekter av implikasjonar og nytteområde, for eksempel for lokalisering av økonomisk betydelege førekomstar av nyttige mineral, i risikovurdering for $CO_2$- og hydrogenlagring, grunnvasshandtering, lokalisering av forureining, og meir.

# List of publications and authorship statement

Papers 1-4 listed below, in which the candidate is first author, form the core of this thesis. In addition, two papers are listed in the appendices; these papers are not part of the main body of the thesis work but are contributions that form part of the backdrop for this work that the candidate contributed to, and which therefore are included here.

**Paper 1:**

Dimmen, V., Rotevatn, A., Peacock, D. C., Nixon, C. W., & Nærland, K. (2017). *Quantifying structural controls on fluid flow: Insights from carbonate-hosted fault damage zones on the Maltese Islands*. Journal of Structural Geology, 101, 43-57.

DOI: https://doi.org/10.1016/j.jsg.2017.05.012

*Authorship statement paper 1:* Dimmen collected the data, did the analysis, drafted all figures, and drafted the manuscript text (70% total contribution). Rotevatn initiated the ideas behind the paper, which were further developed by Dimmen and co-authors. Rotevatn also contributed with supervision and guidance and assisted with the analysis. Nixon contributed to concept development and analysis of node and branch topology. Peacock contributed to field data collection and informal guidance to the analysis. Nærland assisted with field data collection. All authors contributed to discussions, manuscript review and revisions.

**Paper 2:**

Dimmen, V., Rotevatn, A., & Nixon, C. W. (2020). *The relationship between fluid flow, structures, and depositional architecture in sedimentary rocks: An example-based overview*. Geofluids, 2020, 1-19.

DOI: https://doi.org/10.1016/j.marpetgeo.2022.105980

*Authorship statement paper 2:* The ideas in this paper were developed jointly by Dimmen and Rotevatn. Dimmen collected most of the data, did the analysis, drafted all figures, and drafted the manuscript text (75% total contribution). Rotevatn contributed to data collection, supervision and guidance, and assisted with the analysis. Nixon contributed to the analysis of node and branch topology. All authors contributed to discussions, manuscript review and revisions.

**Paper 3:**

Dimmen, V., Rotevatn, A., & Lecomte, I. (2023). *Imaging of small-scale faults in seismic reflection data: Insights from seismic modeling of faults in outcrop*. Marine and Petroleum Geology, 105980.

DOI: https://doi.org/10.1016/j.marpetgeo.2022.105980

*Authorship statement paper 3:* The ideas in this paper were developed jointly by Dimmen and Rotevatn. Dimmen collected most of the data, undertook the seismic modeling, did the analysis, drafted all figures, and drafted the manuscript text (80% total contribution). Rotevatn contributed to data collection, supervision and guidance, and assisted with the analysis. Lecomte contributed to the seismic modeling, assisted with the analysis, and with guidance and supervision. All authors contributed to discussions, manuscript review and revisions.

**Paper 4:**

Dimmen V., Rotevatn A., Lecomte I., Hollis C., Corlett H., Gravendeel W., Gawthorpe R. *Imaging fault-controlled hydrothermal dolomite bodies in the subsurface: insights from 3D seismic modeling of the Hammam Faraun Fault system, Suez Rift, Egypt.* Manuscript.

*Authorship statement paper 4:* The ideas in this paper were jointly developed by Dimmen and Rotevatn. Corlett mainly, but also Hollis, Gawthorpe and Rotevatn, had contributed to outcrop data collection in Egypt in a previous project in 2010-2012. The geocellular model that forms the basis for the seismic modeling in this study was developed by Corlett and published in a previous paper. Dimmen undertook the seismic modeling based on this geocellular model, did the analysis, drafted all figures and drafted the manuscript text (total contribution 60%). Lecomte contributed to the seismic modeling, and with supervision and guidance. Rotevatn contributed with supervision and guidance. Grawendeel contributed with RMS data and one figure. All authors contributed to discussions and manuscript review.

**Appendix A:**

Peacock, D. C. P., Dimmen, V., Rotevatn, A., & Sanderson, D. J. (2017). *A broader classification of damage zones*. Journal of Structural Geology, 102, 179-192.

https://doi.org/10.1016/j.jsg.2017.08.004

*Authorship statement Appendix A:* The ideas in this paper were initiated by Peacock and developed by Peacock and the co-authors. Dimmen contributed with one outcrop data example and drafted several figures (15% total contribution). All authors contributed to discussions, manuscript review and revisions.

**Appendix B:**

Nixon, C. W., Nærland, K., Rotevatn, A., Dimmen, V., Sanderson, D. J., & Kristensen, T. B. (2020). *Connectivity and network development of carbonate-hosted fault damage zones from western Malta.* Journal of Structural Geology, 141, 104212.

https://doi.org/10.1016/j.jsg.2020.104212

*Authorship statement Appendix B:* The ideas in this paper were initiated by Rotevatn and developed with Nærland and Nixon. Nærland did most of the data collection, and Nærland and Nixon did most of the analysis. Dimmen contributed to the data collection, the analysis of node and branch topology, and drafted one figure (10% total contribution). All authors contributed to discussions, manuscript review and revisions.

*Papers 1, 2 and 3, as well as Appendix B, were all published open access and are reproduced in this thesis under the terms of the Creative Commons CC-BY license. The reproduction of Appendix A in this thesis is in line with the retainer rights as a publishing author under copyright agreement with Elsevier: as an author of an Elsevier article, one retains the right to include it in a thesis or dissertation, provided it is not published commercially. Permission is not required, provided correct reference to the journal as the original source is made.*

# Contents

# 1. Introduction

During the past century, a strong drive to image and explore the subsurface have been powered by the economic incentives of hydrocarbon exploration and exploitation. In the more recent past, however, a growing effort to combat climate change has led to a heightened focus on the role of subsurface geology in the green shift, for example its importance for geologic carbon storage, hydrogen storage, geothermal energy, water resources and more (e.g., Kivi et al., 2022; Abiye, 2023; English et al., 2023; Krevor et al., 2023). Crucial for all of this is the role of fault and fracture networks in controlling fluid flow in the subsurface, and the imaging of such flow-controlling structures using seismic reflection data; understanding the subsurface and the processes taking place beneath our feet is important for a wide range or reasons, including (but not limited to) prediction of earthquakes and volcanic eruptions, groundwater management, $CO_2$ storage, geothermal energy, and mining of industrial- and rare earth elements (Curewitz and Karson, 1997; Tavarnelli and Pasqui, 2000; Micklethwaite and Cox, 2004; Shipton et al., 2005b; Verhaert et al., 2009; Zhang et al., 2011; Bense et al., 2013; Davidson et al., 2016). Many of these processes are strongly controlled by, or related to, fluids and fluid flow, and hence, we need to gain knowledge about how fluids move within the subsurface and how to identify possible migration pathways in order to understand the above-mentioned processes better.

This forms the backdrop for this thesis, whose overarching themes are (i) fault and fracture networks and their controls on fluid flow and fluid-rock interaction, as well as (ii) the seismic imaging of such faults and their fluid-rock reactive products in the subsurface.

## 1.1 Fault and fracture networks

Stresses in the upper part of Earths' crust cause brittle deformation, generally in the form of fault- and other fracture networks (e.g., Crider and Peacock, 2004). Of particular importance are the fault- and fracture networks that constitute fault damage zones, since these play a key role in facilitating fluid flow in the proximity of faults (e.g., Faulkner et al., 2010).Damage zones are areas of stress concentration that develop to accommodate strain variations in relation to faults, in which networks of deformation structures such as e.g., deformation bands, faults, folds, and joints of various orientations, geometries and displacements develop (Scholz and Cowie, 1990; Cowie and Scholz, 1992; Kim et al., 2004; Fossen et al., 2007; Ishii, 2016). Damage zones can be classified based upon their location relative to the fault(s) and categories include, but are not limited to, fault bend-, tip-, wall-, intersection-, and approaching damage zones (Fig. 1.1., Peacock and Sanderson, 1991; Kim et al., 2004; Peacock et al., 2017b). There are different models to explain the formation of fault damage zone; some studies suggest that the damage zone forms in response to high strain gradients ahead of the propagating fault tip (as a tip damage zone), and that when the fault propagates onwards the tip damage zone is incorporated as wall damage along the fault (e.g., Ferrill et al., 2011). Other studies have suggested that damage zones develop through frictional processes when fault and/or fault systems evolve, during which the deformation in the damage zones tends to increase and the networks the structures produce will become more complex (Kim et al., 2003, 2004; Savage and Cooke, 2010), and others yet have argued a combination of the two (e.g., Shipton and Cowie, 2001; Shipton and Cowie, 2003; Saillet and Wibberley, 2010).

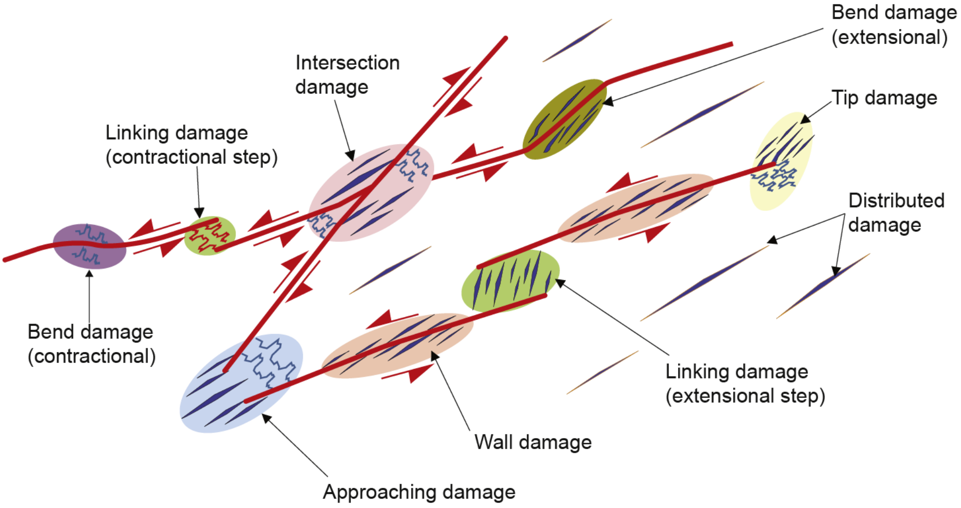

*Figure 1.1: Illustration of different types of damage zones. From Peacock et al. 2017.*

Regardless of which model is preferred for damage zone evolution, the network properties (topology, connectivity; see Sanderson and Nixon, 2015) of fault damage zones evolve during the evolution of the damage zone (e.g., Nixon et al., 2020; Hansberry et al., 2021). The use of branch and node topology allows for quantification and visualization of fracture network properties, by elucidating the relationships between individual structures in a network (e.g., Sanderson and Nixon, 2018). This methodology is used extensively in this thesis and is introduced in more detail in **Paper 1**.

Although damage zone evolution or classification are not part of the core work in this thesis, damage zones are treated in terms of their broader classification in Appendix A, as well as concerning the topology/connectivity of different interacting damage zone types (Appendix B). On the other hand, a key focus in this thesis is the effect that structural networks such as fault damage zones have on fluid flow, and in the following section, structural controls on fluid flow and fluid-rock interaction are therefore introduced.

## 1.2 Structural controls on fluid flow and fluid rock interaction

Structural networks such as those described above may have profound effects on fluid flow, and it is well known that faults, and in particular damage zones and structural complexity along faults (e.g., relay zones and fault intersections, see Fig. 1.2), exert strong controls on fluid flow (e.g., Gartrell et al., 2004; Jolley et al., 2007; Fossen and Rotevatn, 2016).

Structures such as faults, fractures, and deformation bands may act as conduits or barriers to fluid flow, or a combination of the two (Fossen and Bale, 2007; Jolley et al., 2007; Faulkner et al., 2010; Volatili et al., 2019), e.g., open joints are highly conductive while cement filled ones (veins) may be impermeable and function as barriers. The conductivity of faults and fractures may also vary over time as they are cyclic in nature and hence may vary between being open and closed to fluid flow through alternating fracturing and cementation (Ramsay, 1980; Agosta and Kirschner, 2003; Holland and

Urai, 2010; Farrell et al., 2014; Kristensen et al., 2016; Hollis et al., 2017; Salomon et al., 2021). Being able to identify and separate between different types of structures and understand the way fault and fracture networks evolve is therefore essential, since structures in various stages of their cycles may have different effects on flow. Structurally controlled fluid flow may in turn affect a variety of processes in the Earths' crust, such as rock-fluid reactions, mineralization and cementation (e.g., Steefel and Maher, 2009; Koegelenberg et al., 2016; Kristensen et al., 2018; Chauvet, 2019), the distribution of cementation (Williams et al., 2016; Salomon et al., 2020), Liesegang-type reaction diffusion systems (e.g., Balsamo et al., 2013; Dimmen et al., 2020), and hydrothermal dolomites around faults (e.g., Davies and Smith, 2006; Hollis et al., 2017).

Despite the wide consensus that structural complexity exerts strong controls on fluid flow and fluid rock interaction, few attempts have been made to quantify and visualize the relationship between structural complexity and flow. In this thesis, this gap in knowledge is addressed using node and branch topology (Sanderson and Nixon, 2015) to quantitatively investigate the connection between fault/fracture network properties and fluid flow; this part of the thesis work is presented in **Papers 1 and 2**.

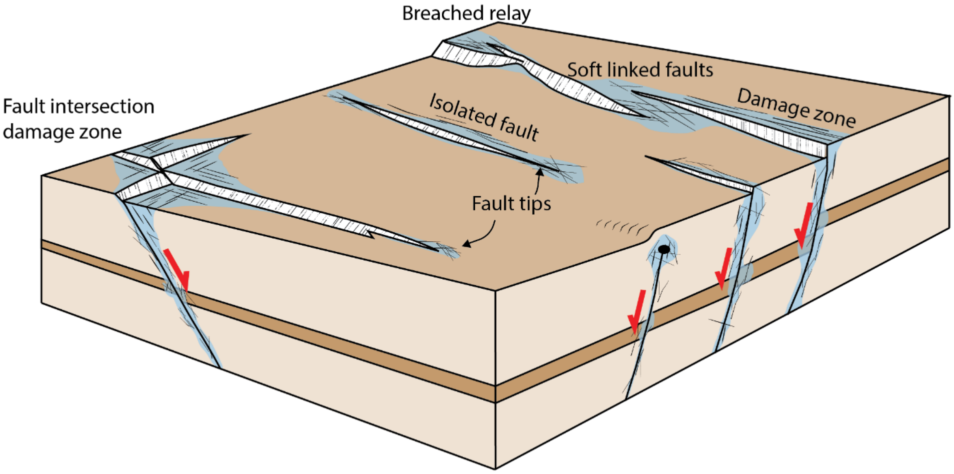

*Fig. 1.2: Schematic illustration of preferential fluid localization, illustrated by the blue color, along faults and fault intersections. From Dimmen et al. (2017). The fluids may be localized in fault damage zones and along fault planes, especially in more complex areas, like linkage points, fault tips and fault intersections.*

## 1.3 Seismic modeling and imaging faults and fractures

A second key focus in this thesis is the seismic imaging of faults and their fluid-rock reactive products. Given the crucial role that faults and fault-controlled fracture networks play with regards to fluid flow, it is of great interest to improve our understanding and prediction of structures in the subsurface. Whereas the damage zone fracture networks themselves are generally not possible to image due to limitations in seismic resolution (e.g., Faleide et al., 2021), reflection seismic may image the faults that control these networks. Outcrops have long been studied as analogues for subsurface geology, and in particular to inform interpretations of what cannot be imaged from reflection seismic data (Howell et al., 2014). Outcrop analogues still play an important role for elucidating subsurface geology, in parallel with seismic reflection data becoming our main tool to document and explore the subsurface over the past decades.

Seismic modeling has become a widely used tool where synthetic seismic is created from known geological models, often based on outcrops (e.g., Eide et al., 2017; Grippa et al., 2019). Seismic modeling can be a quick and cost-efficient way to improve our understanding of seismic imaging, as we can study the seismic of which the input geology is known, and hence investigate and test sensitivities to various input data to elucidate how known structures or lithologies might be portrayed in seismic reflection images.

Small-scale faults that fall below the limits of seismic resolution are generally not possible to image directly using seismic reflection data (Chopra et al., 2006; Simm and Bacon, 2014). These structures may however still affect the seismic images, but an understanding of *how* such sub-seismic faults affect seismic images is largely missing. This knowledge gap is addressed in **Paper 3**, using two-dimensional seismic modeling based on outcrops in Malta.

On the topic of fluid-rock reactive products and their imaging in the subsurface, the detection of fault-controlled hydrothermal dolomites along key bounding faults in rift basins is associated with uncertainty (Dewit et al., 2012). The proximity to faults and the general high-velocity nature carbonate and dolomite rocks makes seismic imaging challenging (Dewit et al., 2012; Abdel-Fattah et al., 2015), and there have so far been few attempts, if any, to use outcrop-based seismic modeling to advance this understanding. This forms the focus for **Paper 4**, where three-dimensional seismic modeling of a previously collected outcrop dataset is used to investigate the imaging of hydrothermal dolomites in the subsurface.

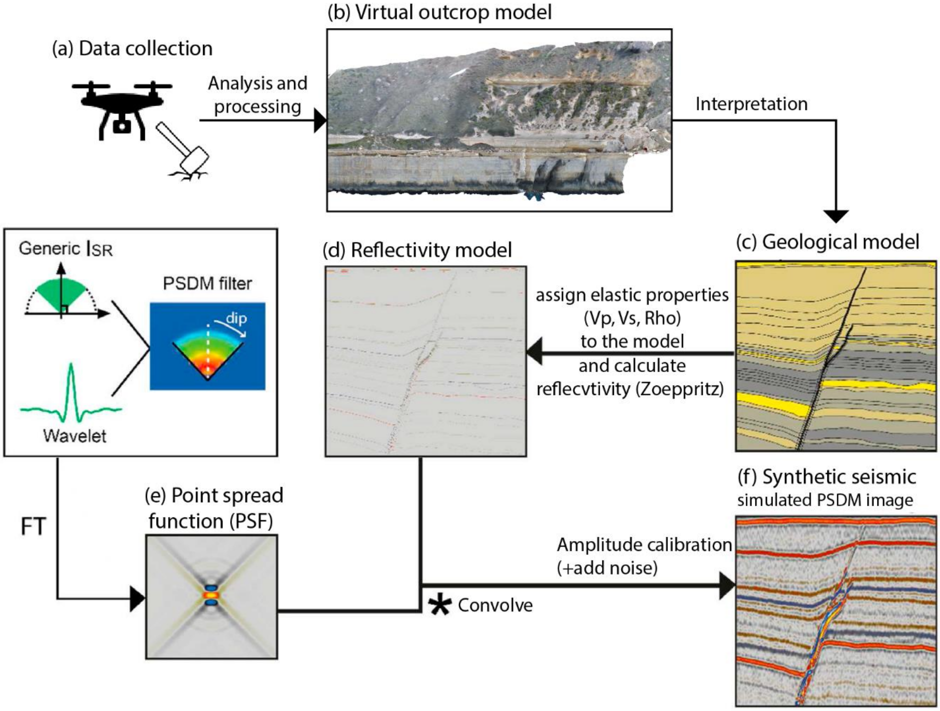

*Fig. 1.3: The main steps of the 2(3)D point spread function (PSF)-based seismic convolution modeling method, from outcrop to synthetic seismic. Illustration after Faleide et al., 2022.*

## 1.4 Research questions

The main aim of this thesis is to advance the knowledge about, and prediction of, structural controls on fluid flow in the subsurface, and the imaging of faults and fluid-rock interactive products in the subsurface. The specific research questions of this thesis follow the two overarching themes detailed in Section 1.1:

*Fault and fracture networks and their controls on fluid flow and fluid-rock interaction*

1. How can the spatial relationship between structural complexity and fluid flow be visualised and quantified? (**Paper 1 and 2**)
2. What is the spatial relationship and key controls of structural complexity on fluid flow and fluid-rock interaction? (**Paper 1 and 2**)
3. How can structural and depositional conduit networks interact to affect fluid flow? (**Paper 2**)

*Seismic imaging of faults and their fluid-rock reactive products in the subsurface.*

4. How are seismic reflection images affected by faults that fall at or below seismic resolution? (**Paper 3**)
5. What are the effects of structural complexity associated with such small-scale faults on reflection seismic images? (**Paper 3**)
6. How may fault-controlled dolomites be imaged using reflection seismic data? **(Paper 4)**
7. Can massive and stratabound dolomites be interpreted/detected using reflection seismic data? (**Paper 4)**

# 2. Paper compilation

**Paper 1**: Quantifying structural controls on fluid flow: Insights from carbonate-hosted fault damage zones on the Maltese Islands

**Paper 2**: The Relationship between Fluid Flow, Structures, and Depositional Architecture in Sedimentary Rocks: An Example-Based Overview

**Paper 3**: Imaging of small-scale faults in seismic reflection data: Insights from seismic modelling of faults in outcrop

**Paper 4**: Imaging fault-controlled hydrothermal dolomite bodies in the subsurface: insights from 3D seismic modeling of the Hammam Faraun Fault system, Suez Rift, Egypt

# I

## Paper 1: Quantifying structural controls on fluid flow: Insights from carbonate-hosted fault damage zones on the Maltese Islands

Vilde Dimmen, Atle Rotevatn, David C.P. Peacock, Casey W. Nixon, Kari Nærland

*Published in Journal of Structural Geology, 101 (2017) 43-57*

http://dx.doi.org/10.1016/j.jsg.2017.05.012

Journal of Structural Geology 101 (2017) 43–57

Contents lists available at ScienceDirect

Journal of Structural Geology

journal homepage: www.elsevier.com/locate/jsg

# Quantifying structural controls on fluid flow: Insights from carbonate-hosted fault damage zones on the Maltese Islands

Vilde Dimmen[*], Atle Rotevatn, David C.P. Peacock, Casey W. Nixon, Kari Nærland [1]

*Department of Earth Science, University of Bergen, PO Box 7800, 5020 Bergen, Norway*

ARTICLE INFO

*Article history:*
Received 16 March 2017
Received in revised form
29 May 2017
Accepted 31 May 2017
Available online 2 June 2017

*Keywords:*
Fluid flow
Fault
Fracture
Damage zone
Connectivity
Topology

ABSTRACT

Structural complexity along faults (e.g., relay zones, fault intersections and jogs) exert strong controls on fluid flow, yet few attempts have been made to quantify and visualise such relationships. This paper does that using an outcrop-based study of fracture networks in carbonate rocks in Malta. We investigate the spatial distribution of low-porosity cemented mounds within the fracture networks, and the geometry and topology of the fracture networks are characterised. The mounds are associated with low porosity due to selective cementation along the faults, as well as with peaks in connecting node frequency (a topological proxy for network connectivity), and fracture intensity (a fracture abundance proxy for network complexity). Considering the mounds as a record of palaeo-fluid flow and palaeo-fluid-rock-interaction, this work therefore quantifies and visualises the relationship between structural complexity and fluid flow.

© 2017 The Author(s). Published by Elsevier Ltd. This is an open access article under the CC BY license (http://creativecommons.org/licenses/by/4.0/).

## 1. Introduction

Faults and fractures may exert strong controls on fluid flow and fluid-rock interaction in the shallow crust, where they can act as conduits, barriers, or a combination of the two (Jolley et al., 2007). On the scale of single faults, important factors that control the flow properties include the type and distribution of damage zone structures, fault core composition, cementation as well as the timing of deformation, fluid flow and diagenesis, and more (Caine et al., 1996; Jolley et al., 2007). At the scale of fault and fracture networks (sensu Peacock et al., 2016), important factors to consider include the locations of fault zone complexity, such as relay zones or fault intersections, as these are particularly prone to act as loci for focused fluid flow (e.g., Gartrell et al., 2004; Fossen and Rotevatn, 2016). Such complex zones can affect the flow of several types of fluids, including magma, hydrocarbons and groundwater, which in turn may further influence a wide variety of processes in the Earth's crust, including earthquakes, volcanism, mineralisation, deformation and sediment remobilisation (e.g., Kerrich, 1986; Curewitz and Karson, 1997; Aydin, 2000; Tavarnelli and Pasqui, 2000; Gartrell et al., 2004; Rowland and Sibson, 2004; Shipton et al., 2004; Yoshida et al., 2008; Verhaert et al., 2009; Micallef et al., 2011; Bense et al., 2013; Rotevatn and Bastesen, 2014; Davidson et al., 2016). The flow of fluids in relation to structural complexity have been a subject for various studies (e.g., Oliver, 1996; Caine and Forster, 1999; Eichhubl et al., 2000; Bense and Van Balen, 2004; Dockrill and Shipton, 2010; Davidson et al., 2016; Ono et al., 2016), all of which appear to underpin a general agreement that there is a strong connection between structural complexity and fluid flow. Despite this general consensus, however, there are currently no studies that attempt to systematically and directly *quantify* and *visualise* the relationship between structural complexity and fluid flow. This paper therefore aims to constrain, quantify and visualise this relationship through field-based investigations.

To do this, we investigate fracture systems in metre-scale fault damage zones in Malta (Fig. 1), where localised cemented mounds (Fig. 2) serve as proxies for palaeo-fluid-rock interaction. The work investigates the relationships between the mounds, and how they relate spatially to variations in the geometries and topologies of the fracture networks, in order to elucidate structural controls on palaeo-fluid flow. The objectives are to (i) determine the porosities of host rocks and of the localised mounds; (ii) to analyse the geometries and topologies of the studied fracture networks; and therefore (iii) to visualise and quantify the spatial distribution of structural complexity; (iv) to investigate the spatial correlation

---

[*] Corresponding author.
*E-mail address:* vilde.dimmen@student.uib.no (V. Dimmen).
[1] Now at: ConocoPhillips, Ekofiskvegen 35, 4056 Tananger, Norway.

http://dx.doi.org/10.1016/j.jsg.2017.05.012
0191-8141/© 2017 The Author(s). Published by Elsevier Ltd. This is an open access article under the CC BY license (http://creativecommons.org/licenses/by/4.0/).

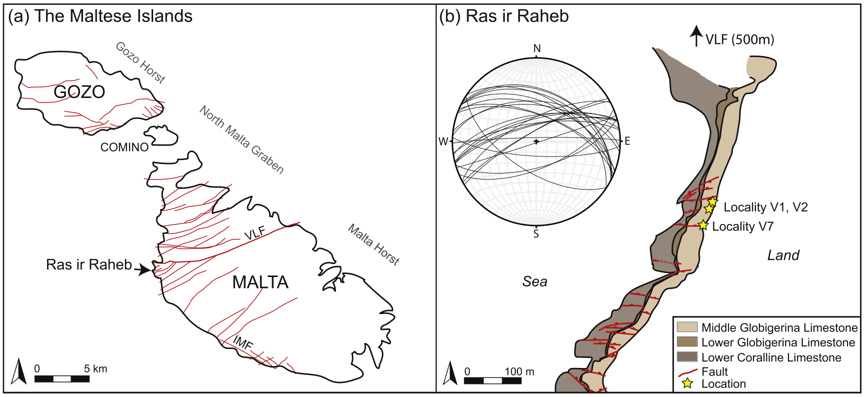

**Fig. 1.** (**a**) Map of the Maltese Islands (Gozo, Comino and Malta), showing the location of the largest faults in red, and the location of the study area at the western coast of Malta. VLF = Victoria Lines Fault, IMF = Il Maghlaq Fault. After Pedley et al. (1976), Michie et al. (2014), and Missenard et al. (2014). (**b**) Map of the study area at Ras ir Raheb. The stereoplot shows the trends of the normal faults found along the wave-cut platform on which the studied networks are situated. The locations of the fracture networks presented within this paper are marked as locality V1, V2, and V7. After Michie et al. (2014). (For interpretation of the references to colour in this figure legend, the reader is referred to the web version of this article.)

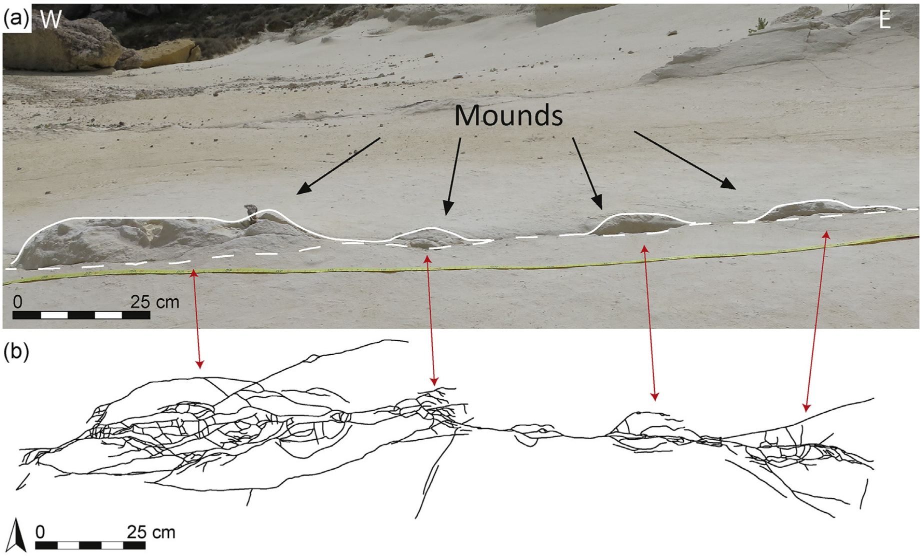

**Fig. 2.** (**a**) Field photograph of topographic highs, or “mounds”, along a fracture network highlighted by the white line. The dashed line indicates ground level/base of the mounds. These mounds were hypothesized to have formed as a result of differential cementation due to localised fluid flow. (**b**) Digitised map of the fracture network depicted in Fig. 2(a). Comparing the digitised map with the photograph of the mounds, we can see how these mounds tend to coincide with the more structurally complex areas of the fracture network.

between cemented mounds and structural complexity within the networks; and, finally, (v) to elucidate structural controls on palaeo-fluid flow and of the interaction between palaeo fluids and host rocks in the studied rocks.

The studied fracture networks are in Miocene-age carbonates of the Globigerina Limestone Formation (Pedley et al., 1976; Dart et al., 1993) located in exceptionally well-exposed outcrops in western Malta (Fig. 1). To quantify and visualise the structural complexity and connectivity of the studied fracture networks, we characterise their *topological properties* (Manzocchi, 2002; Sanderson and Nixon, 2015). Knowledge of the network complexity and connectivity is crucial for the understanding of fluid flow through a rock body, and a topological characterisation offers a more direct route to determine the connectivity and percolation potential of a fracture network than traditional geometric characterisations (Sanderson and Nixon, 2015).

The results of this study have wide-reaching implications, as the ability to quantify and visualise the connection between structural complexity and fluid flow is relevant for a range of geological and economic applications, including for example the generation of exploration fairway maps for structurally controlled ore mineral deposits, structural seal or retention risk maps in hydrocarbon exploration, and environmental or contaminant risk maps for radon gas, radioactive waste leakage and more.

## 2. Terminology

We use the term *mound* in this paper to describe mound-shaped, cemented features that stand out with a topographic positive relief along the described fracture networks.

Structurally, we follow the terminology defined by Peacock et al. (2016), with the following additional clarifications.

- We use the term *structurally complex* zones or areas and *structural complexity*, which refer to parts of a fault or fracture network where fracture frequencies are particularly high, and where a wide variation of fracture orientations occurs. Such structurally complex areas typically occur where faults interact, e.g., at relay zones or fault intersections (Tavarnelli and Pasqui, 2000; Fossen et al., 2005; Peacock et al., 2017). Note that here we use *complexity* as a relative term, indicating fractures being more frequent and with a wider range of orientations than other areas, as is typical in fault damage zones.
- The studied fracture networks form parts of the damage zones of small-scale faults (displacements of <1 m), and comprises a combination of joints and faults with cm-scale displacement. The pavement-nature of the outcrops makes it difficult to distinguish between joints and faults due to lack of displacement markers at the cm scale in the relatively homogenous host rocks, and we therefore use the term *fracture* in the descriptions to encompass both joints and faults.

## 3. Regional tectonic and stratigraphic framework

The Maltese archipelago is on the north-eastern shoulder of the WNW-ESE-trending Pantelleria rift system between Sicily and Tunisia, which formed in the Late Miocene-Early Pliocene due to subduction roll-back associated with the Apennine-Maghrebian subduction zone (e.g., Dart et al., 1993; Jolivet and Faccenna, 2000; Cavazza and Wezel, 2003). The Il Maghlaq Fault (Bonson et al., 2007; Rotevatn et al., 2016), on the southern coast of Malta, is the largest fault (maximum normal displacement of 210 m, Bonson et al., 2007) and is the only tectonic feature on the islands showing the same trend as the Pantelleria Rift system (Fig. 1a) (Illies, 1981; Reuther and Eisbacher, 1985; Gueguen et al., 1998; Micallef et al., 2013). Otherwise, the archipelago is dominated by ENE-WSW trending horst and graben structures, considered to have formed under the same extensional regime as the Pantelleria Rift system (e.g., Dart et al., 1993; Bonson et al., 2007; Putz-Perrier and Sanderson, 2010). The Victoria Lines Fault (VLF), which is the second largest fault on Malta (maximum normal displacement of 90 m), marks the southernmost extent of the North Malta Graben (Fig. 1a) (Pedley et al., 1976). The localities utilised for this study are located 500–1000 m into the footwall of the VLF, at Ras ir Raheb. The studied fracture systems represent damage zones of smaller (displacement less than 1 m) faults, which may be considered as subsidiary faults in the damage zone of the VLF (Fig. 1a).

The stratigraphy of the Maltese islands comprises a shallow marine carbonate succession that can be subdivided into pre-, syn- and post-rift deposits with respect to the Pantelleria rifting event (Fig. 3a; Pedley et al., 1976; Dart et al., 1993; Bonson et al., 2007; Micallef et al., 2013). The pre-rift (> 21 Ma) succession includes the Lower Coralline Limestone Formation platform carbonates and the pelagic carbonates of the Lower Globigerina Limestone Member of the Globigerina Limestone Formation. The syn-rift (21–1.5 Ma) succession consists of the fine-grained foraminiferal and coccolithic Middle (MGLM; the interval of interest in this study) and Upper Globigerina Limestone Members, also of the Globigerina Limestone Formation, followed by the pelagic globigerinid marls and clays of the Blue Clay Formation, the marly glauconite lag of the Greensand Formation, and the Upper Coralline Limestone Formation. A predominantly Quaternary sedimentary succession marks the post-rift depositional sequence, including terrestrial, pelagic and hemipelagic sediments (Pedley et al., 1976; Jongsma et al., 1985; Dart et al., 1993; Micallef et al., 2013).

The MGLM in the study area consists of fine-grained limestones, divided by some thinner layers of phosphoritic conglomerate with an abundance of bivalve-, bryozoan-, solitary coral-, and echinoid-fossils, and is further described in Section 4. The MGLM is here divided into several sub-units (Fig. 3b); the studied fracture networks at Ras ir Raheb are situated within the MGLM-2 unit that consists of a 2–3 m thick interval.

## 4. Methodology

### 4.1. Outcrop analyses

A total of six fracture networks were studied in detail (Dimmen, 2016), three of which were selected for full presentation here. The fracture networks represent damage zones of small-scale (displacement <1 m) faults affecting the MGLM. Detailed mapping and structural characterisation of the studied fracture networks were performed in the field. See Section 4.3 for details on fracture network characterisation and quantitative analyses. Additionally, the stratigraphy was recorded by a stratigraphic log of the MGLM at Ras ir Raheb (Fig. 3b). Rock samples were collected from mounds and host rocks (approximately 2 m from the corresponding fracture network) at each locality for petrographic description and porosity analysis (Section 4.2). To record the location of mounds, topographic profiles were collected along the fracture networks, recording the elevation difference relative to a fixed datum (Fig. 4). The fixed datum lines for the topographic profiles were established by stretching a fixed line c. 20–30 cm above the ground, and topography was recorded by measuring the distance from the datum line to the ground.

### 4.2. Petrographic and porosity analyses

Petrographic- and porosity analysis was undertaken based on thin section analyses using a combination of optical and scanning electron microscopy. Rock samples collected in the field area were saturated with blue epoxy prior to thin section preparation, with the purpose of easier pore space recognition. A Nikon Eclipse 400 POL polarising light microscope was used to analyse the thin sections. A Zeiss Supra 55VP Field Emission Scanning Electron Microscope with a spatial resolution of 0.8 nm and magnification of 500 × , was used for further analysis of the thin sections. Image-based 2D porosity was determined using the image-processing software ImageJ, following the methods outlined by Røgen et al. (2001). Thin section photomicrographs provide a basis for estimating 2D macroporosity (porosity resolvable using optical microscope imagery), whereas the BSE images allows for a determination of 2D macro- and micro-porosity combined, termed *total porosity* herein. Micro-porosity is porosity that falls below the resolution of optical microscope imagery, but that is resolvable using BSE imagery (Rotevatn et al., 2016). A minimum of 10 photomicrographs were analysed for each thin section; for optical microscopy, half of them were analysed at 4 × magnification, and half at 10 × magnification. For BSE microscopy, a minimum of 10

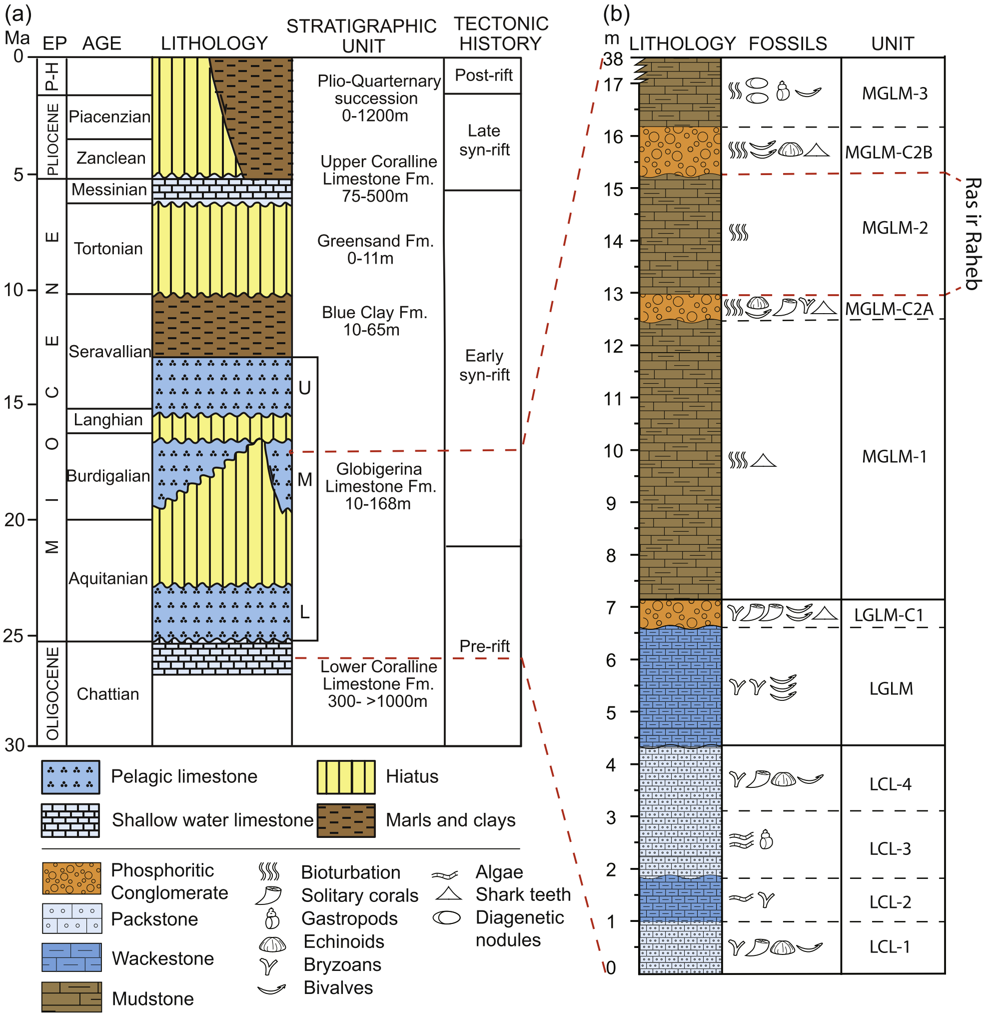

**Fig. 3.** (**a**) General stratigraphy of the Maltese Islands, showing the pre-, syn-, and post-rift sedimentary succession of Oligocene to Quaternary age. EP = epoch, P-H = Pleistocene-Holocene. From Dart et al. (1993) and Bonson et al. (2007). (**b**) Stratigraphic log from the study area at Ras ir Raheb. LCL = Lower Coralline Limestone, LGLM = Lower Globigerina Limestone Member, MGLM = Middle Globigerina Limestone Member.

images with 500 × magnification were analysed for each thin section.

### 4.3. Analysis of node and branch topology and its spatial distribution

Fracture data acquisition was undertaken by acquiring high resolution imagery for subsequent detailed analysis in ArcGIS. The studied fracture networks were digitised from the high-resolution outcrop images, and topological characterisation undertaken using an in-house ArcGIS topology toolbox. Topology describes the geometrical relationships of the fractures (e.g., Sanderson and Nixon, 2015), and can be used to characterise the arrangement of fractures within networks and determine their connectivity (Jing and Stephansson, 1997; Manzocchi, 2002; Sanderson and Nixon, 2015). In two dimensions, the topology of a fracture network consists of nodes and branches between nodes (Fig. 5; Manzocchi, 2002; Sanderson and Nixon, 2015). Nodes can be classified into three types depending on their connectivity and geometry: I-nodes represent isolated tips of fractures; Y-nodes are associated with fracture abutments or splays; and X-nodes represent crossing fractures. Y- and X-nodes connect 3 and 4 branches, respectively. Branches have a node at each end which can be an isolated (I-) node or a connecting (Y- or X-) node, thus they can also be classified into three types: isolated I–I branches; singly connected I–C branches; or doubly connected C–C branches (Sanderson and Nixon, 2015).

Sanderson and Nixon (2015) show how the number counts of the different node types ($N_I$, $N_Y$, $N_X$) can be used to calculate further

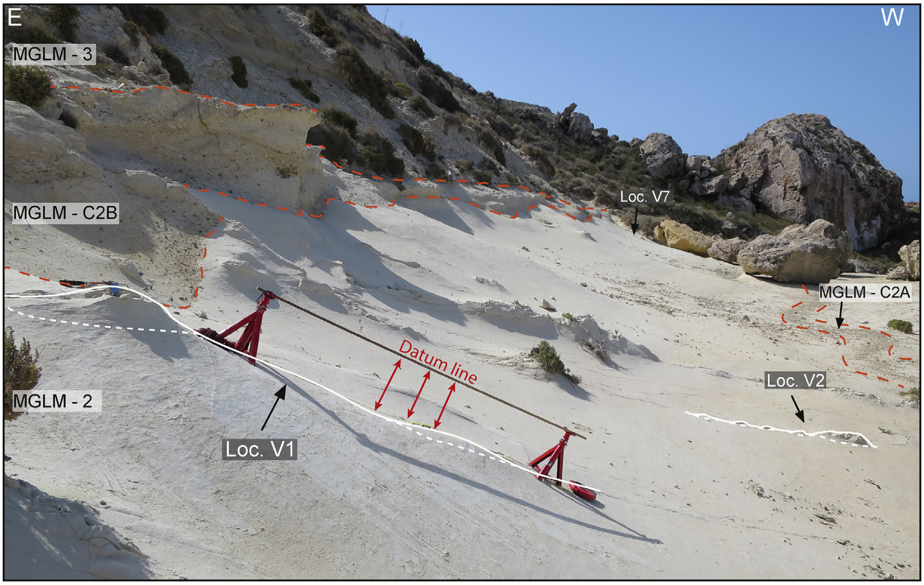

**Fig. 4.** Overview photograph of the study area, showing the three localities presented in this paper. A fixed datum line above the fracture network of locality V1 in the foreground shows how the topographic profiles were sampled. The distance from the fixed line to the ground was measured in a consistent and systematic manner to record the elevation difference caused by the cemented mounds along the fracture networks. Locality V2 and V7 can be seen in the background.

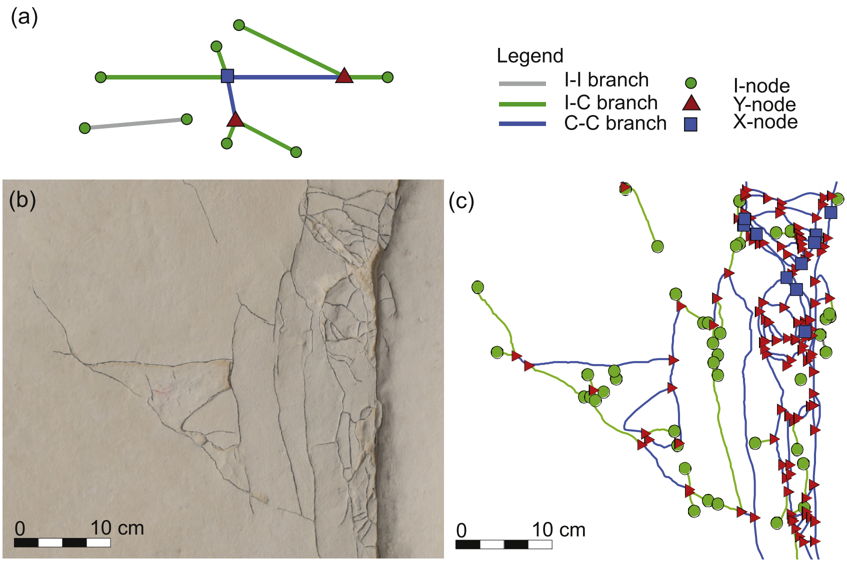

**Fig. 5.** (**a**) Topological nomenclature, as proposed by Sanderson and Nixon (2015). We differentiate between different types of *nodes* and *branches*. Nodes are isolated nodes (I-nodes), abutting or splaying nodes (Y-nodes), or as crossing nodes (X-nodes). Branches are classified as *isolated* (I–I), *partly connected* (I–C) or *fully connected* (C–C). (**b**) Field photograph showing a part of a fracture network before topological characterisation. (**c**) Digitised fracture network and topological characterisation of the outcrop example shown in (**b**).

topological measures and parameters. These can be used to quantify and describe a network's connectivity, such as the average number of connections per branch ($C_B$), which describes the degree of connectivity between branches within the network:

$$C_B = (3N_Y + 4N_X) / N_B \qquad (1)$$

The number of branches ($N_B$) is:

$$N_B = (N_I + 3N_Y + 4N_X) / 2 \tag{2}$$

As branches only have two associated nodes, that can be isolated or connected, then values of $C_B$ range from 0 to 2 (for full derivation see Sanderson and Nixon, 2015).

The spatial distribution and variation of different topological parameters and fracture abundances may be visualised to evaluate the distribution of structures and to define *complexity* and connectivity within fracture networks. For this study, we identify the different nodes and branches for each fracture network as a whole, and use the maps to create contour plots of the following parameters: (i) fracture intensities, which presents the total branch length per square metre ($m/m^2$), illustrating the distribution of branch abundance, and (ii) connecting node frequencies, illustrating variations in the number of connections ($N_C = N_X + N_Y$) per square metre ($N_C/m^2$).

## 5. Host rocks

The host rocks of the studied fracture systems comprise parts of the MGLM unit (MGLM-2 in Fig. 3b). The MGLM is comprised of fine-grained limestones, predominantly featuring skeletal fragments, and most abundantly the planktonic foraminifera *Globigerina*. The globigerinids are generally well-preserved, with most of the chambers being intact, contributing to the dominating intragranular porosity of the rock (Fig. 6a). Inter-granular porosity is found between grains, but is less prominent. The grain sizes of the foraminifera are generally in the range of 10–20 μm, but whole foraminifer shells with sizes up to 250 μm occur. Calcite cement is observed on some of the foraminifer shells and in open spaces around the samples (Fig. 6b), interpreted to be dogtooth cement. The cement growth does not seem to favour any type of foraminifera or other features, but appear at various degrees throughout the samples. Some quartz grains with an average size of 120 μm also occur within the samples but are less common (Fig. 6a).

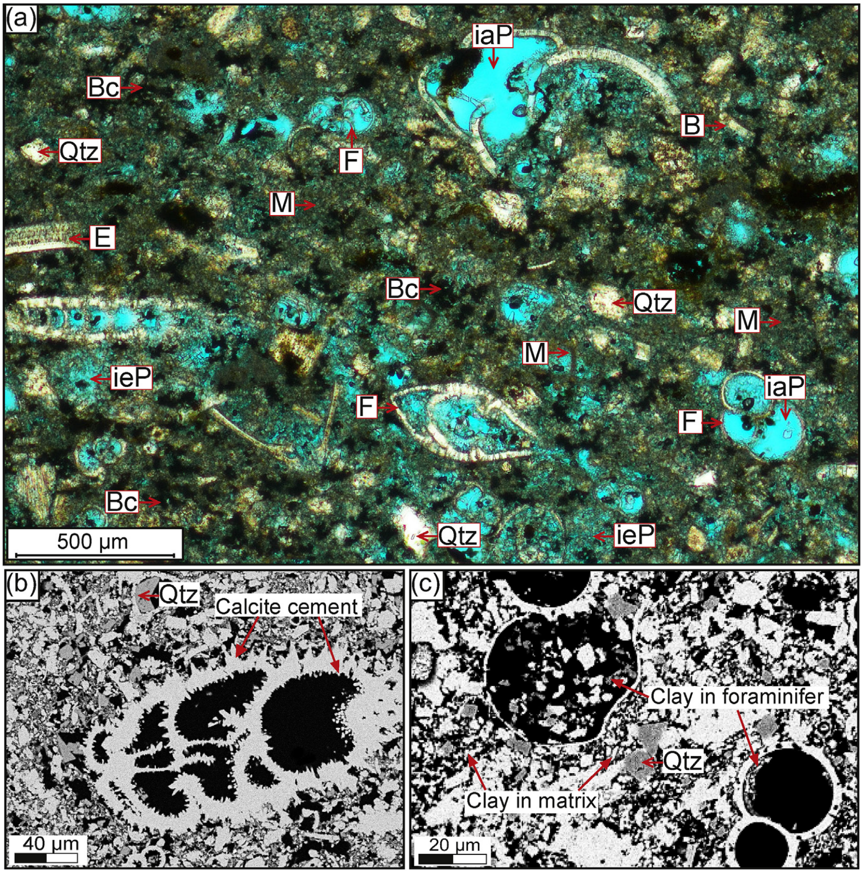

**Fig. 6.** (**a**) Photomicrograph in plane polarised light of the MGLM-2, host rock between locality V1 and V2. The clear blue colour is caused by the epoxy in which the sample was prepared, indicating pore space. Fossils of echinoderm fragments (E), bivalves (B), and foraminifera (F) are highlighted, as well as the inter- (ieP) and intragranular (iaP) porosity and matrix (M). Dark brown to black patches are thought to be bacterial shrubs (Bc) as a result of hydrothermal activity. Qtz = quartz grains. (**b**) BSE-SEM image, showing calcite cement (dog tooth) growth on both the inside and outside of a foraminifer shell. The black areas represent pore space. (**c**) BSE-SEM image, showing how fine-grained clay material can be observed both in the matrix and inside some of the foraminifer chambers. The foraminifera pointed out here do not show calcite cement growth. (For interpretation of the references to colour in this figure legend, the reader is referred to the web version of this article.)

Fine to cryptocrystalline matrix appears under the optical microscope as a dark brown mass between grains and within foraminifer shells and consist of small ($\leq 2$ μm) fragments that based on SEM analyses were identified as carbonate fragments, clay minerals and quartz (Fig. 6a and c).

## 6. Porosity distribution

The digital image analyses of the photomicrographs reveal a subtle but statistically significant difference between the porosity of the host rocks and the localised mounds. The results for 2D macroporosity derived from optical imagery analyses are presented in Fig. 7a, where each data point represents an analysis of one photomicrograph, and each column represents one thin section. The results show great variations within each thin section and each sample. The overall general trend, however, is a slightly higher porosity in the host rock than the corresponding mounds, with a mean porosity of 3.3% for the mounds and 4.1% for the host rocks. This difference is statistically significant, as discussed later in this section.

Fig. 7b shows the total porosity derived from the analysis of BSE-SEM imagery. The analysis of the BSE-SEM images yields overall significantly higher porosity values than the values attained using optical microscopy, showing an average total porosity of 12.2% for the mounds and 14.0% for the host rocks. This is because both macro- and micro-porosity are resolved, in contrast with the optical imagery, where only the macro-porosity is resolved and so lower porosity values are recorded.

The difference in the 2D total porosity between mounds and host rocks can be visually observed when comparing binary BSE-SEM images (Fig. 8). Considering these images from locality V1 as an example, it can be confirmed by visual inspection that it has a higher host rock porosity (measured to 16.5%) compared with the pore space present in the corresponding mound (measured to 10.7%).

Porosity statistics show that the values of the porosity measurements plot linearly ($R = 0.98$ for BSE-SEM images and $R = 0.99$ for photomicrographs) in a cumulative probability scale, indicating that the values are normal graded. They can therefore be used in parametric tests to see if the populations show any significant differences in variance (squared standard deviation) or average values. Snedecor's F-test was used to check if the populations show significant differences in variance, while a Student's t-test was used to check if the average values of the populations show significant

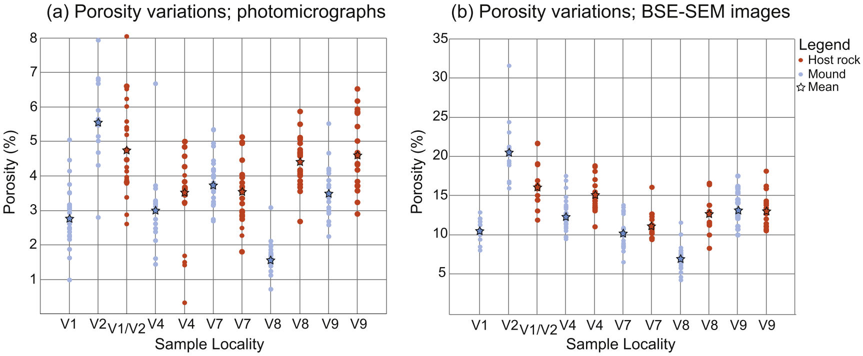

**Fig. 7.** Data from the thin section samples from mound and host rock at each locality. (**a**) Results from the analysis of microphotographs. (**b**) Results from the analysis of BSE-SEM images. Each dot represents one analysed photograph, and each column represents one thin section. The overall general trend shows a slightly higher porosity in the host rock compared with the mounds.

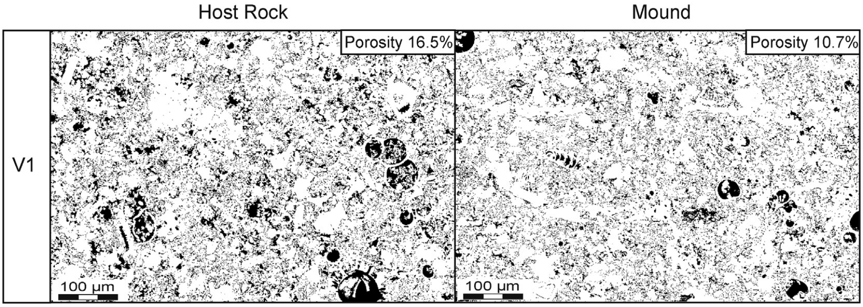

**Fig. 8.** Comparison of binary BSE-SEM images from the host rock and the corresponding mound for localities V1, V2 and V7. The pore space is displayed in black, and the general porosity for each thin section in which the image is retrieved is pointed out in the uppermost right hand corner of each image (i.e., it is not the porosity for the image displayed here).

differences. The level of significance is described by the factor $\alpha$; a low $\alpha$-value indicate a test of high significance.

The results from Snedecor's F-test show that the variance for the mound values are greater than the variance for the host rock values for both the 4 × and 500 × magnification, both with $\alpha = 0.0005$, while the variances are not significantly different for the 10 × magnification dataset, which got $\alpha = 0.005$. The results from the Student's t-test show that average value for the host rock is significantly greater than the average value for the mound for all of the three data sets. The statistical tests confirm that the mounds are associated with an overall lower porosity than the surrounding host rocks, and that the differences are statistically significant. These porosity variations are interpreted to reflect the results of selective and localised cementation of the mounds. Localised cementation does also explain the topographic relief of the mounds, since their increased cementation make them more resistant to weathering than the surrounding host rocks.

## 7. Geometry and topology of the fracture networks

To investigate the spatial and causal relationship between the cemented mounds and the fracture networks, we present a quantitative geometrical and topological analysis of the networks. A total of six localities with cemented mounds were investigated (Dimmen, 2016), all situated in the MGLM-2 unit immediately south of Ras ir Raheb (Fig. 1b). The mounds generally exhibit an elliptical shape and vary in size with the long axis ranging from 10 to 100 cm; the specific size and shape of each mound is recorded by the topographic profiles presented for each locality. The fracture networks represent damage zones of normal faults with less than 2 m of displacement, and are comprised of smaller faults (displacement generally up to a few centimetres) and joints. All of the studied fracture networks show a varying degree of structural complexity along strike. Out of the six localities, we have selected three for full presentation in the following (Localities V1, V2 and V7, shown in Figs. 9–11, respectively). All of the fracture networks have been studied in pavement outcrops (sub-horizontal to ~20° seaward dipping outcrop surfaces), providing excellent map-view exposure where the along-strike variability of the fracture networks may be studied in detail.

Greatest structural complexity occurs in zones where two fracture segments coalesce to form hard-linked relays, or in intersections where one fracture segment splays or abuts against another. The structurally complex zones are distributed along main fault or fracture traces, extending 10–100 cm along strike, separated by less complex zones. Figs. 9–11 portray: (a) the digitised fracture networks; (b) fracture intensity maps; (c) connecting node frequency maps; (d) graphs showing the fracture intensities; (e) connecting node frequencies; and (f) topographic profiles. The graphs and the topographic profiles for each fault zone were recorded along the same line for each locality, marked in (a) in every figure. The more structurally complex zones at each locality generally coincide with mounds along the fracture network. The topological characterisation shows that these zones generally also coincide with areas of higher connecting node frequencies and fracture intensities.

### 7.1. Example 1, locality V1

The fracture network of locality V1 covers 3.5 m of a fault zone, and consists of three main segments oriented E-W to NE-SW (Segments I, II and III in Fig. 9a). Five complex zones, marked A-E, are recognised (Fig. 9a). These zones all correspond with areas of higher fracture intensities and higher connecting node frequencies (Fig. 9b and c). The topography profile in (Fig. 9f) shows that the large topographic high at the eastern end of the profile also corresponds with complex zone E (Fig. 9a), and shows an increase in connecting node frequency (Fig. 9e) and fracture intensity (Fig. 9d). The complex zones C and D (Fig. 9a) correspond with peaks in fracture intensities (Fig. 9d) and connecting node frequencies (Fig. 9e). In the topographic profile (Fig. 9f), a wide (c. 80 cm) mound corresponds with the two complex zones C and D combined. Complex zones A and B (Fig. 9a), are associated with peaks in fracture intensity and connecting node frequencies, (Fig. 9d and e), and represent areas of high intensity intensities and connecting node frequencies (Fig. 9b and c). Complex zones A and B are not associated with mounds, as recorded by the topographic profile (Fig. 9f).

### 7.2. Example 2, locality V2

Locality V2 consists of a 2.75 m long fracture network, oriented E-W (Fig. 10a), which can be divided into two main segments (Segments I and II in Fig. 10a). Segment I consists of one relatively large complex zone, A (Fig. 10a), and connects with segment II through complex zone B (Fig. 10a). Segment II constitutes the eastern half of the system and contains three smaller complex zones, indicated as C, D and E (Fig. 10a).

The complex zones show higher fracture intensities (Fig. 10b) and higher frequencies of connecting nodes (Fig. 10c). The complex zones also coincide with peaks in the graphs of fracture intensity, connecting node frequency, and topography (Fig. 10d–f). The positive correlation is most obvious for the largest mound in complex zone A, for which both the fracture intensity graph (Fig. 10d), the connecting node frequency graph (Fig. 10e), and the topographic profile (Fig. 10f) show positive curves. Complex zone B show positive correlations for both the fracture intensity (Fig. 10d) and the connecting node frequency (Fig. 10e) graphs, but is not as evident in the topographic profile (Fig. 10f). Complex zone C can be recognised through a minor peak in all three graphs (Fig. 10d–f), while complex zones D and E, which is a bit larger than complex zone C, shows a somewhat higher peak in the fracture intensity graph (Fig. 10d) and the connecting node frequency graph (Fig. 10e) than complex zone C.

### 7.3. Example 3, locality V7

This locality is limited to a 3 m portion of a W-trending normal fault, which shows a throw of 7 cm in an overlying bed of phosphoritic conglomerate. The fracture network is composed of two E-W oriented main segments (Segments I and II in Fig. 11a), linked together in a hard-linked relay zone, and four complex zones marked A-D (Fig. 11a). Segment I comprises the western half of the locality, where complex zone A forms the western part of the relay that links the two segments (Fig. 11a). This breached relay constitutes complex zone B (Fig. 11a), which is the largest complex zone of locality V7. The smaller complex zones C and D are located along segment II, in the eastern part of the locality (Fig. 11a).

The complex zones show higher fracture intensities (Fig. 11b) and higher connecting node frequencies (Fig. 11c). Complex zone B is the highest peak in the topographic profile (Fig. 11f), the fracture intensity graph (Fig. 11d), and the connecting node frequency graph (Fig. 11e). Complex zone A shows a positive correlation with the fracture intensity graph (Fig. 11b) and the connecting node frequency graph (Fig. 11c). A peak in all three graphs (Fig. 11d–f) can be correlated with complex zone C, while complex zone D can be recognised in the graph showing the connecting node frequencies (Fig. 11e), but are not recorded in the fracture intensity graph (Fig. 11d) or the topographic profile (Fig. 11f).

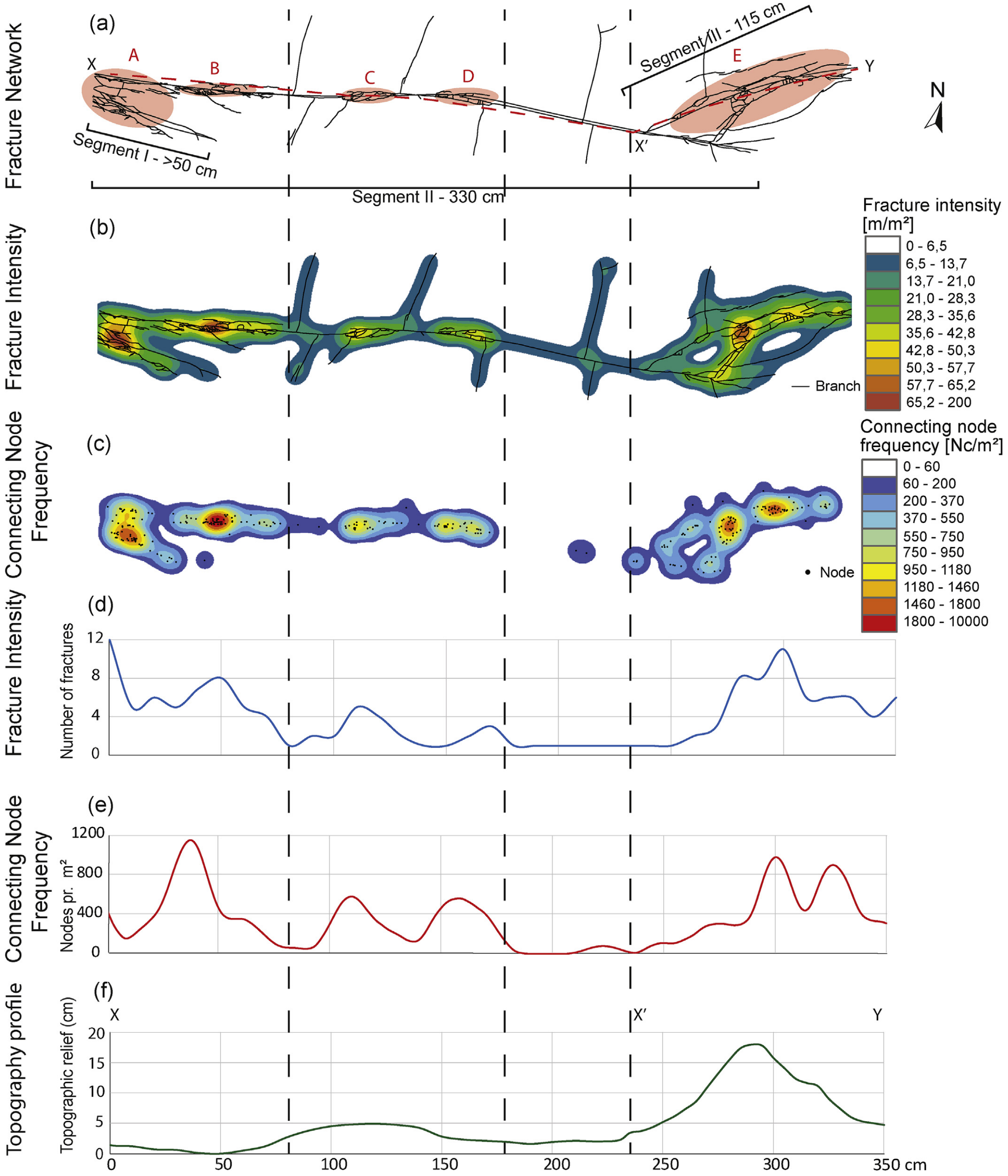

**Fig. 9.** (**a**) Digitised map of the fracture network at locality V1, showing three main segments. The more structurally complex zones are marked with soft red and labelled A-E. (**b**) Contour map, showing the fracture abundance measure “fracture intensity”. (**c**) Contour map showing the topological parameter “connecting node frequency”. (**d**) Graph collected along the red dashed line in Fig. 9(a), showing the fracture intensity-. (**e**) Graph collected along the red dashed line in Fig. 9(a), showing the connecting node frequency along the network. (**f**) Topographic profile, collected along the red, dashed line in Fig. 9(a), showing the relief variations along the fracture network. The dashed black lines are guides for easier correlation between the maps and graphs. (For interpretation of the references to colour in this figure legend, the reader is referred to the web version of this article.)

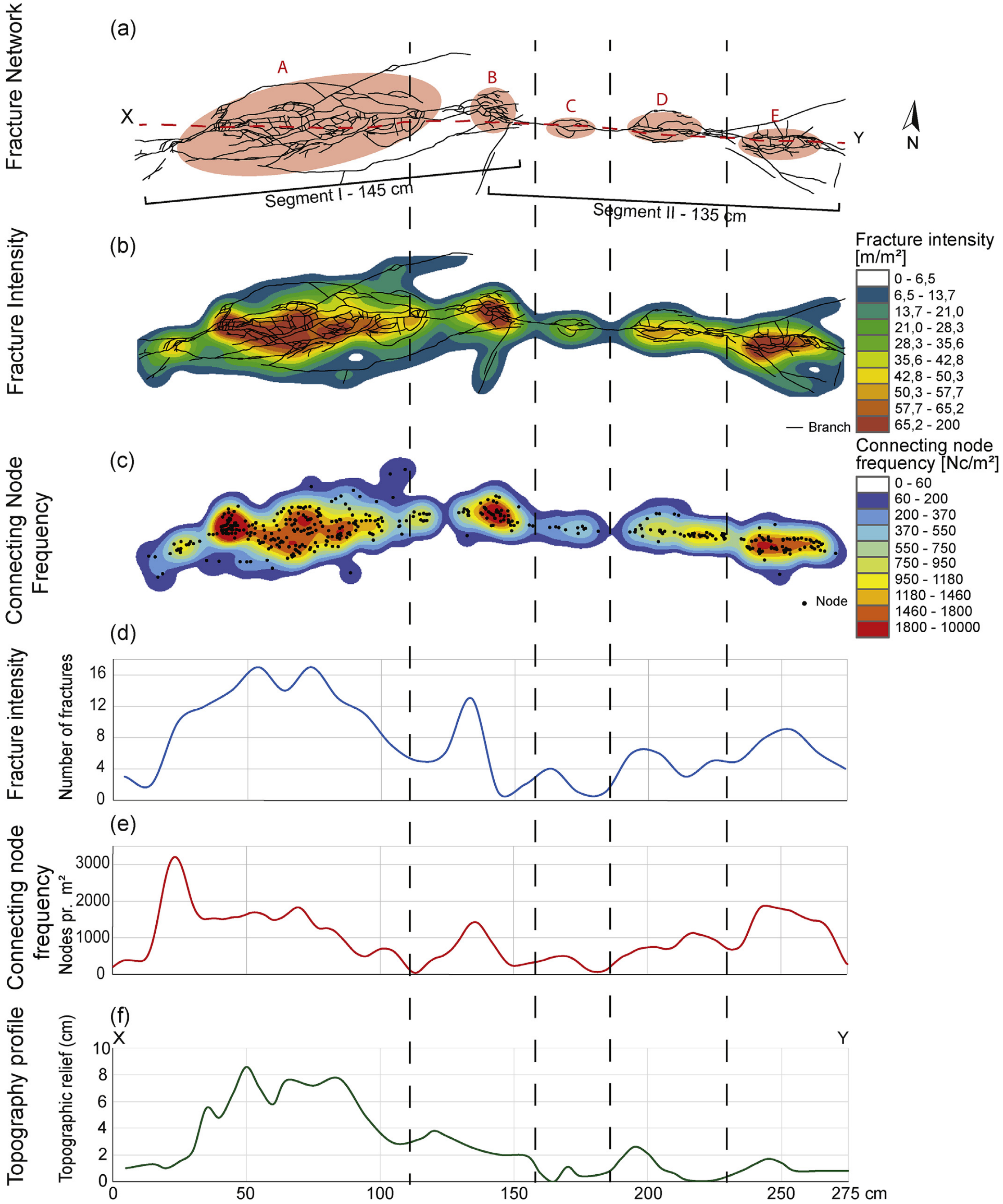

**Fig. 10.** (**a**) Digitised map of the fracture network at locality V2, showing three main segments. The more structurally complex zones are marked with soft red and labelled A-E. (**b**) Contour map, showing the fracture abundance measure “fracture intensity”. (**c**) Contour map showing the topological parameter “connecting node frequency”. (**d**) Graph collected along the red dashed line in Fig. 10(a), showing the fracture intensity. (**e**) Graph collected along the red dashed line in Fig. 10(a), showing the connecting node frequency along the network. (**f**) Topographic profile, collected along the red, dashed line in Fig. 10(a), showing the relief variations along the fracture network. The dashed black lines are guides for easier correlation between the maps and graphs. (For interpretation of the references to colour in this figure legend, the reader is referred to the web version of this article.)

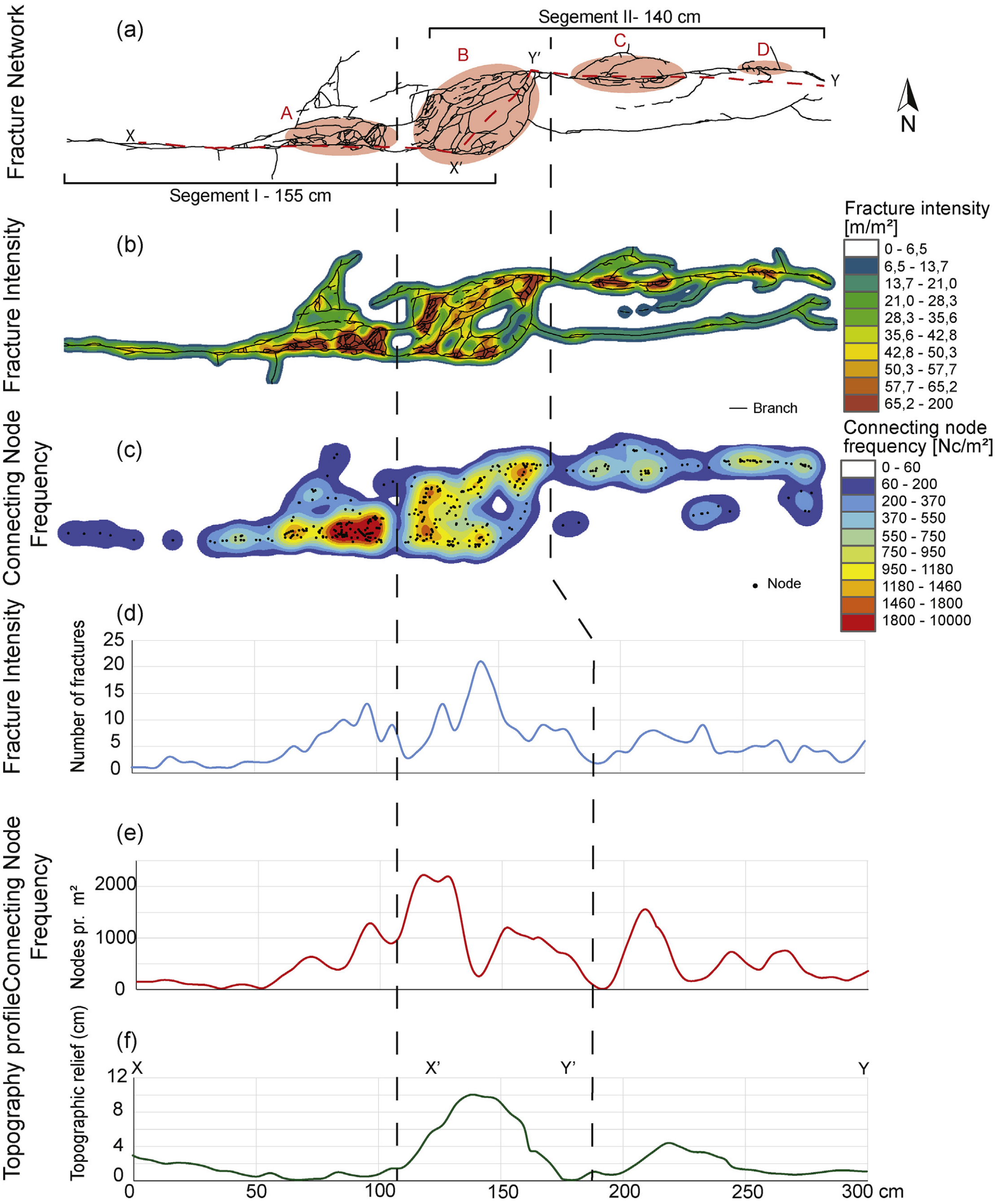

**Fig. 11.** (**a**) Digitised map of the fracture network at locality V7, showing three main segments. The more structurally complex zones are marked with soft red and labelled A-D. (**b**) Contour map, showing the fracture abundance measure "fracture intensity". (**c**) Contour map showing the topological parameter "connecting node frequency". (**d**) Graph collected along the red dashed line in Fig. 11(a), showing the fracture intensity. (**e**) Graph collected along the red dashed line in Fig. 11(a), showing the connecting node frequency along the network. (**f**) Topographic profile, collected along the red, dashed line in Fig. 11(a), showing the relief variations along the fracture network. The dashed black lines are guides for easier correlation between the maps and graphs. (For interpretation of the references to colour in this figure legend, the reader is referred to the web version of this article.)

## 8. Discussion

The porosity analyses presented in Section 6 show that the mounds are associated with lower porosity compared with the surrounding host rocks. Based on this, we attribute the formation of the mounds to localised increases in palaeo-fluid-rock-interaction in the form of selective cementation, which led to the mounds being resistant to weathering and therefore forming topographic highs on the outcrops. In the following, we discuss the spatial distribution of the mounds relative to variability of the geometric and topological properties of the fracture network presented in Section 7, to elucidate the relationship between network complexity and past fluid-rock interaction.

The studied fracture networks show that the low-porosity mounds are preferentially developed in the parts of the fracture networks that are associated with high fracture intensities and connecting node frequencies (Figs. 9–11). High fracture intensity indicates that the network is structurally complex, while high connecting node frequency indicates that the fractures in the network are well connected, and that the network itself is highly connected (cf. Morley and Nixon, 2016). The trend is therefore that the complex and well-connected parts of the fracture networks coincide with evidence for palaeo-fluid-flow in the form of cemented mounds. Having established this spatial correlation, two key questions that arise are “how do the structurally complex zones form?” (Section 8.1), and “what is their role in controlling the localisation of flow?” (Section 8.2).

### 8.1. How do structurally complex zones form?

Faults and other types of fractures generally form zones that consist of several segments that interact, i.e., jog, bifurcate and/or link, creating networks of longer, continuous faults or other types of fractures with irregularities like fault bends and fault intersections (e.g., Peacock and Sanderson, 1991, 1994; Cartwright et al., 1995; Mansfield and Cartwright, 1996; Tavarnelli and Pasqui, 2000; Walsh et al., 2003; Rotevatn and Bastesen, 2014; Peacock et al., 2017). Such irregularities may cause greater stress and local stress concentrations, which further induce small-scale fracturing along and around the fault plane, resulting in zones of higher complexity (Segall and Pollard, 1980; Maerten et al., 2002). Perturbation of the stress field around faults during their growth affects the development of joints in proximity to the fault, tending to make fractures grow at high angles to the faults (Tamagawa and Pollard, 2008). Interaction of the local stress fields around overlapping fault tips leads to a locally increased shear stress (Crider and Pollard, 1998) and rotation of the stress field as a function of the $\sigma_1/\sigma_2$ principal stress ratio (Kattenhorn et al., 2000). Therefore, high fracture intensities and variable fracture orientations are to be expected. As the zones of structural complexity associated with the studied fracture networks are all found in conjunction with relay zones or intersections between the main fracture segments of the networks, we interpret that the areas of structural complexity formed due to fracture interaction, stress enhancement and stress perturbation during fault growth.

### 8.2. What is the role of structural complexity for controlling flow?

Structurally complex zones are areas of elevated fracture abundance and complexity, which tend to act as fluid flow conduits (e.g., Berkowitz, 1995; Gartrell et al., 2004). Fluids tend to localise and flow in and along the abundant fractures (if open) in the structurally complex zones (Davatzes and Aydin, 2003) (Fig. 12). Two types of fluid flow conduits along active faults can be identified. One type are conduits along the fault plane caused by dilation associated with slip, and the second type are created by secondary structures near fault tips and other structurally complex zones such as relays and fault intersections (Martel, 1990; Barton et al., 1995; Martel and Boger, 1998; Kattenhorn et al., 2000; Davatzes and Aydin, 2003; Tamagawa and Pollard, 2008). These secondary structures are an especially important pathway for fluid flow in tight carbonate rocks with low matrix permeability (Tamagawa and Pollard, 2008; Casini et al., 2011; Rotevatn and Bastesen, 2014).

The complex zones documented at the localities in this study show high fracture intensities and high degrees of network connectivity recorded by high connecting node frequencies. In the following, we discuss the physical mechanisms that explain why structurally complex zones can represent conduits for localised flow. One reason is that open fractures are associated with high permeability in contrast to a low-porous host rock, and a structurally complex zone with high fracture intensity, various fracture orientations and high connectivity would represent a particularly high-permeable fluid conduit (e.g., Rotevatn and Bastesen, 2014). Secondly, stress perturbation may also provide wider fracture apertures to further increase permeability in areas of fault interaction, relay zones or fault tips (Tamagawa and Pollard, 2008). Thirdly, the great variety of fracture orientations in such areas mean that for any given stress field, there is a great chance that some of the fractures are optimally oriented to be kept open (Sanderson and Zhang, 2004).

### 8.3. The relative roles of increased flow vs. increased fluid-rock reactions

The mounds along the studied fracture networks show a lower porosity than the host rock, which we interpret to be a result of increased fluid flow because the mounds coincide with structurally complex zones. Increased fluid flow could cause more cementation, as more mineralising fluids can pass through the rock (e.g., Flügel, 2010). The mounds may not only be a record of increased flow, however, and other mechanisms may operate. For example, the increased cementation may be a result of increased fluid-rock reactions in the complex areas, caused by intense fracturing. The increased number of fractures in the complex zones fragment the rock volume, leading to a larger reactive surface area available to the mineralising fluids (Lüttge et al., 1999; Flügel, 2010). We suggest that, in the structurally complex zones in this study area, a combination of (i) increased fluid flow and (ii) high reactive surface area caused increased fluid-rock interaction and, therefore, localised cementation and mound formation.

### 8.4. Implications of being able to understand and quantify structural controls on fluid flow

As shown here, structural complexity may control localised flow and fluid-rock reactions, and structural complexity may be quantified by characterising the geometric and topological properties of fault and fracture networks. In the following, we elaborate on the implications of understanding structural controls on flow, and the applications of being able to quantify structural complexity.

Understanding structural complexity and its controls on fluid flow has a wide range of implications and applications. For example, Davidson et al. (2016) examine radon ($^{222}$Rn) anomalies due to upward migration of fluids along fault zones in New Zealand. They show that the concentration of radon isotopes is generally higher near faults and fault intersections, indicating a positive correlation between structural complexity and the flow of radon gas. Similar results have been reported from India (Virk and Singh, 1993), California (King et al., 1996), Egypt (Moussa and El Arabi, 2003), and Japan (Igarashi et al., 1995). Rowland and Sibson

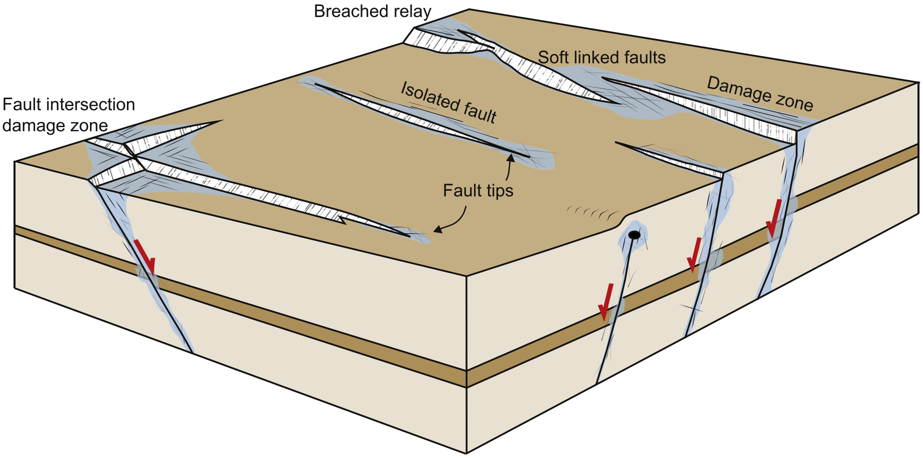

**Fig. 12.** Schematic illustration of preferential fluid localisation, illustrated by the blue colour, along faults and fault intersections (after Peacock et al., 2016). Fluid flow may localise in fault damage zones and along fault planes, especially in more complex zones, such as linkage points, fault tips and fault intersections. (For interpretation of the references to colour in this figure legend, the reader is referred to the web version of this article.)

(2004) and Curewitz and Karson (1997) identify relationships between structural complexity and hydrothermal activity, and show that concentrations of geothermal zones and the positions of hot springs coincide with increased vertical flow at fault steps, relays and fault intersections. Gartrell et al. (2004) examine the effect of fault intersections on hydrocarbon seal breach through three-dimensional numerical modelling, and show that zones of high dilation are generated close to fault intersections, leading to high permeable zones with a concentration of open fractures ideal for fluid migration, and therefore escape of hydrocarbons. Fluid flow associated with fault intersections may also affect earthquake rupture, as changes in increase fluid pressure may promote fault slip (Sibson, 1996; Talwani, 1999; Kim et al., 2004). Faults, fractures, and structurally complex zones in the shallow crust can also impact environmental issues, such as $CO_2$ storage, leakage from radioactive waste disposal sites, contaminant transport, and flow patterns of groundwater (Yoshida et al., 2008; Dockrill and Shipton, 2010; Bense et al., 2013).

The above examples highlight the importance of understanding structural controls on fluid flow for a range of purposes. The techniques used in this study, where we correlate proxies for palaeo-fluid-flow with quantified structural complexity and connectivity, may improve how structural controls on flow are analysed and assessed. For example, being able to quantify and visualise the distribution and magnitude of structural complexity and fault/fracture network connectivity may find applications in the generation of hazard maps for radon gas, earthquake prediction, hydrocarbon seal risk assessment, ore mineral deposits exploration and more.

## 9. Conclusions

The aims of this paper have been to improve the understanding of structurally controlled fluid flow, and, specifically, to demonstrate a novel approach to quantify and visualise the relationships between fluid flow and structural complexity. Field-based investigation, characterisation of the geometry and topology of fracture networks, and porosity analysis have been used to investigate the relationship between structural complexity and proxies (cemented mounds) for palaeo-fluid flow around small-scale normal faults in carbonate rocks, Malta. The following conclusions are made:

- Mounds exhibit an overall lower porosity (0.3–6% difference) than the host rock, as a result of selective, localised cementation.
- Topological analyses of the fracture networks indicate that areas of fracture interaction (relays, fault intersections), which we term *structurally complex areas*, are associated with higher connecting node frequency and fracture intensities than elsewhere, which indicates that these parts of the fracture networks are highly connected.
- The low-porosity cemented mounds spatially coincide with the structurally most complex and well-connected parts of the fracture networks, indicating that the complex areas are associated with increased fluid-rock interaction.
- Increased fluid-rock interaction in the structurally complex areas are attributed to a combination of two effects. Firstly, the structurally complex areas represent conduits for localised flow of mineralising fluids, due to higher fracture abundancy and high fracture connectivity. Secondly, the intense fracturing in the structurally complex areas lead to greater reactive surface area, promoting an increase in fluid-rock reactions.

The findings have great implications for understanding the relationship between structural complexity and fluid flow, and the quantification and visualisation of structural complexity. Quantification of the relationship between structural complexity and flow has the potential to bring about improvements in the prediction of fluid flow properties in the subsurface. For example, topological characterisation of seismic-scale fault networks based on subsurface data, combined with similar data from analogue studies, may offer a more direct route to quantify and predict subsurface flow properties.

## Acknowledgements

We thank Enrico Tavarnelli and an anonymous reviewer for their constructive and positive reviews, leading to improvement and clarification of this paper, and editor Cees Passchier for editorial guidance. Ray Leadbitter at the Independent Petrographic Services Ltd. in Aberdeen, UK, are thanked for preparation of excellent thin sections. Thanks are given to Gunnar Sælen for helpful discussions concerning the host rock characterisation and for carrying out the geostatistical analysis. Irina Korneva and Toms Buls contributed with advice regarding *ImageJ* and the porosity estimations. Thomas B. Kristensen, Ulrike Freitag and Arild Andresen are thanked for great company and inspiring discussions during fieldwork in Malta, while Carmelo Agius and his wife Anna Aguis, are thanked for hosting us all. BKK is thanked for fundings through the BKK-UiB agreement. Nixon and Dimmen are also supported by scholarships from VISTA, a collaborative program for fundamental research by the Norwegian Academy of Science and Letters, and Statoil. Rotevatn, Peacock, and Nixon further acknowledge support for the ANIGMA project from the Research Council of Norway (project no. 244129/E20) through the ENERGIX program, and Statoil through the Akademia agreement. We thank the University of Bergen for partial funding for publishing this paper open access.

## References

Aydin, A., 2000. Fractures, faults, and hydrocarbon entrapment, migration and flow. Mar. Petrol. Geol. 17, 797–814.

Barton, C.A., Zoback, M.D., Moos, D., 1995. Fluid flow along potentially active faults in crystalline rock. Geology 23, 683–686.

Bense, V.F., Gleeson, T., Loveless, S.E., Bour, O., Scibek, J., 2013. Fault zone hydrogeology. Earth-Sci. Rev. 127, 171–192.

Bense, V.F., Van Balen, R., 2004. The effect of fault relay and clay smearing on groundwater flow patterns in the Lower Rhine Embayment. Basin Res. 16, 397–411.

Berkowitz, B., 1995. Analysis of fracture network connectivity using percolation theory. Math. Geol. 27, 467–483.

Bonson, C.G., Childs, C., Walsh, J.J., Schöpfer, M.P.J., Carboni, V., 2007. Geometric and kinematic controls on the internal structure of a large normal fault in massive limestones: the Maghlaq Fault, Malta. J. Struct. Geol. 29, 336–354.

Caine, J.S., Evans, J.P., Forster, C.B., 1996. Fault zone architecture and permeability structure. Geology 24, 1025–1028.

Caine, J.S., Forster, C.B., 1999. Fault zone architecture and fluid flow: insights from field data and numerical modeling. Geophys. Monogr. 113, 101–127.

Cartwright, J.A., Trudgill, B.D., Mansfield, C.S., 1995. Fault growth by segment linkage: an explanation for scatter in maximum displacement and trace length data from the Canyonlands Grabens of SE Utah. J. Struct. Geol. 17, 1319–1326.

Casini, G., Gillespie, P., Vergés, J., Romaire, I., Fernández, N., Casciello, E., Saura, E., Mehl, C., Homke, S., Embry, J.-C., 2011. Sub-seismic fractures in foreland fold and thrust belts: insight from the Lurestan Province, Zagros Mountains, Iran. Pet. Geosci. 17, 263–282.

Cavazza, W., Wezel, F.C., 2003. The Mediterranean region-a geological primer. Episodes 26, 160–168.

Crider, J.G., Pollard, D.D., 1998. Fault linkage: three-dimensional mechanical interaction between echelon normal faults. J. Geophys. Res. Solid Earth 103, 24373–24391.

Curewitz, D., Karson, J.A., 1997. Structural settings of hydrothermal outflow: fracture permeability maintained by fault propagation and interaction. J. Volcanol. Geotherm. Res. 79, 149–168.

Dart, C., Bosence, D., McClay, K., 1993. Stratigraphy and structure of the Maltese graben system. J. Geol. Soc. Lond. 150, 1153–1166.

Davatzes, N.C., Aydin, A., 2003. Overprinting faulting mechanisms in high porosity sandstones of SE Utah. J. Struct. Geol. 25, 1795–1813.

Davidson, J.R.J., Fairley, J., Nicol, A., Gravley, D., Ring, U., 2016. The origin of radon anomalies along normal faults in an active rift and geothermal area. Geosphere 12, 1656–1669.

Dimmen, V., 2016. Structural controls on fluid flow in carbonate rocks: quantitative insights from the Maltese Islands. MSc. thesis. Department of Earth Science. University of Bergen, p. 88. unpublished.

Dockrill, B., Shipton, Z.K., 2010. Structural controls on leakage from a natural CO 2 geologic storage site: central Utah, USA. J. Struct. Geol. 32, 1768–1782.

Eichhubl, P., Greene, H., Naehr, T., Maher, N., 2000. Structural control of fluid flow: offshore fluid seepage in the Santa Barbara Basin, California. J. Geochem. Explor. 69, 545–549.

Flügel, E., 2010. Microfacies of Carbonate Rocks, Analysis, Interpretation and Application, second ed. Springer, Heidelberg.

Fossen, H., Johansen, T.E.S., Hesthammer, J., Rotevatn, A., 2005. Fault interaction in porous sandstone and implications for reservoir management; examples from southern Utah. AAPG Bull. 89, 1593–1606.

Fossen, H., Rotevatn, A., 2016. Fault linkage and relay structures in extensional settings - a review. Earth-Sci. Rev. 154, 14–28.

Gartrell, A., Zhang, Y., Lisk, M., Dewhurst, D., 2004. Fault intersections as critical hydrocarbon leakage zones: integrated field study and numerical modelling of an example from the Timor Sea, Australia. Mar. Petrol. Geol. 21, 1165–1179.

Gueguen, E., Doglioni, C., Fernandez, M., 1998. On the post-25 Ma geodynamic evolution of the western Mediterranean. Tectonophysics 298, 259–269.

Igarashi, G., Saeki, S., Takahata, N., Sumikawa, K., 1995. Ground-water radon anomaly before the Kobe earthquake in Japan. Science 269, 60–61.

Illies, J.H., 1981. Graben formation — the Maltese Islands — a case history. Tectonophysics 73, 151–168.

Jing, L., Stephansson, O., 1997. Network topology and homogenization of fractured rocks. In: Jamtveit, B., Yardley, B.W.D. (Eds.), Fluid Flow and Transport in Rocks. Springer, pp. 191–202.

Jolivet, L., Faccenna, C., 2000. Mediterranean extension and the Africa-Eurasia collision. Tectonics 19, 1095–1106.

Jolley, S.J., Barr, D., Walsh, J., Knipe, R., 2007. Structurally complex reservoirs: an introduction. In: Jolley, S.J., Barr, D., Walsh, J., Knipe, R. (Eds.), Structurally Complex Reservoirs. Geological Society, London, pp. 1–24. Special Publications.

Jongsma, D., van Hinte, J.E., Woodside, J.M., 1985. Geologic structure and neotectonics of the North African continental margin south of Sicily. Mar. Petrol. Geol. 2, 156–179.

Kattenhorn, S.A., Aydin, A., Pollard, D.D., 2000. Joints at high angles to normal fault strike: an explanation using 3-D numerical models of fault-perturbed stress fields. J. Struct. Geol. 22, 1–23.

Kerrich, R., 1986. Fluid infiltration into fault zones: chemical, isotopic, and mechanical effects. Pure Appl. Geophys. 124, 225–268.

Kim, Y.-S., Peacock, D.C.P., Sanderson, D.J., 2004. Fault damage zones. J. Struct. Geol. 26, 503–517.

King, C.-Y., King, B.-S., Evans, W.C., Zhang, W., 1996. Spatial radon anomalies on active faults in California. Appl. Geochem. 11, 497–510.

Lüttge, A., Bolton, E.W., Lasaga, A.C., 1999. An interferometric study of the dissolution kinetics of anorthite: the role of reactive surface area. Am. J. Sci. 299, 652–678.

Maerten, L., Gillespie, P., Pollard, D.D., 2002. Effects of local stress perturbation on secondary fault development. J. Struct. Geol. 24, 145–153.

Mansfield, C.S., Cartwright, J.A., 1996. High resolution fault displacement mapping from three-dimensional seismic data: evidence for dip linkage during fault growth. J. Struct. Geol. 18, 249–263.

Manzocchi, T., 2002. The connectivity of two-dimensional networks of spatially correlated fractures. Water Resour. Res. 38, 1–20.

Martel, S.J., 1990. Formation of compound strike-slip fault zones, Mount Abbot quadrangle, California. J. Struct. Geol. 12, 869–882.

Martel, S.J., Boger, W.A., 1998. Geometry and mechanics of secondary fracturing around small three-dimensional faults in granitic rock. J. Geophys. Res. Solid Earth 103, 21299–21314.

Micallef, A., Berndt, C., Debono, G., 2011. Fluid flow systems of the Malta plateau, central Mediterranean Sea. Mar. Geol. 284, 74–85.

Micallef, A., Foglini, F., Le Bas, T., Angeletti, L., Maselli, V., Pasuto, A., Taviani, M., 2013. The submerged paleolandscape of the Maltese Islands: morphology, evolution and relation to Quaternary environmental change. Mar. Geol. 335, 129–147.

Michie, E., Haines, T., Healy, D., Neilson, J., Timms, N.E., Wibberley, C., 2014. Influence of carbonate facies on fault zone architecture. J. Struct. Geol. 65, 82–99.

Missenard, Y., Bertrand, A., Vergély, P., Benedicto, A., Cushing, M.-E., Rocher, M., 2014. Fracture-fluid relationships: implications for the sealing capacity of clay layers - insights from field study of the Blue Clay formation, Maltese islands. Bull. Soc. Géol. Fr. 185, 51–63.

Morley, C., Nixon, C., 2016. Topological characteristics of simple and complex normal fault networks. J. Struct. Geol. 84, 68–84.

Moussa, M.M., El Arabi, A.-G.M., 2003. Soil radon survey for tracing active fault: a case study along Qena-Safaga road, Eastern Desert, Egypt. Radiat. Meas. 37, 211–216.

Oliver, N., 1996. Review and classification of structural controls on fluid flow during regional metamorphism. J. Metamorph. Geol. 14, 477–492.

Ono, T., Yoshida, H., Metcalfe, R., 2016. Use of fracture filling mineral assemblages for characterizing water-rock interactions during exhumation of an accretionary complex: an example from the Shimanto Belt, southern Kyushu Japan. J. Struct. Geol. 87, 81–94.

Peacock, D.C.P., Nixon, C., Rotevatn, A., Sanderson, D., Zuluaga, L., 2016. Glossary of fault and other fracture networks. J. Struct. Geol. 92, 12–29.

Peacock, D.C.P., Nixon, C.W., Rotevatn, A., Sanderson, D.J., Zuluaga, L.F., 2017. Interacting faults. J. Struct. Geol. 97, 1–22.

Peacock, D.C.P., Sanderson, D.J., 1991. Displacements, segment linkage and relay ramps in normal fault zones. J. Struct. Geol. 13, 721–733.

Peacock, D.C.P., Sanderson, D.J., 1994. Geometry and development of relay ramps in normal fault systems. AAPG Bull. 78, 147–165.

Pedley, H., House, M., Waugh, B., 1976. The geology of Malta and Gozo. Proc. Geolo. Assoc. 87, 325–341.

Putz-Perrier, M.W., Sanderson, D.J., 2010. Distribution of faults and extensional strain in fractured carbonates of the North Malta Graben. Am. Assoc. Petrol. Geol. Bull. 94, 435–456.

Reuther, C.-D., Eisbacher, G., 1985. Pantelleria Rift - crustal extension in a convergent intraplate setting. Geol. Rundsch. 74, 585–597.

Rotevatn, A., Bastesen, E., 2014. Fault linkage and damage zone architecture in tight carbonate rocks in the Suez Rift (Egypt): implications for permeability structure along segmented normal faults. In: Spence, G.H., Redfern, J., Aguilera, R., Bevan, T.G., Cosgrove, J.W., Couples, G.D., Daniel, J.-M. (Eds.), Advances in the Study of Fractured Reservoirs. Geological Society, London, pp. 79–95. Special

Publications.

Rotevatn, A., Thorsheim, E., Bastesen, E., Fossmark, H.S.S., Torabi, A., Sælen, G., 2016. Sequential growth of deformation bands in carbonate grainstones in the hangingwall of an active growth fault: implications for deformation mechanisms in different tectonic regimes. J. Struct. Geol. 90, 27–47.

Rowland, J., Sibson, R., 2004. Structural controls on hydrothermal flow in a segmented rift system, Taupo Volcanic Zone, New Zealand. Geofluids 4, 259–283.

Røgen, B., Gommesen, L., Fabricius, I.L., 2001. Grain size distributions of chalk from image analysis of electron micrographs. Comput. Geosci. 27, 1071–1080.

Sanderson, D.J., Nixon, C.W., 2015. The use of topology in fracture network characterization. J. Struct. Geol. 72, 55–66.

Sanderson, D.J., Zhang, X., 2004. Stress-Controlled Localization of Deformation and Fluid Flow in Fractured Rocks. Geological Society, London, Special Publications 231, pp. 299–314 unpublished.

Segall, P., Pollard, D.D., 1980. Mechanics of discontinuous faults. J. Geophys. Res. Solid Earth 85, 4337–4350.

Shipton, Z.K., Evans, J.P., Kirschner, D., Kolesar, P.T., Williams, A.P., Heath, J., 2004. Analysis of CO2 leakage through 'low-permeability'faults from natural reservoirs in the Colorado Plateau, east-central Utah. In: Baines, S.J., Worden, R.H. (Eds.), Geological Storage of Carbon Dioxide. Geological Society, London, pp. 43–58. Special Publications.

Sibson, R.H., 1996. Structural permeability of fluid-driven fault-fracture meshes. J. Struct. Geol. 18, 1031–1042.

Talwani, P., 1999. Fault geometry and earthquakes in continental interiors. Tectonophysics 305, 371–379.

Tamagawa, T., Pollard, D.D., 2008. Fracture permeability created by perturbed stress fields around active faults in a fractured basement reservoir. Am. Assoc. Petrol. Geol. Bull. 92, 743–764.

Tavarnelli, E., Pasqui, V., 2000. Fault growth by segment linkage in seismically active settings: examples from the Southern Apennines, Italy, and the Coast Ranges, California. J. Geodyn. 29, 501–516.

Verhaert, G., Muchez, P., Keppens, E., Sintubin, M., 2009. Fluid impact and spatial and temporal evolution of normal faulting in limestones. A case study in the Burdur-Isparta Region (SW Turkey). Geol. Belg. 12, 59–73.

Virk, H., Singh, B., 1993. Radon anomalies in soil-gas and groundwater as earthquake precursor phenomena. Tectonophysics 227, 215–224.

Walsh, J., Bailey, W., Childs, C., Nicol, A., Bonson, C., 2003. Formation of segmented normal faults: a 3-D perspective. J. Struct. Geol. 25, 1251–1262.

Yoshida, H., Metcalfe, R., Yamamoto, K., Murakami, Y., Hoshii, D., Kanekiyo, A., Naganuma, T., Hayashi, T., 2008. Redox front formation in an uplifting sedimentary rock sequence: an analogue for redox-controlling processes in the geosphere around deep geological repositories for radioactive waste. Appl. Geochem. 23, 2364–2381.

II

# Paper 2: The Relationship between Fluid Flow, Structures, and Depositional Architecture in Sedimentary Rocks: An Example-Based Overview

Vilde Dimmen, Atle Rotevatn, Casey W. Nixon

*Published in Geofluids, 2020 (2020) 1-19*

https://doi.org/10.1155/2020/3506743

Hindawi
Geofluids
Volume 2020, Article ID 3506743, 19 pages
https://doi.org/10.1155/2020/3506743

*Review Article*

# The Relationship between Fluid Flow, Structures, and Depositional Architecture in Sedimentary Rocks: An Example-Based Overview

**Vilde Dimmen, Atle Rotevatn, and Casey W. Nixon**

*Department of Earth Science, University of Bergen, PO Box 7800, 5020 Bergen, Norway*

Correspondence should be addressed to Vilde Dimmen; vilde.dimmen@uib.no

Received 12 August 2019; Revised 16 March 2020; Accepted 15 June 2020; Published 14 July 2020

Academic Editor: Rudy Swennen

Copyright © 2020 Vilde Dimmen et al. This is an open access article distributed under the Creative Commons Attribution License, which permits unrestricted use, distribution, and reproduction in any medium, provided the original work is properly cited.

Fluid flow in the subsurface is fundamental in a variety of geological processes including volcanism, metamorphism, and mineral dissolution and precipitation. It is also of economic and societal significance given its relevance, for example, within groundwater and contaminant transport, hydrocarbon migration, and precipitation of ore-forming minerals. In this example-based overview, we use the distribution of iron oxide precipitates as a proxy for palaeofluid flow to investigate the relationship between fluid flow, geological structures, and depositional architecture in sedimentary rocks. We analyse and discuss a number of outcrop examples from sandstones and carbonate rocks in New Zealand, Malta, and Utah (USA), showing controls on fluid flow ranging from simple geological heterogeneities to more complex networks of structures. Based on our observations and review of a wide range of the published literature, we conclude that flow within structures and networks is primarily controlled by structure type (e.g., joint and deformation band), geometry (e.g., length and orientation), connectivity (i.e., number of connections in a network), kinematics (e.g., dilation and compaction), and interactions (e.g., relays and intersections) within the network. Additionally, host rock properties and depositional architecture represent important controls on flow and may interfere to create hybrid networks, which are networks of combined structural and stratal conduits for flow.

## 1. Introduction

It is well known that besides the intrinsic rock and fluid properties (i.e., porosity, permeability, fluid density, and viscosity), geological structures such as faults, fractures, and deformation bands may also strongly influence fluid flow (e.g., [1–4]). Understanding the interaction between fluid flow and geological structures is key for the comprehension of flow-and-reaction-related phenomena that tend to localize around faults and fractures (e.g., [5, 6]), and hence fundamental for a variety of geological processes such as volcanism and metamorphism, as well as mineral dissolution and precipitation. Understanding subsurface fluid flow and reactions is also of economic and/or societal significance, given its relevance for the exploration and exploitation of ore mineral deposits, hydrocarbons, geothermal energy, contaminant transport, carbon storage, and groundwater aquifer management (e.g., [7–17]).

Different types of structures have different effects on flow. Open fractures, such as joints, may be highly conductive, whereas cemented fractures (veins) or deformation bands may be nonconductive or have very low permeability (e.g., [18–20]). Being able to identify and separate between different types of structures is therefore essential since they may have different effects on flow. Geological structures may act as conduits or barriers for fluid flow, or as a combination of the two. They may also have strongly anisotropic flow properties, e.g., acting as a barrier for cross-fault flow but as a conduit for fault-parallel flow (see [21–25]). It is common that flow properties of faults and fractures are transient and/or cyclic in nature, as faults and fractures vary between being open and closed for fluid flow through alternating fracturing, cementation/sealing, and refracturing (the so-called crack-seal behaviour; [26–30]). Numerous studies have offered insight into how single structures, or pairs of interacting faults and their damage zones, may affect flow [13, 31, 32].

However, faults and fractures commonly occur in networks [33–35]. The relationship between fault and fracture network properties (topology, connectivity) on one hand, and fluid flow in rocks on the other, is still poorly constrained (e.g., [36]). Furthermore, it is well recognized that depositional architecture may strongly affect flow (e.g., [37]), yet there are few studies that address the interaction of depositional architecture and geological structures and their influence on fluid flow in and around fracture networks (e.g., [38]).

Motivated by the above, the main aim of this work is to give an overview, exemplify, and investigate both the depositional, architectural, and structural controls on fluid-rock interactive phenomena. To do this, we examine the spatial relationship between faults and fractures, fracture network topology, depositional architecture, and the distribution of Liesegang-type reaction-diffusion systems (Liesegang bands, e.g., [39]) and iron oxide deposits (collectively referred to herein as iron oxide precipitates (IOPs)).

In a recent study [40], we investigated the role of fracture network connectivity in controlling localized calcite cementation along small-scale faults and damage zones in limestone. Here, we investigate a fuller range of controls on flow as we discuss how fluid flow is affected by (i) host rock properties and depositional architecture and (ii) geological structures and structure networks, as well as their anisotropy, geometry, connectivity, kinematics, and mutual interaction. Finally, we look at the effect of hybrid networks of stratal and structural conduits. To do this, we study a variety of geological structures, both fractures, joints, and deformation bands, from New Zealand, Malta, and Utah (Figure 1), where IOPs represent a record of paleofluid flow in sandstones and limestones. Given the recent advances in fracture network analysis (e.g., [35, 41–44]), our overview of geologic controls on fluid flow, that also incorporates and quantifies the role of network properties on flow, is pertinent.

## 2. Terminology

We follow the structural terminology defined in Peacock et al. [45], but for clarification, we additionally provide a short explanation of some important terms used herein:

1. *Fractures*: encompasses both joints and faults, as some of the studied fracture networks form parts of the damage zones of small-scale faults (displacements of <1 m), and comprises a combination of joints and faults. The joints and faults are hard to distinguish in an outcrop because of the centimeter-scale and lack of displacement markers
2. *Hybrid network*: used herein to describe networks where geological structures such as joints or faults interact with more permeable layers or beds of a heterogenic sedimentary rock to increase the connectivity and create conduit networks
3. *Deformation bands*: described as tabular, millimeter-wide zones of localized but nondiscrete and distributed shear and/or compaction, and are typically low-permeable structures (generally 2-3, but occasionally up to 6 orders of magnitude lower permeability than host rock) that adversely affect flow properties [2, 46–51]
4. *Iron oxide precipitates (IOPs)*: used herein as a term to cover both Liesegang-type reaction-diffusion systems (Liesegang bands, e.g., [39]) and other iron oxide deposits (e.g., [20, 52]). IOPs are a common by-product of fluid flow in rocks such as sandstone, limestone, and mudstone. Where IOPs occur preferentially in association with depositional heterogeneities (e.g., specific facies, strata, or bounding surfaces) and/or structural heterogeneities (e.g., faults and/or other types of fractures) in rocks, they may be used to infer the history of paleofluid flow and reconstruct how such heterogeneities acted to control flow [16, 39, 52–55]

## 3. Geological Framework of the Study Sites

New data presented herein are collected from various sites in New Zealand, Malta, and Utah. We combine qualitative field photographs of examples of simple structures like single fractures and deformation bands from New Zealand and Utah, with a more quantitative study of more complex fracture networks mainly from Malta but also from New Zealand.

*3.1. Tongaporutu, Taranaki Basin, New Zealand.* Present-day New Zealand is an active plate boundary that accommodates oblique convergence of the Australian and Pacific plates [56, 57]. Deformation band examples presented herein are from coastal exposures of faulted deep-water turbidites of the Upper Miocene Mount Messenger Formation in the Taranaki Basin on the West Coast of New Zealand's North Island (Figure 1(a)) [58–60]. The Taranaki Basin, exposed onshore along the Taranaki coastline, initially formed in Late Cretaceous times as a result of extension related to Gondwanan continental breakup and opening of the Tasman Sea (e.g., [61, 62]). The basin has since seen a complex history, ranging from initial rift and passive margin phases, oblique reactivation, and overprint by convergent and extensional tectonics in Neogene times (e.g., [59, 63]). Deformation bands in the Mount Messenger Formation have previously been described by Childs et al. [64] and Nicol et al. [65]; included in this study are examples of cataclastic shear bands in the cliffs along the Taranaki coast.

*3.2. Hokianga, Northland Allochthon, New Zealand.* The second study area in New Zealand is located on the southern shores of Hokianga in Northland (Figure 1(a)). Here, the Late Cretaceous Punakitere Sandstone [66–68] consists of massive to well-bedded sandstones with occasional conglomerate horizons, and sits within the Northland Allochthon [69, 70], the low-angle emplacement that occurred at the Oligocene-Miocene boundary [71]. The Punakitere Sandstone in Hokianga is affected by small-scale fracture networks, oriented NNE-SSW and NE-SW with associated IOPs.

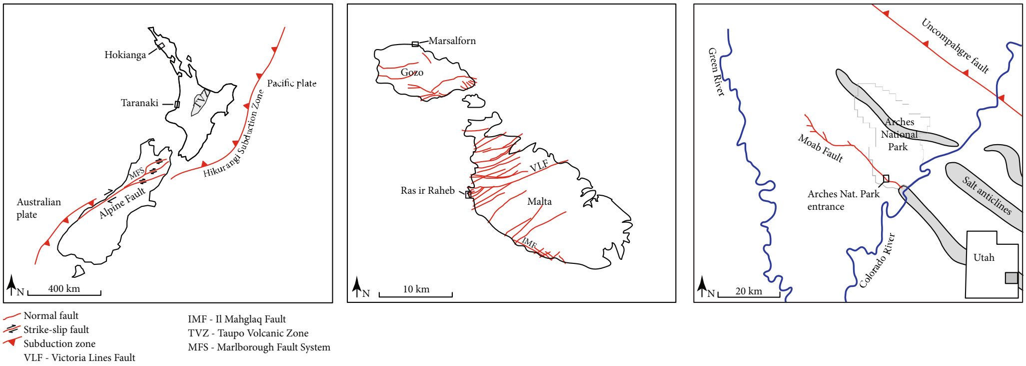

(a) New Zealand (b) The Maltese Islands (c) Arches National Park

Figure 1: (a) Overview map of New Zealand, showing the field areas at Hokianga and the Taranaki coast on the North Island (after Sporli and Rowland, 2007). (b) Overview map of the Maltese Islands, showing the location of the field areas at Ras ir Raheb and Marsalforn (after [20, 79, 80]). (c) Overview map of the area of Arches National Park in SW Utah, USA, showing the field location by the entrance of Arches National Park (after Doelling, 1985; [53]).

*3.3. Ras ir Raheb, Malta.* The Maltese archipelago, consisting of the islands of Malta, Gozo, and Comino (Figure 1(b)), is situated on the north-eastern shoulder of the ESE-WNW-trending Pantelleria rift system [72], which formed as a response to back-arc extension related to Apennine-Maghrebian subduction in Late Miocene-Early Pliocene times [73–76]. The back-arc extension also led to the formation of ENE-WSW-trending horsts and grabens, which dominate the Maltese structural framework (e.g., [74, 77, 78]). The localities studied at Ras ir Raheb on the west coast of Malta, are situated approximately 1 km into the footwall of the Victoria Lines Fault (VLF) (Figure 1(b); [40, 78, 79]), which is a normal fault with a maximum displacement of c. 90 m [80]. The fault and fracture networks (displacement $< 1$ m) examined here may be considered to be subsidiary faults in the damage zone of the Victoria Lines Fault [40, 81]. The host rocks are Miocene-age, syn-rift, fine-grained foraminiferal limestones of the Middle Globigerina Limestone Member [74, 80].

*3.4. Marsalforn, Gozo.* Like the main island of Malta, Gozo is also characterized by ENE-WSW striking normal faults. However, the north-western part of the island stands out, as regional extensional strain related to the Pantelleria rifting event is expressed here as arrays of strike-slip faults [82]. The faults at the studied locality at Marsalforn (Figure 1(b)) occur in the Lower Globigerina Limestone Member, which outcrops as a yellow to orange, massive wackestone, packed with foraminifera and bivalves [80].

*3.5. Arches National Park, Utah, USA.* The last study areas are located close to the entrance of Arches National Park in SE Utah, USA (Figure 1(c)). Examples from here include deformation band clusters in the hanging wall of the Moab Fault and an anisotropic fracture network studied in a limestone bed in the footwall of the fault, just 5-15 m from the fault plane [18, 83, 84]. The deformation bands are found in the aeolian Entrada sandstone, which forms part of the latest Triassic to Early Jurassic San Rafael Group [85, 86]. It consists of aeolian dunes and interdunes deposited in a hot and arid coastal environment in Mid-Jurassic times [84, 86, 87].

## 4. Data and Methods

Fieldwork involved the acquisition of structural field data and digital imagery from hand-held cameras. IOPs, and the extent of these, were mapped from photographs and field sketches, and length-displacement profiles were recorded for fractures that exhibited evidence for shear displacement.

For analysis of the fracture network examples, high-resolution photography was used to digitize the networks using the NetworkGT toolbox in ArcGIS [88]. This was done to quantify the node and branch topology of the studied networks [44, 89]. The elements in the two-dimensional networks are divided into nodes and branches, where nodes are ends or intersection points of fractures, and branches are segments of a fracture trace, bound by a node at each end (Figure 2) [42, 44]. The degree of connectivity of the network can be determined by the proportion of different nodes and branches, as elaborated in Sanderson and Nixon [44]. From the digitized maps of the networks, we used the Kernel Density tool in the built in ArcToolbox in ArcGIS to extract contour maps of (i) fracture intensities, which represent the total branch length per square meter ($m/m^2$), and (ii) the connecting node frequencies, to illustrate the frequency of connections per square meter ($N_C/m^2$) [44]. These maps provide a good visualisation of the internal variations of the network complexity and connectivity.

## 5. Examples of Fluid Flow Relationships with Structures and Networks: Field Observations and Characterization

*5.1. Depositional Architecture.* We studied the relationship between depositional architecture and paleofluid flow at

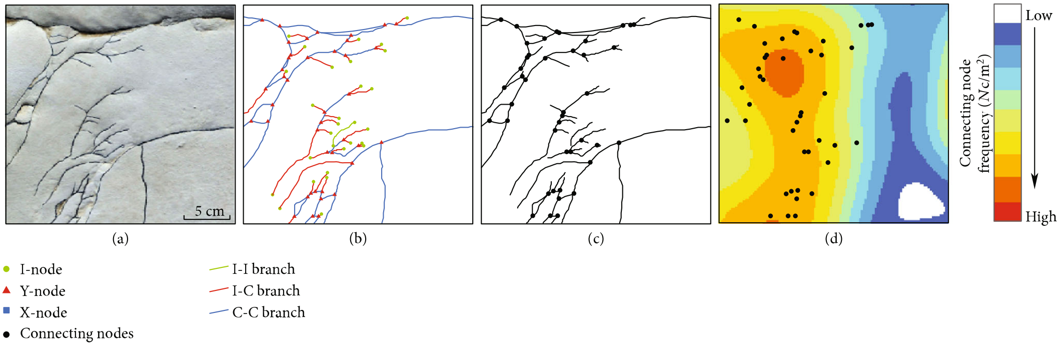

(a) (b) (c) (d)

Figure 2: (a) Example of a fracture network from the field at Ras ir Raheb, Malta. (b) Topological characterization of the example shown in (a), using topological nomenclature proposed by Sanderson and Nixon [44]. We differentiate between different types of nodes and branches. Nodes are classified as isolated nodes (I-nodes), abutting or splaying nodes (Y-nodes), or as crossing nodes (X-nodes). Branches are classified as isolated (I-I), partly connected (I-C), or fully connected (C-C). (c) Network showing only the connecting nodes. (d) Illustration of the connecting node frequency (connecting nodes/$m^2$) of the fracture network.

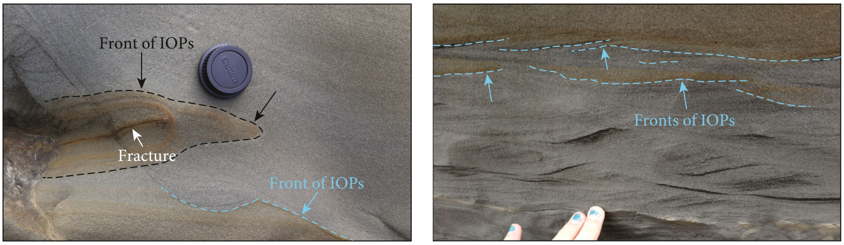

(a) (b)

Figure 3: (a) Example of how a fracture (white arrow) can control the formation and extent of iron oxide precipitates (black, dashed line) and how depositional architecture (blue arrow) may control the flow of oxidizing fluids (blue, dashed line); Hokianga, New Zealand. (b) Another example of how depositional architecture, here in the form of crossbedding, can control the extent of iron oxide precipitates; Taranaki, New Zealand.

several locations around New Zealand's North Island, and two were chosen as examples herein. Figure 3(a) shows a photo from an outcrop along the Hokianga coast, where millimeter- to centimeter-scale depositional structures create heterogeneities in the otherwise homogenous Punakitere Sandstone. Parts of the rock have a brown-orange colour, due to IOPs, which stands out against the grey sandstone. An ~15 cm long joint cuts through the depositional structures in the middle of the photograph. This joint is associated with a highly localized IOP envelope that tapers out ahead of the joint tip. This IOP envelope is also to some extent controlled by sedimentological heterogeneity, in that its upper boundary follows a sandstone crossbed. This illustrates how fluid flow may be influenced by both depositional heterogeneities and structural heterogeneities in one example. The second example, Figure 3(b), is showing centimeter-sized crossbedding in a cliff along the Taranaki coast. The muddy sandstone is mainly grey in colour, but some IOPs have stained parts of the rock, filling in the crossbeds in the uppermost part of the photo. Both of these examples illustrate how depositional architecture can create spatial heterogeneities in porosity/permeability producing local flow paths through otherwise homogenous rocks.

*5.2. Simple Geological Structures.* Figure 4 shows examples of joints and their relationship to IOPs from Hokianga, North Island, New Zealand. The first example (Figure 4(a)) shows two subparallel joints—one through-going joint from left to right and another joint, ~10 cm above, coming in from the left and terminating at a tip to the right. An envelope of IOPs encloses the joints, staining the surrounding sandstone brown-orange, and clearly deflects and narrows ahead of the terminating joint tip. This illustrates the fact that the spatial distribution of iron oxide deposits can be controlled by multiple (two) fractures: the envelope is widest where it is controlled by two main joints, and narrowest where it is only controlled by one. Another example from Hokianga shows a joint set comprising two right-stepping segments (Figure 4(b)). This joint set is associated with a brown-orange iron oxide envelope, which closely trails the segmented

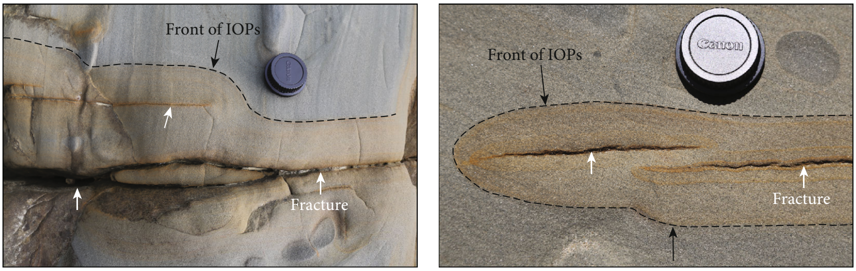

(a) (b)

Figure 4: (a) Example of fracture tip interaction, where the front of the iron oxide precipitates (black, dashed line) curves out where the fracture tips overlap; Hokianga, New Zealand. (b) Example of how iron oxide precipitates respond to fracture-tip interaction: the front of the iron oxide precipitates (black, dashed line) narrows as the fractures (white arrows) tip out; Hokianga, New Zealand.

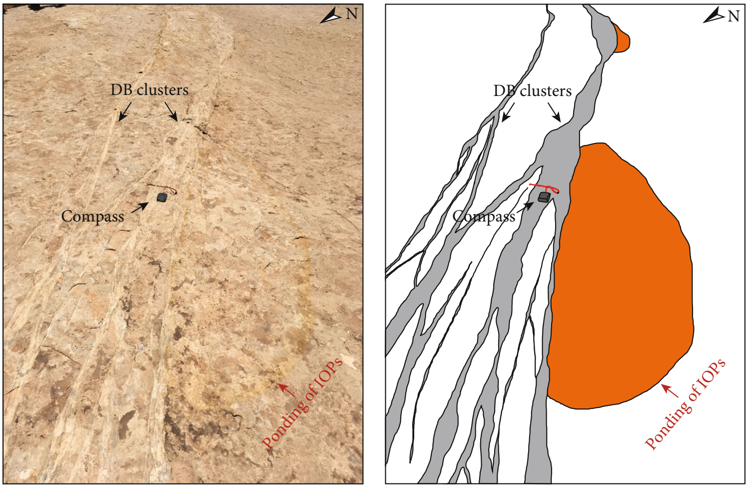

(a) (b)

Figure 5: (a) Field photo and (b) sketch of deformation band cluster causing ponding of iron oxide precipitates (IOPs) found in Arches National Park, Utah, USA.

joint system. Where the joint system steps right-laterally, the envelope similarly makes a gentle right-lateral shift. Hence, the IOPs, and inferred paleofluid flow, are clearly affected by the joints, as the fronts of the IOPs follow the extent of the joints. These examples show how simple geological structures can act as conduits, controlling and localizing the distribution and flow of fluids.

Figure 5 presents an example of deformation bands formed within the Entrada sandstone in Utah. The locality shows a NW-SE-oriented cluster of deformation bands on a gently SW-sloping pavement. The cluster stretches tens of meters in length with a variable width of up to ~1 m. The front of IOPs are located on the pavement immediately down dip of the cluster, towards the SW, locally forming orange-coloured half circles in the sandstone. These represent ponding of fluids against the deformation band cluster which has acted as a barrier to fluid flow.

Examples of deformation bands were also documented in the cliffs along the Taranaki coast, New Zealand (Figure 6). In Figures 1(c) and 6(b), two oblique deformation bands cross each other with an intersection angle of approximately 60 degrees. One deformation band is visible as a distinct grey line crossing the photograph from left to right and appears to have no associated IOPs. Whereas the second deformation band has a clear association with IOPs, visible as a rusty orange line crossing the grey deformation band. An additional example in Figures 6(c) and 6(d) shows a single deformation band crossed by a series of IOP fronts, which are clearly not affected by the deformation band. Even though these are all examples of deformation bands, they show very different relationships with fluids, i.e., some act as conduits localizing flow, some act as barriers, and others have little or no effect on the distribution of IOPs.

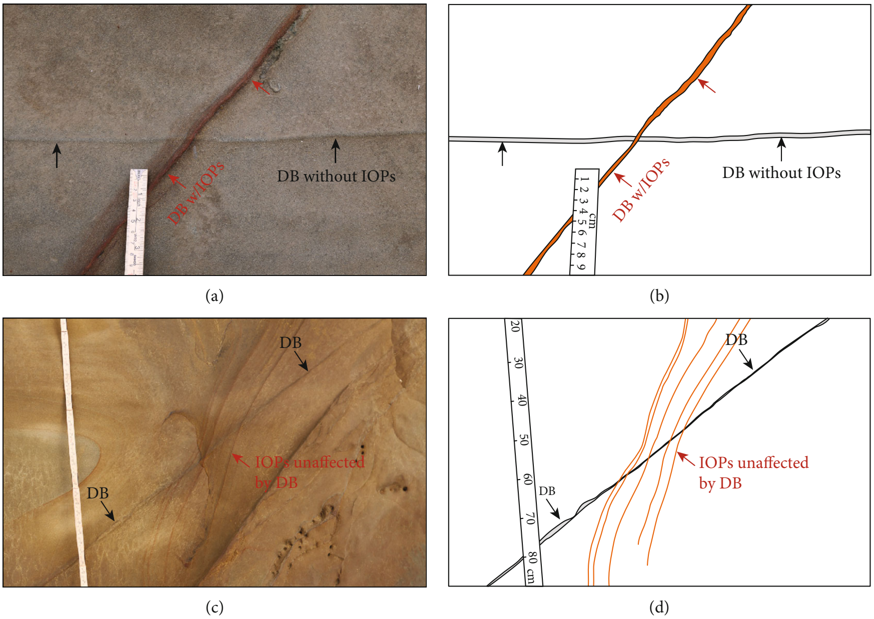

(a) (b)

(c) (d)

Figure 6: (a) Field photo and (b) sketch of a deformation band functioning as a capillary conduit controlling oxidation (red arrows) and a deformation band without any oxidation at all (black arrows: horizontal in picture, dipping away from perspective); Taranaki coast, New Zealand. (c) Field photo and (d) sketch of example where bands of iron oxide precipitates (pointed out by red arrow) clearly ignore a deformation band (black arrows); Taranaki coast, New Zealand.

(a) (b)

Figure 7: Not all fractures act as conduits for fluid flow, and hence iron oxide precipitates do not surround all fractures. Along-strike variability of the fractures may cause along-strike variability in the distribution of iron oxide precipitates. Examples from (a) Hokianga, New Zealand and (b) the footwall of the Moab Fault in Arches National Park. White arrows point to the areas of fractures associated with iron oxide precipitates, while the red arrows point towards some of the fractures which do not promote formation of iron oxide precipitates.

*5.3. Simple Structural Networks.* As previously mentioned, geological structures can interact and form networks. Within the Punakitere Sandstone at Hokianga, New Zealand, we documented a fracture network comprising two orthogonal joint sets; one systematic joint set (trending right to left; Figure 7(a)) abutted by a set of cross-joints (trending top to bottom; Figure 7(a)). Elongated haloes of orange-coloured IOPs form around the systematic joint set whereas the cross-joints are unaffected by IOPs. A similar example is shown in Figure 7(b), which comprises two orthogonal fracture sets that mutually cross-cut and abut one another in a limestone bed, located in the footwall of the Moab Fault in Arches National Park, Utah. Again in this example, one fracture set is surrounded by a brown-red halo of IOPs (trending right to left; Figure 7(b)), whereas the orthogonal cross-cutting fracture set (trending top to bottom; Figure 7(b)) has no association with IOPs. Both examples illustrate that not all structures within a network are conductive to flow, which is important as it will produce an anisotropy in the flow properties of a fractured rock mass.

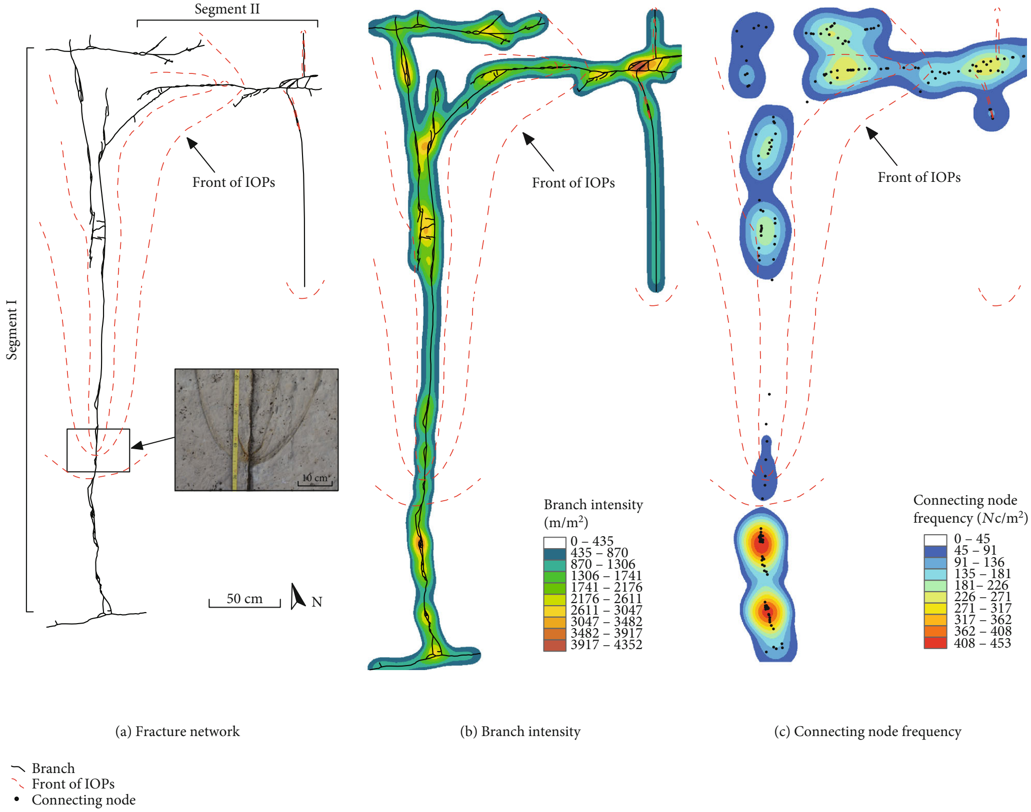

(a) Fracture network

(b) Branch intensity

(c) Connecting node frequency

Figure 8: (a) Digitized map of the fracture network at Ras ir Raheb, Malta, with iron oxide precipitates shown as red dashed lines. A photo of a clear front of iron oxide precipitates is included. (b) The branch intensity map indicates higher density in complex zones. (c) Connecting node frequency map of the locality shows that zones with high branch intensity generally tend to coincide with high connecting node frequency.

*5.4. Complex Structural Networks.* The examples in Figure 7 are relatively simple fracture networks with two orthogonal sets. However, fractures often form more complex networks consisting of different fracture types as well as a range of fracture sizes and orientations. In the following examples (Figures 8, 9, 10 and 11), we explore more complex fracture networks and investigate the relationships between different fracture network attributes (e.g., fracture intensity, connectivity, and displacement) and the distribution of IOPs. These examples of more complex fracture networks are associated with a number of mesoscale fault systems formed in carbonate rocks located in Malta. The first example consists of two intersecting segments (I and II; Figure 8(a)), each comprised of several joints and minor normal faults with displacement of up to ~2.5 cm. The N-S-oriented segment I comprises two smaller, hard-linked fault segments. The E-W-oriented segment II continues 2-3 meters towards the east, outside of the area covered by Figure 8, where it tips out and overlaps with another segment to form a relay ramp (see Figure 1(a) in the supplementary materials (available here)). Distinct, red IOPs are widest around the intersection point of segments I and II. The intersection is also characterized by higher branch intensities and connecting node frequencies (Figures 8(b) and 8(c)). The strong IOP front tapers off to the south and east along segment I and segment II, respectively. Although some local, smaller maxima in branch intensity and node frequency are found further south and east along the main segments, outside the intersection, only weaker, discontinuous fronts are observed locally and often around fracture tips.

In Figure 9, we have an example of a normal fault system with an outcropping trace length of ~22 m and a maximum displacement of ~25 cm (see also Figure 2 in the supplementary materials). The fault system consists of a network of small faults and fractures that trend SE-NW and dip ~60° towards the SW. For ease of description, the system is divided into two distinct main segments (segments I and II; Figure 9(a)), which are linked through a more intensely fractured zone. Contour maps of fracture intensity and connecting node frequency are presented in Figures 9(b) and 9(c),

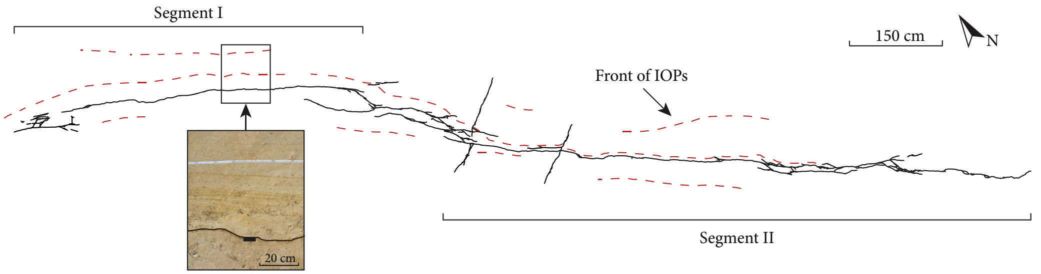

(a) Fracture network

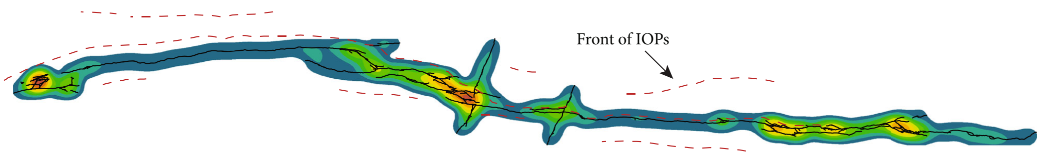

(b) Branch intensity

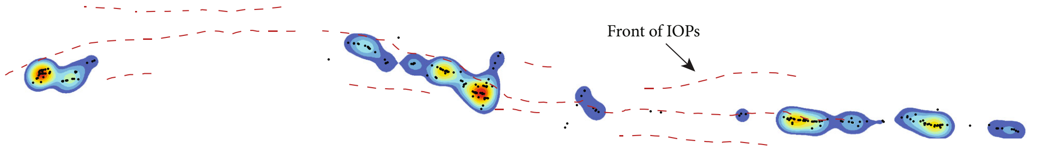

(c) Connecting node frequency

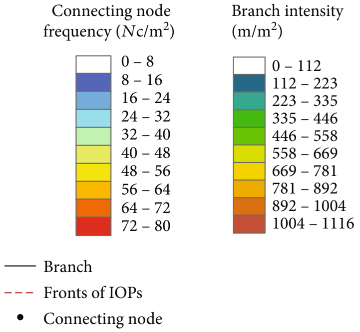

Figure 9: (a) Digitized map of the fracture network at Ras ir Raheb, Malta, with iron oxide precipitates shown as red dashed lines. (b) The branch intensity map indicates higher density in the areas of segment linkage. (c) Map of the connecting node frequency, which also increases in the areas where fault segments link indicating higher connectivity in linkage areas.

respectively, generally showing that high connecting node frequencies correspond with areas of high fracture intensity. A series of profound red-stained IOP fronts, predominantly in the footwall of the fault system, form an envelope of ~50 cm around the main fault segments (see inset in Figure 9(a)). Weaker, discontinuous fronts can be observed locally further away from the main segments, as well as a few, discontinuous fronts in the hanging wall (Figures 9(a)–9(c) and Figure 2(b) in the supplementary materials). A widening of the IOP front can be observed at the linkage of the two fault segments. However, this is the only location where IOP width coincides with increases in fracture intensity and connecting node frequency. Instead, the width of the IOP fronts appear to reflect relative changes in displacement along strike of the fault system (Figure 10).

The final complex fracture network example is a 2 m section of a longer strike-slip fault system with decimeter-scale displacements (Figure 11). The fault system comprises NNE-trending right-lateral strike-slip segments that separate a series of ENE-striking centimeter–decimeter-scale pull-

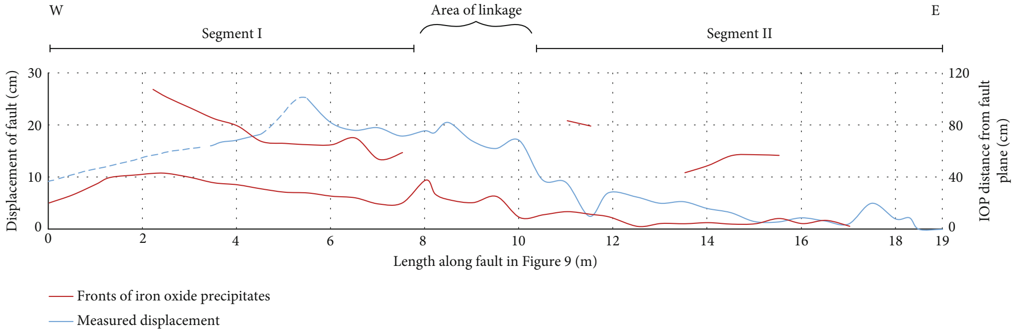

Figure 10: The graph shows the extent of the fronts of iron oxide precipitates (in red) vs. the length of the fault, as well as the length-displacement relationship (in blue) of the studied network in Figure 9. The prominent fronts of iron oxide precipitates exhibit an overall widening from E to W, tapering towards the E and terminating along what is segment II in Figure 9. This coincides with the eastward decrease of displacement.

apart structures (see also Figure 3 in the supplementary materials). Branch intensity and connecting node frequency maps in Figures 11(b) and 11(c) show peaks where the main strike-slip faults intersect; however, there is no obvious correlation between IOP distributions. Instead, zones of bleaching/reduction of iron in the limestone can be observed along the pull-apart structures, followed by a zone of higher IOPs (Figure 11(a)), indicating that these pull-apart structures were the main flow conduits along the fault system.

*5.5. Hybrid Structural Networks.* At Hokianga, New Zealand, we documented a hybrid network where fractures are interacting with highly permeable layers (Figure 12). This hybrid network consists of a fracture network with a conjugate set of fractures trending NNE-SSW and NE-SW, intersecting at an angle of approximately 70° (Figures 12(a) and 12(b)). In this example, the orange-brown colour of the IOPs are not only localized along fractures but also along selected facies/strata in the host sandstone. Contour maps of the connecting node frequency and branch intensity of the fracture network show local highs distributed across the network (Figures 12(c) and 12(d)). When the highly permeable layers are also included, making it a *hybrid* network, there is an obvious increase in the connecting node frequencies and branch intensities (Figures 12(e) and 12(f)). In this case, the later fracture network appears to provide connections between the highly permeable layers, thus creating a hybrid network of flow conduits.

## 6. Discussion

In the following subchapters, we will first discuss how simple geological heterogeneities affect fluid flow, before moving on to fracture network properties and their spatial variations.

### *6.1. How Do Simple Geological Heterogeneities Affect Flow?*

*6.1.1. Controls of Depositional Architecture on Fluid Flow.* Fluid flow, and therefore also the distribution of IOPs, are sensitive to the inherent pore network variability in the host rocks in which they occur. The depositional architecture of a sediment or sedimentary rock is the end product of depositional processes and following diagenesis, which control the distribution of grain type, size, sorting, cementation, alteration, and therefore also host rock properties and the configuration of the pore space (i.e., porosity and permeability) in a rock. Contrasts in flow properties across bounding surfaces, facies boundaries, bed sets, and individual laminae may be significant and may thus be considered a first-order control on variations in flow behaviour (see e.g., [90, 91]). For example, Chandler et al. [92] reported permeability contrast spanning 5 orders of magnitude in a 41 m thick aeolian sandstone succession, and 1-2 magnitude-order permeability contrast between individual crossbeds within a single aeolian dune unit. Fluid flow and iron oxide deposition can hence be spatially controlled by depositional architecture, as illustrated in Figure 3(a) (lower part of image) and Figure 3(b), where IOPs are delineated by crossbeds in sandstone. Depositional architecture as such represents a fundamental control on fluid flow in sedimentary rocks; appreciating the controls of depositional architecture on flow, and the effect of depositional heterogeneities, is a prerequisite that should go hand-in-hand with considering structural controls on flow.

*6.1.2. Structure Type: Conduit or Barrier?* Having briefly discussed the controls of depositional architectural variability, we move on to structural controls on flow and iron oxide deposition. Structures such as faults, other types of fractures, and deformation bands also represent an important control on fluid flow, and whereas joints and unsealed faults may form significant conduits for fluid flow, cataclastic deformation bands, veins, and sealing faults (e.g., faults with shale smear, cataclastic fault rocks, and cementation) may represent effective seals or baffles for flow (e.g., [2, 93, 94]).

Any open or permeable fracture (e.g., an uncemented extension fracture or fault) may transmit fluid flow [95–97]. By localizing fluid flow, fractures may therefore cause iron oxide precipitates to be deposited locally around them (e.g., [5, 39, 52, 98]). The examples in Figures 3 and 4 illustrate this

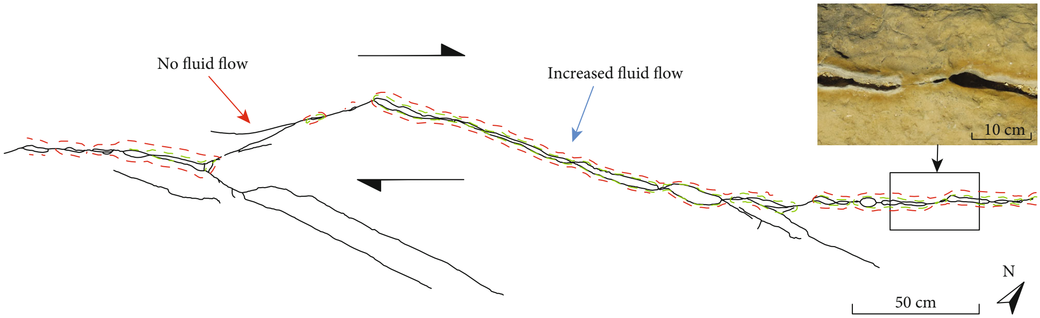

(a) Fracture network

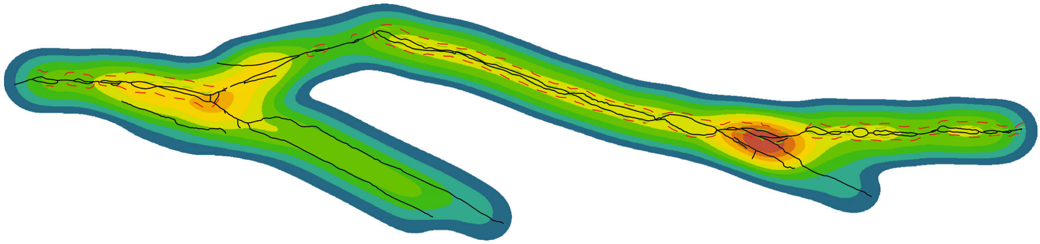

(b) Branch intensity

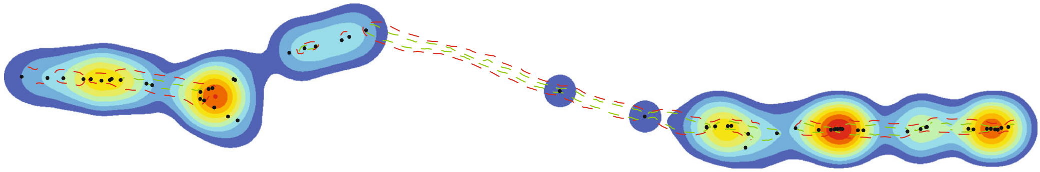

(c) Connecting node frequency

Figure 11: (a) Digitized map of a fracture network at Marsalforn, Malta, with iron oxide precipitates shown as red dashed lines and a front of bleaching shown with a green dashed line. (b) Branch intensity map indicating higher density in complex zones. (c) Connecting node frequency map of the locality. There is no obvious correlation between iron oxide precipitates and higher branch intensity/connecting node frequency in this example; the iron oxide precipitates are rather localized along the pull-apart segments.

nicely. The IOP envelope in Figure 3(a) is highly localized to the joint, as it closely follows its extent and tapers out ahead of the tip. We can hence assume that the joint has served as a fluid flow conduit. The example in Figure 4 is similar, but illustrates the fact that the spatial distribution of iron oxide deposits can be controlled by multiple (two) fractures. Here,

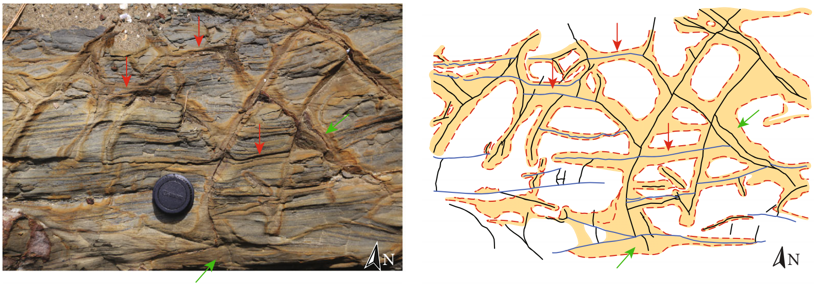

(a) Field photo (b) Network of conduits

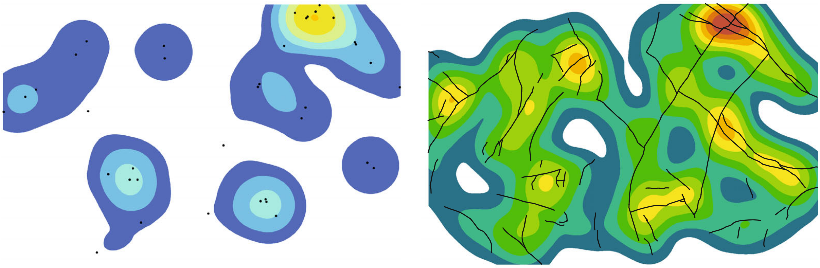

(c) Connecting node frequency (d) Branch intensity

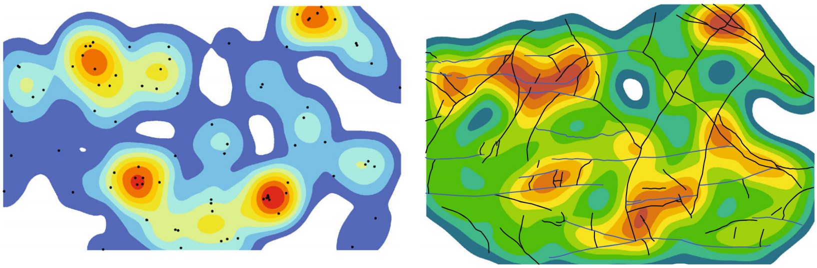

(e) Connecting node frequency, including conductive layers (f) Branch intensity, including conductive layers

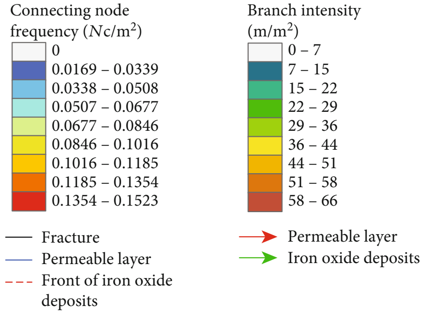

Figure 12: (a) Field photo of a simple cross-cutting fracture network from Hokianga, New Zealand, interacting with highly permeable layers in the host rock. (b) A digitized fracture network (black lines) and highly permeable layers (blue lines), surrounded by iron oxide precipitates (orange). Red arrows point to examples of where more permeable layers work as conduits between fractures. (c) Map of the connecting node frequency of the studied part of the fracture network. (d) Map of the branch intensity of the studied part of the fracture network. (e) Map showing the connecting node frequency, including connection points between fractures and highly permeable layers, forming a hybrid network. (f) Branch intensity of the studied network, including the highly permeable layers in the host rock forming a hybrid network.

the IOP envelope also follows the extent of the joints, but widens where two joints are present, indicating enhanced fluid flow.

As opposed to creating space for enhanced fluid flow, structures may also act as barriers. This is often due to clay smear or juxtaposition of impermeable layers, but also through cementation of fractures or low-permeable deformation bands (e.g., [20, 94, 99, 100]). Deformation bands typically have a different effect on flow and iron oxide deposition compared to open fractures, and are capable of baffling and/or redirecting flow (e.g., [101–103]). This is exemplified in Figure 5, where the front of IOPs form a half circle underneath the deformation band cluster. The deformation bands seem to have served as a barrier for fluids, which have ponded against the low-permeable cluster.

However, because of changes in grain size/shape and pore space within deformation bands, capillary properties also change. Despite having a low permeability, some deformation bands can therefore work as capillary conduits in the vadose zone [104, 105]. Iron oxide-bearing fluids may thus saturate relatively low-permeability bands and precipitate localized iron oxide deposits exclusively to the band itself. This is shown in Figures 6(a) and 6(b), where a deformation band highly affected by the IOPs can be seen alongside a second deformation band which in contrast is completely unaffected by the fluids.

Finally, many structures have little or no effect on fluid flow; in such cases, IOPs may be distributed across and irrespective of any structures present. Figures 6(c) and 6(d) exhibit an example of this, where bands of oxidized iron cut right across a deformation band; the deformation band appears to have had no effect on fluid flow, or at least not on the deposition/distribution of IOPs. Deformation bands, fractures, and faults may have little or no effect on flow if the contrast between the flow properties of rocks and structures is low. Additionally, structures that do exhibit a high permeability contrast to host rock may also have a limited practical effect on flow. For example, if the structures are isolated or poorly connected with other low-permeable structures (the fluids will flow around the tips) and the host rock is too highly permeable for any structure to affect flow to any significant degree. In such cases, the effects of structure will be highly dependent on how structures form part of fracture *networks*, the properties of which may strongly contribute to controlling flow [13, 40]. This is discussed further in the following section.

### 6.2. How Do Fracture Network Properties and Their Spatial Variations Affect Flow?

*6.2.1. Anisotropic Fracture Populations.* Although the above examples mainly highlight fractures that either positively localize and conduct flow or clearly prohibit flow, the effect of fractures on flow can be highly variable. As stated earlier, in a population of fractures some fractures may be conductive whereas others may not, or if a population is comprised of two or more fracture sets one set may be conductive while the other sets may not be conductive (e.g., [106]). The latter is exemplified in Figure 7(a), where one out of two orthogonal fracture sets in the sandstone is associated with IOPs. Note also that the IOPs in the example (Figure 7(a)) are only localized to parts of the along-strike extent of each fracture in this set. A similar situation can be observed in Figure 7(b), where IOPs are localized along a restricted part of one out of two interacting fracture sets in a limestone bed, showing that this is not restrictive to certain lithologies. The irregular distribution of IOPs may be related to along-strike variability of flow properties of the fractures (cf; [107, 108]), which can be significant over short distances; only parts of the fracture may be conductive at the time of fluid migration, whereas other parts may have too low permeability for fluid transmission.

*6.2.2. Geometry and Connectivity in Fracture Networks.* The *geometry* of fractures and fracture networks is another key control on flow in sedimentary rocks (e.g., [36, 40, 109]). The length, orientation, segmentation, and intensity of fractures determine their effect on flow. For example, fracture length and intensity determine the total amount of fractures (length and/or volume of fractures/fractured rock), which translates to the amount of fluid conduits or fluid barriers, present in the rock [36, 110]. The geometry of fractures affects the dynamics of flow and the localization of fluid-rock interaction, such as seen in the examples presented in Figures 4(a) and 4(b). The length, orientation, and intensity of fractures also determine how they interact in networks, and hence, the geometry controls the *connectivity*, which is another crucial control on fluid flow in a fracture network as it governs its percolation potential [36, 88].

This is highlighted by the example shown in Figure 8, where the widest front of IOPs is located around the intersection point of the two fault segments. The intersection is also characterized by areas of higher branch intensity and connecting node frequency (Figures 8(b) and 8(c)), which confirms this as an area of higher connectivity, hence having the potential to be an area for increased fluid flow. A high concentration of connecting nodes in the southern end of segment I is on the other hand not associated with, or affecting, the IOPs. We propose that this is caused by the lower connectivity (as reflected by the lack of connecting nodes) along the middle part of segment I, or anisotropy along the segment such as potential cementation prohibiting flow along the southernmost part of segment I.

Similar examples have previously been presented in the literature, where fluid flow is directly associated with fault and fracture intersections. Nixon et al. [111] investigated a normal fault relay at Kilve, UK, and illustrated that calcite veins, which represent past conduits, with larger apertures occur at intersections and in areas with high vein intensity (frequency of veins with apertures >1 mm per unit length). Dockrill and Shipton [10] present another example where they looked at structural controls on leakage from a natural $CO_2$ storage site along the Little Grand Wash fault and Salt Wash faults in Utah. $CO_2$-charged groundwater precipitates travertine mounds when reaching the surface, and field observations show how these mounds tend to localize at fault intersections. Dockrill and Shipton [10] also use traces of iron-oxide reduction as evidence of paleofluid flow in relation to the faults and their associated damage zones. Other precipitates that have served as proof of fluid flow and revealed fault and fracture intersections as conduits are stalactites. Stalactites in carbonate caves indicate high amount of fluid flow in dilational jogs and fracture intersections, where the stalactites are larger than along the rest of the fractures [112].

*6.2.3. The Effects of Kinematics and Interaction on Flow.* The kinematics of structures are also important. The rates, distribution, timing, and magnitude of slip may control the extent to which faults act as conduits for flow. Greater slip is generally associated with greater deformation and, therefore, also a greater tendency to transmit fluids, such as seen in the example in Figure 9, where the general width distribution of IOP bands around the fracture network appears to correlate with displacement distribution on the main normal fault in the network (Figure 10). The prominent, red-stained IOPs in the footwall exhibit an overall widening from E to W, tapering towards the E. This general westward widening of the oxidation fronts is matched by a corresponding westward increase in normal displacement. Timing and episodicity of slip are also important; for example, fault reactivation and rejuvenated slip are known to cause reopening of sealed faults (e.g., [25, 32, 113]).

For most fracture and deformation band types, it is generally true that structures affected by a net volume gain (e.g., joints and dilation bands) have a tendency to positively affect flow, whereas structures affected by a net volume loss (e.g., stylolites and compaction bands) may reduce flow properties (e.g., [19, 114, 115]). Structures affected by shear movement may form conduits or barriers to flow depending on the presence of low-permeable fault rocks, any aperture/opening present, or cements. This is highlighted in the example shown in Figure 11, where the distribution and extent of the IOPs show that they are preferentially localized along the opening-dominated pull-apart segments of the fracture network, whereas they are not present around the shear-dominated strike-slip segments. This corresponds with previous findings, from both the field and modelling, of fluid flow localizing particularly at fault/fracture jogs or intersections (e.g., [15, 115, 116]).

Furthermore, the relative orientation of fracture sets versus past and present stress fields may also determine their flow properties; fractures that are favourably oriented relative to the axes of maximum principal stress may be kept open (conductive), whereas those unfavourably oriented may be closed (nonconductive) [117]. This can cause some fracture sets in a network to form open conduits, whereas other fracture sets in the same network are nonconductive. This is one possible explanation for the contrasting behaviours of the two fracture sets shown in Figures 7(a) and 7(b). The behaviour may also reflect properties that change through time and space, as some fractures change between being open and closed due to cementation and dissolution/refracturing, and depending on the relative timing of fluid flow, cementation, and deformation at the time fluids are present in the system (e.g., [53, 93, 94]). However, a more complex fault or fracture network, as often found in relay zones of fault linkage zones, would increase the possibility of open fractures as it includes higher fracture intensity with a wider range of fracture orientations making the chance of favourably oriented fractures present higher [40, 107].

*6.2.4. Hybrid Networks of Conduits.* The different aspects discussed in the previous sections are all independently important controls on fluid flow. However, it is often the interplay between all of the above effects that is key to controlling fluid flow, i.e., the interaction between depositional and structural heterogeneities. This has been treated in previous studies, and may for example affect (i) production-related fluid flow in petroleum reservoirs (e.g., [37]), (ii) dolomitization in rift basins [28], and (iii) diagenetic alteration of fault-bound clastic deposits in rift basins (e.g., [25]). However, the interaction between depositional and structural controls on flow can also be considered from a network perspective (sensu [44]), a relationship which is poorly documented in literature, and hence the contribution herein is a novel addition to the research database.

Through Figure 12, we present an example of a hybrid network of structural and depositional conduits, where the IOPs follow both the fractures in the network as well as some layers of the sandstone. This combination of facies-selective and fracture-controlled IOPs portrays a complex network of palaeoconduits. The example shows that a combination of open fractures and high-permeable layers can provide a very well-connected hybrid network of fluid conduits, as demonstrated through the increased branch intensity (compare Figure 12(e) with Figure 12(f)) and connecting node frequency (compare Figure 12(c) with Figure 12(d)), where the fracture network contributes to create a connection between the permeable layers and vice versa. This highlights the interaction between fracture-controlled conduits and facies-controlled conduits, and illustrates how considering depositional or structural elements in isolation may lead to an incomplete understanding of potential paleofluid conduits (Figures 12(c) and 12(e)).

*6.3. Implications for Assessing Fluid Flow in the Subsurface.* This paper presents a new perspective on structural and stratigraphic controls on fluid flow, incorporating network analysis into an overview on geologic controls on flow in sedimentary rocks. An understanding of fluid flow through geological structures and fracture networks is important for a wide range of reasons. This includes hydrocarbon seal risk assessment, hazard maps for radon gas, prediction of earthquake localization, resource management in connection to groundwater and geothermal energy, and more. For example, Gartrell et al. [93] examined fault intersections as hydrocarbon leakage zones through numerical modelling, and they found that zones of high dilation were generated close to fault intersections, leading to highly permeable zones with a concentration of open fractures ideal for fluid migration. As such, understanding the locations of fluid conduits, which we have listed and presented

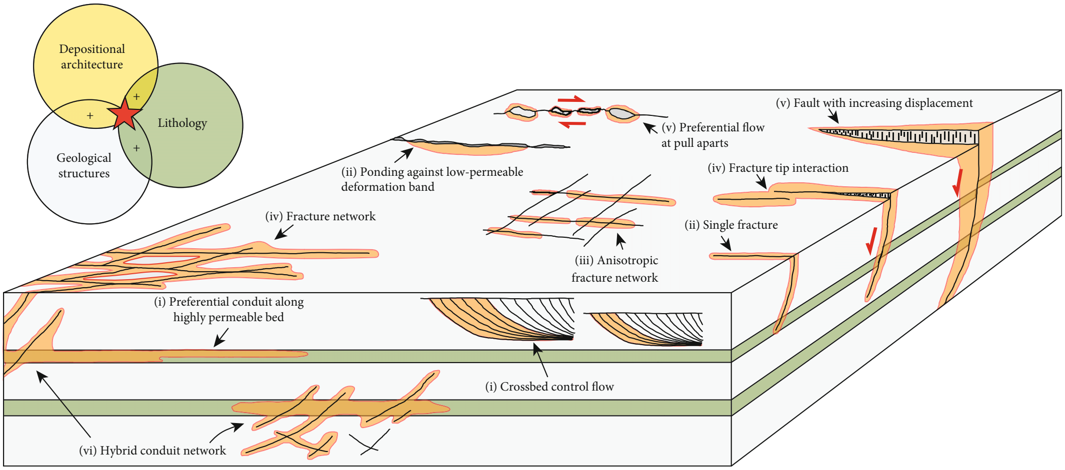

Figure 13: Schematic illustration of the examples of controls on fluid flow in sedimentary rocks presented herein, using iron oxide precipitates (orange) as indicator of palaeofluid flow. The fluid flow controls are divided into six groups based upon the main control: (i) host rock properties and depositional architecture, as shown in Figure 3; (ii) geological structures as conduits or barriers, as shown in Figures 4, 5 and 6; (iii) anisotropy in fracture populations, as shown in Figure 7; (iv) geometry and connectivity, as shown in Figure 8; (v) kinematics and interaction, as shown in Figures 9 and 11; (vi) hybrid depositional-structural conduit networks, as shown in Figure 12. All of these controls may also interact with each other, as illustrated in the top left corner.

examples of herein, can be of economic importance in terms of understanding the risk for hydrocarbon leakage or locating economically significant ore deposits [8, 13, 17, 96, 118].

Understanding the relationship between fluid flow, structures, and depositional architecture in sedimentary rocks also strongly applies to environmental issues, like storage of $CO_2$, radioactive waste disposal contaminant transport, and flow patterns of groundwater [7, 10, 16]. Mechanisms associated with deeper situated (below groundwater table), high-level radioactive waste, e.g., groundwater radiolysis, can form fronts of IOPs around the zones with high-level radioactive waste [6, 16, 52]. This makes fluid flow, and hence IOPs, important for the understanding of radioactive waste migration. Another fluid stored in underground repositories is $CO_2$, which is also highly dependent on conduits or barriers. Shipton et al. [119] examined evidence of $CO_2$ migration along normal faults and found that geysers and hydrocarbon seep were localizing along faults. Their observations are supported by Dockrill and Shipton [10], who investigated the structural control on $CO_2$ leakage from a natural storage site and did field observations of bleaching and mineralization indicating that the paleofluid flow followed the fracture network in the damage zone of the faults. Those results show the importance of knowledge about the structure characteristics to prevent $CO_2$ leakage into the atmosphere.

The understanding and prediction of fluid flow in sedimentary rocks are also highly valuable in subsurface modelling [7, 11, 16, 82, 96, 120–122]. As such, a quantification of fluid flow in relation to fractures, fracture networks, and depositional structures can help to improve our understanding and prediction of fluid flow in the subsurface, and is of high value.

## 7. Conclusions

In this paper we have discussed the key structural controls on fluid flow in sedimentary rocks and the relationship between fluid flow, structures, and depositional architecture. In particular, we focused on the role of fracture *network* properties on flow, and the role of *hybrid networks*, which is poorly documented. Our study offers an overview of simple, direct observational evidence for the different controls on fluid flow, using iron oxide precipitates (IOPs) as evidence of paleofluid flow patterns. The examples herein are assembled in a schematic illustration in Figure 13. Along with the literature review, these examples allow us to identify some key factors that are instrumental in controlling fluid flow patterns in sedimentary rocks globally:

(1) *Depositional architecture and host rock properties* represent a first-order control on fluid flow in sedimentary rocks, and flow property contrasts associated with different bounding surfaces, facies, beds, and individual laminae may be sufficient to control and redirect flow

(2) *The conduit and/or barrier potential of geological structures* such as faults, fractures, and deformation bands are key to their effect on flow; whereas joints and unsealed faults may form significant conduits for fluid flow, cataclastic deformation bands, veins, and sealing faults (e.g., faults with shale smear,

cataclastic fault rocks, and cementation) may represent effective seals or baffles for flow

(3) *Anisotropy in fracture populations*, such as where fracture properties vary spatially and/or temporally along single structures or within a network, may cause differential effects on flow

(4) In fracture networks, *geometry and connectivity* of the fractures forming part of the network are key to understanding flow. The length, orientation, and intensity of fractures determine how individual fractures interact in the network, which in turn controls network connectivity and therefore percolation threshold and flow properties within the network

(5) *Kinematics and interaction* within a network are other key factors controlling flow. Whereas structures dominated by opening-mode displacement generally have a positive effect on flow, closing-mode displacement generally reduces flow, and structures affected by shear movement may form conduits or barriers depending on the presence of low-permeable fault rocks, existing aperture, or cements

(6) Finally, we have shown that *hybrid networks* represent a strong control on flow, as structural and stratal conduits can interact to form a well-connected network of conduits

Besides these factors, structural controls on fluid flow are highly dependent on timing, as the properties of both rocks and geological structures may transiently and cyclically vary over time.

## Conflicts of Interest

The authors declare that they have no conflicts of interest.

## Acknowledgments

We acknowledge funding for a personal PhD grant for Vilde Dimmen from VISTA—a basic research program in collaboration between the Norwegian Academy of Science and Letters and Equinor (grant number 6272). Atle Rotevatn also acknowledges funding for the ANIGMA project from the Norwegian Research Council in the context of the ENERGIX program (grant number 244129/E20), and from Equinor through the Akademia agreement. David Peacock, Kari Nærland, Thomas Berg Kristensen, Eivind Bastesen, and Arild Andresen are thanked for inspiring discussions. Peacock is also thanked for introducing us to the Gozo locality used herein.

## Supplementary Materials

Example 1: (a) overview field photo of example 1, Ras ir Raheb, Malta, with close-up photograph showing a halo of iron oxide precipitates; (b) photomosaic of the fracture network; (c) digitized fracture network of the locality. Example 2: (a) overview field photo of example 2, Ras ir Raheb, Malta; (b) close-up photograph showing the iron oxide precipitate bands in the foot wall along the fault; (c) photomosaic of the fracture network along the fault; (d) digitized fracture network of the locality. Example 3: (a) overview field photo of example 3, Marsalforn, Malta; (b) photomosaic of the fracture network with close-up photograph showing the iron oxide precipitates around pull aparts; (c) digitized fracture network of the locality. *(Supplementary Materials)*

## References

[1] D. R. Faulkner, C. A. L. Jackson, R. J. Lunn et al., "A review of recent developments concerning the structure, mechanics and fluid flow properties of fault zones," *Journal of Structural Geology*, vol. 32, no. 11, pp. 1557–1575, 2010.

[2] H. Fossen and A. Bale, "Deformation bands and their influence on fluid flow," *AAPG Bulletin*, vol. 91, no. 12, pp. 1685–1700, 2007.

[3] W. T. Parry, M. A. Chan, and B. Beitler, "Chemical bleaching indicates episodes of fluid flow in deformation bands in sandstone," *AAPG Bulletin*, vol. 88, no. 2, pp. 175–191, 2004.

[4] T. Volatili, M. Zambrano, A. Cilona et al., "From fracture analysis to flow simulations in fractured carbonates: the case study of the Roman Valley Quarry (Majella Mountain, Italy)," *Marine and Petroleum Geology*, vol. 100, pp. 95–110, 2019.

[5] K. Ogata, K. Senger, A. Braathen, and J. Tveranger, "Fracture corridors as seal-bypass systems in siliciclastic reservoir-cap rock successions: field-based insights from the Jurassic Entrada Formation (SE Utah, USA)," *Journal of Structural Geology*, vol. 66, pp. 162–187, 2014.

[6] H. Yoshida, K. Yamamoto, S. Yogo, and Y. Murakami, "An analogue of matrix diffusion enhanced by biogenic redox reaction in fractured sedimentary rock," *Journal of Geochemical Exploration*, vol. 90, no. 1-2, pp. 134–142, 2006.

[7] V. F. Bense, T. Gleeson, S. E. Loveless, O. Bour, and J. Scibek, "Fault zone hydrogeology," *Earth-Science Reviews*, vol. 127, pp. 171–192, 2013.

[8] N. J. Beukes, J. Gutzmer, and J. Mukhopadhyay, "The geology and genesis of high-grade hematite iron ore deposits," *Applied Earth Science*, vol. 112, no. 1, pp. 18–25, 2013.

[9] J. R. J. Davidson, J. Fairley, A. Nicol, D. Gravley, and U. Ring, "The origin of radon anomalies along normal faults in an active rift and geothermal area," *Geosphere*, vol. 12, no. 5, pp. 1656–1669, 2016.

[10] B. Dockrill and Z. K. Shipton, "Structural controls on leakage from a natural $CO_2$ geologic storage site: Central Utah, USA," *Journal of Structural Geology*, vol. 32, no. 11, pp. 1768–1782, 2010.

[11] K. Katsanou, K. Stratikopoulos, E. Zagana, and N. Lambrakis, "Radon changes along main faults in the broader Aigion region, NW Peloponnese," *Bulletin of the Geological Society of Greece*, vol. 43, pp. 1726–1736, 2017.

[12] J. D. Muirhead, G. Airoldi, J. V. Rowland, and J. D. L. White, "Interconnected sills and inclined sheet intrusions control shallow magma transport in the Ferrar Large Igneous Province, Antarctica," *Geological Society of America Bulletin*, vol. 124, no. 1-2, pp. 162–180, 2012.

[13] A. Rotevatn and H. Fossen, "Simulating the effect of subseismic fault tails and process zones in a siliciclastic reservoir analogue: implications for aquifer support and trap

definition," *Marine and Petroleum Geology*, vol. 28, no. 9, pp. 1648–1662, 2011.

[14] J. V. Rowland and R. H. Sibson, "Structural controls on hydrothermal flow in a segmented rift system, Taupo Volcanic Zone, New Zealand," *Geofluids*, vol. 4, no. 4, 283 pages, 2004.

[15] D. J. Sanderson and X. Zhang, "Critical stress localization of flow associated with deformation of well-fractured rock masses, with implications for mineral deposits," *Geological Society, London, Special Publications*, vol. 155, no. 1, pp. 69–81, 1999.

[16] H. Yoshida, R. Metcalfe, K. Yamamoto et al., "Redox front formation in an uplifting sedimentary rock sequence: an analogue for redox-controlling processes in the geosphere around deep geological repositories for radioactive waste," *Applied Geochemistry*, vol. 23, no. 8, pp. 2364–2381, 2008.

[17] Y. Zhang, B. E. Hobbs, A. Ord et al., "The influence of faulting on host-rock permeability, fluid flow and ore genesis of gold deposits: a theoretical 2D numerical model," *Journal of Geochemical Exploration*, vol. 78-79, pp. 279–284, 2003.

[18] N. C. Davatzes, P. Eichhubl, and A. Aydin, "Structural evolution of fault zones in sandstone by multiple deformation mechanisms: Moab fault, southeast Utah," *GSA Bulletin*, vol. 117, no. 1, pp. 135–148, 2005.

[19] H. Fossen, R. A. Schultz, Z. K. Shipton, and K. Mair, "Deformation bands in sandstone: a review," *Journal of the Geological Society*, vol. 164, no. 4, pp. 755–769, 2007.

[20] Y. Missenard, A. Bertrand, P. Vergely, A. Benedicto, M. E. Cushing, and M. Rocher, "Fracture-fluid relationships: implications for the sealing capacity of clay layers—insights from field study of the Blue Clay formation, Maltese islands," *Bulletin de la Societe Geologique de France*, vol. 185, no. 1, pp. 51–63, 2014.

[21] F. Agosta and D. L. Kirschner, "Fluid conduits in carbonate-hosted seismogenic normal faults of central Italy," *Journal of Geophysical Research: Solid Earth*, vol. 108, no. B4, 2003.

[22] E. Bastesen and A. Rotevatn, "Evolution and structural style of relay zones in layered limestone-shale sequences: insights from the Hammam Faraun Fault Block, Suez Rift, Egypt," *Journal of the Geological Society*, vol. 169, no. 4, pp. 477–488, 2012.

[23] A. Billi, F. Salvini, and F. Storti, "The damage zone-fault core transition in carbonate rocks: implications for fault growth, structure and permeability," *Journal of Structural Geology*, vol. 25, no. 11, pp. 1779–1794, 2003.

[24] N. J. C. Farrell, D. Healy, and C. W. Taylor, "Anisotropy of permeability in faulted porous sandstones," *Journal of Structural Geology*, vol. 63, pp. 50–67, 2014.

[25] T. B. Kristensen, A. Rotevatn, D. C. P. Peacock, G. A. Henstra, I. Midtkandal, and S. A. Grundvag, "Structure and flow properties of syn-rift border faults: the interplay between fault damage and fault-related chemical alteration (Dombjerg Fault, Wollaston Forland, NE Greenland)," *Journal of Structural Geology*, vol. 92, pp. 99–115, 2016.

[26] J. Hirani, E. Bastesen, A. Boyce et al., "Controls on the formation of stratabound dolostone bodies, Hammam Faraun Fault block, Gulf of Suez," *Sedimentology*, vol. 65, no. 6, pp. 1973–2002, 2018.

[27] M. Holland and J. L. Urai, "Evolution of anastomosing crack-seal vein networks in limestones: insight from an exhumed high-pressure cell, Jabal Shams, Oman Mountains," *Journal of Structural Geology*, vol. 32, no. 9, pp. 1279–1290, 2010.

[28] C. Hollis, E. Bastesen, A. Boyce et al., "Fault-controlled dolomitization in a rift basin," *Geology*, vol. 45, no. 3, pp. 219–222, 2017.

[29] S. E. Laubach, J. E. Olson, and J. F. W. Gale, "Are open fractures necessarily aligned with maximum horizontal stress?," *Earth and Planetary Science Letters*, vol. 222, no. 1, pp. 191–195, 2004.

[30] J. G. Ramsay, "The crack-seal mechanism of rock deformation," *Nature*, vol. 284, no. 5752, pp. 135–139, 1980.

[31] V. F. Bense and M. A. Person, "Faults as conduit-barrier systems to fluid flow in siliciclastic sedimentary aquifers," *Water Resources Research*, vol. 42, no. 5, 2006.

[32] D. Wiprut and M. D. Zoback, "Fault reactivation and fluid flow along a previously dormant normal fault in the northern North Sea," *Geology*, vol. 28, no. 7, pp. 595–598, 2000.

[33] E. Bonnet, O. Bour, N. E. Odling et al., "Scaling of fracture systems in geological media," *Reviews of Geophysics*, vol. 39, no. 3, pp. 347–383, 2001.

[34] A. Gudmundsson, S. S. Berg, K. B. Lyslo, and E. Skurtveit, "Fracture networks and fluid transport in active fault zones," *Journal of Structural Geology*, vol. 23, no. 2-3, pp. 343–353, 2001.

[35] D. J. Sanderson, D. C. P. Peacock, C. W. Nixon, and A. Rotevatn, "Graph theory and the analysis of fracture networks," *Journal of Structural Geology*, vol. 125, pp. 155–165, 2019.

[36] D. J. Sanderson and C. W. Nixon, "Topology, connectivity and percolation in fracture networks," *Journal of Structural Geology*, vol. 115, pp. 167–177, 2018.

[37] A. Rotevatn, S. J. Buckley, J. A. Howell, and H. Fossen, "Overlapping faults and their effect on fluid flow in different reservoir types: a LIDAR-based outcrop modeling and flow simulation study," *AAPG Bulletin*, vol. 93, no. 3, pp. 407–427, 2009.

[38] P. S. Ringrose, K. S. Sorbie, P. W. M. Corbett, and J. L. Jensen, "Immiscible flow behaviour in laminated and cross-bedded sandstones," *Journal of Petroleum Science and Engineering*, vol. 9, no. 2, pp. 103–124, 1993.

[39] F. Balsamo, F. H. R. Bezerra, M. M. Vieira, and F. Storti, "Structural control on the formation of iron-oxide concretions and Liesegang bands in faulted, poorly lithified Cenozoic sandstones of the Paraiba Basin, Brazil," *Geological Society of America Bulletin*, vol. 125, no. 5-6, pp. 913–931, 2013.

[40] V. Dimmen, A. Rotevatn, D. C. P. Peacock, C. W. Nixon, and K. Nærland, "Quantifying structural controls on fluid flow: insights from carbonate-hosted fault damage zones on the Maltese Islands," *Journal of Structural Geology*, vol. 101, pp. 43–57, 2017.

[41] O. B. Duffy, C. W. Nixon, R. E. Bell et al., "The topology of evolving rift fault networks: single-phase vs multi-phase rifts," *Journal of Structural Geology*, vol. 96, pp. 192–202, 2017.

[42] T. Manzocchi, "The connectivity of two-dimensional networks of spatially correlated fractures," *Water Resources Research*, vol. 38, no. 9, pp. 1–20, 2002.

[43] C. K. Morley and C. W. Nixon, "Topological characteristics of simple and complex normal fault networks," *Journal of Structural Geology*, vol. 84, pp. 68–84, 2016.

[44] D. J. Sanderson and C. W. Nixon, "The use of topology in fracture network characterization," *Journal of Structural Geology*, vol. 72, pp. 55–66, 2015.

[45] D. C. P. Peacock, C. W. Nixon, A. Rotevatn, D. J. Sanderson, and L. F. Zuluaga, "Glossary of fault and other fracture networks," *Journal of Structural Geology*, vol. 92, pp. 12–29, 2016.

[46] M. A. Antonellini, A. Aydin, and D. D. Pollard, "Microstructure of deformation bands in porous sandstones at Arches National Park, Utah," *Journal of Structural Geology*, vol. 16, no. 7, pp. 941–959, 1994.

[47] G. Ballas, R. Soliva, J.-P. Sizun, A. Benedicto, T. Cavailhes, and S. Raynaud, "The importance of the degree of cataclasis in shear bands for fluid flow in porous sandstone, Provence, France," *AAPG Bulletin*, vol. 96, no. 11, pp. 2167–2186, 2012.

[48] A. Rotevatn, H. S. Fossmark, E. Bastesen, E. Thorsheim, and A. Torabi, "Do deformation bands matter for flow? Insights from permeability measurements and flow simulations in porous carbonate rocks," *Petroleum Geoscience*, vol. 23, no. 1, pp. 104–119, 2017.

[49] A. Rotevatn, A. Torabi, H. Fossen, and A. Braathen, "Slipped deformation bands: a new type of cataclastic deformation bands in Western Sinai, Suez Rift, Egypt," *Journal of Structural Geology*, vol. 30, no. 11, pp. 1317–1331, 2008.

[50] K. R. Sternlof, J. R. Chapin, D. D. Pollard, and L. J. Durlofsky, "Permeability effects of deformation band arrays in sandstone," *AAPG Bulletin*, vol. 88, no. 9, pp. 1315–1329, 2004.

[51] W. L. Taylor and D. D. Pollard, "Estimation of in situ permeability of deformation bands in porous sandstone, Valley of Fire, Nevada," *Water Resources Research*, vol. 36, no. 9, pp. 2595–2606, 2000.

[52] F. Akagawa, H. Yoshida, S. Yogo, and K. Yamomoto, "Redox front formation in fractured crystalline rock: an analogue of matrix diffusion in an oxidizing front along water-conducting fractures," *Geochemistry-Exploration Environment Analysis*, vol. 6, no. 1, pp. 49–56, 2006.

[53] P. Eichhubl, N. C. Davatzes, and S. P. Becker, "Structural and diagenetic control of fluid migration and cementation along the Moab fault, Utah," *AAPG Bulletin*, vol. 93, no. 5, pp. 653–681, 2009.

[54] L. Fu, K. L. Milliken, and J. M. Sharp Jr., "Porosity and permeability variations in fractured and Liesegang-banded Breathitt sandstones (Middle Pennsylvanian), eastern Kentucky: diagenetic controls and implications for modeling dual-porosity systems," *Journal of Hydrology*, vol. 154, no. 1-4, pp. 351–381, 1994.

[55] P. Ortoleva, G. Auchmuty, J. Chadam et al., "Redox front propagation and banding modalities," *Physica D: Nonlinear Phenomena*, vol. 19, no. 3, pp. 334–354, 1986.

[56] P. M. Barnes and B. M. de Lépinay, "Rates and mechanics of rapid frontal accretion along the very obliquely convergent southern Hikurangi margin, New Zealand," *Journal of Geophysical Research: Solid Earth*, vol. 102, no. B11, pp. 24931–24952, 1997.

[57] R. J. Norris, P. O. Koons, and A. F. Cooper, "The obliquely-convergent plate boundary in the South Island of New Zealand: implications for ancient collision zones," *Journal of Structural Geology*, vol. 12, no. 5-6, pp. 715–725, 1990.

[58] G. H. Browne and R. M. Slatt, "Outcrop and behind-outcrop characterization of a late Miocene slope fan system, Mt. Messenger Formation, New Zealand," *AAPG Bulletin*, vol. 86, pp. 841–862, 2002.

[59] P. R. King, G. H. Browne, R. M. Slatt, and P. Weimer, "Sequence architecture of exposed late Miocene basin floor fan and channel-levee complexes (Mount Messenger Formation), Taranaki Basin, New Zealand," in *Submarine Fans and Turbidite Systems: Sequence Stratigraphy, Reservoir Architecture and Production Characteristics; Gulf of Mexico and International: Proceedings Gulf Coast Section Society of Economic Paleontologists and Mineralogists Foundation Fifteenth Annual Research Conference, GCS017*, pp. 177–192, Houston, TX, USA, December 1994.

[60] S. D. Nodder, C. S. Nelson, and P. J. J. Kamp, "Mass-emplaced siliciclastic-volcaniclastic-carbonate sediments in Middle Miocene shelf-to-slope environments at Waikawau, northern Taranaki, and some implications for Taranaki Basin development," *New Zealand Journal of Geology and Geophysics*, vol. 33, no. 4, pp. 599–615, 1990.

[61] M. G. Laird and J. D. Bradshaw, "The break-up of a long-term relationship: the Cretaceous separation of New Zealand from Gondwana," *Gondwana Research*, vol. 7, no. 1, pp. 273–286, 2004.

[62] R. Sutherland, P. King, and R. Wood, "Tectonic evolution of Cretaceous rift basins in south-eastern Australia and New Zealand: implications for exploration risk assessment," in *Eastern Australasian Basins Symposium, a Refocussed Energy Perspective for the Future*, K. Hill and T. Bernecker, Eds., pp. 3–14, Petroleum Exploration Society of Australia, Special Publication, 2001.

[63] M. Giba, J. J. Walsh, and A. Nicol, "Segmentation and growth of an obliquely reactivated normal fault," *Journal of Structural Geology*, vol. 39, pp. 253–267, 2012.

[64] C. Childs, J. J. Walsh, T. Manzocchi et al., "Definition of a fault permeability predictor from outcrop studies of a faulted turbidite sequence, Taranaki, New Zealand," *Geological Society, London, Special Publications*, vol. 292, no. 1, pp. 235–258, 2007.

[65] A. Nicol, C. Childs, J. J. Walsh, and K. W. Schafer, "A geometric model for the formation of deformation band clusters," *Journal of Structural Geology*, vol. 55, pp. 21–33, 2013.

[66] C. J. Adams, N. Mortimer, H. J. Campbell, and W. L. Griffin, "Detrital zircon geochronology and sandstone provenance of basement Waipapa terrane (Triassic-Cretaceous) and Cretaceous cover rocks (Northland allochthon and Houhora complex) in northern North Island, New Zealand," *Geological Magazine*, vol. 150, no. 1, pp. 89–109, 2013.

[67] R. B. Evans, "Tertiary tectonic development of Whangaroa district, northeastern Northland, New Zealand," *New Zealand Journal of Geology and Geophysics*, vol. 35, no. 4, pp. 549–559, 1992.

[68] R. F. Hay, "The geology of Mangakahia Subdivision," in *New Zealand Department of Scientific and Industrial Research*, vol. 61, pp. 1–109, New Zealand Geological Survey Bulletine, 1960.

[69] P. F. Ballance and K. B. Spörli, "Northland allochthon," *Journal of the Royal Society of New Zealand*, vol. 9, no. 2, pp. 259–275, 1979.

[70] M. J. Isaac, *Geology of the Kaitaia area: scale 1 : 250 000*, Institute of Geological and Nuclear Sciences, Geological map +41 folded map, Lower Hutt, 1996.

[71] R. B. Evans, "Profile of a piggyback basin: early Miocene Otaua Group and Waipoua Subgroup, western Northland, New Zealand," *New Zealand Journal of Geology and Geophysics*, vol. 37, no. 1, pp. 87–99, 1994.

[72] C. -D. Reuther and G. H. Eisbacher, "Pantelleria Rift—crustal extension in a convergent intraplate setting," *Geologische Rundschau*, vol. 74, no. 3, pp. 585–597, 1985.

[73] W. Cavazza and F. C. Wezel, "The Mediterranean region—a geological primer," *Episodes*, vol. 26, no. 3, pp. 160–168, 2003.

[74] C. J. Dart, D. W. J. Bosence, and K. R. Mcclay, "Stratigraphy and structure of the Maltese Graben System," *Journal of the Geological Society*, vol. 150, no. 6, pp. 1153–1166, 1993.

[75] K. C. Hill and A. B. Hayward, "Structural constraints on the Tertiary plate tectonic evolution of Italy," *Marine and Petroleum Geology*, vol. 5, no. 1, pp. 2–16, 1988.

[76] L. Jolivet and C. Faccenna, "Mediterranean extension and the Africa-Eurasia collision," *Tectonics*, vol. 19, no. 6, pp. 1095–1106, 2000.

[77] C. G. Bonson, C. Childs, J. J. Walsh, M. P. J. Schöpfer, and V. Carboni, "Geometric and kinematic controls on the internal structure of a large normal fault in massive limestones: the Maghlaq Fault, Malta," *Journal of Structural Geology*, vol. 29, no. 2, pp. 336–354, 2007.

[78] M. W. Putz-Perrier and D. J. Sanderson, "Distribution of faults and extensional strain in fractured carbonates of the North Malta Graben," *AAPG Bulletin*, vol. 94, no. 4, pp. 435–456, 2010.

[79] E. A. H. Michie, T. J. Haines, D. Healy, J. E. Neilson, N. E. Timms, and C. A. J. Wibberley, "Influence of carbonate facies on fault zone architecture," *Journal of Structural Geology*, vol. 65, pp. 82–99, 2014.

[80] H. M. Pedley, M. R. House, and B. Waugh, "The geology of Malta and Gozo," *Proceedings of the Geologists' Association*, vol. 87, no. 3, pp. 325–341, 1976.

[81] T. J. Haines, E. A. H. Michie, J. E. Neilson, and D. Healy, "Permeability evolution across carbonate hosted normal fault zones," *Marine and Petroleum Geology*, vol. 72, pp. 62–82, 2016.

[82] Y. S. Kim, D. C. P. Peacock, and D. J. Sanderson, "Mesoscale strike-slip faults and damage zones at Marsalforn, Gozo Island, Malta," *Journal of Structural Geology*, vol. 25, no. 5, pp. 793–812, 2003.

[83] S. S. Berg and T. Skar, "Controls on damage zone asymmetry of a normal fault zone: outcrop analyses of a segment of the Moab fault, SE Utah," *Journal of Structural Geology*, vol. 27, no. 10, pp. 1803–1822, 2005.

[84] K. A. Foxford, J. J. Walsh, J. Watterson, I. R. Garden, S. C. Guscott, and S. D. Burley, "Structure and content of the Moab Fault Zone, Utah, USA, and its implications for fault seal prediction," *Geological Society, London, Special Publications*, vol. 147, no. 1, pp. 87–103, 1998.

[85] K. Foxford, I. Garden, S. Guscott et al., "The field geology of the Moab fault," in *Geology and Resources of the Paradox Basin*, A. C. Huuffman Jr., W. R. Lund, and L. H. Godwin, Eds., vol. 25, pp. 265–283, Utah Geological Association Guidebook, 1996.

[86] B. D. Trudgill, "Evolution of salt structures in the northern Paradox Basin: controls on evaporite deposition, salt wall growth and supra-salt stratigraphic architecture," *Basin Research*, vol. 23, no. 2, pp. 208–238, 2011.

[87] M. Crabaugh and G. Kocurek, "Entrada Sandstone: an example of a wet aeolian system," *Geological Society, London, Special Publications*, vol. 72, no. 1, pp. 103–126, 1993.

[88] B. Nyberg, C. W. Nixon, and D. J. Sanderson, "NetworkGT: a GIS tool for geometric and topological analysis of two-dimensional fracture networks," *Geosphere*, vol. 14, no. 4, pp. 1618–1634, 2018.

[89] L. Jing and O. Stephansson, "Network topology and homogenization of fractured rocks," in *Fluid Flow and Transport in Rocks*, B. Jamtveit and B. W. D. Yardley, Eds., pp. 191–202, Springer, 1997.

[90] A. Hurst and K. J. Rosvoll, *Permeability variations in sandstones and their relationship to sedimentary structures, Reservoir Characterization II*, Elsevier, 1991.

[91] M. D. Jackson and A. H. Muggeridge, "Effect of discontinuous shales on reservoir performance during horizontal waterflooding," *SPE Journal*, vol. 5, no. 4, pp. 446–455, 2013.

[92] M. A. Chandler, G. Kocurek, D. J. Goggin, and L. W. Lake, "Effects of stratigraphic heterogeneity on permeability in eolian sandstone sequence, Page Sandstone, northern Arizona," *AAPG Bulletin*, vol. 73, pp. 658–668, 1989.

[93] A. Gartrell, Y. Zhang, M. Lisk, and D. Dewhurst, "Fault intersections as critical hydrocarbon leakage zones: integrated field study and numerical modelling of an example from the Timor Sea, Australia," *Marine and Petroleum Geology*, vol. 21, no. 9, pp. 1165–1179, 2004.

[94] S. J. Jolley, D. Barr, J. J. Walsh, and R. J. Knipe, "Structurally complex reservoirs: an introduction," *Geological Society, London, Special Publications*, vol. 292, no. 1, pp. 1–24, 2007.

[95] C. A. Barton, M. D. Zoback, and D. Moos, "Fluid flow along potentially active faults in crystalline rock," *Geology*, vol. 23, no. 8, pp. 683–686, 1995.

[96] R. H. Sibson, "Structural permeability of fluid-driven fault-fracture meshes," *Journal of Structural Geology*, vol. 18, no. 8, pp. 1031–1042, 1996.

[97] R. W. Zimmerman, A. Al-Yaarubi, C. C. Pain, and C. A. Grattoni, "Non-linear regimes of fluid flow in rock fractures," *International Journal of Rock Mechanics and Mining Sciences*, vol. 41, no. 3, pp. 384–384, 2004.

[98] P. Eichhubl, W. L. Taylor, D. D. Pollard, and A. Aydin, "Paleo-fluid flow and deformation in the Aztec Sandstone at the Valley of Fire, Nevada—evidence for the coupling of hydrogeologic, diagenetic, and tectonic processes," *GSA Bulletin*, vol. 116, no. 9, pp. 1120–1136, 2004.

[99] Z. K. Shipton, J. P. Evans, and L. B. Thompson, "The geometry and thickness of deformation-band fault core and its influence on sealing characteristics of deformation-band fault zones," *AAPG Memoir*, vol. 85, pp. 181–195, 2005.

[100] G. Verhaert, P. Muchez, E. Keppens, and M. Sintubin, "Fluid impact and spatial and temporal evolution of normal faulting in limestones. A case study in the Burdur-Isparta Region (SW Turkey)," *Geologica Belgica*, vol. 12, pp. 59–73, 2009.

[101] S. K. Matthäi, A. Aydin, D. D. Pollard, and S. G. Roberts, "Numerical simulation of departures from radial drawdown in a faulted sandstone reservoir with joints and deformation bands," *Geological Society, London, Special Publications*, vol. 147, no. 1, pp. 157–191, 1998.

[102] A. Rotevatn, J. Tveranger, J. A. Howell, and H. Fossen, "Dynamic investigation of the effect of a relay ramp on simulated fluid flow: geocellular modelling of the Delicate Arch Ramp, Utah," *Petroleum Geoscience*, vol. 15, no. 1, pp. 45–58, 2009.

[103] L. F. Zuluaga, H. Fossen, and A. Rotevatn, "Progressive evolution of deformation band populations during Laramide fault-propagation folding: Navajo Sandstone, San Rafael

monocline, Utah, USA," *Journal of Structural Geology*, vol. 68, pp. 66–81, 2014.

[104] T. Cavailhes, R. Soliva, A. Benedicto, D. Loggia, R. A. Schultz, and C. A. J. Wibberley, "Are cataclastic shear bands fluid barriers or capillarity conduits? Insight from the analysis of redox fronts in porous," in *2nd EAGE International Conference on Fault and Top Seals—From Pore to Basin Scale 2009*, Montpellier, France, September 2009.

[105] J. M. Sigda and J. L. Wilson, "Are faults preferential flow paths through semiarid and arid vadose zones?," *Water Resources Research*, vol. 39, no. 8, p. 1225, 2003.

[106] S. E. Laubach, "Practical approaches to identifying sealed and open fractures," *AAPG Bulletin*, vol. 87, no. 4, pp. 561–579, 2003.

[107] A. Rotevatn and E. Bastesen, "Fault linkage and damage zone architecture in tight carbonate rocks in the Suez Rift (Egypt): implications for permeability structure along segmented normal faults," in *Advances in the Study of Fractured Reservoirs*, G. H. Spence, J. Redfern, R. Aguilera, T. G. Bevan, J. W. Cosgrove, G. D. Couples, and J.-M. Daniel, Eds., pp. 79–95, Geological Society, Special Publications, London, 2014.

[108] A. Torabi and H. Fossen, "Spatial variation of microstructure and petrophysical properties along deformation bands in reservoir sandstones," *AAPG Bulletin*, vol. 93, no. 7, pp. 919–938, 2009.

[109] M. Antonellini and A. Aydin, "Effect of faulting on fluid flow in porous sandstones: geometry and spatial distribution," *AAPG Bulletin*, vol. 79, pp. 642–671, 1995.

[110] C. Zeeb, E. Gomez-Rivas, P. D. Bons, and P. Blum, "Evaluation of sampling methods for fracture network characterization using outcrops," *AAPG Bulletin*, vol. 97, no. 9, pp. 1545–1566, 2013.

[111] C. W. Nixon, S. Vaagan, D. J. Sanderson, and R. L. Gawthorpe, "Spatial distribution of damage and strain within a normal fault relay at Kilve, UK," *Journal of Structural Geology*, vol. 118, pp. 194–209, 2019.

[112] Y.-S. Kim and D. J. Sanderson, "Inferred fluid flow through fault damage zones based on the observation of stalactites in carbonate caves," *Journal of Structural Geology*, vol. 32, no. 9, pp. 1305–1316, 2010.

[113] I. Moeck, G. Kwiatek, and G. Zimmermann, "Slip tendency analysis, fault reactivation potential and induced seismicity in a deep geothermal reservoir," *Journal of Structural Geology*, vol. 31, no. 10, pp. 1174–1182, 2009.

[114] L. J. Pyrak-Nolte and J. P. Morris, "Single fractures under normal stress: the relation between fracture specific stiffness and fluid flow," *International Journal of Rock Mechanics and Mining Sciences*, vol. 37, no. 1-2, pp. 245–262, 2000.

[115] X. Zhang, D. J. Sanderson, and A. J. Barker, "Numerical study of fluid flow of deforming fractured rocks using dual permeability model," *Geophysical Journal International*, vol. 151, no. 2, pp. 452–468, 2002.

[116] N. H. S. Oliver and P. D. Bons, "Mechanisms of fluid flow and fluid–rock interaction in fossil metamorphic hydrothermal systems inferred from vein–wallrock patterns, geometry and microstructure," *Geofluids*, vol. 1, no. 2, 162 pages, 2001.

[117] T. Tamagawa and D. D. Pollard, "Fracture permeability created by perturbed stress fields around active faults in a fractured basement reservoir," *AAPG Bulletin*, vol. 92, no. 6, pp. 743–764, 2008.

[118] W. H. Newhouse, *Ore Deposits as Related to Structural Features*, Princeton University Press, Princeton, New Jersey, 1942.

[119] Z. K. Shipton, J. P. Evans, D. Kirschner, P. T. Kolesar, A. P. Williams, and J. Heath, "Analysis of $CO_2$ leakage through "low-permeability" faults from natural reservoirs in the Colorado Plateau, east-central Utah," in *Geological Storage of Carbon Dioxide*, S. J. Baines and R. H. Worden, Eds., pp. 43–58, Geological Society, Special Publications, London, 2004.

[120] A. Aydin, "Fractures, faults, and hydrocarbon entrapment, migration and flow," *Marine and Petroleum Geology*, vol. 17, no. 7, pp. 797–814, 2000.

[121] S. D. Harris, E. McAllister, R. J. Knipe, and N. E. Odling, "Predicting the three-dimensional population characteristics of fault zones: a study using stochastic models," *Journal of Structural Geology*, vol. 25, no. 8, pp. 1281–1299, 2003.

[122] C.-Y. King, "Gas geochemistry applied to earthquake prediction: an overview," *Journal of Geophysical Research: Solid Earth*, vol. 91, no. B12, pp. 12269–12281, 1986.

# III

# Paper 3: Imaging of small-scale faults in seismic reflection data: Insights from seismic modelling of faults in outcrop

Vilde Dimmen, Atle Rotevatn, Isabelle Lecomte

*Published in Marine and Petroleum Geology, 147 (2023) 105980*

https://doi.org/10.1016/j.marpetgeo.2022.105980

Marine and Petroleum Geology 147 (2023) 105980

Contents lists available at ScienceDirect

Marine and Petroleum Geology

journal homepage: www.elsevier.com/locate/marpetgeo

# Imaging of small-scale faults in seismic reflection data: Insights from seismic modelling of faults in outcrop

Vilde Dimmen *, Atle Rotevatn, Isabelle Lecomte

*Department of Earth Science, University of Bergen, PO Box 7800, 5020 Bergen, Norway*

ARTICLE INFO

*Keywords:*
seismic Imaging
Sub-seismic
Carbonates
Normal faults
Ormsby wavelet
PSDM

ABSTRACT

Faults with throws that fall below vertical seismic resolution are challenging to identify in reflection seismic datasets. Nevertheless, such small-scale faults may still affect the seismic images, and in this study, we build seismic models of outcrop analogues to investigate *how*. Using photogrammetry from faults affecting Oligocene to Miocene carbonate rocks in Malta, we build a series of geological models from which synthetic seismic images are produced. The resulting seismic images are analysed to elucidate the effects of varying geologic input, signal properties and introduction of noise, and compared to real seismic data from the SW Barents Sea, offshore Norway. Our results suggest that at signal peak frequencies of 30 Hz and higher, using the classic Ricker wavelet type and without introducing noise, graben forming faults with a combined displacement down to ~5 m affect the seismic image by slight downwarping of reflections, whereas single faults with displacement down to ~10 m show detectable non-discrete reflection offsets in form of a monoclinal geometry at signal peak frequencies at 60 Hz. Using an Ormsby wavelet, we get seismic images with a quality that lie in between that of the 30 Hz and 60 Hz Ricker, even though the peak frequency is lower. The identified structures can also be seen when noise is included, although the reflections are more irregular and harder to detect. This suggests that under relatively noise-free conditions in high-quality reflection seismic datasets, lower-throw faults (as low as 5 m in this study) that do not induce discrete reflection offsets in seismic images may still produce reflection distortions. Additionally, seismic modelling using the Ormsby wavelet, and its effect on the seismic image, is lacking in literature as of today. We suggest that the results and examples shown in this study may be used to geologically inform fault interpretations in real seismic datasets and may form an empirical basis for geologically concept-driven fault interpretation strategies.

## 1. Introduction

Faults of all scales play a crucial role for accommodating deformation and fluid flow within the upper crust (Caine and Forster, 1999; Faulkner et al., 2010). Understanding the role of faults in for example exploration for, and exploitation of, petroleum, mining, and groundwater resources, are of great economic significance since faults often control fluid migration, induce reservoir/aquifer compartmentalisation, and determine the location of ore deposits (e.g. Aydin, 2000; Gartrell et al., 2004; Bense and Person, 2006; Rotevatn and Fossen, 2011; Beukes et al., 2013; Dimmen et al., 2020; Bradaric et al., 2022). Fault-controlled fluid flow is also important from an environmental/hazards perspective, and relevant for example in subsurface carbon storage, contaminant transport and the storage of nuclear waste (Talwani, 1999; Moussa and El Arabi, 2003; Shipton et al., 2005; Yoshida et al., 2008; Krawczyk et al., 2015). For most of the above applications, fault detection and mapping in the subsurface is key to understanding fault geometry, dimensions, distribution, and properties.

The detection of faults in the subsurface often depends on the use of reflection seismic data, coming with several limitations. The vertical resolution i.e., of seismic datasets constrains our ability to identify geological layers, the minimum vertical distance between two features (reflectors) that are possible to define separately rather than as one. Vertical seismic resolution is controlled by the wavelength of the seismic signal; the Rayleigh criterion states that the vertical resolution limit is a quarter-wavelength (e.g. Knapp, 1990). For modern, commercial, high-quality 3D seismic data sets this may translate to a vertical resolvability of 10–30 m at best. This defines an approximate lower practical constraint on seismically resolvable fault offsets. The relatively high-angle nature of most extensional faults means that the seismic

---

* Corresponding author. (V. Dimmen).
*E-mail address:* vilde.dimmen@uib.no (V. Dimmen).

https://doi.org/10.1016/j.marpetgeo.2022.105980
Received 3 March 2022; Received in revised form 13 September 2022; Accepted 16 October 2022
Available online 22 October 2022
0264-8172/© 2022 The Authors. Published by Elsevier Ltd. This is an open access article under the CC BY license (http://creativecommons.org/licenses/by/4.0/).

waves will not hit and illuminate the actual fault surface, except when using very wide offsets. Therefore, most faults are so-called non-illuminated faults, and are detected from breaks in reflection continuity rather than by discrete imaging of the fault itself. In addition, limited lateral resolution blurs the seismic images (Fresnel zone effect) and may induce lateral smearing across non-illuminated fault zones; this can prevent accurate dip estimations, even if 3D migration reduces the Fresnel-zone down to half-wavelength (Simm and Bacon, 2014). Also, faults dipping at an angle greater than ~40–50° are generally too steep to be illuminated and imaged in reflection seismic data (Simm and Bacon, 2014; Chen and Huang, 2015), and their presence is therefore generally inferred by the identification of discontinuous reflections of the displaced geological strata. There are also other limitations that come into effect in the imaging of subsurface geology with reflection seismic data, such as noise and decrease of signal/image quality with depth due to geometrical spreading, attenuation of seismic energy with the high frequencies being especially absorbed, and scattering of the seismic signal by e.g. faults and fault-block crests (Simm and Bacon, 2014; Lecomte et al., 2015).

Small-scale faults and other types of fractures that fall below seismic resolution are very important, since i) fault/fracture sizes in nature follow a power-law distribution, which means there are infinitely greater numbers of smaller (sub-seismic) structures than greater (seismically resolvable) structures in any rock deformed in a brittle manner (e.g. Hatton et al., 1994; Vermilye and Scholz, 1995; Renshaw and Park, 1997); ii) sub-seismic structures may accommodate significant crustal strains; for example, Walsh et al. (1991) suggest that seismic-based summations of fault throws may underestimate regional extension by up to 40% (depending on the seismic resolution of the datasets used), due to sub-seismic strains; and iii) sub-seismic structures are critical for controlling permeability and fluid flow patterns in the sub-surface (e.g. Damsleth et al., 1998; Walsh et al., 1998; Mitchell and Faulkner, 2012), because they provide structural connectivity between larger seismically mappable structures (e.g. Gartrell et al., 2004; Dimmen et al., 2017; Sanderson and Nixon, 2018). Hence, it is important to be aware of these structures and get the best possible understanding of them.

Although structural features that fall below seismic resolution cannot be directly resolved, they may still affect the seismic image. To the best of our knowledge, no previous seismic modelling studies have attempted to investigate the effect of such structures on seismic images. Motivated by this, we explore the effects that sub-seismic faults may have on a seismic image, to better understand how some sub-seismic structures may be inferred.

In this paper, we study carbonate-hosted normal faults from the west coast of Malta with displacements of 20 m and below and conduct seismic modelling to investigate their effect on seismic images. As such, the studied faults fall approximately at or below the limits of what is practically resolvable in modern, commercial reflection seismic data. The key question we ask is “*how do faults that are borderline seismically resolvable, or that fall below seismic resolution, affect seismic images?*“. Secondly, we look into how structural complexity associated with such small-scale faults affect a seismic image, and whether the seismic image of simpler fault geometries (e.g., a single fault strand) differ from seismic images of more complex fault geometries (in this case a fault comprised of two fault strands forming a fault-bounded lens). In addition to looking into how the structural geometries affect the seismic image, we also investigate the effect of various signal properties on the seismic images by varying wavelet type and wave frequencies, and by varying lateral resolution. We also look at the effect of introducing noise, which is generally present in real seismic data, and, finally, compare our synthetic images with real, high-quality seismic images from a carbonate-dominated succession in the Barents Sea, offshore Norway.

## 2. Geologic framework of the faults used in the seismic models

The normal faults that form the basis for the seismic models herein are hosted in Late Oligocene to Early Miocene limestones in western Malta (Fig. 1 a). The Maltese islands are situated on the NE shoulder of the Pantelleria rift system, which formed in Late Miocene-Early Pliocene as a result of roll-back and eastward migration of the Apennine-Maghrebian subduction zone (Dart et al., 1993; Gueguen et al., 1998; Cavazza and Wezel, 2003). The rifting event caused the formation of ENE-WSW trending horst and graben structures that now dominate the Maltese archipelago (Bonson et al., 2007; Putz-Perrier and Sanderson, 2010). The studied areas are located in cliff sections at Ras-Ir-Raheb, immediately south of Fomm-Ir-Rih bay and approximately 500 m into the footwall of the regionally significant Victoria Lines Fault (~90 m displacement; Fig. 1 a). The cliff sections, which are easily accessible, host a range of smaller-scale normal faults with displacements in the range of <1–20 m (Michie et al., 2014; Dimmen, 2016; Nixon et al., 2020). The faults are hosted within a shallow-marine carbonate succession that comprises the middle part of the Oligocene-Quaternary stratigraphy of the Maltese archipelago (Fig. 1 b).

The regional stratigraphy of Malta is divided into pre-, syn-, and post-rift successions, with respect to the Pantelleria rifting event (e.g. Pedley et al., 1976; Dart et al., 1993). The pre-rift succession includes platform carbonates comprising the Lower Coralline Limestone Formation of Late Oligocene age and the pelagic Early Miocene Lower Globigerina Limestone Member of the Globigerina Limestone Formation (Pedley et al., 1976). The syn-rift stage (21–1.5 Ma) is represented by i) fine-grained foraminiferal limestones of the Middle and Upper Globigeringa Limestone members, followed by ii) pelagic marls and clays constituting the Blue Clay Formation, iii) a marly glauconite lag named the Greensand Formation (however not present in our study area) and iv) shallow-water limestones and marls of the Upper Coralline Limestone Formation (Pedley et al., 1976; Dart et al., 1993). The post-rift sequence consists predominantly of Quaternary deposits, and includes terrestrial, pelagic and hemipelagic sediments (Pedley et al., 1976; Jongsma et al., 1985; Dart et al., 1993). The studied faults are mainly hosted in the Lower Coralline Limestone Formation and Globigerina Limestone Formation, although some continue up-dip into overlying strata.

## 3. Methodology

### 3.1. Collection and processing of outcrop imagery and observations

Faults were mapped along the studied cliff sections at two localities at Ras-Ir-Raheb (Fig. 1 a), and map-view and cliff-section imagery with 60–80% overlap was collected using a drone (DJI Mavic Pro). The imagery was used to create photo panels and 3D photogrammetric models (Fig. 2 a) through AgiSoft PhotoScan Professional (v. 1.3.4). Structures and stratigraphic boundaries were then digitized/interpreted on the 3D photogrammetric models with help from the data collected in the field using the software LIME (Buckley et al., 2019). The 3D interpretations were then projected onto a vertical 2D panel (a 2D surface), that formed the basis for our 2D geological models (Fig. 2 b). In areas where erosion and vegetation obscure continuous exposure, faults and stratigraphic boundaries were extrapolated from exposed areas. The 2D geological models were then converted to grayscale and populated with elastic properties using a Matlab script. The script generates the input files containing the elastic properties needed for the seismic modelling described below.

### 3.2. Seismic modelling methodology

Seismic modelling can be a cost-efficient and effective way of improving interpretation of seismic data while helping better understanding the seismic response of the subsurface (e.g. Botter et al., 2016; Eide et al., 2017; Grippa et al., 2019; Faleide et al., 2021). The methodology used in this paper will be briefly described here; for a more detailed account of the method and workflow, see Lecomte (2008) and Lecomte et al. (2015).

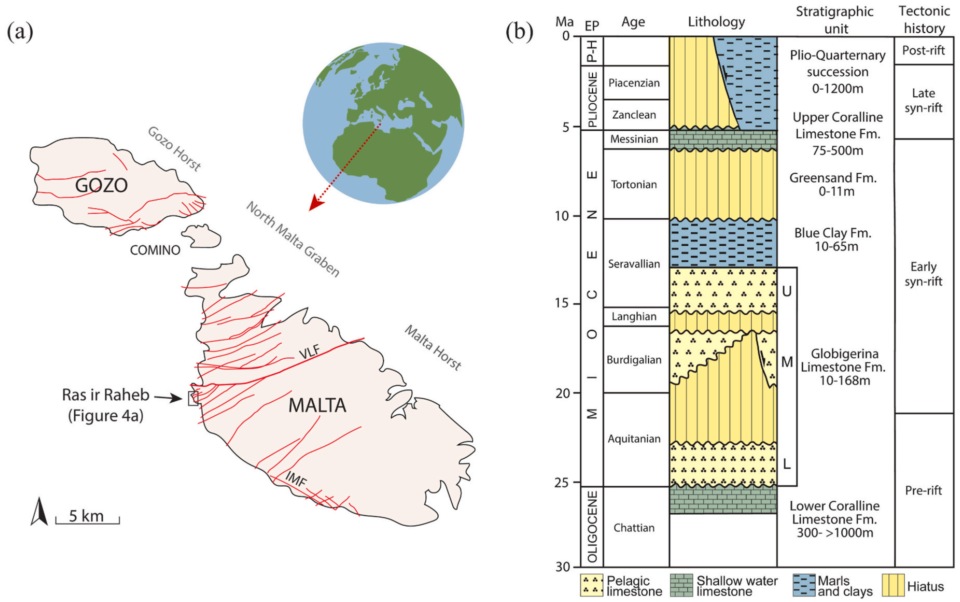

**Fig. 1.** a) The Maltese Islands in the Mediterranean Sea, showing the study area of Ras-Ir-Raheb on the west coast of Malta, just south of the Victoria Lines Fault (VLF). (After Pedley et al., 1976; Michie et al., 2014; Dimmen et al., 2017). b) General stratigraphy of the Maltese Islands (From Dart et al. (1993) and Bonson et al. (2007)).

We use a 2D convolution approach because the standard and most-applied 1D convolution method (either implemented as purely 1D for simulating well ties, or 'pseudo-2D' using serial-1D convolution when modelling seismic sections) does not properly account for laterally varying structures, limited illumination and lateral resolution (Lecomte et al., 2016; Jafarian et al., 2018; Lubrano-Lavadera et al., 2018). The convolution method used here is also available in 3D; however, the 2D version is preferred since it is ideal for representing the cliff sections studied herein, and since 2D representation involves fewer assumptions and extrapolations of fault geometries.

The 2D convolution method is originally a ray-based approach, which generate one (or several) point-spread function (PSF, see Fig. 2 c/d) as the convolution kernel which is applied to an input reflectivity model (Fig. 2 c) to create a synthetic seismic image (Fig. 2 d). Compared to the 1D convolution method, the 2D method produces a more realistic seismic image, simulating pre-stack depth-migrated (PSDM) seismic sections (Lecomte et al., 2016; Eide et al., 2017). In lack of a specific overburden model and survey geometry, especially when studying outcrops, the PSF can be simply created from a few key parameters (Lecomte et al., 2016), i.e. an angle of illumination, an incident angle, an average velocity for the targeted zone (here, the outcrop), and a wavelet (as in 1D convolution). For this study, we keep the incident angle at 0°, while the maximum illumination dip angle is set to 45°, as seismic surveys typically illuminate reflectors dipping up to 40°–50° (Eide et al., 2017; Wrona et al., 2020). Higher angle of illumination generally gives a better image, and an illumination angle of 90° would theoretically give 'perfect illumination'. We used three different wavelets, described more thoroughly in the following sub-chapter.

The models also need to be given realistic petrophysical properties; the P- and S-wave velocities ($V_p$ and $V_s$, respectively) used to populate the models are based on $V_p/V_s$ values from literature (see Table 1 and references therein) and adjusted for variation based on actual $V_p$ and $V_s$ from soft and hard carbonate rocks in the Barents Sea (J. Herredsvela, pers. comm., 2018). Petrophysical properties were added to the models using a Matlab script, and each geological formation was given a couple of values in order to create some internal variation.

We do not include an overburden model since the effect of overburden is factored into our selection of petrophysical properties that reflect a burial depth of ~2 km. Densities were calculated using the original Gardner relation which describes the relationship between density and $V_p$ (Gardner et al., 1974).

$$\rho = aVp^{1/4} \tag{1}$$

where ρ is the density (g/cm$^3$), a = 0.31 and Vp is in km/s (Gardner et al., 1974; Dey and Stewart, 1997).

### 3.3. Varying signal properties and noise

#### 3.3.1. Wavelet types

We ran each model with two different wavelet types: the Ricker and Ormsby wavelet (Ryan, 1994). The Ricker wavelet was chosen because it is frequently used in seismic modelling (e.g. Botter et al., 2016; Eide et al., 2017; Lubrano-Lavadera et al., 2018; Wrona et al., 2020) due to its simple relation between peak frequency and wavelet breadth, while the Ormsby wavelet is made to mimic a more realistic wavelet as extracted from the real seismic data we will use to compare our results with. The Ricker wavelet was run using two different peak frequencies: a 30 Hz peak was chosen to emulate relatively low-resolution seismic data, while a 60 Hz peak was used to emulate high-resolution seismic data. The synthetic Ormsby wavelet was created in Petrel using the low-cut, low-pass, high-pass and high-cut frequencies of 1-3-15-110 Hz, respectively.

Fig. 3 shows the three wavelets (a) and their frequency range (b). The Ormsby wavelet has much smaller side lobes compared to both the 30- and 60 Hz Ricker wavelets, while having a main-peak width (here defined between the first zero crossings) closer to the one of the 30 Hz Ricker rather than that of the 60 Hz Ricker (Fig. 3 a). Looking at the frequency contents (Fig. 3 b), the dominant frequency of the 30 Hz

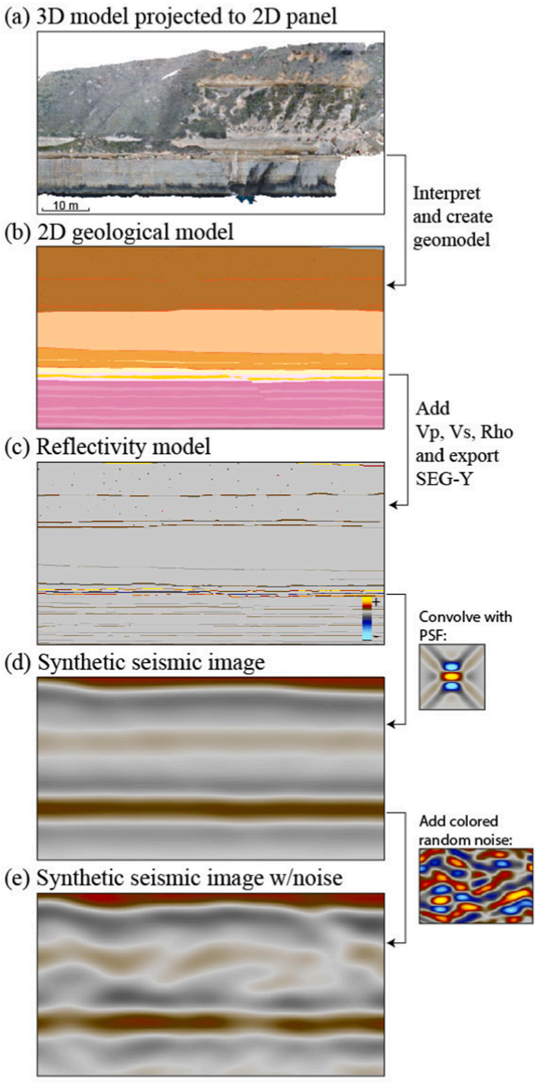

**Fig. 2.** a) A 3D outcrop model as portrayed in AgiSoft PhotoScan Professional. The model is interpreted and extrapolated to create the 2D geological model in (b). The Geological model is exported in gray scale and populated with elastic properties using a matlab-script that provides SEG-Y files for input to SeisRoX. c) A reflectivity model is created in SeisRoX and convolved with a point spread function (PSF) to create the synthetic seismic image as seen in d). e) For more realism, the seismic is combined with random noise.

Ricker (i.e., 30 Hz per definition in such idealized Ricker wavelet) is actually higher than the one of the Ormsby (15 Hz), but its bandwidth is considerably smaller than those of the two other wavelets. Shallow targets generally have higher bandwidth than deeper targets, and higher bandwidth essentially means greater power of resolution (Simm and Bacon, 2014). The peak frequency of the Ormsby wavelet is closer to the 30 Hz Ricker than the 60 Hz one, though its lack of significant side lobes – due to the progressive dimming of the high frequencies - makes it a better wavelet in terms of resolution.

**Table 1**
Petrophysical properties given to geological 2D models through a MATLAB-script creating SEG-Y files.

| Formation | $V_p$ (km/s) | $V_s$ (km/s) | Density (kg/m$^3$) | Reference |
|---|---|---|---|---|
| Upper Coralline Limestone Fm. | 4.80–5.90 | 2.53–3.12 | 2.58–2.72 | Pickett, 1963; Anselmetti and Eberli, 1993 |
| Blue Clay Fm. | 1.90–2.50 | 1.00–1.32 | 2.05–2.19 | Pickett, 1963; Castagna et al., 1993Castagna et al., 1993 |
| Upper Globigerina Limestone Mbr. | 4.00–4.50 | 2.11–2.37 | 2.47 | Pickett, 1963 |
| Middle Globigerina Limestone Mbr. | 4.20–4.35 | 2.21–2.29 | 2.52 | Pickett, 1963; Healy et al., 2015 |
| Lower Globigerina Limestone Mbr. | 3.80–4.50 | 2.00–2.37 | 2.43 | Pickett, 1963,; Healy et al., 2015 |
| Lower Coralline Limestone Fm. | 5.50–5.80 | 2.89–3.05 | 2.67–2.71 | Pickett, 1963; Healy et al., 2015 |

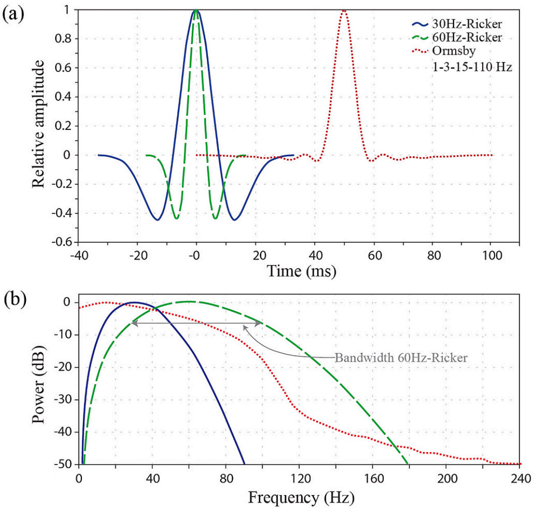

**Fig. 3.** a) Shape of the three wavelets used for this study. The Ormsby wavelet clearly has much smaller side lobes than the Ricker wavelets. b) corresponding frequency spectrum for the three wavelets. The 30 Hz-Ricker wavelet has a bandwidth of ~15–50 Hz, the 60 Hz-Ricker wavelet ~30–100 Hz, while the Ormsby wavelet spans ~0–70 Hz.

### *3.3.2. Adding random noise*

The 2D PSF-based convolution method used to create the seismic does not add any noise except for the imaging noise from side lobes of the PSF. In the case of a known overburden, the PSF could have been efficiently estimated by ray-based approaches to further constrain a more realistic illumination pattern, this PSF thus possibly showing other sources of imaging noise due to, e.g., too coarse sampling of the survey or irregular illumination due to the wave propagation through the overburden. However, we restrained the study to a more “ideal” case, with a PSF simply constrained by a few key parameters as described above. The synthetic seismic images that are produced are therefore very ‘clean’, yet reproducing a complete resolution pattern, both vertically and laterally, and with the (realistic) lack of imaging of steep dips. Nevertheless, in real seismic data, the signal-to-noise ratio is one of the parameters affecting the detectability of structures (Simm and Bacon, 2014; Lubrano-Lavadera et al., 2018) and in order to detect reflections from geological structures in the seismic, the amplitude needs to be significantly higher than that of the seismic noise (Eide et al., 2017).

We therefore added random noise to the modelling and considered a signal-to-noise ratio of 4 (20% noise) to emulate such detectability issues. This was chosen based on the results from Andersen (2020), who found that carbonate hosted faults may be visible in seismic with ≥25% noise, but hardly detectable when the noise is increased to 50%. The noise was created as an additional seismic image by convolving random (white) noise, given as an input reflectivity grid, with the PSF of the associated synthetic seismic, thus colouring the random noise with the same frequency and wavenumber range as the modelled seismic sections (PSDM-coloured noise). The PSF-convolved random noise was then added to the seismic images of the outcrop models as an individual step (Fig. 2 d/e). All synthetic seismic images are presented *with* and *without* noise in the results section. All seismic (and noise) was also amplitude-calibrated, so that a peak of a certain strength in reflectivity would correspond to a peak of the same strength in the seismic images. The seismic are displayed with normal polarity, whereby an increase in acoustic impedance is represented by a peak (red), and a decrease by a trough (blue).

## 4. Experimental design

The models used herein are based on two main outcrops in the study area (Fig. 4) From each of the outcrops, we created a modelling series consisting of three different geological models, giving a total of six cases, covering fault offsets from ~1 to 20 m (Fig. 5). Variation of wavelet type and frequency, and addition or absence of noise in the six models lead to a total of 36 seismic images for discussion. As previously mentioned, the results will be compared to real, high-quality seismic images (TopSeis) from a carbonate-dominated succession in the SW Barents Sea, offshore Norway, of Carboniferous to Triassic age. The area we will be looking at lies at approximately 2000 m depth, in the proximity of a km-scale rotated fault block with several horst-and-graben forming faults in the overburden.

### 4.1. *Outcrop 1; model series 1*

The area where the first outcrop is located sits approximately 500 m into the footwall of the larger (displacement D = 90 m) Victoria Lines Fault at Ras-Ir-Raheb (Fig. 4 a). The outcrop displays several smaller faults with offsets <1 m in the fine grained, homogenous Middle and Lower Globigerina Limestone Members (Fig. 4 b). The faults cut through the boundary between the two members, which is marked by a layer of phosphoritic conglomerate. The outcrop selected for modelling from this area is a compound graben structure with a combined offset of c. 1 m, distributed across several faults. The models are extended to include significantly more of the outcrop than the compound graben itself; the models are therefore 300 m wide and 200 m tall, extending approximately 30 m into the Upper Coralline Formation at the top and the Lower Coralline Formation at the bottom (Fig. 4 c).

Three models were created based on the compound graben structure from the first outcrop (Fig. 5). First, a fault-free reference model with sub-horizontal bedding (Model 1.1) was created to serve as baseline for comparison with the faulted models. The actual fault geometries recorded at the outcrop are represented in Model 1.2, whereas in Model 1.3 the combined offsets were exaggerated to 5 m. Model 1.3 is otherwise identical to Model 1.1 and 1.2.

### 4.2. *Outcrop 2; model series 2*

The area where the second outcrop is situated sits ~700 m south of Outcrop 1 and ~1.2 km into the footwall of the Victoria Lines Fault (Fig. 4 a). The outcrop of interest features a fault with a displacement of approximately 11 m (Fig. 4 b). The fault is comprised of two strands and dissects the uppermost part of the Lower Coralline Limestone and continues down-dip below sea level. Up-dip, it extends through the Lower-, Middle- and Upper Globigerina Limestone members, and into the Blue Clay Formation. The fault does not extend further up-dip into the Upper Coralline Formation and, although the tip itself is not exposed, we infer that the fault tips out below the base of this formation. The two fault strands bound a lens-shaped geometry, where the total throw of the fault is shared between the two strands (Haines et al., 2016).

Three different models were created with the aim of investigating the effects of the fault itself and the lens-shaped geometry on seismic images (Fig. 5). To do this, we created a reference model where the fault

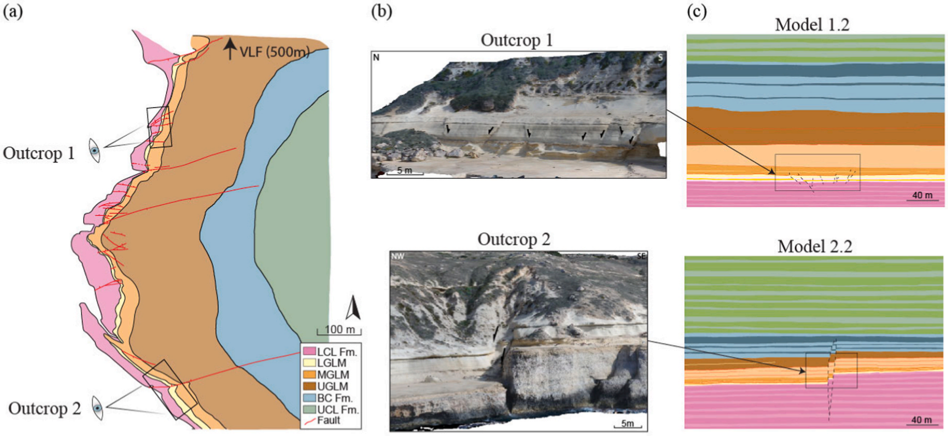

**Fig. 4.** a) Overview of Ras-Ir-Raheb and the location of the two outcrops, outcrop 1 in the northern part and outcrop 2 in the southern part of the map. LCL = Lower Coralline Limestone, LGLM = Lower Globigerina Limestone Member, MGLM = Middle Globigerina Limestone Member, UGLM= Upper Globigerina Limestone Member, BC = Blue Clay, UCL= Upper Coralline Limestone b) 3D models of the selected outcrops and their position in the finished geological models in c). (For interpretation of the references to colour in this figure legend, the reader is referred to the Web version of this article.)

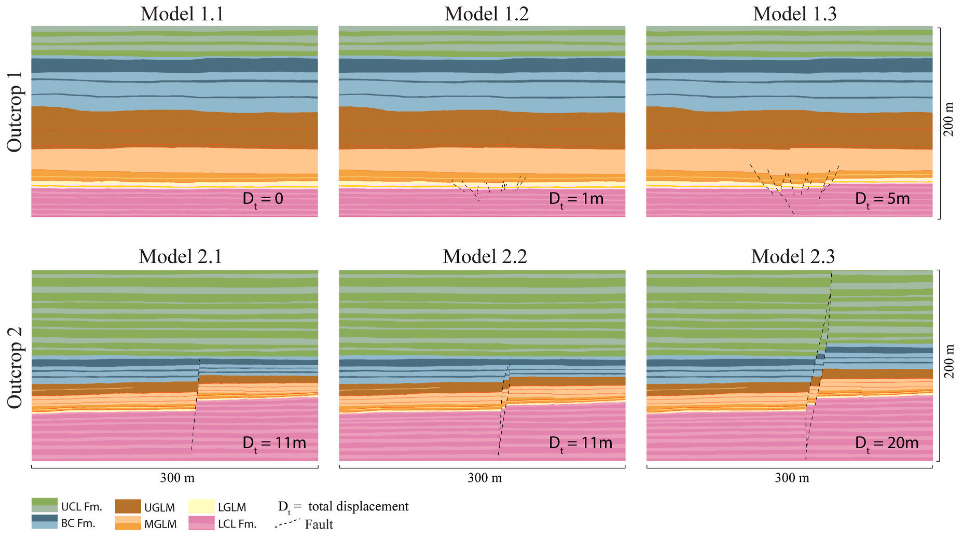

**Fig. 5.** Overview of the six geological 2D models created from the two outcrops at Ras-Ir-Raheb. Model 1.2 and 2.2 gives the most precise portrayal of the actual outcrop 1 and 2, respectfully. All models are 200 × 300 m and scaled 1:1.

geometry was simplified to consist of a single planar fault strand of 11 m offset (Model 2.1), for comparison with a model of the true geometry where the two-strand lens geometry was included (Model 2.2). In Model 2.2, the throw is split between the two fault strands, with a combined displacement of 11 m, i.e., equal to that of the single fault in Model 1.1. The third model (Model 2.3) was created with a total combined displacement across the two-strand fault zone exaggerated to 20 m, where the up-dip (and partly down-dip) extent of the fault was increased.

## 5. Results

We here present the results, starting with the effect the wavelet shape and frequency have on the seismic (Fig. 6), before moving on to the resulting synthetic seismic. With the variables presented in section 4, our models result in 36 different seismic images (Figs. 7 and 8). The results from the two model-series are presented in the following subsections. Model Series 1 are based on Outcrop 1, whereas Model Series 2 are based on Outcrop 2.

### 5.1. *Effect of the different seismic wavelet types*

The effect of the different wavelet shapes and frequencies can be seen in Fig. 6, where an example of synthetic seismic created with the 30 Hz Ricker (Fig. 6 a) and the Ormsby wavelets (Fig. 6 b) are presented with wiggle trace of both the wavelet and the reflectivity of a chosen line. The wiggle trace clearly shows how the two wavelets affect the seismic images. The wiggle trace for the 30 Hz Ricker wavelet shows little variation in amplitude with few, high-amplitude peaks and troughs (Fig. 6 a), leading to the few and thick reflections we see in the seismic image. The wiggle trace from the Ormsby wavelet is very different, showing several narrower peaks and troughs in the upper half of the wiggle trace before one higher amplitude trough followed by a double peak (Fig. 6 b). The shape of the 30 Hz Ricker wavelet with the negative side lobes leads to a seismic image where only the strongest reflectors show as thick reflections, and anything located too close to these disappear within the side lobes. The negative side lobes contribute to the strong negative reflection we observe in the centre of the image and enhance the adjoining positive reflections. In the seismic image using the Ormsby wavelet (Fig. 6 b), we can see that the negative reflection is weaker than

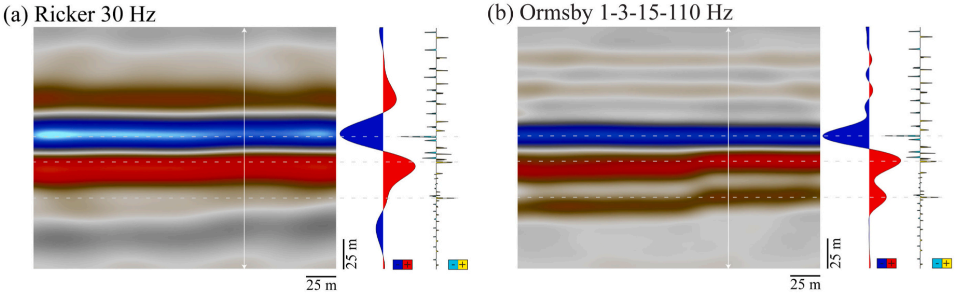

**Fig. 6.** a) Seismic image produced using the 30 Hz Ricker wavelet, with wiggle trace and reflectivity trace on the right – extracted from the placement of the white vertical line in the seismic image. b) Seismic image produced using the Ormsby 1-3-15-110 Hz wavelet, with wiggle trace and reflectivity trace on the right – extracted from the placement of the white vertical line in the seismic image.

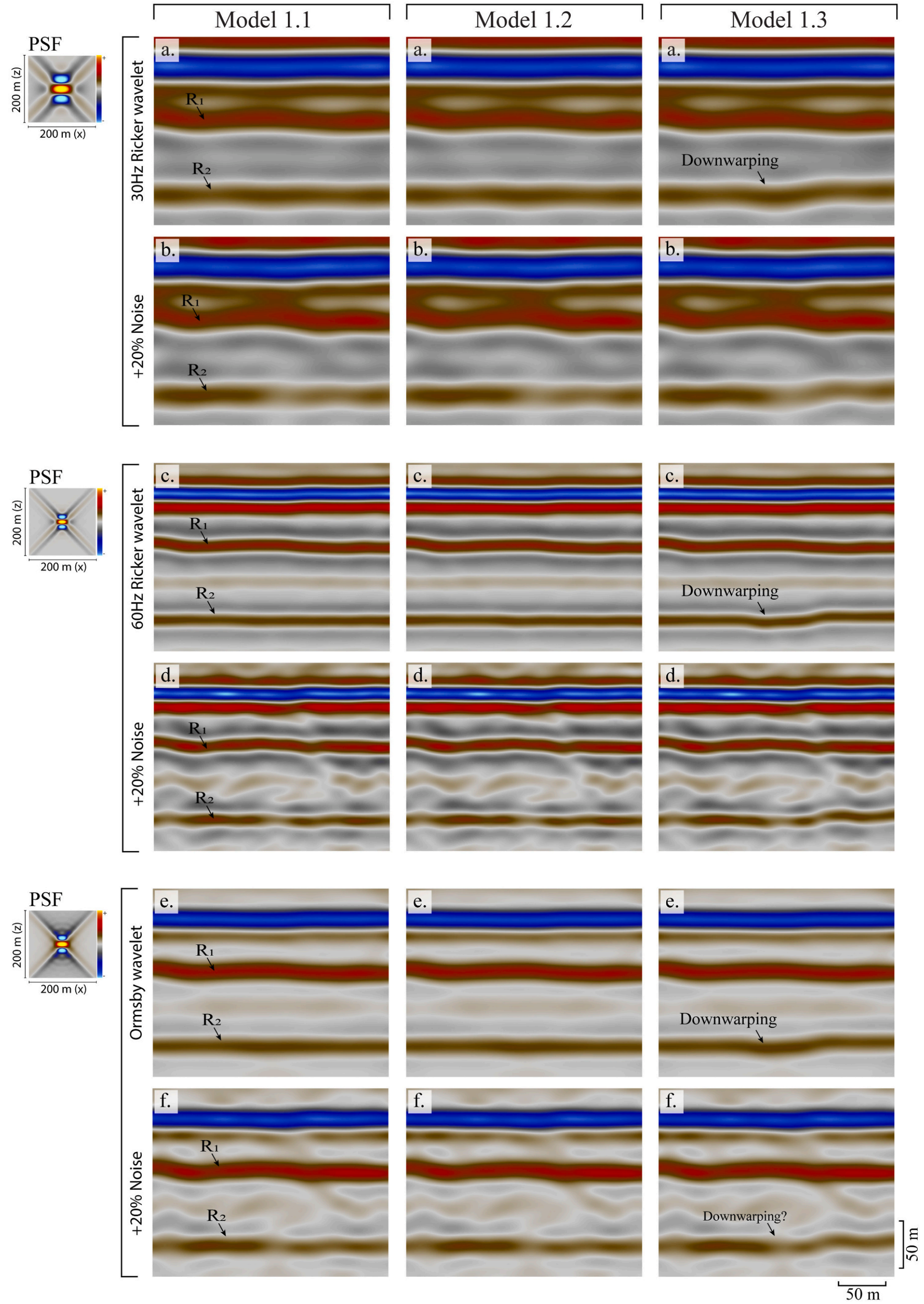

**Fig. 7.** All seismic images within model series 1. Showing the seismic images of Model 1.1 (a–f) vertically on the left, all seismic images of Model 1.2 (a–f) vertically in the middle, and all seismic images of Model 1.3 (a–f) vertically to the right.

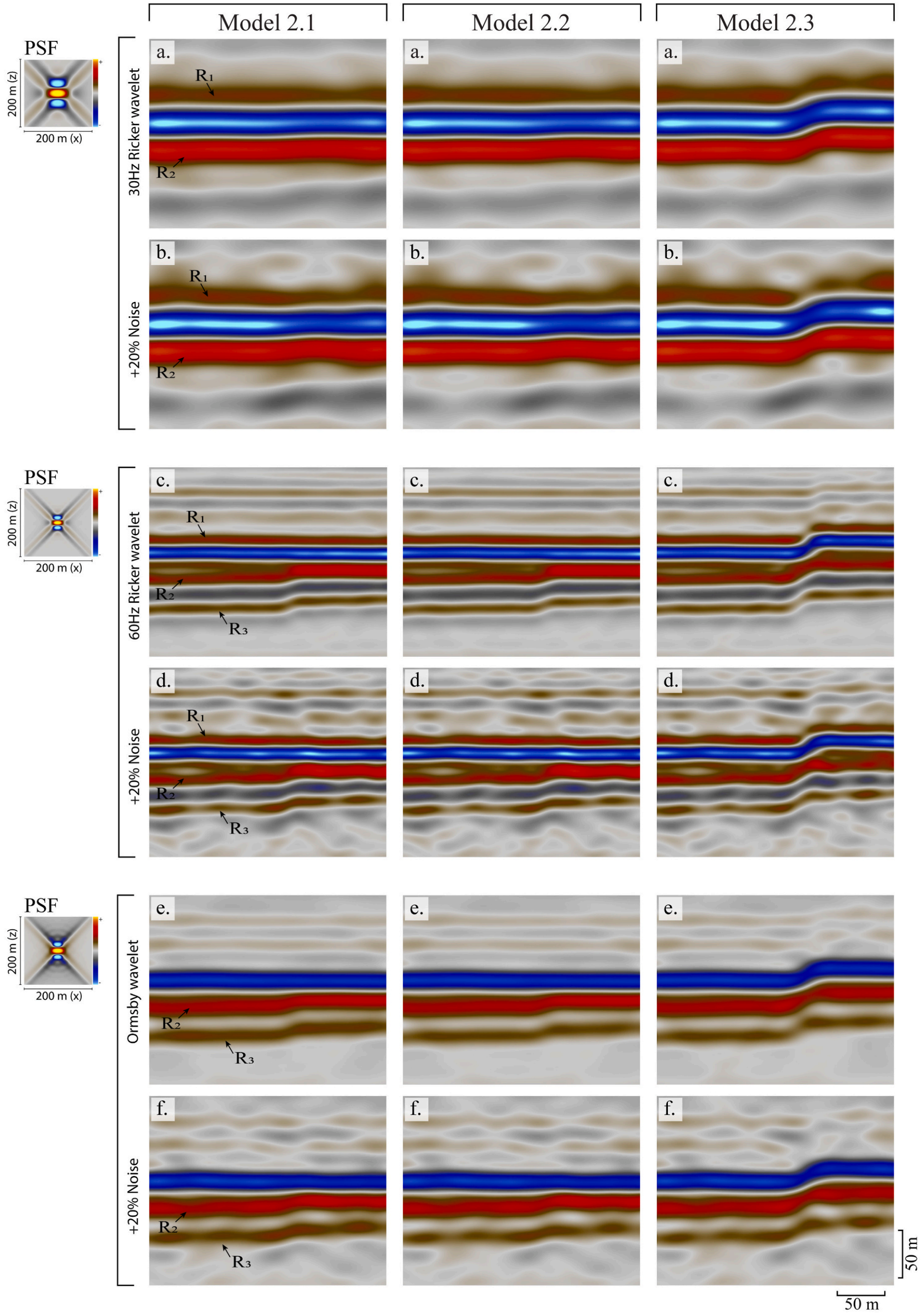

**Fig. 8.** All seismic images within model series 2. Showing the seismic images of Model 2.1 (a–f) vertically on the left, all seismic images of Model 2.2 (a–f) vertically in the middle, and all seismic images of Model 2.3 (a–f) vertically to the right.

in the 30 Hz Ricker image, and the amplitude trough of the wavelet to the right is less wide. Instead of one continuous amplitude peak below the trough of the wavelet we here see two peaks following each other. In the seismic image this is seen as two distinguishable positive reflections. This matches up well with the reflectivity trace on the far right in the figure where we can see corresponding peaks.

### *5.2. Model series 1 (compound graben; 0–5 m displacement)*

Common for all the seismic images from Model Series 1 is the strong negative amplitude reflection (blue) seen near the top of all the images, representing the stratigraphic boundary between the Upper Coralline Limestone Fm. and the Blue Clay Fm. (Fig. 7). Additionally, there are two strong positive-amplitude reflections (red) visible throughout all images, called $R_1$ and $R_2$ (marked with arrows in Fig. 7). $R_1$ is the reflection from the boundary between the Upper Coralline Limestone Fm. and the Upper Globigerina Limestone Fm., while $R_2$ is the reflection from the boundary between the Lower Coralline Limestone Fm. and the Lower Globigerina Limestone Fm. The character of these two reflections varies in the different seismic images, due to the changing survey parameters and input geology. The variations of the fault-affected reflection $R_2$ is key to the detailed seismic image descriptions below.

#### *5.2.1. Model series 1 results using the 30 Hz ricker wavelet*

The fault-free reference model (Model 1.1, Fig. 7 a), without any structures, produces a very simple seismic image, with Reflection $R_2$ being continuous. The seismic image created with the 30 Hz Ricker wavelet shows strong, sub-horizontal reflections with no reflectivity between $R_1$ and $R_2$. The seismic images of Model 1.2 (Fig. 7 1.2 a) are practically identical to the images of the reference model (Fig. 7 1.1 a), and the small faults have no notable effect on the seismic image. In Model 1.3, the seismic image produced using the 30 Hz Ricker wavelet shows a slight downwarping of reflection $R_2$, in the area of the compound graben with the combined displacement of 5 m (Fig. 7 1.3 a). Adding noise to the seismic images has a limited effect on the images in the 30 Hz Ricker wavelet scenarios (Fig. 7 b).

#### *5.2.2. Model series 1 results using the 60 Hz ricker wavelet*

The seismic images based on the 60 Hz Ricker wavelet resolves more reflections, since the vertical seismic resolution is improved relative to the 30 Hz images (Fig. 7 c), and the reflections are narrower and more well-defined. A strong positive reflection (red) can now be observed immediately below the strong negative reflection (blue) that was also seen in the 30 Hz Ricker images, and a lower-amplitude positive reflection can be seen between $R_1$ and $R_2$. Model 1.1 (Fig. 7 1.1 c) and Model 1.2 (Fig. 7 1.2 c) are practically identical, whereas in Model 1.3 (Fig. 7 1.3 c) reflection $R_2$ is downwarped at the location of the compound graben. Compared to the 30 Hz image of Model 1.3, the downwarped part of reflection $R_2$ is slightly more rugose and defined, reflecting more of the detailed structure of the compound graben. Adding noise again distorts the images and results in poorer reflectivity between $R_1$ and $R_2$, and slightly blurs the downwarping of R2 at the location of the compound graben in the seismic image of Model 1.3.

#### *5.2.3. Model series 1 results using the ormsby wavelet*

The Ormsby-type wavelet produces seismic images of similar quality to those produced using the 30 Hz Ricker wavelet, but with a ‘cleaner’ appearance. The reference Model 1.1 (Fig. 7 1.1 e) clearly shows the negative reflection (blue) near the top of the model, as well as the strong, positive reflections $R_1$ and $R_2$. Model 1.2 (Fig. 7 1.2 e) is again identical to the reference model, whereas in Model 1.3 (Fig. 7 1.3 e) we can observe a slight downwarping of reflection $R_1$ as also seen in the images using the Ricker wavelets. The addition of noise to the Ormsby wavelet images still leaves the reflections interpretable, but noise distorts reflectivity between reflections $R_1$ and $R_2$.

### *5.3. Model series 2 (11–20 m displacement)*

The negative amplitude marking the stratigraphic boundary between the Upper Coralline Limestone Fm. and the Blue Clay Fm., seen as a strong negative amplitude reflection (blue) in the seismic, is present in all the seismic images produced in the Model 2 series (Fig. 8). Otherwise, the different geological models in combination with the various petrophysical properties created variations within the seismic images that will be described in the following.

#### *5.3.1. Model series 2 results using the 30 Hz ricker wavelet*

The single-strand reference Model 2.1 (D = 11 m) shows one negative and two positive strong reflections in the (vertically) central part of the seismic image (Fig. 8 2.1 a). The two positive reflections are marked as $R_1$ and $R_2$. A very weak, positive reflection is shown just below $R_2$, slightly tapering towards the right. The seismic image derived from the double-strand Model 2.2 (combined D = 11 m, Fig. 8 2.2 a) is overall similar to the image of Model 2.1, however, a slight difference can be noticed in the weak reflector below $R_2$, which is here a bit cloudier than in Model 2.1. Importantly, fault offsets are not resolved in neither of the Models 2.1 or 2.2. A more obvious change is seen from the latter two models when looking at Model 2.3 (Fig. 8 2.3 a). The location of the fault is clearly detectable in this seismic image where the fault displacement is exaggerated to 20 m and offsets the boundary between the Upper Globigerina Limestone Member and the Blue Clay Formation (Fig. 8 2.3 a). Although there are no discrete reflection offsets, the offset is imaged as a monoclinal shape of the strong reflections in the vertically middle part of the seismic image. When noise is added to the 30 Hz seismic images (Fig. 8 b), the two strong reflections are still clear but the weak reflection just below $R_2$ are blurrier and partly split. Notably, even when adding noise, the imaging of the fault offsets as a monoclinal geometry remains clear in Model 2.3, whereas in Models 1.1 and 1.2 the reflections remain horizontal.

#### *5.3.2. Model series 2 results using the 60 Hz ricker wavelet*

In general, the seismic images produced with the 60 Hz Ricker wavelet exhibit narrower and more well-defined reflectors than the 30 Hz Ricker images (Fig. 8 c and d). In the upper half of the seismic image of the single strand fault model, Model 2.1 (D = 11 m, Fig. 8 2.1 c), we can observe several weaker, horizontal and continuous reflections above $R_1$. $R_1$ is shown as a clear reflection immediately above a strong negative reflection and can be followed continuously from left to right in the image. Reflection $R_2$ can again be found just underneath the negative reflection but appears to be horizontally split in two towards the left side of the image, while stepping up on the right-hand side in a monoclinal shape where it is expressed as one, thicker reflection. Below $R_2$ there is another positive reflection, $R_3$, whit slightly lower amplitude and following the monoclinal shape of $R_2$. The seismic image of the double strand fault model, Model 2.2 (combined D = 11 m, Fig. 8 2.2 c), is almost identical to that of Model 2.1 except for some very slight amplitude strength variations in the stepping part of the monoclinal. More variation is seen when looking at the seismic image of Model 2.3 where the faults displacement is exaggerated to 20 m and breaches all the way through the Upper Coralline Limestone (Fig. 8 2.3 c). Here, all reflections show a monoclinal shape, and Reflection $R_1$ is discretely offset. Reflectivity in the upper and lower part of the model is distorted when noise is added, whereas all reflections in the high-reflective central part of the images are still well-resolved (Fig. 8 d).

#### *5.3.3. Model series 2 results using the ormsby wavelet*

The resultant images using the Ormsby wavelet (Fig. 8 e and f) are of a quality and resolution that lies between that of the 30 Hz and the 60 Hz Ricker wavelet images. Considering Model 2.1 (D = 11 m, Fig. 8 2.1 e), the image is dominated by the strong negative reflection (blue) as well as positive reflections $R_2$ and $R_3$. Reflection $R_1$ seen in previous models is no longer observable. Reflections $R_2$ and $R_3$ show a slight monoclinal shape. The seismic image of Model 2.2 (combined $D = 11$ m, Fig. 8 2.2 e) is practically identical to that of Model 2.1. The reflectivity pattern of Model 2.3 (combined $D = 20$ m, Fig. 8 2.3 e) is similar, although in this model all the reflections have a monoclinal shape. Adding noise distorts reflectivity in the upper and lower part of the images and make the uppermost reflections cloudy (Fig. 8 f). The strong negative reflection and $R_2$ appear relatively undisturbed by the noise, while $R_3$ is slightly more rugose (Fig. 8 2.3 f).

## 6. Summary and discussion

Here we summarize and discuss our observations and findings from the seismic, draw comparisons to real seismic data, and comment on the wider implications/applications of our results.

### 6.1. Summary of results

For seismic models without noise, we summarize that:

- compound grabens with cumulative $D = 1$ m were not visible in the seismic images.
- compound grabens with cumulative $D = 5$ m were visible in seismic images as a subtle downwarping of reflections.
- single-strand normal faults with $D = 11$ m were visible as monoclinal distortions of reflections when the quality of the seismic is adequate (60 Hz Ricker wavelet and Ormsby wavelet).
- double strand faults with cumulative $D = 20$ m were visible in seismic images as discrete reflection offset or as monoclinal reflection geometries.

For seismic models with a seismic-to-noise ratio of 4:1, we summarize that:

- compound grabens with cumulative $D < 5$ m are reflected only as extremely subtle reflection distortion in the seismic images with noise, and are therefore practically undetectable.
- single-strand normal faults with $D = 11$ m were visible in the seismic images when the quality of the seismic is adequate (60 Hz Ricker wavelet and Ormsby wavelet).
- double-strand normal faults with cumulative $D = 11$ m were visible in the seismic images when the quality of the seismic is adequate (60 Hz Ricker wavelet and Ormsby wavelet).
- double-strand normal faults with cumulative $D = 20$ m were visible as a subtle monoclinal shape of the seismic reflections.

### 6.2. Detectability and effect of small-scale ($D = 1$–$20$ m) faults in seismic

Our results indicate that, at signal peak frequencies of 30 Hz (Ricker wavelet) and higher, and *without introducing random noise*, faults down to ~5 m of throw affect the seismic image by slight downwarping of reflections, whereas faults down to ~11 m throw show detectable offsets of reflections in form of a down-stepping monoclinal geometry at signal peak frequencies of 60 Hz (Ricker wavelet). Real seismic will, however, never be noise free even though methods for seismic acquisition and processing have come a long way the last few decades (e.g. Schneider, 1971; Rost and Thomas, 2009; Zhong et al., 2015; Schmelzbach et al., 2016; Li et al., 2018). In our data, the same structures can be identified when noise is included (20% random noise), although the reflections are more irregular and harder to detect. This suggests that under relatively noise-free conditions in high-quality reflection seismic datasets, lower-throw faults (as low as 5 m in this study) that do not induce discrete reflection offsets in seismic images may still produce reflection distortions. As widely documented and discussed in literature (Faulkner et al., 2010), sub-seismic structures such as faults have a large impact on the permeability and fluid flow in the subsurface (e.g. Shipton et al., 2002), and these results are examples that may help seismic interpreters infer what observed distortions in real seismic data may reflect geologically, and highlights how seismic modelling adds further value and insight to the use of outcrop analogues to understand subsurface geology as imaged by seismic.

### 6.3. Wavelet and resolution effects

#### 6.3.1. Seismic wavelets and their effect on the seismic image

The shape of the wavelet is a fundamental aspect of seismic interpretation (Simm and Bacon, 2014), and is also crucial for the results herein. The Ricker wavelet is commonly used in seismic modelling (Eide et al., 2017; Rabbel et al., 2018; Wrona et al., 2020) due to its simple structure, while studies using the more realistic Ormsby wavelet in seismic modelling is until now lacking. We will therefore discuss the differences of the two wavelet types here.

Generally, the 60 Hz Ricker wavelet has a narrower peak in time, due to a wider frequency bandwidth, compared to the Ormsby and 30 Hz Ricker wavelets, thus giving higher-quality seismic images with a higher number of distinguishable reflections, showing more detail. The Ormsby wavelet and Ricker wavelets have very similar peaks in time but where the Ormsby wavelet have several small side lobes with almost no negative parts, the Ricker wavelets have only two, but much more pronounced negative side lobes (Fig. 3).

So, although the peaks of the 30 Hz Ricker wavelet and the Ormsby wavelet are very similar (as presented in Fig. 3), their seismic expression becomes very different due to the side lobes, as showed in Fig. 6. While the “lack” of side lobes in the Ormsby wavelet provide higher vertical resolution and produce a cleaner seismic image, the side lobes of the 30 Hz Ricker wavelet interfere with the reflectors in the model and disturb the signal. In many ways, the seismic response of the Ormsby wavelet is more like that of the 60 Hz Ricker wavelet. It is important to note that the effects from the side lobes affect the seismic in all directions; herein we look at 2D images but in 3D we would have to consider such effects in a three-dimensional manner and nearby lateral reflectivity may affect the trace. Additionally, all reflectivity might not be illuminated, depending on the dip of the underlying strata.

From our data, we can observe that the shape of the Ormsby wavelet gives a better result. The Ricker wavelet has been criticized in literature earlier, and already in 1988, Hosken (1988) published his scepticism towards the extended use of the Ricker wavelet (especially in the industry), and simply concluded that “*Ricker wavelets should never be used*”. However the simplicity of the Ricker wavelet makes it very convenient for the creation of synthetic data, and it is still commonly used (e.g. Eide et al., 2017; Wrona et al., 2020). Contrary to other wavelet types (e.g. Ormsby, Butterworth) the Ricker wavelet can be described by its peak frequency and a relatively simple mathematical equation (Ryan, 1994). “Real” seismic wavelets from surveys, however, are more complex and usually asymmetrical in respect to time, opposed to the symmetrical Ricker wavelet (Wang, 2015). Hence, our asymmetrical Ormsby wavelet, which mimics a real seismic wavelet, is a better option for creating synthetic seismic that is more like real seismic.

However, the wavelets shape and behaviour may vary, and Andersen (2020) concludes in her MSc thesis that a 40 Hz Ricker wavelet is more suitable than a 5-10-60-90 Hz Ormsby wavelet for seismic modelling. To get a better understanding of the difference between the three seismic wavelets we used herein, we have superimposed their wiggle traces altogether in Fig. 9 and placed them alongside the corresponding reflectivity trace.

Looking at the 30 Hz Ricker wavelet vs. the Ormsby wavelet we can see the effect the different wavelet shapes have on the wiggle trace and hence the seismic images; a high-amplitude trough at the top followed by a peak that for the Ormsby wavelet can be observed as two peaks, but for the 30 Hz Ricker wavelet is more continuous. Below these, at 100–150 m depth, we can see a trough of the 30 Hz Ricker wavelet with two trough-maximums at about 110 m and 140 m depth, whereas the Ormsby wavelet show no negative part here but a small peak in the

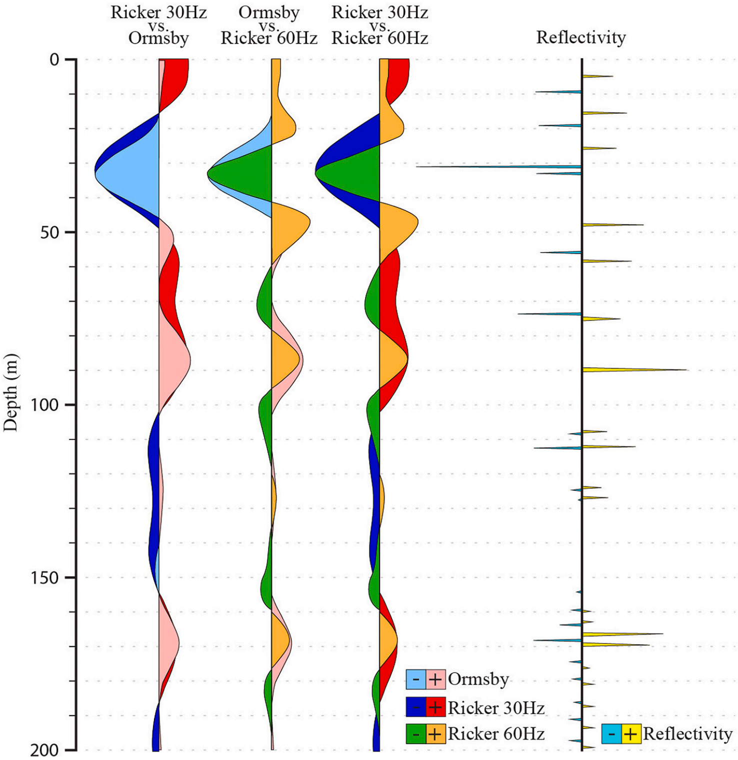

**Fig. 9.** Wiggle trace of the three wavelets used herein, superimposed to allow for comparison. The associated reflectivity trace to the right in the figure allows for comparison between reflectivity and seismic wave pattern.

middle, at about 125 m depth. Looking at the Ormsby wavelet vs. the 60 Hz Ricker wavelet, we see more similarities on the positive side of the wiggle trace where all peaks are found at the same places. On the negative side however, we can still only observe the one trough at the uppermost part of the wiggle trace for the Ormsby wavelet, while the 60 Hz Ricker wiggle trace show several troughs throughout, alternating with the peaks. The two Ricker wavelets are similar in the way that they both have alternating peaks and troughs along the wiggle trace. However, due to the narrower amplitude spectra and wider bandwidth of the 60 Hz Ricker wavelet, the 60 Hz Ricker wiggle trace better distinguish and show the various events (peaks and troughs). When comparing the wiggle traces to the reflectivity trace, it is evident that (especially from 170 m and below) the closely spaced events with opposite polarity eradicate each other and hence do not show in any of the wiggle traces.

### *6.3.2. Resolution effects*

Related to the wavelet shapes and their corresponding frequency bandwidth is the vertical and horizontal seismic resolution. The seismic resolution controls the ability of seismic reflection data to image geological features, including faults and fault zones (e.g. Osagiede et al., 2014; Alaei and Torabi, 2017). We often tend to focus on the vertical resolution, i.e., the minimum vertical distance between two features (reflectors) that are possible to define separately rather than as one (e.g. Chopra et al., 2006; Osagiede et al., 2014), but as we will discuss here, the horizontal resolution is equally important (cf. Faleide et al., 2021). To elucidate this, we will consider the seismic image of Model 2.3 with the 60 Hz Ricker wavelet as an example (Fig. 10). Here, the positive reflection $R_1$ shows a discrete offset in the area where the fault is cutting through. Further down in the seismic image, reflection $R_3$ shows a monoclinal shape and is stepping up where the fault cuts through. This is similar to what we can often see with e.g. sill intrusions and related bridges in sedimentary basins; the bridges are often resolved only as kinks on the sill reflections rather than as discrete reflection discontinuities, and knowledge of sill geometries from nature is necessary for a sound geological interpretation (see e.g. Magee et al., 2015; Eide et al., 2017).

In the geological model and hence also the reflectivity model (Fig. 10 a), the total displacement of the reflector for reflection $R_3$ is slightly larger than that of the reflector for reflection $R_1$. Therefore, one would perhaps initially assume that in a seismic image, the offset would be more easily detected in reflection $R_3$ than in $R_{1,}$ if we consider vertical resolution only. However, the fault lens is also slightly wider at the point where it cuts through $R_3$, and hence the horizontal distance between the two faults bounding the lens is slightly wider for $R_3$ than for $R_1$. As a consequence, despite the reflector for $R_3$ having a larger total offset, reflection $R_3$ shows as a monoclinal shape rather than being resolved as discrete reflection offsets in the seismic image due to a combination of two resolution effects: firstly, the offsets of the two faults are resolved individually, as they are sufficiently far apart to be seen as separate features (the fault distance being greater than *horizontal* seismic resolution); secondly, however, with total fault offset effectively being split across two faults when the two are resolved individually rather than as one, each individual fault offset then falls below the *vertical* seismic resolution. The reflectivity model (Fig. 10 a) has been superimposed with the synthetic seismic (Fig. 10 b) in Fig. 10 c to illustrate this resolution effect. Similar effects may be seen e.g., with narrow and closely

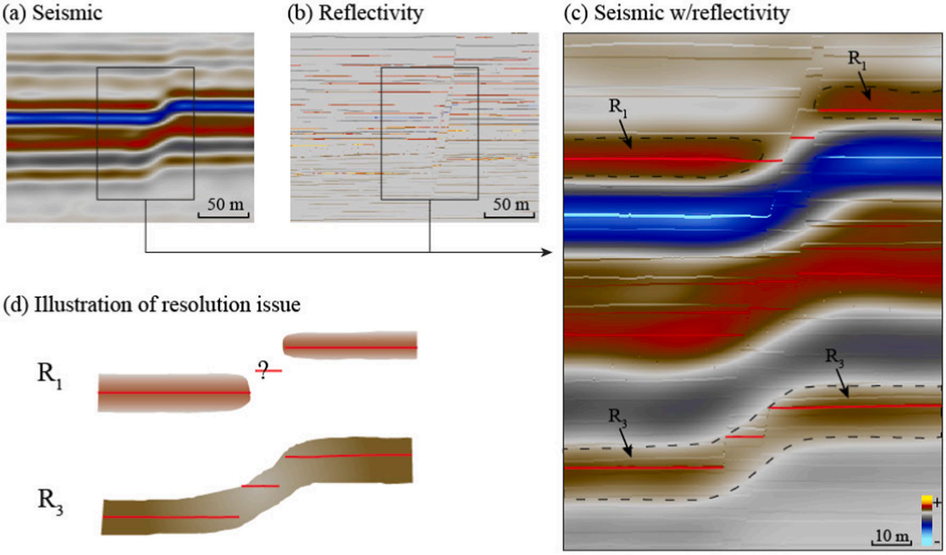

**Fig. 10.** a) seismic image of Model 2.3 using the Ricker 60 Hz wavelet are superimposed with the reflectivity model. The reflectors of $R_1$ and $R_3$ are highlighted by bright red color for easier identification across the image. b) Illustration of the difference of the imaging of reflector $R_1$ and $R_3$. (For interpretation of the references to colour in this figure legend, the reader is referred to the Web version of this article.)

spaced fluvial channels or channel belts in seismic images, that are difficult to separate as individual depositional objects (e.g. Al-Masgari et al., 2021). The fault offsets are therefore resolved as a monoclinal geometry rather than as discrete reflection offsets for reflection $R_3$. For reflection $R_1$ on the other hand, the (shorter) distance between the two faults bounding the fault lens falls below *horizontal* seismic resolution. This has the effect that the two faults cannot be resolved individually and are 'seen' as one fault, and with the throws of the two faults combined, the total offset is greater than the *vertical* seismic resolution, and the fault offset of Reflection $R_1$ is therefore resolved discretely (Fig. 10 d).

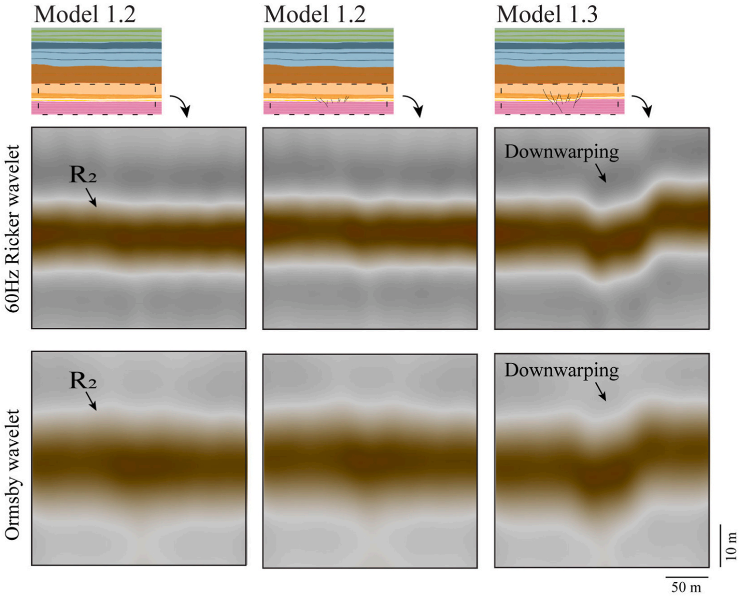

**Fig. 11.** Areas of interest in the seismic images of Model series 1, with a vertical exaggeration with the factor of five. Noise is not included.

### 6.4. Relevance to practical seismic interpretation and comparisons with real seismic data

#### 6.4.1. Vertical exaggeration in seismic interpretation

When interpreting seismic data, interpreters often use vertical exaggeration to better visualize and interpret the imaged geologic features in the vertical dimension, such as faults, dykes, stratigraphic boundaries, unconformities etc. (Stewart, 2011; Alcalde et al., 2019). To make our results more applicable, we will therefore look at some of the more interesting areas of our synthetic seismic where the Y-axis (depth) is exaggerated by a factor of 5 (Figs. 11 and 12). Noise was not included in these images as our previous results showed that the main features were still visible with a seismic-to-noise ratio of 4:1, and we want instead to check if any distortion caused by the smaller faults (with $D \leq 1$ m) would be easier to pick up with vertical exaggeration. Exaggerating the vertical scale of the seismic images of model series 1 (Fig. 11) does not bring any change to our initial summary of observations. We here present the results using the 60 Hz Ricker and the Ormsby wavelets; no observable change can be seen in the seismic images of Model 1.1 vs. 1.2, hence we can conclude faults with displacement $\leq 1$ m are not detectable in seismic, even with vertical exaggeration. The downwarp of R$_2$ in the seismic images of Model 1.3 is still visible but may actually be harder to observe in the seismic images with the Ormsby wavelet as vertically exaggerated reflection irregularities obtuse the feature. With the 60 Hz Ricker wavelet, however, the downwarp of the reflection becomes more prominent in the seismic image and hence makes the graben easier to detect.

When studying the seismic images of the Model 2 series in Fig. 7, no visible difference between the seismic images of the single strand fault (Model 2.1) and the double strand fault (Model 2.2) were observed. To see if any changes could be detected, the seismic images with the highest seismic resolution (60 Hz Ricker wavelet) were vertically exaggerated by a factor of 5 (Fig. 12). Considering Fig. 12, only a very slight increase in amplitude can be seen just at the bend of the monocline in the vertically exaggerated seismic image of Model 2.1 (marked by a red arrow in Fig. 12) compared to the seismic image of Model 2.2. When applying vertical exaggeration to the seismic image of Model 2.3 (Fig. 12) the offset of reflection R$_1$ and the monoclinal shape of reflections R$_2$ and R$_3$ are easier to observe.

In summary, increased vertical exaggeration may help the identification of subtle reflection distortions or offsets (Stewart, 2011, 2012); however, their geological interpretation will be uncertain and may rely more on the interpreter's conceptual understanding of subseismic faulting as well as of local geology. This may involve a more conceptual approach to seismic interpretation, which is associated with certain pitfalls. For example, the study by Alcalde et al. (2019) show that early anchoring into specific conceptual models may introduce bias to the interpretation of faults from seismic reflection data. However, the same study showed that increasing vertical exaggeration had limited effects of introducing bias in fault interpretations. Such a conceptual bias may not be negative but may actually be a desired conceptual bias that for example favours the interpretation of faults in an area where faults are to be expected. As such, provided that such conceptual bias is used purposely, we suggest it may help achieve a geologically overall sounder interpretation.

#### 6.4.2. Comparison with real seismic data

We here compare our results with an image from a high-quality, high-resolution 3D reflection seismic dataset from the SW Barents Sea, as previously mentioned. Comparing our results with real seismic data provides an opportunity to put our synthetic seismic in context of a real seismic dataset with similar lithology/geology. Our Ormsby-wavelet was created to match that of the interval of interest in the real seismic data, a carbonate-dominated succession near the crest of a rotated fault block. Furthermore, the rock properties within our models are comparable to those expected at the burial depths of the interval of interest in the real seismic data as described earlier. Comparing our models with the real seismic, several subtle features in the actual seismic reflection images show similarities to our synthetic seismic images. Fig. 13 shows a seismic image from the real data set and side-by-side comparisons with examples from the synthetic images for comparison.

In Fig. 13 a, small bend in the reflections (marked by the arrow) can

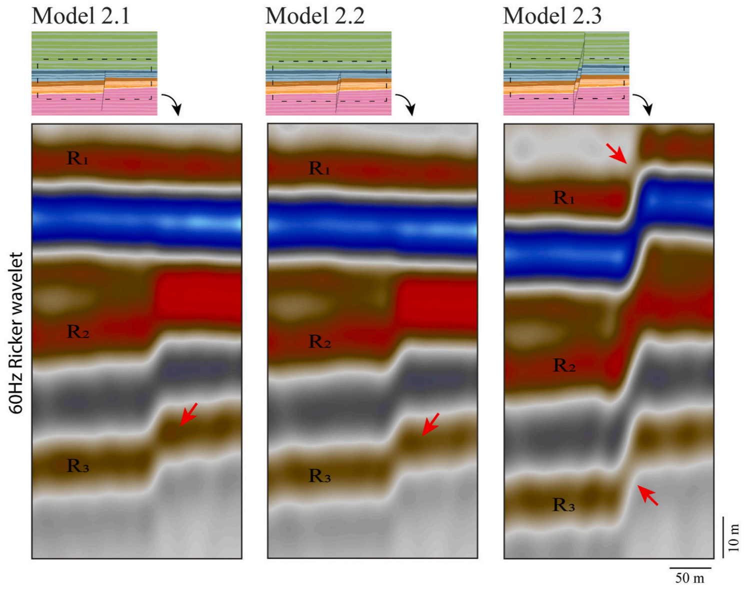

**Fig. 12.** Areas of interest in the seismic images of Model series 2, with the 60 Hz Ricker wavelet and a vertical exaggeration with the factor of five. Noise is not included.

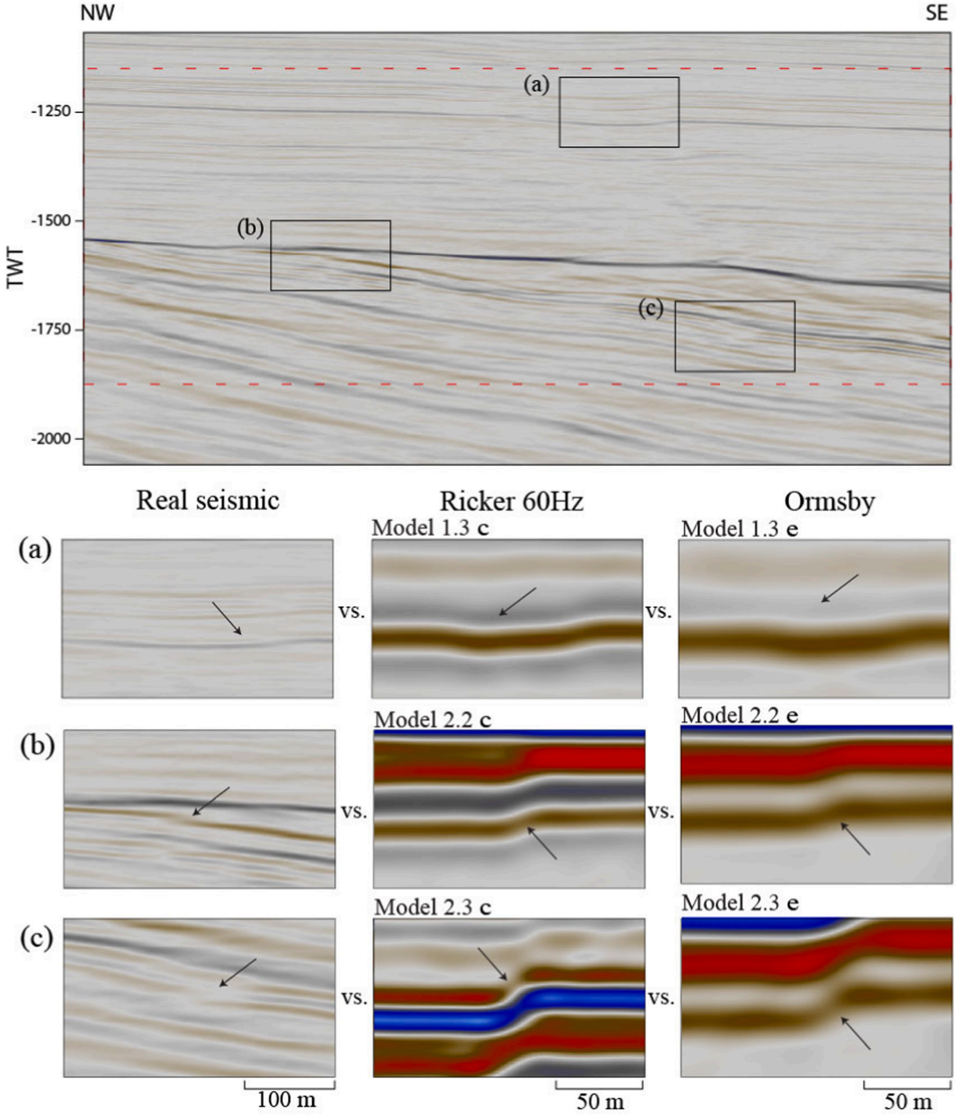

**Fig. 13.** Example of real seismic data (Topseis) from the SW Barents Sea for comparison with our results. a) Example of a slight downwarping geometry b) example of monoclinal shaped reflection c) example with descrete offset of reflections.

be seen in the overburden above the rotated fault block, giving the reflections a graben like, downwarping geometry - similar in appearance to that observed in the synthetic seismic images of Model 1.3. The seismic sections shown in Fig. 13 b and c are found deeper in the stratigraphy (at reservoir level), near the crest of the rotated fault block. In Fig. 13 b we can see an example of a monoclinal geometry in the real seismic data, similar to that observed in the seismic images of Model 2.2, both when using the 60 Hz Ricker wavelet and the Ormsby wavelet. The example in Fig. 13 c show a discrete offset of a positive amplitude reflection in the real seismic, similar to what we can observe in reflection $R_1$ above the strong negative amplitude reflection in the seismic image of Model 2.3 with the 60 Hz Ricker wavelet. From using the Ormsby wavelet, a similar but not as clear example to compare with can be found in reflection $R_2$, just below the strong negative reflection.

The results from this study do not constitute evidence that the reflection distortions seen in the real seismic are caused by discrete faults. However, our seismic modelling results do demonstrate that faults with throws at or below seismic resolution may indeed cause such subtle reflection distortions, which are common features in seismic images of faulted strata. Our results therefore provide an empirical basis for geological interpretation of such subtle reflection distortions.

## 7. Concluding remarks

We have addressed the question of how small-scale faults (D = 1–20 m) affect seismic images, and whether such faults may be observed or inferred from the seismic images, for several given seismic survey conditions and parameters. We found that within relatively noise-free, high-quality reflection seismic datasets, faults with offsets down to 5 m may cause distortions and downwarping geometries to reflections that may help seismic interpreters infer or hypothesize their presence. Somewhat larger normal faults and normal fault pairs (here, D = 11–20 m) may cause discrete reflection offsets, or monoclinal shape of reflections, depending on the horizontal and lateral seismic resolution of the dataset. It is worth noting that although small scale faults down to a few meters of throw may distort reflections, the inference of faults from subtle reflection distortions in real seismic data is inherently uncertain. Nevertheless, evidence from studies such as this may offer empirical support for more geologically concept-driven interpretation strategies, for example suggesting that in certain geological settings, subtle reflection distortions should generally be interpreted as discrete faults. Although previous studies have pointed out the biases and potential pitfalls of conceptually driven fault interpretation (Alcalde et al., 2019), we suggest that when used with caution a concept driven approach may be justified.

## Declaration of competing interest

The authors declare that they have no known competing financial interests or personal relationships that could have appeared to influence the work reported in this paper.

## Data availability

Data will be made available on request.

## Acknowledgements

We acknowledge funding for a personal PhD grant for Vilde Dimmen from VISTA – a basic research program in collaboration between The Norwegian Academy of Science and Letters, and Equinor (grant number 6272). We further acknowledge NORSAR for an academic license of the seismic modelling software SeisRoX. The virtual outcrop was partly visualized and interpreted using LIME (http://virtualoutcrop.com/lime). We are grateful to Lundin Energy Norway for access and permission to publish the seismic image shown in Fig. 13, and to Roy Davies, Jostein Herredsvela and Wintershall DEA for helpful discussions. Dr. David Peacock is thanked for invaluable assistance during data collection in Malta. We are grateful to the reviewers Dr. Charlotte Botter and Dr. Alexandre Maul for their constructive reviews that helped improve the final version of this manuscript. We also acknowledge Dr. Marcos Fetter and Dr. Massimo Zecchin for helpful and constructive editorial handling.

## References

Al-Masgari, A.A.-S., Elsaadany, M., Siddiqui, N.A., Latiff, A.H.A., Bakar, A.A., Elkurdy, S., Hermana, M., Babikir, I., Imran, Q.S., Adeleke, T., 2021. Geomorphological geometries and high-resolution seismic sequence stratigraphy of Malay basin's fluvial succession. Appl. Sci. 11, 5156. https://doi.org/10.3390/app11115156.

Alaei, B., Torabi, A., 2017. Seismic imaging of fault damaged zone and its scaling relation with displacement. Interpretation 5, SP83–SP93. https://doi.org/10.1190/INT-2016-0230.1.

Alcalde, J., Bond, C.E., Johnson, G., Kloppenburg, A., Ferrer, O., Bell, R., Ayarza, P., 2019. Fault interpretation in a vertically exaggerated seismic section: evidence of conceptual model uncertainty and anchoring. Solid Earth Discussions 1–20. https://doi.org/10.5194/se-2019-66.

Andersen, I.G., 2020. Effects of Geophysical Parameters on the Seismic Expression of the Maghlaq Fault, Malta: Insights from Outcrop-Based 2D Seismic Modeling, Mathematic and Natural Sciences. University of Bergen, p. 102.

Anselmetti, J.D., Eberli, G.P., 1993. Controls on sonic velocities in carbonates. Pure and Applied Geophysics 141, 287–323. https://doi.org/10.1007/BF00998333.

Aydin, A., 2000. Fractures, faults, and hydrocarbon entrapment, migration and flow. Mar. Petrol. Geol. 17, 797–814. https://doi.org/10.1016/S0264-8172(00)00020-9.

Bense, V.F., Person, M.A., 2006. Faults as conduit-barrier systems to fluid flow in siliciclastic sedimentary aquifers. Water Resour. Res. 42 https://doi.org/10.1029/2005WR004480.

Beukes, N.J., Gutzmer, J., Mukhopadhyay, J., 2013. The geology and genesis of high-grade hematite iron ore deposits. B. Appl. Earth Sci. 112, 18–25. https://doi.org/10.1179/037174503225011243.

Bonson, C.G., Childs, C., Walsh, J.J., Schopfer, M.P.J., Carboni, V., 2007. Geometric and kinematic controls on the internal structure of a large normal fault in massive limestones: the Maghlaq Fault, Malta. J. Struct. Geol. 29, 336–354. https://doi.org/10.1016/j.jsg.2006.06.016.

Botter, C., Cardozo, N., Hardy, S., Lecomte, I., Paton, G., Escalona, A., 2016. Seismic characterisation of fault damage in 3D using mechanical and seismic modelling. Mar. Petrol. Geol. 77, 973–990. https://doi.org/10.1016/j.marpetgeo.2016.08.002.

Bradaric, A.D., Andersen, T., Lecomte, I., Løseth, H., Eide, C.H., 2022. Recognition and characterization of small-scale sand injectites in seismic data: implications for reservoir development. J. Geol. Soc. 179 https://doi.org/10.1144/jgs2021-041.

Buckley, S.J., Ringdal, K., Naumann, N., Dolva, B., Kurz, T.H., Howell, J.A., Dewez, T.J., 2019. LIME: software for 3-D visualization, interpretation, and communication of virtual geoscience models. Geosphere 15, 222–235. https://doi.org/10.1130/GES02002.1.

Caine, J.S., Forster, C.B., 1999. Fault zone architecture and fluid flow: insights from field data and numerical modeling. Faults and Subsurface Fluid Flow in the Shallow Crust 101–127.

Castagna, J.P., Batzle, M.L., Kan, T.K., Backus, M.M., 1993. Rock Physics - The Link Between Rock Properties and AVO Response: *Offset-Dependent Reflectivity—Theory and Practice of AVO Analysis*. Investigations in Geophysics, Soc. Expl. Geophys., Tulsa, Oklahoma. 8, 135–171.

Cavazza, W., Wezel, F.C., 2003. The Mediterranean region - a geological primer. Episodes 26, 160–168. https://doi.org/10.18814/epiiugs/2003/v26i3/002.

Chen, T., Huang, L., 2015. Directly imaging steeply-dipping fault zones in geothermal fields with multicomponent seismic data. Geothermics 57, 238–245. https://doi.org/10.1016/j.geothermics.2015.07.003.

Chopra, S., Castagna, J., Portniaguine, O., 2006. Seismic resolution and thin-bed reflectivity inversion. CSEG recorder 31, 19–25. https://doi.org/10.1190/1.2369941.

Damsleth, E., Sangolt, V., Aamodt, G., 1998. Sub-seismic faults can seriously affect fluid flow in the njord field off western Norway-a stochastic fault modeling case study. In: SPE Annual Technical Conference and Exhibition. Society of Petroleum Engineers.

Dart, C.J., Bosence, D.W.J., Mcclay, K.R., 1993. Stratigraphy and structure of the Maltese graben system. J. Geol. Soc. 150, 1153–1166. https://doi.org/10.1144/gsjgs.150.6.11.

Dey, A.K., Stewart, R.R., 1997. Predicting density using vs and Gardner's relationship. CREWES Res Rep 9, 1–9.

Dimmen, V., 2016. Structural Controls on Fluid Flow in Carbonate Rocks: Quantitative Insights from the Maltese Islands. MSc. thesis. Department of Earth Science. University of Bergen, p. 88.

Dimmen, V., Rotevatn, A., Nixon, C.W., 2020. The relationship between fluid flow, structures, and depositional architecture in sedimentary rocks: an example-based overview. Geofluids 2020, 211–230. https://doi.org/10.1155/2020/3506743, 2020.

Dimmen, V., Rotevatn, A., Peacock, D.C., Nixon, C.W., Nærland, K., 2017. Quantifying structural controls on fluid flow: insights from carbonate-hosted fault damage zones on the Maltese Islands. J. Struct. Geol. 101, 43–57. https://doi.org/10.1016/j.jsg.2017.05.012.

Eide, C.H., Schofield, N., Lecomte, I., Buckley, S.J., Howell, J.A., 2017. Seismic interpretation of sill complexes in sedimentary basins: implications for the sub-sill imaging problem. J. Geol. Soc. 175, 193–209. https://doi.org/10.1144/jgs2017-096.

Faleide, T.S., Braathen, A., Lecomte, I., Mulrooney, M.J., Midtkandal, I., Bugge, A.J., Planke, S., 2021. Impacts of seismic resolution on fault interpretation: insights from seismic modelling. Tectonophysics 816. https://doi.org/10.1016/j.tecto.2021.229008.

Faulkner, D.R., Jackson, C.A.L., Lunn, R.J., Schlische, R.W., Shipton, Z.K., Wibberley, C.A.J., Withjack, M.O., 2010. A review of recent developments concerning the structure, mechanics and fluid flow properties of fault zones. J. Struct. Geol. 32, 1557–1575. https://doi.org/10.1016/j.jsg.2010.06.009.

Gardner, G., Gardner, L., Gregory, A., 1974. Formation velocity and density—the diagnostic basics for stratigraphic traps. Geophysics 39, 770–780. https://doi.org/10.1190/1.1440465.

Gartrell, A., Zhang, Y.H., Lisk, M., Dewhurst, D., 2004. Fault intersections as critical hydrocarbon leakage zones: integrated field study and numerical modelling of an example from the Timor Sea, Australia. Mar. Petrol. Geol. 21, 1165–1179. https://doi.org/10.1016/j.marpetgeo.2004.08.001.

Grippa, A., Hurst, A., Palladino, G., Lacopini, D., Lecomte, I., Huuse, M., 2019. Seismic imaging of complex geometry: forward modeling of sandstone intrusions. Earth Planet Sci. Lett. 513, 51–63. https://doi.org/10.1016/j.epsl.2019.02.011.

Gueguen, E., Doglioni, C., Fernandez, M., 1998. On the post-25 Ma geodynamic evolution of the western Mediterranean. Tectonophysics 298, 259–269. https://doi.org/10.1016/S0040-1951(98)00189-9.

Haines, T.J., Michie, E.A.H., Neilson, J.E., Healy, D., 2016. Permeability evolution across carbonate hosted normal fault zones. Mar. Petrol. Geol. 72, 62–82. https://doi.org/10.1016/j.marpetgeo.2016.01.008.

Hatton, C., Main, I., Meredith, P., 1994. Non-universal scaling of fracture length and opening displacement. Nature 367, 160–162. https://doi.org/10.1038/367160a0.

Healy, D., Neilson, J.E., Haines, T.J., Michie, E.A., Timms, N.E, Wilson, M.E., 2015. An Investigation of Porosity–velocity Relationships in Faulted Carbonates Using Outcrop Analogues. Geological Society, London, Special Publications 406, 261–280. https://doi.org/10.1144/SP406.13.

Hosken, J., 1988. Ricker wavelets in their various guises. First Break 6 (1), 24–33. https://doi.org/10.3997/1365-2397.1988002.

Jafarian, E., de Jong, K., Kleipool, L.M., Scheibner, C., Blomeier, D.P., Reijmer, J.J., 2018. Synthetic seismic model of a Permian biosiliceous carbonate–carbonate depositional system (Spitsbergen, Svalbard Archipelago). Mar. Petrol. Geol. 92, 78–93. https://doi.org/10.1016/j.marpetgeo.2018.01.034.

Jongsma, D., van Hinte, J.E., Woodside, J.M., 1985. Geologic structure and neotectonics of the North African continental margin south of Sicily. Mar. Petrol. Geol. 2, 156–179. https://doi.org/10.1016/0264-8172(85)90005-4.

Knapp, R.W., 1990. Vertical resolution of thick beds, thin beds, and thin-bed cyclothems. Geophysics 55 (9), 1183–1190. https://doi.org/10.1190/1.1442934.

Krawczyk, C.M., Tanner, D.C., Henk, A., Trappe, H., Ziesch, J., Beilecke, T., Aruffo, C.M., Weber, B., Lippmann, A., Görke, U.J., 2015. Seismic and sub-seismic deformation prediction in the context of geological carbon trapping and storage. Geological Storage of CO2–Long Term Security Aspects 97–113. Springer.

Lecomte, I., 2008. Resolution and illumination analyses in PSDM: a ray-based approach. Lead. Edge 27, 650–663. https://doi.org/10.1190/1.2919584.

Lecomte, I., Lavadera, P.L., Anell, I., Buckley, S.J., Schmid, D.W., Heeremans, M., 2015. Ray-based seismic modeling of geologic models: understanding and analyzing seismic images efficiently. Interpretation-A Journal of Subsurface Characterization 3, Sac71–Sac89. https://doi.org/10.1190/INT-2015-0061.1.

Lecomte, I., Lavadera, P.L., Botter, C., Anell, I., Buckley, S.J., Eide, C.H., Grippa, A., Mascolo, V., Kjoberg, S., 2016. 2 (3) D convolution modelling of complex geological targets beyond–1D convolution. First Break 34, 99–107. https://doi.org/10.3997/1365-2397.34.5.84451.

Li, H., Yang, W., Yong, X., 2018. Deep Learning for Ground-Roll Noise Attenuation, SEG Technical Program Expanded Abstracts 2018. Society of Exploration Geophysicists, pp. 1981–1985.

Lubrano-Lavadera, P., Senger, K., Lecomte, I., Mulrooney, M.J., Kühn, D., 2018. Seismic modelling of metre-scale normal faults at a reservoir-cap rock interface in Central Spitsbergen, Svalbard: implications for CO2 storage. Norw. J. Geol. 99, 329–347. https://doi.org/10.17850/njg003.

Magee, C., Maharaj, S.M., Wrona, T., Jackson, C.A.-L., 2015. Controls on the expression of igneous intrusions in seismic reflection data. Geosphere 11, 1024–1041. https://doi.org/10.1130/GES01150.1.

Michie, E.A.H., Haines, T.J., Healy, D., Neilson, J.E., Timms, N.E., Wibberley, C.A.J., 2014. Influence of carbonate facies on fault zone architecture. J. Struct. Geol. 65, 82–99. https://doi.org/10.1016/j.jsg.2014.04.007.

Mitchell, T., Faulkner, D., 2012. Towards quantifying the matrix permeability of fault damage zones in low porosity rocks. Earth Planet Sci. Lett. 339, 24–31. https://doi.org/10.1016/j.epsl.2012.05.014.

Moussa, M.M., El Arabi, A.G.M., 2003. Soil radon survey for tracing active fault: a case study along Qena-Safaga road, Eastern Desert, Egypt. Radiat. Meas. 37, 211–216. https://doi.org/10.1016/S1350-4487(03)00039-8.

Nixon, C.W., Nærland, K., Rotevatn, A., Dimmen, V., Sanderson, D.J., Kristensen, T.B., 2020. Connectivity and network development of carbonate-hosted fault damage zones from western Malta. J. Struct. Geol. 141, 104212 https://doi.org/10.1016/j.jsg.2020.104212.

Osagiede, E.E., Duffy, O.B., Jackson, C.A.-L., Wrona, T., 2014. Quantifying the growth history of seismically imaged normal faults. J. Struct. Geol. 66, 382–399. https://doi.org/10.1016/j.jsg.2014.05.021.

Pedley, H., House, M., Waugh, B., 1976. The geology of Malta and Gozo. Proc. Geologists' Assoc. 87, 325–341. https://doi.org/10.1016/S0016-7878(76)80005-3.

Pickett, G.R., 1963. Acoustic character logs and their applications in formation evaluation. J. Petrol. Technol. 15 (6), 659–667. https://doi.org/10.2118/452-PA.

Putz-Perrier, M.W., Sanderson, D.J., 2010. Distribution of faults and extensional strain in fractured carbonates of the North Malta Graben. AAPG Bull. 94, 435–456. https://doi.org/10.1306/08260909063.

Rabbel, O., Galland, O., Mair, K., Lecomte, I., Senger, K., Spacapan, J.B., Manceda, R., 2018. From field analogues to realistic seismic modelling: a case study of an oil-producing andesitic sill complex in the Neuquén Basin, Argentina. J. Geol. Soc. 175, 580–593. https://doi.org/10.1144/jgs2017-11.

Renshaw, C., Park, J., 1997. Effect of mechanical interactions on the scaling of fracture length and aperture. Nature 386, 482–484. https://doi.org/10.1038/386482a0.

Rost, S., Thomas, C., 2009. Improving seismic resolution through array processing techniques. Surv. Geophys. 30, 271–299. https://doi.org/10.1007/s10712-009-9070-6.

Rotevatn, A., Fossen, H., 2011. Simulating the effect of subseismic fault tails and process zones in a siliciclastic reservoir analogue: implications for aquifer support and trap definition. Mar. Petrol. Geol. 28, 1648–1662. https://doi.org/10.1016/j.marpetgeo.2011.07.005.

Ryan, H., 1994. Ricker, Ormsby, Klauder, Butterworth - A Choice of Wavelets. CSEG Recorder, pp. 8–9.

Sanderson, D.J., Nixon, C.W., 2018. Topology, connectivity and percolation in fracture networks. J. Struct. Geol. 115, 167–177. https://doi.org/10.1016/j.jsg.2018.07.011.

Schmelzbach, C., Greenhalgh, S., Reiser, F., Girard, J.-F., Bretaudeau, F., Capar, L., Bitri, A., 2016. Advanced seismic processing/imaging techniques and their potential for geothermal exploration. Interpretation 4, SR1–SR18. https://doi.org/10.1190/INT-2016-0017.1.

Schneider, W.A., 1971. Developments in seismic data processing and analysis (1968–1970). Geophysics 36, 1043–1073. https://doi.org/10.1190/1.1440232.

Shipton, Z.K., Evans, J.P., Dockrill, B., Heath, J., Williams, A., Kirchner, D., Kolesar, P.T., Thomas, D., Benson, S., 2005. Natural leaking CO2-charged systems as analogs for failed geologic storage reservoirs. Carbon dioxide capture for storage in deep geologic formations 699–712.

Shipton, Z.K., Evans, J.P., Robeson, K.R., Forster, C.B., Snelgrove, S., 2002. Structural heterogeneity and permeability in faulted eolian sandstone: implications for subsurface modeling of faults. AAPG Bull. 86, 863–883. https://doi.org/10.1306/61EEDBC0-173E-11D7-8645000102C1865D.

Simm, R., Bacon, M., 2014. Seismic Amplitude: an Interpreter's Handbook. Cambridge University Press.

Stewart, S., 2011. Vertical exaggeration of reflection seismic data in geoscience publications 2006–2010. Mar. Petrol. Geol. 28, 959–965. https://doi.org/10.1016/j.marpetgeo.2010.10.003.

Stewart, S., 2012. Interpretation validation on vertically exaggerated reflection seismic sections. J. Struct. Geol. 41, 38–46. https://doi.org/10.1016/j.jsg.2012.02.021.

Talwani, P., 1999. Fault geometry and earthquakes in continental interiors. Tectonophysics 305, 371–379. https://doi.org/10.1016/S0040-1951(99)00024-4.

Vermilye, J.M., Scholz, C.H., 1995. Relation between vein length and aperture. J. Struct. Geol. 17, 423–434. https://doi.org/10.1016/0191-8141(94)00058-8.

Walsh, J., Watterson, J., Heath, A., Gillespie, P., Childs, C., 1998. Assessment of the effects of sub-seismic faults on bulk permeabilities of reservoir sequences. Geological Society, London, Special Publications 127, 99–114. https://doi.org/10.1144/GSL.SP.1998.127.01.0.

Walsh, J., Watterson, J., Yielding, G., 1991. The importance of small-scale faulting in regional extension. Nature 351, 391–393. https://doi.org/10.1038/351391a0.

Wang, Y., 2015. Generalized seismic wavelets. Geophys. J. Int. 203 (2), 1172–1178. https://doi.org/10.1093/gji/ggv346.

Wrona, T., Fossen, H., Lecomte, I., Eide, C.H., Gawthorpe, R., 2020. Seismic expression of shear zones: insights from 2-D point-spread-function based convolution modelling. Journal of Structural Geology 140, 104121. https://doi.org/10.1016/j.jsg.2020.104121.

Yoshida, H., Metcalfe, R., Yamamoto, K., Murakami, Y., Hoshii, D., Kanekiyo, A., Naganuma, T., Hayashi, T., 2008. Redox front formation in an uplifting sedimentary rock sequence: an analogue for redox-controlling processes in the geosphere around deep geological repositories for radioactive waste. Appl. Geochem. 23 (8), 2364–2381. https://doi.org/10.1016/j.apgeochem.2008.03.015.

Zhong, T., Li, Y., Wu, N., Nie, P., Yang, B., 2015. Statistical properties of the random noise in seismic data. J. Appl. Geophys. 118, 84–91. https://doi.org/10.1016/j.jappgeo.2015.04.011.

# SYNTHESIS

# 3. Synthesis

The research herein has been focused around two main themes (i) structural controls on fluid flow and (ii) the seismic imaging of such structures; where the first theme is covered in **Papers 1 and 2** (as well as Appendix I and II) and theme two is discussed in **Papers 3 and 4**.

The size of faults, fractures and other types of structures in nature tend to follow a power-law distribution, meaning that there is an infinitely greater number of small (sub-seismic) structures than larger (seismically resolvable) structures (e.g., Torabi and Berg, 2011; Torabi et al., 2017). These small-scale structures may accommodate significant crustal strain, and need to be taken into consideration; Walsh et al. (1991*)* suggest that seismic-based summations of fault throws may underestimate regional extension by up to 40% due to sub-seismic strains. Due to the abundance of such sub-seismic structures they can play a crucial role in controlling the permeability distribution and fluid flow patterns in the subsurface, both as fluid flow conduits in themselves and as connecting links between larger transmissive structures and high-permeable lithologies (e.g., Walsh et al., 1998; Gartrell et al., 2004; Mitchell and Faulkner, 2012; Sanderson and Nixon, 2018). Hence, the possible presence of such small-scale structures needs to be taken into consideration when fluid flow is being investigated in the subsurface, and we need to have some understanding of how such structures could be connected and how they might appear in reflection seismic data. In the following, this will be discussed in relation to the work presented in papers 1-4 (section 2) that form this thesis, revisiting and summarizing how this thesis work has addressed the research questions presented in Section 1.4.

## 3.1 Synthesis and discussion

In this section, the main finds of this thesis are synthesized in context of the research questions outlined in the introduction chapter, and the wider implications of the work are discussed.

### How can the spatial relationship between structural complexity and fluid flow be visualised and quantified?

A core aim of this thesis has been to provide documentation, visualization and quantification of the relationship between geological structures and fluid flow, with emphasis on how structural complexity affects localized flow. Combining knowledge and methods from Peacock et al. (2017a) and Nixon et al. (2020) (**Appendix A and B**) on damage zone classifications and network properties,  the novel approach developed by Sanderson and Nixon (2015) and used in **Appendix B** was extended to also include looking at the relationship with flow in **Papers 1 and 2**, in order to address this research question.

The visualization and quantification of the relationship between fluid flow and structural complexity in was demonstrated **Paper 1**, by investigating spatially the correlation between topological network properties and paleo-fluid flow proxies. Topology utilize different types of nodes and branches in order to define and visualise the connectivity of a network, and can be used for fault and fracture networks on all scales (Sanderson and Nixon, 2015; Sanderson et al., 2019), and for both simple and more complex fault and fracture networks (Morley and Nixon, 2016). Topological characterization is an excellent tool for quantification and visualisation of network properties (Nyberg et al., 2018), and can be used on all scales and on all types of networks, as illustrated for example by Vagle (2020, Fig. 3.1) who used topology for characterization of deformation band networks. Topological characterization is also very useful for quantifying and visualizing the spatial relationship between structural complexity and (paleo-)fluid flow (e.g., Duffy et al., 2017; Espejel et al., 2020; Igbokwe et al., 2020; Nixon et al., 2020; Hansberry et al., 2021; Ireland et al., 2021; Zhu et al., 2021; Heggernes et al., 2022). This is extensively demonstrated both in **Paper 1 and 2**.

A main advance represented by papers 1 and 2 is that, contrary to earlier works in literature that document the relationship between fluid flow and structures (Parry et al., 2004; Fossen and Bale, 2007; Faulkner et al., 2010; Ogata et al., 2014; Kristensen et al., 2016; Volatili et al., 2019), **Papers 1 and 2** include a quantitative visualisation of the spatial relationship between fluid flow in form of rock reactive products on one hand, and structural complexity on the other.

The demonstration of this as a concept/approach is significant and important, since such a quantification/visualization as that shown herein may be a powerful tool that can be extended to use topological fracture network characterization to visualize and spatially predict likely loci for structurally controlled fluid flow in the subsurface (c.f. Dockrill and Shipton, 2010; Hermanrud et al., 2014). Analysis of node and branch topology can be used on fault- and fracture networks from seismic (e.g., through seismic attribute analysis, cf. Torabi et al. (2017) or wellbore cores to provide a useful visualisation of the fracture network connectivity and the relationship with the loci for active or past fluid flow in the subsurface.

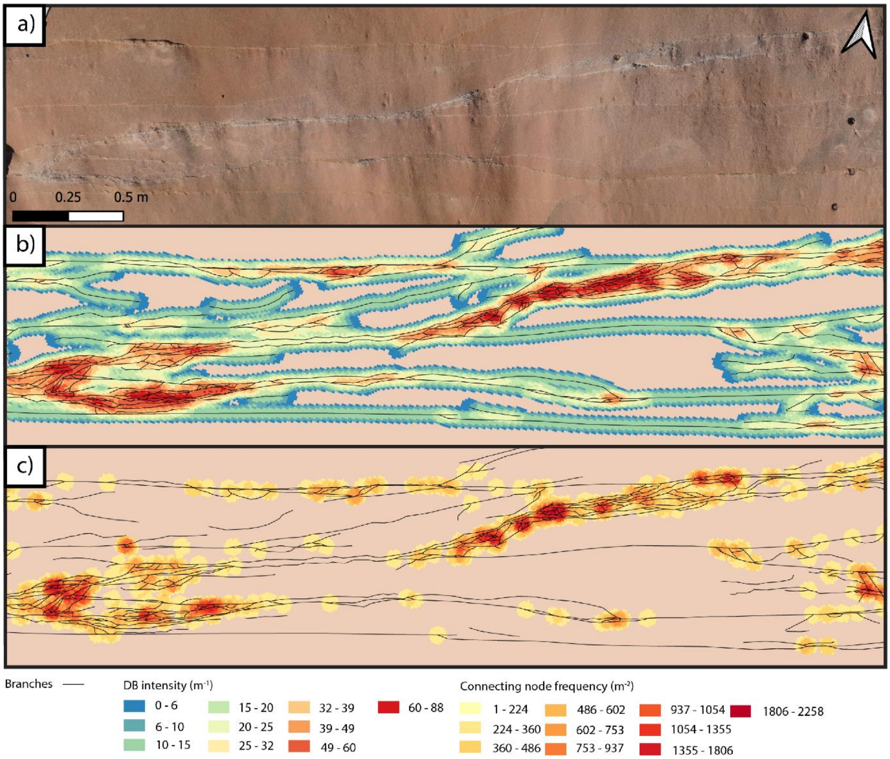

*Fig. 3.1: Topological characterization of a deformation band network at the NE flank of the San Rafael Swell, Utah (Vagle, 2020). a) Outcrop image. b) Mapped deformation band network. c) Deformation band intensity. d) Connecting node frequency.*

### What is the spatial relationship and key controls of structural complexity on fluid flow and fluid-rock interaction?

There is an abundance of examples that demonstrate how structures and structural complexity exert strong controls on fluid flow (Oliver, 1996; Caine and Forster, 1999; Eichhubl et al., 2000; Eichhubl et al., 2009; Dockrill and Shipton, 2010; Faulkner et al., 2010; Davidson et al., 2016; Ono et al., 2016; Orellana et al., 2022). Nevertheless, the quantification and visualization of the relationship between fluid flow, structural complexity and network properties has so far been lacking. To this end, **Paper 1** fills a gap in literature. Using cemented mounds as proxies for paleo-fluid flow, we quantitatively explore and visualize the spatial correlation between structural complexity and flow. This quantitative analysis documents that areas with high numbers of connecting nodes and branches (i.e. high degree of connectivity) coincide with areas where the cemented mounds are located, and hence provide a quantification of how structural complexity acts as a control on localized fluid flow.

In **Paper 2** the motivation shifts to a wider perspective, where literature review is combined with the analysis of select outcrop examples to present an overview of a wider range of fluid flow controls that includes both depositional, architectural and structural controls as well as the combination of these. Several studies have presented examples of the role of e.g., single structures, or pairs of interacting faults in relation to fluid flow (Wiprut and Zoback, 2000; Bense and Person, 2006; Rotevatn and Fossen, 2011; Freitag et al., 2022). However, as previously mentioned, faults and fractures often occur in networks (Bonnet et al., 2001; Sanderson et al., 2019), and the relationship between fault and fracture networks and fluid flow in the subsurface has been poorly constrained, at least quantitatively (e.g., Sanderson and Nixon, 2018). In **Paper 2**, the distribution of iron oxide precipitates were used as a proxy for paleo-fluid flow (Ortoleva et al., 1986; Yoshida et al., 2008; Balsamo et al., 2013), enabling the identification and exemplification of a set of generic principles and factors that are instrumental for understanding key controls on fluid flow patterns in sedimentary rocks globally (Fig. 3.2).

### How can structural and depositional conduit networks interact to affect fluid flow?

Fluid flow within a rock body is highly dependent on the pore structure and its variability, and hence also the depositional and diagenetic history. The depositional processes and diagenesis control the distribution of grain size, -type, sorting, cementation, alteration, etc. and therefore also the porosity and permeability of the rock itself (Chandler et al., 1989; Hurst and Rosvoll, 1991). When considering fluid flow properties both the structural and stratal properties need to be taken into consideration, as it is often the interplay between these that control the overall permeability and fluid flow properties in the rock body. Fluid flow in the subsurface is clearly not restricted to fault- and fracture networks, and the complexity of fluid flow conduits that need to be considered also include lithological/depositional conduits and their architecture, host rock properties, and anisotropy. Structures and networks of e.g., faults, joints, deformation bands, and veins can interact with more or less permeable strata to form fluid flow pathways and connected conduit systems, or may work as flow barriers/baffles and cut off flow in an area (Caine et al., 1996; Bense and Person, 2006; Wibberley et al., 2017; Dávalos-Elizondo and Laó-Dávila, 2023).

Such combined networks of structures and depositional conduits are referred to as *hybrid networks* (Fig. 3.2) and are one of the focal points of **Paper 2,** where an example of a hybrid network with facies selective and fracture-controlled iron oxide precipitates is presented. The iron oxide precipitates show a complex network of paleo-conduits and showcase that a combination of fractures and highly permeable layers within the host rock can provide a very well-connected conduit network. Notably, this paper demonstrates how structural and depositional/architectural conduits may interact to control flow and fluid-rock interaction (here in the form of iron-oxide precipitates), and how such hybrid structural/depositional networks can also be quantitatively and jointly considered as one conduit network, rather than considering the structural networks in isolation.

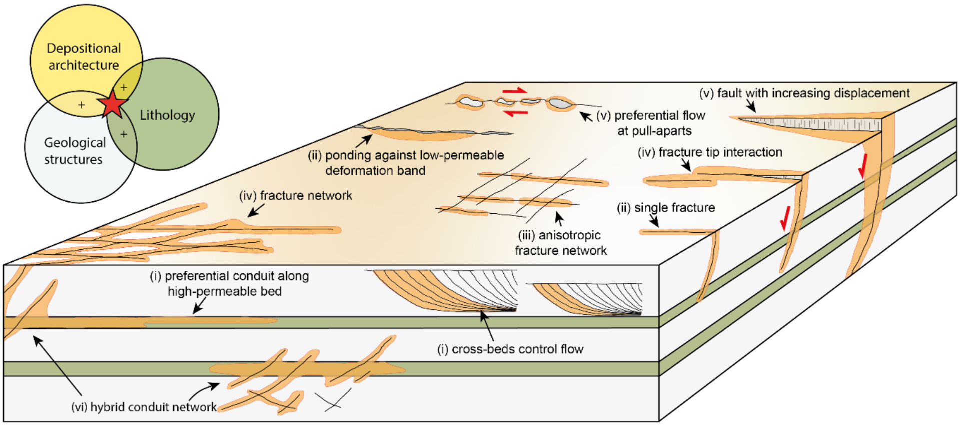

*Fig. 3.2: Schematic overview of controls on fluid flow in sedimentary rocks. The fluid flow controls are divided into six groups based upon the main control: (i) host rock properties and depositional architecture, (ii) geological structures as conduits or barriers; (iii) anisotropy in fracture populations, (iv) geometry and connectivity, (v) kinematics and interaction, and (vi) hybrid depositional-structural conduit networks. All these controls may also interact with each other, as illustrated in the top left corner. Figure from Dimmen et al., 2020 (Paper 2).*

**How are seismic reflection images affected by faults that fall at or below seismic resolution?**

The various types of structures and networks discussed above and in **Papers 1 and 2** can be found at all scales, but seismic reflection imaging can only image structures that are sufficiently large to be seismically resolvable (Misra and Mukherjee, 2018; Reilly et al., 2023). As documented in **Papers 1 and 2**, small-scale structures can have a great impact on fluid flow (e.g., Walsh et al., 1998; Rotevatn and Fossen, 2011), either as individual networks or as fluid flow pathways, connecting larger scale fault- and fracture networks, and it is of both economic, environmental and societal interest to be able to detect such structures in the subsurface. A second key topic in this thesis has therefore been the seismic imaging of structures and their fluid-rock reactive products in the subsurface. In **Paper 3**, seismic modeling of outcrop analogues is used to document that faults that are *at or below seismic resolution* (D = 1-20 m) may have notable effects on seismic reflection images, producing reflection distortions of various kinds. The paper demonstrates that within high quality seismic and relatively noise-free conditions, small-scale faults with total offset as low as 5 m may cause distortions and down-warping geometries to reflections (Fig. 3.3), while faults with offsets of 11-

20 m may cause discrete offset or monoclinal shape of reflections. This is a significant finding, adding a new observational basis from which seismic interpreters may more confidently hypothesize or infer fault presence.

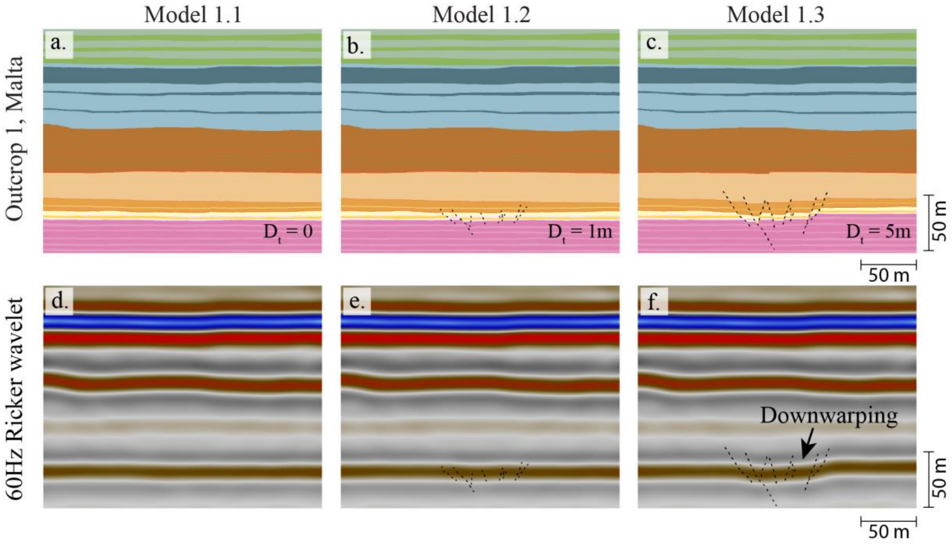

*Fig. 3.3: An example of seismic modeling of sub-seismic structures based on an outcrop in Malta. a) Fault-free reference model. b) geological model presenting the actual geometry of the outcrop, including faults with a total displacement of 1 m. c) geological model including an exaggerated version of the faults in (b), total displacement of 5 m. d) synthetic seismic corresponding to the model in (a). e) synthetic seismic corresponding to the model in (b). f) synthetic seismic corresponding to the model in (c). After Dimmen et al., 2023 (Paper 3).*

**What are the effects of structural complexity associated with such small-scale faults on reflection seismic images?**

Interpreting simple structures such as a single-strand normal fault in seismic can be challenging in itself, but, as we know, faults are often more complex and may for example consist of more than one segment/strand (Jackson and McKenzie, 1983; Childs et al., 1997; van der Zee and Urai, 2005; Faleide et al., 2021; Muksin et al., 2023). But how does such complexity affect reflection seismic images?

Using seismic modeling presented in **Paper 3**, we document that differentiating between faults that are single-stranded and multi-stranded from seismic data is challenging, and that there are only subtle differences to the seismic response in the modelled cases. In the paper, a synthetic seismic image of the geomodel containing a fault consisting of two fault strands forming a lens shaped geometry with total displacement of 11 m was compared to the seismic image of an identical geomodel but with a single strand fault. When comparing the seismic from these two models there was only very subtle differences in the two seismic images. Using vertical exaggeration (with a factor of 5), as is often done when interpreting seismic (Stewart, 2011), brings out a very subtle decrease in reflection amplitude at the bend on the monoclinal shape of one of the prominent seismic reflections. It is unlikely that any interpreter would be able to pick this up to infer the presence of the double strand fault if not already aware, but it tells us that such small variations within the fault geometry will impact the seismic, albeit subtly.

In the same paper (**Paper 3**), we also model the effect of a low-displacement (D in the range of 1 to 5 m) compound graben on the seismic images, as mentioned in the previous. The seismic modeling clearly shows that the presence of the graben system has a subtle effect, causing reflection downwarping (Fig. 3.3 f), but that individual faults are impossible to discern.

Altogether, the modeling presented in **Paper 3** shows that for faults that fall at or below seismic resolution, although the presence of the structure may be interpreted or inferred, imaging or inferring the details of any complexity associated with such small-scale structure is generally not possible.

### How may fault-controlled dolomites be imaged using reflection seismic data?

Fault-controlled fluid flow can lead to dissolution, mineral precipitation, and alteration in the vicinity of the fault(s). Fault-controlled dolomitization affect the properties of the host rock, including their permeability and impact on fluid flow dynamics (Mazzullo, 2004; Shipton et al., 2004; Steefel and Maher, 2009; Hollis et al., 2017; Bai et al., 2022). The ability to detect potential dolomite bodies is therefore crucial for fluid flow controlled processes such as mineral exploration and mining, geothermal energy and groundwater management, geohazard assessment, and more (Virk and Singh, 1993; Beukes et al., 2013; Koegelenberg et al., 2016; Yadav and Sircar, 2020).

In **Paper 4** we elucidate the imaging of fault-controlled dolomite bodies using three-dimensional synthetic seismic, documenting the seismic response and expression of fault-controlled dolomite bodies in a series of scenarios. Since the massive dolomite bodies are modelled as a heterogenous mass with no internal variation in petrophysical properties, they appear in the synthetic seismic as bland and transparent with limited reflectivity. Stratabound dolomites, on the other hand, provide high reflectivity contrasts and strong seismic reflections compared with non-dolomite bearing intervals.

The work presented in **Paper 4** on the seismic imaging of fault-controlled dolomite bodies has several connections with that presented in **Paper 1**, where cemented “mounds” (nodules) were shown to be preferentially localized to structurally complex zones. The preferential localization of fault controlled dolomite bodies to fault intersections and relays is well known (e.g., Hollis et al., 2017; Rustichelli et al., 2017; Hirani et al., 2018), and the combined knowledge advances represented by **Papers 1 and 4** are both important in this regard, since (i) topological analysis of rift fault networks may help visualize and predict the location of fault-controlled dolomites through a similar approach to that used in **Paper 1**, and (ii) seismic detection of fault-controlled dolomites in the subsurface may be better-informed by the seismic modeling work presented in **Paper 4**.

### Can massive and stratabound dolomites be interpreted/detected using reflection seismic data?

Having established that the seismic expression of fault-controlled dolomite bodies show that their general presence is detectable from seismic data, another research question addressed in this work was whether *individual* massive and stratabound dolomite bodies could be interpreted/detected.

As mentioned above, the massive dolomites studied in **Paper 4** appear in the synthetic seismic as non-reflective areas due to the lack of internal reflectors and it is relatively easy to distinguish individual bodies in the seismic image. Their size (500 m wide) also helps in terms of resolution. In real seismic data, however, one would expect more noise within the dolomite body which may make it harder to distinguish. Within the parts of our synthetic seismic containing the stratabound dolomites, we can see strong reflections due to high velocity contrasts, but it is generally not possible to distinguish individual dolomite bodies. We do, however see general trends in the presence of stratabound dolomite both vertically (stratigraphically) and laterally in the synthetic seismic; vertically, there is a clear shift in the amplitude of seismic reflections between the dolomite-free Upper Thebes and the dolomite-bearing Lower Thebes. Laterally, the seismic reflections get weaker moving away from the fault(s), coinciding with the decrease of stratabound dolomites away from the fault(s) (Fig. 3.4). The same trends can be observed in the RMS amplitude maps.

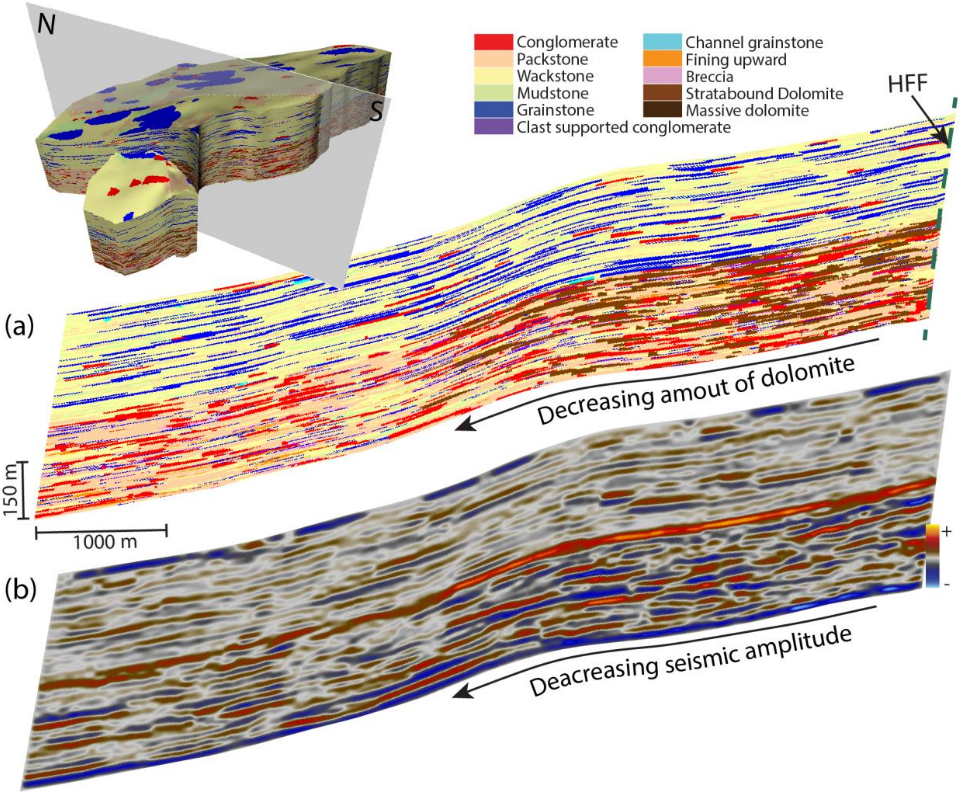

*Fig. 3.4: a) NS-section of the geomodel, with stratabound dolomite in brown located in the southern end of the lower section. b) Synthetic seismic from the same section, created with the Ormsby wavelet.*

The results from **Paper 4** show how both the massive and stratabound dolomites in this case affect the reflection seismic data, which is key to inform geological interpretations of real seismic data in similar settings. Being able to detect dolomite in a seismic section is a means to elucidate paleo fluid flow in the subsurface; the dolomites are in this case controlled by the stratigraphy and structural conduits which further allows for better understanding and ability to map structural controls on fluid flow.

## 3.2 Wider implications

The documentation, quantification, and visualization of the relationship between geological structures such as faults, deformation bands, joints etc., and fluid flow (**Paper 2**), and in particular the relationship between structural complexity and fluid flow (**Papers 1 and 2**), is fundamental to a wide range of processes in the subsurface and has an abundance of applications.

The application of topological characterization to understand the network properties of fault- and fracture networks has become increasingly widely used (Sanderson and Nixon, 2015; Duffy et al., 2017; Sanderson and Nixon, 2018; Hansberry et al., 2019; Andrews et al., 2020; Espejel et al., 2020; Hansberry et al., 2021; Forstner and Laubach, 2022; Menegoni et al., 2022), but less so in context of the relationship to fluid flow (e.g., Bonato et al., 2022). The application of topological network characterization has the potential to bring new insight, for example by being applied to numerous published examples of structure-fluid relationships, including within CO2 storage (e.g., Shipton et al., 2005a; Dockrill and Shipton, 2010; Gholami et al., 2021), flow patterns of groundwater (e.g., Bense et al., 2013), radioactive waste disposal and leakage (e.g., Yoshida et al., 2008; Rao et al., 2021), monitoring of hydrothermal activity (e.g., Curewitz and Karson, 1997; Rowland and Sibson, 2004) along faults, and many more. Notably, network topology can add a quantitative basis for (i) identifying and visualizing hotspots for fluid flow, (ii) quantitatively correlating flow anomalies with structural intensity/connectivity, and (iii) improved estimation of effective permeability (e.g., Sanderson and Nixon, 2015; Sævik and Nixon, 2017). As such, the methods and results of this aspect of the thesis work have wide-reaching implications and applications.

The use of topology as a tool to identify and visualize structurally complex zones and hotspots for fluid flow could be incorporated to add new insight in published studies, for example in Edmundson et al. (2020; their Fig. 4), to add a more quantitative correlation between hydrocarbon column height and structural complexity, and hence identifying and visualizing potential fluid migration pathways. Another example where this could be applied is found in Pour et al. (2013), where topological analysis could be applied to quantitatively map the relationship between faults, fault complexity and mineralized zones (Pour et al. 2013; their Fig. 16).

Fluid flow and fluid-rock interaction occurs at all scales, and when investigating flow in the subsurface the mapping of structures is based on reflection seismic and other subsurface data. Sub-seismic structures might form complex networks in themselves, or they can create connections between larger structures to create extensive fluid migration pathways. The results from **Paper 3** provide examples of how sub-seismic faults affect reflection seismic data. This offers new insight that has specific implications for our understanding of seismic response to small-scale faults, which may be applied in seismic interpretation in any structural setting globally. This is significant, since the identification of small-scale faults from seismic is important for instance in structural mapping of subsurface petroleum, groundwater or other reservoirs/aquifers (e.g., Townsend et al., 1998), for understanding potential structural fluid conduits in the subsurface (e.g., Ligtenberg, 2005), for estimation of seismic and sub-seismic strains (e.g., Pickering et al., 1996; Krawczyk et al., 2015), for constraining the relationship between larger and smaller structures (e.g., Schlische et al., 1996), and for mapping the damage around larger faults (e.g., Botter et al., 2016). New insights to the seismic response to small-scale faults (**Paper 3**) also contributes to a collective knowledge base that interpreters may draw on, which in turn may help reduce conceptual uncertainty or bias related to the interpretation of such faults (e.g., Bond et al., 2007; Alcalde et al., 2019).

Fluid-rock interaction may lead to the formation of dolomite in the sub-surface (e.g., Boni et al., 2000; Davies and Smith, 2006; Quan et al., 2022). In **Paper 4**, we investigated the seismic impression of dolomite in an outcrop-to-seismic study that provided insight about the imaging of dolomites in the sub-surface. Being able to identify dolomites in the sub-surface is of broad interest and has wide-reaching implications, for instance since it elucidates the relationship between paleo-fluid-flow and fluid rock interaction, and further contributes to our understanding and ability to constrain structural controls on fluid flow. For instance, our results show that one from seismic may establish that dolomites are clearly spatially controlled by faults, and that their presence decreases with distance from key faults. Being able to map dolomite bodies from seismic has implications for understanding and mapping petroleum (e.g., Dewit et al., 2012) and geothermal (e.g., Benjakul et al., 2020) reservoirs/aquifers, and for subsurface storage of carbon or hydrogen within dolomite reservoir rocks (e.g., Greb et al., 2012). For example, Hart et al. (2009) discuss the many challenges associated with imaging of hydrothermal dolomite reservoirs, specifically highlighting that three-dimensional reflection imaging is key to mapping and understanding the distribution of faults, dolomites and their properties. The insights from three-dimensional seismic modeling such as that presented in **Paper 4** has direct implications and helps address this.

# 4. Conclusions and outlook

## 4.1 Summary and conclusions

This thesis contributes with new knowledge that improves the understanding of structural controls on fluid flow, and the seismic imaging of faults and fluid-rock reactive products in the subsurface. The relationships between fluid flow and structural complexity are quantified and visualized through topological characterization of fracture networks in cemented mounds, as presented in **Paper 1**. The main outcome of this paper is the novel approach presented for the quantification and visualization of structural controls on fluid flow, and the quantitative analysis of the relationship between such flow and network properties at a level of detail that has been lacking in literature until now.

Further, the relationship between fluid flow, structures and depositional architecture of sedimentary rocks has been documented, analysed, visualized, and discussed in **Paper 2**, with an emphasis on the role of fracture networks and *hybrid* networks of structural and depositional flow conduits. The main outcome of this paper is the review of controls on fluid flow in sedimentary rocks, including a new *network and topology* perspective to key geologic controls on flow; the novel approach is used to elucidate, quantify and visualize such controls, and in particular what concerns the role of hybrid networks, which is poorly documented. This is achieved by a combination with literature review; iron oxide precipitates were used as evidence of paleo-fluid flow patterns and used to document examples to identify and discuss some generic principles and factors that are instrumental for understanding key controls on fluid flow patterns in sedimentary rocks globally.

In addition to improve the general understanding of how fluids move in relation to geological structures, lithology and structural complexity in the subsurface, this thesis also provide examples of how small-scale structures might affect reflection seismic data (**Paper 3**) through two-dimensional seismic modeling of geological input models with small-scale faults (displacements in the range of 1 to 20 m) based on outcrops in shallow marine carbonates in Malta. The main outcome of this paper is the documentation of the effect that faults that are borderline seismically resolvable, or that fall below seismic resolution, may have on seismic data; notably, the paper illustrates how subtle reflector distortions may reflect discrete faults in the subsurface, which is an important new insight that may help improve and geologically-inform structural seismic interpretation.

Having analyzed key structural and other controls on fluid flow (**Papers 1 and 2**) and the imaging of small-scale faults in seismic data (**Paper 3**), **Paper 4** continues to investigate the seismic imaging of fluid-rock interactive products, using three-dimensional seismic modeling of fault-controlled dolomites in the Suez Rift, Egypt. The main outcome of this paper is new insights to how fault-controlled hydrothermal dolomite bodies are imaged in seismic data; the paper documents that whereas the general presence and trends of dolomite occurrence in the subsurface is possible to infer from seismic data, the identification of individual stratabound dolomite bodies might not possible.

The specific key conclusions from this work are:

- In **Paper 1**, topological analyses of fracture networks indicate that areas of fracture interaction (relays, fault intersections), are associated with higher connecting node frequency and fracture intensities than elsewhere, which indicates that these parts of the fracture networks are highly connected.
- Low-porosity cemented mounds were shown to spatially coincide with the structurally most complex and well-connected parts of these fracture networks, indicating that the complex areas are associated with increased fluid-rock interaction.
- Increased fluid-rock interaction in the structurally complex areas are attributed to a combination of two effects. Firstly, the structurally complex areas represent conduits for enhanced localized flow of mineralizing fluids, due to higher fracture intensity and a degree of high fracture connectivity. Secondly, the

intense fracturing in the structurally complex areas lead to greater reactive surface area, promoting an increase in fluid-rock reactions.

- In **Paper 2**, the combination of literature review and analysis of outcrop examples allows for the identification, documentation and illustration of some key factors and principles that are instrumental in controlling fluid flow patterns in sedimentary rocks globally. These are:
    - *Depositional architecture and host rock properties* represent a first-order control on fluid flow in sedimentary rocks.
    - *The conduit and/or barrier potential of geological structures* such as faults, fractures and deformation bands is key to their effect on flow. Whereas joints and unsealed faults may form significant conduits for fluid flow, cataclastic deformation bands, veins, and sealing faults may represent effective seals or baffles for flow.
    - *Anisotropy in fracture populations,* such as where fracture properties vary spatially and/or temporally along single structures or within a network, may cause differential effects on flow.
    - *The geometry and connectivity* of the fractures in a network is key to understanding flow. The length, orientation and intensity of fractures determines how individual fractures interact in the network, which in turn controls network connectivity and therefore percolation threshold and flow properties within the network.
    - *Kinematics and interaction* within a network are key factors controlling flow. Whereas structures dominated by opening-mode displacement generally have a positive effect on flow, closing-mode generally reduce flow, and structures affected by shear movement may form conduits or barriers depending on the presence of low-permeable fault rocks, existing aperture, or cements.
    - *Hybrid networks* may represent a significant control on flow, as structural and stratal conduits can interact to form a well-connected network of conduits.

- In **Paper 3**, based on outcrop-based seismic modeling of small-scale faults, we conclude that:
    - In relatively noise-free, high-quality reflection seismic datasets, faults with offsets down to 5 m may cause distortions and downwarping geometries to reflections that may help seismic interpreters infer or hypothesize their presence.
    - Normal faults and normal fault pairs with displacement in the range of 11-20 m were able to cause discrete reflection offsets, or monoclinal bending of reflections, depending on the horizontal and lateral seismic resolution of the dataset.
- The evidence and documentation presented in **Paper 3** offers empirical support for geologically concept-driven fault interpretation, and documents that in real seismic datasets, subtle reflection distortions should be considered as potential discrete faults.

- In **Paper 4**, we find that, in general, the 'harder and faster' Lower Thebes, shows much stronger positive amplitude reflections than the overlying 'softer and slower' and more porous Upper Thebes; the difference in amplitude reflection between the Lower and Upper Thebes is amplified when the presence of massive- and stratabound dolomites is introduced in the Lower Thebes.
- Regarding identification of the stratabound dolomites:
    - From the synthetic seismic there is a clear difference in the seismic response between the stratabound-dolomite-bearing Lower Thebes and the non-dolomite bearing Upper Thebes.
    - Seismic attribute analysis of the RMS (Root Mean Square) amplitude of the seismic signal also clearly highlights the different response between the dolomite bearing Lower Thebes and the non-dolomite bearing Upper Thebes.
    - Both the seismic response and the RMS amplitude allow for the identification of trends in the presence of dolomite.

  - The identification/interpretation of individual bodies of stratabound dolomite is not possible, neither based on the overall seismic reflection response, nor based on the analysis of RMS amplitudes.
- Regarding identification of the massive dolomite bodies:
  - The massive dolomite bodies are clearly imaged in the seismic with a non-reflective and transparent seismic character.
  - A small amount of noise from the PSF (point spread function) can be seen within the otherwise generally transparent massive dolomites in some of synthetic seismic images.
- Regarding the effect of adding random noise to the models:
  - In noise free or low-noise conditions (<<50%) the key features such as the massive dolomite bodies can easily be distinguished in the seismic data.
  - When increasing the amount of random noise in the seismic, structures and features are harder to identify; at 50% noise, also the massive dolomite bodies are hard to identify.

## 4.2 Future work and outlook

The work herein contribute to the understanding of controls on fluid flow and fluid-rock interaction in sedimentary rocks as well as seismic imaging of faults (as fluid flow conduits) and fluid-rock reactive products in the subsurface. Building on the results and conclusions of the thesis, several suggestions for future work (using the same and similar methods) extending from this are outlined below:

*Applying node and branch topology to elucidate network properties and fluid flow:*

- Apply the node-and-branch-topology approach used in **Papers 1 and 2** to deformation band networks in the hangingwall of the Maghlaq fault (see Rotevatn et al., 2016) to investigate deformation band network properties (currently under-researched, see e.g., Bonato et al., 2022), and potential controls on paleo-fluid flow.
- Extend the approach used in **Paper 1** to correlate network properties and flow to larger scale structural networks in the subsurface, correlating fluid seeps and pockmarks with fault network properties. There are several excellent reflection seismic datasets that would be well suited to map the relationship between pockmarks and underlying fault networks for this purpose, for example in the Barents Sea (see e.g., Chand et al., 2012).
- During field work for **Paper 2**, a suite of samples of spectacularly exposed shear-enhanced compaction bands were collected in faulted deep-water turbidites in the Taranaki Basin on the west coast of New Zealand's North Island. Microstructural analysis of these bands is being undertaken and will be completed in the near future in order to improve the understanding of the geometry and evolution of shear-enhanced compaction bands.
- Topological characterization of both the outcrop model, geological model, and the resulting synthetic seismic of an area (e.g., SE Malta, including the Maghlaq fault) would be highly interesting in order to investigate comparatively the connectivity of fault systems in outcrop vs. what could reasonably be interpreted form the resulting synthetic seismic.

*Seismic modeling to further explore the effects of fault structure in seismic images:*

- Work conducted in two associated MSc thesis projects (Andersen, 2020; Prestegård, 2020), co-supervised by the candidate, complements the work presented herein by undertaking seismic modeling of larger-scale faults. Prestegård (2020) and Andersen (2020) built geological models based on outcrops along the 210 m offset Maghlaq Fault in Malta, in which they carried out seismic modeling in order to improve the understanding of seismic imaging of meso-scale (100s m displacement) fault zones in carbonates. While Prestegård (2020) focused on how varying fault zone geometries and structural features within the fault zone affected the seismic images, Andersen (2020) investigated the sensitivity of the seismic expression of the fault zone to varying geophysical survey parameters. The methods, aims and the scale of the work make these very suitable for further development and comparative analysis with the work presented herein, which would help advance our knowledge of fault zone imaging beyond the scales investigate in this thesis.
- Large amounts of outcrop data and UAV imagery from faults have been collected in Malta through the current as well as related projects over the last decade. It would be of interest to generate geological models from these data in order to investigate 3D fault zone imaging and variability through 3D seismic modeling of the entire Maghlaq fault system (see also Bonson et al., 2007). This has the potential to help elucidate the imaging of along-fault segmentation and variability, relay zones, drag folding along a fault system with offsets that fall well above seismic resolution.
- The imaging of, or effect of, deformation bands in seismic reflection data would be an interesting continuation of the effect sub-seismic scale structures have on seismic reflection images, as investigated in **Paper 3**. Although deformation bands fall below seismic resolution, their effect on overall seismic response is of interest to investigate, particularly where deformation bands exist in abundance. At the Taranaki coast, NZ, (location for example in **Paper 2**) dm-

thick deformation bands are found in cliff sections, which are planned for inclusion in seismic modeling of these outcrops.

- In **Paper 3** we presented an example of synthetic seismic of a single strand vs. double-strand fault (fault lens) in order to investigate how the difference (the displacement split between two segments) would be noticeable in seismic. This was a simple example, which showed that the difference in geometry in this case did not produce notably different seismic images. Building out from this, an interesting avenue for future research would be to investigate a wider range of examples with varying number of strands, distance between strands, offsets etc., to investigate under what conditions the fault lens would be imaged as two faults rather than as one.

# References cited in introduction and synthesis

Abdel-Fattah, M., Gameel, M., Awad, S., Ismaila, A., 2015. Seismic interpretation of the aptian Alamein dolomite in the razzak oil field, Western Desert, Egypt. Arabian Journal of Geosciences 8, 4669-4684.

Abiye, T.A., 2023. Contribution of hydrogeology to solving community water supply problems in South Africa. South African Journal of Science 119.

Agosta, F., Kirschner, D.L., 2003. Fluid conduits in carbonate-hosted seismogenic normal faults of central Italy. Journal of Geophysical Research-Solid Earth 108.

Alcalde, J., Bond, C.E., Johnson, G., Kloppenburg, A., Ferrer, O., Bell, R., Ayarza, P., 2019. Fault interpretation in seismic reflection data: an experiment analysing the impact of conceptual model anchoring and vertical exaggeration. Solid earth 10, 1651-1662.

Andersen, I.G., 2020. Effects of geophysical parameters on the seismic expression of the Maghlaq Fault, Malta: insights from outcrop-based 2D seismic modeling, Mathematic and Natural Sciences. University of Bergen, p. 102.

Andrews, B.J., Shipton, Z.K., Lord, R., McKay, L., 2020. The growth of faults and fracture networks in a mechanically evolving, mechanically stratified rock mass: a case study from Spireslack Surface Coal Mine, Scotland. Solid Earth 11, 2119-2140.

Bai, Y., Liu, W., Xu, W., 2022. Dolomite genesis and dolomitization mechanisms of the Ordovician lower Yingshan Formation, Gucheng area, Tarim Basin, China. Journal of Petroleum Science and Engineering 215, 110570.

Balsamo, F., Bezerra, F.H.R., Vieira, M.M., Storti, F., 2013. Structural control on the formation of iron-oxide concretions and Liesegang bands in faulted, poorly lithified Cenozoic sandstones of the Paraiba Basin, Brazil. Geological Society of America Bulletin 125, 913-931.

Benjakul, R., Hollis, C., Robertson, H.A., Sonnenthal, E.L., Whitaker, F.F., 2020. Understanding controls on hydrothermal dolomitisation: insights from 3D reactive transport modeling of geothermal convection. Solid Earth 11, 2439-2461.

Bense, V., Person, M., 2006. Faults as conduit-barrier systems to fluid flow in siliciclastic sedimentary aquifers. Water Resources Research 42.

Bense, V.F., Gleeson, T., Loveless, S.E., Bour, O., Scibek, J., 2013. Fault zone hydrogeology. Earth-Science Reviews 127, 171-192.

Beukes, N.J., Gutzmer, J., Mukhopadhyay, J., 2013. The geology and genesis of high-grade hematite iron ore deposits. Applied Earth Science 112, 18-25.

Bonato, J., Tognoli, F.M.W., Nogueira, F.C.C., de Miranda, T.S., Inocencio, L.C., 2022. The use of network topology to assess connectivity of deformation bands in sandstone: A quantitative approach based on digital outcrop models. Journal of Structural Geology 161, 104682.

Bond, C.E., Gibbs, A.D., Shipton, Z.K., Jones, S., 2007. What do you think this is?``Conceptual uncertainty"in geoscience interpretation. GSA today 17, 4.

Boni, M., Bechstädt, T., Gasparrini, M., 2000. Hydrothermal dolomites in SW Sardinia (Italy) and Cantabria (NW Spain).

Bonnet, E., Bour, O., Odling, N.E., Davy, P., Main, I., Cowie, P., Berkowitz, B., 2001. Scaling of fracture systems in geological media. Reviews of Geophysics 39, 347-383.

Bonson, C.G., Childs, C., Walsh, J.J., Schopfer, M.P.J., Carboni, V., 2007. Geometric and kinematic controls on the internal structure of a large normal fault in massive limestones: The Maghlaq Fault, Malta. Journal of Structural Geology 29, 336-354.

Botter, C., Cardozo, N., Hardy, S., Lecomte, I., Paton, G., Escalona, A., 2016. Seismic characterisation of fault damage in 3D using mechanical and seismic modeling. Marine and Petroleum Geology 77, 973-990.

Caine, J.S., Evans, J.P., Forster, C.B., 1996. Fault zone architecture and permeability structure. Geology 24, 1025-1028.

Caine, J.S., Forster, C.B., 1999. Fault zone architecture and fluid flow: Insights from field data and numerical modeling. Faults and Subsurface Fluid Flow in the Shallow Crust, 101-127.

Chand, S., Thorsnes, T., Rise, L., Brunstad, H., Stoddart, D., Bøe, R., Lågstad, P., Svolsbru, T., 2012. Multiple episodes of fluid flow in the SW Barents Sea (Loppa High) evidenced by gas flares, pockmarks and gas hydrate accumulation. Earth and Planetary Science Letters 331, 305-314.

Chandler, M.A., Kocurek, G., Goggin, D.J., Lake, L.W., 1989. Effects of Stratigraphic Heterogeneity on Permeability in Eolian Sandstone Sequence, Page Sandstone, Northern Arizona. Aapg Bulletin-American Association of Petroleum Geologists 73, 658-668.

Chauvet, A., 2019. Structural control of ore deposits: The role of pre-existing structures on the formation of mineralised vein systems. Minerals 9, 56.

Childs, C., Walsh, J.J., Watterson, J., 1997. Complexity in fault zone structure and implications for fault seal prediction, in: Møller-Pedersen, P., Koestler, A.G. (Eds.), Hydrocarbon Seals - Importance for Exploration and Production. Elsevier, pp. 61-72.

Chopra, S., Castagna, J., Portniaguine, O., 2006. Seismic resolution and thin-bed reflectivity inversion. CSEG recorder 31, 19-25.

Cowie, P.A., Scholz, C.H., 1992. Displacement Length Scaling Relationship for Faults - Data Synthesis and Discussion. Journal of Structural Geology 14, 1149-1156.

Crider, J.G., Peacock, D.C.P., 2004. Initiation of brittle faults in the upper crust: a review of field observations. Journal of Structural Geology 26, 691-707.

Curewitz, D., Karson, J.A., 1997. Structural settings of hydrothermal outflow: Fracture permeability maintained by fault propagation and interaction. Journal of Volcanology and Geothermal Research 79, 149-168.

Dávalos-Elizondo, E., Laó-Dávila, D.A., 2023. 3D structural model and slip-dilation tendency analysis of the Chiweta Zone: Geothermal system implications and fault reactivation potential. Journal of African Earth Sciences 198, 104809.

Davidson, J.R.J., Fairley, J., Nicol, A., Gravley, D., Ring, U., 2016. The origin of radon anomalies along normal faults in an active rift and geothermal area. Geosphere 12, 1656-1669.

Davies, G.R., Smith, L.B., 2006. Structurally controlled hydrothermal dolomite reservoir facies: An overview. AAPG bulletin 90, 1641-1690.

Dewit, J., Huysmans, M., Muchez, P., Hunt, D., Thurmond, J., Vergés, J., Saura, E., Fernández, N., Romaire, I., Esestime, P., 2012. Reservoir characteristics of fault-controlled hydrothermal dolomite bodies: Ramales Platform case study. Geological Society, London, Special Publications 370, 83-109.

Dimmen, V., Rotevatn, A., Nixon, C.W., 2020. The relationship between fluid flow, structures, and depositional architecture in sedimentary rocks: an example-based overview. Geofluids 2020.

Dockrill, B., Shipton, Z.K., 2010. Structural controls on leakage from a natural CO 2 geologic storage site: Central Utah, USA. Journal of Structural Geology 32, 1768-1782.

Duffy, O.B., Nixon, C.W., Bell, R.E., Jackson, C.A.L., Gawthorpe, R.L., Sanderson, D.J., Whipp, P.S., 2017. The topology of evolving rift fault networks: Single-phase vs multi-phase rifts. Journal of Structural Geology 96, 192-202.

Edmundson, I., Rotevatn, A., Davies, R., Yielding, G., Broberg, K., 2020. Key controls on hydrocarbon retention and leakage from structural traps in the Hammerfest Basin, SW Barents Sea: implications for prospect analysis and risk assessment. Petroleum Geoscience 26, 589-606.

Eichhubl, P., Davatzes, N.C., Becker, S.P., 2009. Structural and diagenetic control of fluid migration and cementation along the Moab fault, Utah. Aapg Bulletin 93, 653-681.

Eichhubl, P., Greene, H.G., Naehr, T., Maher, N., 2000. Structural control of fluid flow: offshore fluid seepage in the Santa Barbara Basin, California. Journal of Geochemical Exploration 69, 545-549.

Eide, C.H., Schofield, N., Lecomte, I., Buckley, S.J., Howell, J.A., 2017. Seismic interpretation of sill complexes in sedimentary basins: implications for the sub-sill imaging problem. Journal of the Geological Society 175, 193-209.

English, J.M., English, K.L., Dunphy, R.B., Blake, S., Walsh, J., Raine, R., Vafeas, N.A., Salgado, P.R., 2023. An Overview of Deep Geothermal Energy and Its Potential on the Island of Ireland. First Break 41, 33-43.

Espejel, R.L., Alves, T.M., Blenkinsop, T.G., 2020. Multi-scale fracture network characterisation on carbonate platforms. Journal of Structural Geology 140, 104160.

Faleide, T.S., Braathen, A., Lecomte, I., Mulrooney, M.J., Midtkandal, I., Bugge, A.J., Planke, S., 2021. Impacts of seismic resolution on fault interpretation: Insights from seismic modeling. Tectonophysics 816, 229008.

Farrell, N.J.C., Healy, D., Taylor, C.W., 2014. Anisotropy of permeability in faulted porous sandstones. Journal of Structural Geology 63, 50-67.

Faulkner, D.R., Jackson, C.A.L., Lunn, R.J., Schlische, R.W., Shipton, Z.K., Wibberley, C.A.J., Withjack, M.O., 2010. A review of recent developments concerning the structure, mechanics and fluid flow properties of fault zones. Journal of Structural Geology 32, 1557-1575.

Ferrill, D.A., Morris, A.P., McGinnis, R.N., Smart, K.J., Ward, W.C., 2011. Fault zone deformation and displacement partitioning in mechanically layered carbonates: The Hidden Valley fault, central Texas. Aapg Bulletin 95, 1383-1397.

Forstner, S.R., Laubach, S.E., 2022. Scale-dependent fracture networks. Journal of Structural Geology 165, 104748.

Fossen, H., Bale, A., 2007. Deformation bands and their influence on fluid flow. Aapg Bulletin 91, 1685-1700.

Fossen, H., Rotevatn, A., 2016. Fault linkage and relay structures in extensional settings-A review. Earth-Science Reviews 154, 14-28.

Fossen, H., Schultz, R.A., Shipton, Z.K., Mair, K., 2007. Deformation bands in sandstone: a review. Journal of the Geological Society 164, 755-769.

Freitag, S., Klaver, J., Malai, I.S., Klitzsch, N., Urai, J.L., Stollhofen, H., Bauer, W., Schmatz, J., 2022. Petrophysical characterization, BIB-SEM imaging, and permeability models of tight carbonates from the Upper Jurassic (Malm ß), SE Germany. Geothermal Energy 10, 1-45.

Gartrell, A., Zhang, Y.H., Lisk, M., Dewhurst, D., 2004. Fault intersections as critical hydrocarbon leakage zones: integrated field study and numerical modeling of an example from the Timor Sea, Australia. Marine and Petroleum Geology 21, 1165-1179.

Gholami, R., Raza, A., Iglauer, S., 2021. Leakage risk assessment of a CO2 storage site: A review. Earth-Science Reviews 223, 103849.

Greb, S.F., Bowersox, J.R., Solis, M.P., Harris, D.C., Riley, R.A., Rupp, J.A., Kelley, M., Gupta, N., 2012. Ordovician Knox carbonates and sandstones of the eastern mid-continent: Potential geologic carbon storage reservoirs and seals.

Grippa, A., Hurst, A., Palladino, G., Lacopini, D., Lecomte, I., Huuse, M., 2019. Seismic imaging of complex geometry: Forward modeling of sandstone intrusions. Earth and Planetary Science Letters 513, 51-63.

Hansberry, R., Holford, S., King, R., Debenham, N., 2019. Using network topology to constrain fracture network permeability. ASEG Extended Abstracts 2019, 1-4.

Hansberry, R.L., King, R.C., Holford, S.P., Hand, M., Debenham, N., 2021. How wide is a fault damage zone? Using network topology to examine how fault-damage zones overprint regional fracture networks. Journal of Structural Geology 146, 104327.

Hart, B.S., Sagan, J.A., Ogiesoba, O.C., 2009. Lessons learned from 3-D seismic attribute studies of hydrothermal dolomite reservoirs. CSEG Recorder 34, 18-24.

Heggernes, H., Rotevatn, A., Demurtas, M., Nixon, C., Fossen, H., 2022. Geometry, Topology and Variability of Deformation Band Networks: Examples from the Jurassic Entrada Sandstone, Utah, Sixth International Conference on Fault and Top Seals. European Association of Geoscientists & Engineers, pp. 1-5.

Hermanrud, C., Halkjelsvik, M.E., Kristiansen, K., Bernal, A., Strömbäck, A.C., 2014. Petroleum column-height controls in the western Hammerfest Basin, Barents Sea.

Hirani, J., Bastesen, E., Boyce, A., Corlett, H., Gawthorpe, R., Hollis, C., John, C.M., Robertson, H., Rotevatn, A., Whitaker, F., 2018. Controls on the formation of stratabound dolostone bodies, Hammam Faraun Fault block, Gulf of Suez. Sedimentology 65, 1973-2002.

Holland, M., Urai, J.L., 2010. Evolution of anastomosing crack-seal vein networks in limestones Insight from an exhumed high-pressure cell, Jabal Shams, Oman Mountains. Journal of Structural Geology 32, 1279-1290.

Hollis, C., Bastesen, E., Boyce, A., Corlett, H., Gawthorpe, R., Hirani, J., Rotevatn, A., Whitaker, F., 2017. Fault-controlled dolomitization in a rift basin. Geology 45, 219-222.

Howell, J.A., Martinius, A.W., Good, T.R., 2014. The application of outcrop analogues in geological modeling: a review, present status and future outlook. Geological Society, London, Special Publications 387, 1-25.

Hurst, A., Rosvoll, K.J., 1991. Permeability variations in sandstones and their relationship to sedimentary structures, Reservoir Characterization II. Elsevier, pp. 166-196.

Igbokwe, O.A., Mueller, M., Bertotti, G., Timothy, J.J., Abah, O., Immenhauser, A., 2020. Morphology and topology of dolostone lithons in the regional Carboneras Fault Zone, Southern Spain. Journal of Structural Geology 137, 104073.

Ireland, M.T., Morley, C.K., Davies, R.J., 2021. Systematic spacing and topological variations in layer-bound fault systems. Basin Research 33, 2745-2762.

Ishii, E., 2016. Far-field stress dependency of the failure mode of damage-zone fractures in fault zones: Results from laboratory tests and field observations of siliceous mudstone. Journal of Geophysical Research: Solid Earth 121, 70-91.

Jackson, J., McKenzie, D., 1983. The geometrical evolution of normal fault systems. Journal of Structural Geology 5, 471-482.

Jolley, S., Barr, D., Walsh, J., Knipe, R., 2007. Structurally complex reservoirs: an introduction. Geological Society, London, Special Publications 292, 1-24.

Kim, Y.S., Peacock, D.C.P., Sanderson, D.J., 2003. Mesoscale strike-slip faults and damage zones at Marsalforn, Gozo Island, Malta. Journal of Structural Geology 25, 793-812.

Kim, Y.S., Peacock, D.C.P., Sanderson, D.J., 2004. Fault damage zones. Journal of Structural Geology 26, 503-517.

Kivi, I., Makhnenko, R., Oldenburg, C., Vilarrasa, V., 2022. Multi-layered systems for permanent geologic storage of CO2 at the gigatonne scale. Geophysical Research Letters, e2022GL100443.

Koegelenberg, C., Kisters, A.F., Harris, C., 2016. Structural controls of fluid flow and gold mineralization in the easternmost parts of the Karagwe-Ankole Belt of north-western Tanzania. Ore Geology Reviews 77, 332-349.

Krawczyk, C.M., Tanner, D.C., Henk, A., Trappe, H., Ziesch, J., Beilecke, T., Aruffo, C.M., Weber, B., Lippmann, A., Görke, U.-J., 2015. Seismic and sub-seismic deformation prediction in the context of geological carbon trapping and storage, Geological Storage of CO2–Long Term Security Aspects. Springer, pp. 97-113.

Krevor, S., de Coninck, H., Gasda, S.E., Ghaleigh, N.S., de Gooyert, V., Hajibeygi, H., Juanes, R., Neufeld, J., Roberts, J.J., Swennenhuis, F., 2023. Subsurface carbon dioxide and hydrogen storage for a sustainable energy future. Nature Reviews Earth & Environment, 1-17.

Kristensen, T.B., Rotevatn, A., Marvik, M., Henstra, G.A., Gawthorpe, R.L., Ravnås, R., 2018. Structural evolution of sheared margin basins: the role of strain partitioning. Sørvestsnaget Basin, Norwegian Barents Sea. Basin Research 30, 279-301.

Kristensen, T.B., Rotevatn, A., Peacock, D.C.P., Henstra, G.A., Midtkandal, I., Grundvag, S.A., 2016. Structure and flow properties of syn-rift border faults: The interplay between fault damage and fault-related chemical alteration (Dombjerg Fault, Wollaston Forland, NE Greenland). Journal of Structural Geology 92, 99-115.

Ligtenberg, J., 2005. Detection of fluid migration pathways in seismic data: implications for fault seal analysis. Basin Research 17, 141-153.

Mazzullo, S., 2004. Overview of porosity evolution in carbonate reservoirs. Kansas Geological Society Bulletin 79, 20-28.

Menegoni, N., Inama, R., Panara, Y., Crozi, M., Perotti, C., 2022. Relations between Fault and Fracture Network Affecting the Lastoni di Formin Carbonate Platform (Italian Dolomites) and Its Deformation History. Geosciences 12, 451.

Micklethwaite, S., Cox, S.F., 2004. Fault-segment rupture, aftershock-zone fluid flow, and mineralization. Geology 32, 813-816.

Misra, A.A., Mukherjee, S., 2018. Atlas of structural geological interpretation from seismic images. John Wiley & Sons.

Mitchell, T., Faulkner, D., 2012. Towards quantifying the matrix permeability of fault damage zones in low porosity rocks. Earth and Planetary Science Letters 339, 24-31.

Morley, C.K., Nixon, C.W., 2016. Topological characteristics of simple and complex normal fault networks. Journal of Structural Geology 84, 68-84.

Muksin, U., Arifullah, A., Simanjuntak, A.V., Asra, N., Muzli, M., Wei, S., Gunawan, E., Okubo, M., 2023. Secondary fault system in Northern Sumatra, evidenced by recent seismicity and geomorphic structure. Journal of Asian Earth Sciences, 105557.

Nixon, C.W., Nærland, K., Rotevatn, A., Dimmen, V., Sanderson, D.J., Kristensen, T.B., 2020. Connectivity and network development of carbonate-hosted fault damage zones from western Malta. Journal of Structural Geology 141, 104212.

Nyberg, B., Nixon, C.W., Sanderson, D.J., 2018. NetworkGT: A GIS tool for geometric and topological analysis of two-dimensional fracture networks. Geosphere 14, 1618-1634.

Ogata, K., Senger, K., Braathen, A., Tveranger, J., 2014. Fracture corridors as seal-bypass systems in siliciclastic reservoir-cap rock successions: Field-based insights from the Jurassic Entrada Formation (SE Utah, USA). Journal of Structural Geology 66, 162-187.

Oliver, N.H.S., 1996. Review and classification of structural controls on fluid flow during regional metamorphism. Journal of Metamorphic Geology 14, 477-492.

Ono, T., Yoshida, H., Metcalfe, R., 2016. Use of fracture filling mineral assemblages for characterizing water-rock interactions during exhumation of an accretionary complex: An example from the Shimanto Belt, southern Kyushu Japan. Journal of Structural Geology 87, 81-94.

Orellana, L.F., Nussbaum, C., Grafulha, L., Henry, P., Violay, M., 2022. Physical characterization of fault rocks within the Opalinus Clay formation.

Ortoleva, P., Auchmuty, G., Chadam, J., Hettmer, J., Merino, E., Moore, C.H., Ripley, E., 1986. Redox Front Propagation and Banding Modalities. Physica D 19, 334-354.

Parry, W.T., Chan, M.A., Beitler, B., 2004. Chemical bleaching indicates episodes of fluid flow in deformation bands in sandstone. Aapg Bulletin 88, 175-191.

Peacock, D.C.P., Dimmen, V., Rotevatn, A., Sanderson, D.J., 2017a. A broader classification of damage zones. Journal of Structural Geology 102, 179-192.

Peacock, D.C.P., Nixon, C.W., Rotevatn, A., Sanderson, D.J., Zuluaga, L.F., 2017b. Interacting faults. Journal of Structural Geology 97, 1-22.

Peacock, D.C.P., Sanderson, D.J., 1991. Displacements, Segment Linkage and Relay Ramps in Normal-Fault Zones. Journal of Structural Geology 13, 721-&.

Pickering, G., Bull, J.M., Sanderson, D.J., 1996. Scaling of fault displacements and implications for the estimation of sub-seismic strain. Geological Society, London, Special Publications 99, 11-26.

Pour, A.B., Hashim, M., van Genderen, J., 2013. Detection of hydrothermal alteration zones in a tropical region using satellite remote sensing data: Bau goldfield, Sarawak, Malaysia. Ore Geology Reviews 54, 181-196.

Prestegård, M., 2020. Controls of fault zone structure on synthetic seismic images of the Maghlaq Fault, Malta. The University of Bergen.

Quan, L., Wang, G., Zhang, Y., Hao, F., Xu, R., Zhou, L., Liu, Z., 2022. Early dolomitization and subsequent hydrothermal modification of the middle Permian Qixia

Formation carbonate in the northwest Sichuan Basin. Geoenergy Science and Engineering, 211384.

Ramsay, J.G., 1980. The crack–seal mechanism of rock deformation. Nature 284, 135.

Rao, Z., Li, G., Liu, X., Liu, P., Li, H., Liu, S., Zhu, M., Guo, C., Ni, F., Gong, Z., 2021. Fault Activity in Clay Rock Site Candidate of High Level Radioactive Waste Repository, Tamusu, Inner Mongolia. Minerals 11, 941.

Reilly, J.M., Aharchaou, M., Neelamani, R., 2023. A brief overview of seismic resolution in applied geophysics. The Leading Edge 42, 8-15.

Rotevatn, A., Fossen, H., 2011. Simulating the effect of subseismic fault tails and process zones in a siliciclastic reservoir analogue: Implications for aquifer support and trap definition. Marine and Petroleum Geology 28, 1648-1662.

Rotevatn, A., Fossmark, H.S., Bastesen, E., Thorsheim, E., Torabi, A., 2016. Do deformation bands matter for flow? Insights from permeability measurements and flow simulations in porous carbonate rocks. Petroleum Geoscience 23, 15.

Rowland, J., Sibson, R., 2004. Structural controls on hydrothermal flow in a segmented rift system, Taupo Volcanic Zone, New Zealand. Geofluids 4, 259-283.

Rustichelli, A., Iannace, A., Tondi, E., Di Celma, C., Cilona, A., Giorgioni, M., Parente, M., Girundo, M., Invernizzi, C., 2017. Fault-controlled dolomite bodies as palaeotectonic indicators and geofluid reservoirs: New insights from Gargano Promontory outcrops. Sedimentology 64, 1871-1900.

Saillet, E., Wibberley, C.A., 2010. Evolution of cataclastic faulting in high-porosity sandstone, Bassin du Sud-Est, Provence, France. Journal of Structural Geology 32, 1590-1608.

Salomon, E., Rotevatn, A., Kristensen, T.B., Grundvåg, S.-A., Henstra, G.A., 2021. Microstructure and fluid flow in the vicinity of basin bounding faults in rifts–The Dombjerg Fault, NE Greenland rift system. Journal of Structural Geology 153, 104463.

Salomon, E., Rotevatn, A., Kristensen, T.B., Grundvåg, S.-A., Henstra, G.A., Meckler, A.N., Albert, R., Gerdes, A., 2020. Fault-controlled fluid circulation and diagenesis along basin-bounding fault systems in rifts–insights from the East Greenland rift system. Solid Earth 11, 1987-2013.

Sanderson, D.J., Nixon, C.W., 2015. The use of topology in fracture network characterization. Journal of Structural Geology 72, 55-66.

Sanderson, D.J., Nixon, C.W., 2018. Topology, connectivity and percolation in fracture networks. Journal of Structural Geology 115, 167-177.

Sanderson, D.J., Peacock, D.C.P., Nixon, C.W., Rotevatn, A., 2019. Graph theory and the analysis of fracture networks. Journal of Structural Geology 125, 155-165.

Savage, H.M., Cooke, M.L., 2010. Unlocking the effects of friction on fault damage zones. Journal of Structural Geology 32, 1732-1741.

Schlische, R.W., Young, S.S., Ackermann, R.V., Gupta, A., 1996. Geometry and scaling relations of a population of very small rift-related normal faults. Geology 24, 683-686.

Scholz, C., Cowie, P.A., 1990. Determination of total strain from faulting using slip measurements. Nature 346, 837-839.

Shipton, Z., Cowie, P., 2001. Damage zone and slip-surface evolution over μm to km scales in high-porosity Navajo sandstone, Utah. Journal of Structural Geology 23, 1825-1844.

Shipton, Z.K., Cowie, P.A., 2003. A conceptual model for the origin of fault damage zone structures in high-porosity sandstone. Journal of Structural Geology 25, 333-344.

Shipton, Z.K., Evans, J.P., Dockrill, B., Heath, J., Williams, A., Kirchner, D., Kolesar, P.T., Thomas, D., Benson, S., 2005a. Natural leaking CO2-charged systems as analogs for failed geologic storage reservoirs. Carbon dioxide capture for storage in deep geologic formations, 699-712.

Shipton, Z.K., Evans, J.P., Kirschner, D., Kolesar, P.T., Williams, A.P., Heath, J., 2004. Analysis of CO2 leakage through 'low-permeability'faults from natural reservoirs in the Colorado Plateau, east-central Utah, in: Baines, S.J., Worden, R.H. (Eds.), Geological Storage of Carbon Dioxide. Geological Society, London, Special Publications, pp. 43-58.

Shipton, Z.K., Evans, J.P., Thompson, L.B., 2005b. The geometry and thickness of deformation-band fault core and its influence on sealing characteristics of deformation-band fault zones. AAPG Memoir 85, 181-195.

Simm, R., Bacon, M., 2014. Seismic Amplitude: An interpreter's handbook. Cambridge University Press, Cambridge, UK.

Steefel, C.I., Maher, K., 2009. Fluid-rock interaction: A reactive transport approach. Reviews in mineralogy and geochemistry 70, 485-532.

Stewart, S., 2011. Vertical exaggeration of reflection seismic data in geoscience publications 2006–2010. Marine and Petroleum Geology 28, 959-965.

Sævik, P., Nixon, C., 2017. Inclusion of topological measurements into analytic estimates of effective permeability in fractured media. Water Resources Research 53, 9424-9443.

Tavarnelli, E., Pasqui, V., 2000. Fault growth by segment linkage in seismically active settings: Examples from the Southern Apennines, Italy, and the Coast Ranges, California. Journal of Geodynamics 29, 501-516.

Torabi, A., Alaei, B., Kolyukhin, D., 2017. Analysis of fault scaling relations using fault seismic attributes. Geophysical Prospecting 65, 581-595.

Torabi, A., Berg, S.S., 2011. Scaling of fault attributes: A review. Marine and Petroleum Geology 28, 1444-1460.

Townsend, C., Firth, I., Westerman, R., Kirkevollen, L., Hårde, M., Andersen, T., 1998. Small seismic-scale fault identification and mapping. Geological Society, London, Special Publications 147, 1-25.

Vagle, E.B., 2020. Topology and distribution of deformation bands in normal fault damage zones, Utah, Department of Earth Science. University of Bergen, The University of Bergen, p. 117.

van der Zee, W., Urai, J.L., 2005. Processes of normal fault evolution in a siliciclastic sequence: a case study from Miri, Sarawak, Malaysia. Journal of Structural Geology 27, 2281-2300.

Verhaert, G., Muchez, P., Keppens, E., Sintubin, M., 2009. Fluid Impact and Spatial and Temporal Evolution of Normal Faulting in Limestones. A Case Study in the Burdur-Isparta Region (Sw Turkey). Geologica Belgica 12, 59-73.

Virk, H.S., Singh, B., 1993. Radon Anomalies in Soil-Gas and Groundwater as Earthquake Precursor Phenomena. Tectonophysics 227, 215-224.

Volatili, T., Zambrano, M., Cilona, A., Huisman, B.A.H., Rustichelli, A., Giorgioni, M., Vittori, S., Tondi, E., 2019. From fracture analysis to flow simulations in fractured carbonates: The case study of the Roman Valley Quarry (Majella Mountain, Italy). Marine and Petroleum Geology 100, 95-110.

Walsh, J., Watterson, J., Heath, A., Gillespie, P., Childs, C., 1998. Assessment of the effects of sub-seismic faults on bulk permeabilities of reservoir sequences. Geological Society, London, Special Publications 127, 99-114.

Walsh, J., Watterson, J., Yielding, G., 1991. The importance of small-scale faulting in regional extension. Nature 351, 391-393.

Wibberley, C.A., Gonzalez-Dunia, J., Billon, O., 2017. Faults as barriers or channels to production-related flow: insights from case studies. Petroleum Geoscience 23, 134-147.

Williams, J.N., Toy, V.G., Massiot, C., McNamara, D.D., Wang, T., 2016. Damaged beyond repair? Characterising the damage zone of a fault late in its interseismic cycle, the Alpine Fault, New Zealand. Journal of Structural Geology 90, 76-94.

Wiprut, D., Zoback, M.D., 2000. Fault reactivation and fluid flow along a previously dormant normal fault in the northern North Sea. Geology 28, 595-598.

Yadav, K., Sircar, A., 2020. Geothermal energy provinces in India: A renewable heritage. International Journal of Geoheritage and Parks.

Yoshida, H., Metcalfe, R., Yamamoto, K., Murakami, Y., Hoshii, D., Kanekiyo, A., Naganuma, T., Hayashi, T., 2008. Redox front formation in an uplifting sedimentary rock sequence: An analogue for redox-controlling processes in the geosphere around deep geological repositories for radioactive waste. Applied Geochemistry 23, 2364-2381.

Zhang, Y., Robinson, J., Schaubs, P., 2011. Numerical modeling of structural controls on fluid flow and mineralization. Geoscience Frontiers 2, 449-461.

Zhu, W., Khirevich, S., Patzek, T.W., 2021. Impact of fracture geometry and topology on the connectivity and flow properties of stochastic fracture networks. Water Resources Research 57, e2020WR028652.

# Appendix

Appendix A: A broader classification of damage zones.

Appendix B: Connectivity and network development of carbonate-hosted fault damage zones from western Malta.

A

# Appendix A: A broader classification of damage zones

David C.P. Peacock, Vilde Dimmen, Atle Rotevatn, David J. Sanderson

*Published in Journal of Structural Geology, 102 (2017) 179-192*

http://dx.doi.org/10.1016/j.jsg.2017.08.004

Journal of Structural Geology 102 (2017) 179–192

Contents lists available at ScienceDirect

Journal of Structural Geology

journal homepage: www.elsevier.com/locate/jsg

# A broader classification of damage zones

D.C.P. Peacock [a], [*], V. Dimmen [a], A. Rotevatn [a], D.J. Sanderson [b]

[a] *Department of Earth Science, University of Bergen, Allégaten 41, 5007, Bergen, Norway*
[b] *Engineering and the Environment, University of Southampton, Highfield, Southampton, SO17 1BJ, UK*

ARTICLE INFO

*Article history:*
Received 31 March 2017
Received in revised form
19 July 2017
Accepted 6 August 2017
Available online 9 August 2017

*Keywords:*
Faults
Damage zones
Interaction
Approaching
Intersection

ABSTRACT

Damage zones have previously been classified in terms of their positions at fault tips, walls or areas of linkage, with the latter being described in terms of sub-parallel and synchronously active faults. We broaden the idea of linkage to include structures around the intersections of non-parallel and/or non-synchronous faults. These *interaction* damage zones can be divided into *approaching* damage zones, where the faults kinematically interact but are not physically connected, and *intersection* damage zones, where the faults either abut or cross-cut. The damage zone concept is applied to other settings in which strain or displacement variations are taken up by a range of structures, such as at fault bends. It is recommended that a prefix can be added to a wide range of damage zones, to describe the locations in which they formed, e.g., *approaching*, *intersection* and *fault bend* damage zone. Such interpretations are commonly based on limited knowledge of the 3D geometries of the structures, such as from exposure surfaces, and there may be spatial variations. For example, approaching faults and related damage seen in outcrop may be intersecting elsewhere on the fault planes.

Dilation in intersection damage zones can represent narrow and localised channels for fluid flow, and such dilation can be influenced by post-faulting stress patterns.

© 2017 Elsevier Ltd. All rights reserved.

## 1. Introduction

The initiation, propagation, interaction and build-up of slip along faults creates a volume of deformed wall rocks around a fault surface called a *damage zone* (Cowie and Scholz, 1992; McGrath and Davison, 1995; Caine et al., 1996; Kim et al., 2004; Childs et al., 2009; Choi et al., 2016). The damage zone concept is useful because it relates localised zones of deformation to the structures that formed them. For example, Kim et al. (2004) define *tip*, *wall* and *linking* damage zones based on the location around the segmented faults in which they form (Figs. 1 and 2), while Choi et al. (2016, Fig. 3) define *along-fault*, *around-tip* and *cross-fault* damage zones based on their location around an exposed fault. Fault damage zones generally develop to accommodate strain or displacement variations along, around and between faults. Damage zones are areas of stress concentration and perturbation, within which deformation is concentrated and structures commonly have different frequencies and orientations than in the surrounding areas (e.g., Ishii, 2016), with different fault geometries and displacements (e.g., Scholz and Cowie, 1990). Thus they give useful information about the deformation histories and kinematics of the parent faults (e.g., Bastesen and Rotevatn, 2012; Rotevatn and Bastesen, 2014; Storti et al., 2015). Structures within damage zones also influence fluid flow along, across and around fault zones (e.g., Caine et al., 1996; Billi et al., 2003).

Damage zones generally show increased fracture frequencies and linkage. Fig. 3 shows damage zone around a normal fault zone in Miocene carbonates on Malta, which accommodated less than a metre of displacement (Pedley et al., 1976; Michie et al., 2014; Dimmen, 2016). Deformation, as indicated by branch intensities and connecting node frequencies (e.g., Morley and Nixon, 2016), is concentrated at fault bends and in areas of fault interaction. This deformation will tend to increase as the displacement increases and the fault system evolves. The examples we present are ancient, extinct, “static” faults, but the evolution of such structures can be inferred by observing cross-cutting and abutting relationships within individual fault zones, and by making about a range of different examples (e.g., Kim et al., 2003).

A wide range of structures can occur within damage zones, including: folds (e.g., McGrath and Davison, 1995, Fig. 5); antithetic faults (e.g., Kim et al., 2003, Fig. 5); synthetic faults (e.g., Kim et al., 2003, Fig. 10a); deformation bands (e.g., Fossen and Rotevatn, 2012;

---

[*] Corresponding author.
*E-mail address:* hermangedge@gmail.com (D.C.P. Peacock).

http://dx.doi.org/10.1016/j.jsg.2017.08.004
0191-8141/© 2017 Elsevier Ltd. All rights reserved.

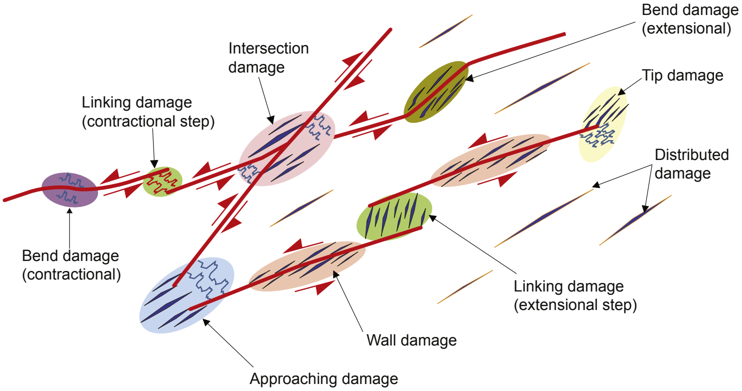

**Fig. 1.** Different types of damage zones, including our terms *approaching* and *intersection* damage zones. These, and the *linking* damage zone of Kim et al. (2004), are types of *interaction* damage zone. *Bend* and *distributed* damage zones, as defined in this paper, are also shown.

Qu and Tveranger, 2016; Rotevatn et al., 2016); veins (e.g., Caine et al., 1996); breccias (e.g., Billi, 2005, Fig. 2); joints (e.g., Mollema and Antonellini, 1999, Fig. 4); and stylolites (e.g., Tondi et al., 2006, Fig. 14). These structures give information about the kinematics, mechanics and history of the damage zones in which they occur.

In this paper, we generalise the Kim et al. (2004) model that deals with segmented faults that are sub-parallel and synchronous (Fig. 1). We describe a new category of *interaction* damage zones, which are created as two faults with any orientation and relative age approach each other and interact kinematically. The intention is not to add confusion through adding more terms, but to broaden usage of damage zones to include structures formed in a wider range of settings. We recommend that a descriptive term (qualifier) be prefixed to *damage zone* to describe the location or origin of the structures. Any classification scheme in geology may have the effect of simplifying a complex and subtle reality, but can still be of use in helping people describe and interpret a range of features. Our scheme probably excludes some damage zone types and includes some ambiguities. We hope, however, that the scheme helps in the understanding of structures that develop within fault networks.

The wider definition of damage zones presented here is important because it includes a greater range of fault relationships, including interaction between any two faults, irrespective of relative orientation or age. This broader usage, along with highlighting the role of post-fault deformation, mineralisation and stresses, is particularly helpful in predicting fluid flow related to fault interaction. For example, such interaction has been shown to control leakage from hydrocarbon reservoirs (e.g., Gartrell et al., 2004; Hermanrud et al., 2014; Simmenes et al., 2016).

## 2. Types of damage zones

Fig. 1 illustrates, schematically, the damage zone types classified by Kim et al. (2004), along with the broader range of damage zone types defined here. We use examples from the Mesozoic sedimentary rocks of Somerset, U.K. (e.g., Whittaker and Green, 1983; Willemse et al., 1997; Peacock and Sanderson, 1999; Peacock et al., 2017), from the Miocene carbonate rocks of Malta (e.g., Michie et al., 2014; Dimmen et al., 2017) and from the literature to illustrate the range of damage zones that can occur. These literature examples include a spread of different lithologies, tectonic settings and scales. Damage zones have been described from carbonate rocks (e.g., Billi et al., 2003; Kim et al., 2003), sandstones (e.g., Shipton and Cowie, 2003; Rotevatn et al., 2007), volcanic rocks (e.g., Hayman and Karson, 2007; Walker et al., 2013), intrusive igneous rocks (e.g., Mitchell and Faulkner, 2009), and metamorphic rocks (e.g., Wibberley and Shimamoto, 2003; Kristensen et al., 2016). Similarly, damage zones have been described in relation to normal (e.g., Shipton and Cowie, 2003), reverse (e.g., McGrath and Davison, 1995) and strike-slip (e.g., Kim et al., 2004) faults. Kim and Sanderson (2006) show that damage zones occur across a wide range of scales, and suggest that well-exposed small-scale damage zones observed in the field can be used to gain useful insights into deformation patterns along and around much larger faults, including those that influence or delimit hydrocarbon fields or plate boundaries.

### 2.1. Tip, wall and linking damage zones

Kim et al. (2004) define three classes of damage zone based on the locations with respect to the faults with which they are related (Figs. 1 and 2):

#### 2.1.1. Tip damage zone

Area of deformation formed in response to stress concentration at a fault tip. Fig. 2(a) shows the tip of a sinistral fault that is in the form of calcite-filled pull-aparts connected by shear fractures. Within the damage zone, a set of stylolites take up contraction in the contractional quadrant of the fault tip, while wing cracks and veins take up extension. Other examples of tip damage zones are shown by Kim and Sanderson (2006, Figs. 4–8) and Rotevatn and Fossen (2011, Fig. 10).

#### 2.1.2. Wall damage zone

Area of deformation resulting from the propagation of faults through rock, or from damage associated with the increase in slip on a fault. Fig. 2(b) shows calcite veins in the walls of a sinistral fault zone. It is possible that the veins were formed as an array prior to linkage to form the fault zone, but it is also possible the veins formed by friction along the fault. Other examples of wall damage zones are shown by Braathen et al. (2009, Fig. 5) and Srivastava et al. (2016, Fig. 4).

#### 2.1.3. Linking damage zone

Area of deformation at a step between two sub-parallel coeval

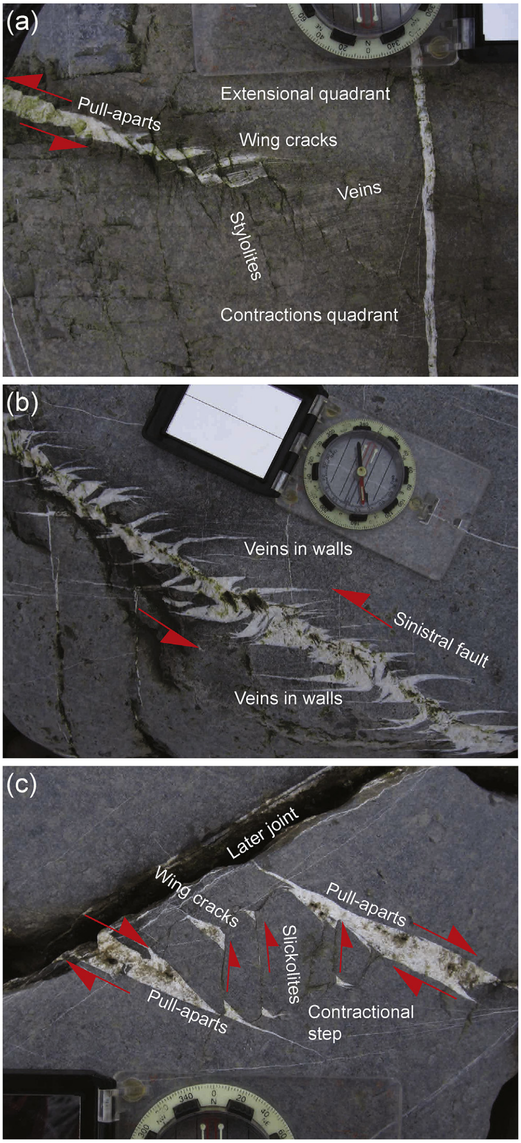

**Fig. 2.** Examples of damage zones from the Liassic limestones of Somerset, UK, using the classification of Kim et al. (2004). (a) *Tip* damage zone. A sinistral fault is marked by calcite-filled pull-aparts. It dies out into a network of stylolites (taking up contraction) and calcite-filled veins and wing cracks (representing extension). (b) *Wall* damage zone. The sinistral fault is marked by calcite mineralisation, with veins representing either wall damage caused by friction along the fault or an initial set of en echelon veins than became linked to form the fault. (c) *Linking* damage zone. Clockwise block rotation, accommodated by slickolites and wing cracks, occur within a contractional step between two dextral faults that are marked by calcite-filled pull-aparts.

faults. Fig. 2(c) shows sinistral slickolites and wing cracks between two stepping dextral faults. The network of slickolites and wing cracks represent strain and rotation in the contractional step between the dextral faults. Other examples of linking damage zones are shown by de Joussineau et al. (2007, Fig. 13) and Fossen and Rotevatn (2016, Figs. 2 and 6). Linking damage zones occur around the tips of interacting faults, potentially leading to ambiguity between tip damage zones and linking damage zones. Tip damage zones should be named where there is no evidence of interaction with other faults, while linking damage zones should be named where there is such evidence.

Whilst these classes are useful, we suggest there are a range of other settings in which fault damage may occur (Table 1).

### 2.2. Interaction damage zones

*Interaction* damage zones are areas of deformation caused by kinematic and/or geometric interaction between any two or more faults (Peacock et al., 2016, 2017). It is a more general term than *linking* damage zone of Kim et al. (2004) because it specifically includes deformation between faults of any orientation and relative age that interact with each other. In addition to the linking damage zones of Kim et al. (2004), interaction damage also includes the following:

#### 2.2.1. Approaching damage zone

The area of deformation related to interaction between two or more faults that do not intersect. Examples of approaching damage zones are shown in Fig. 4. Such approaching faults are kinematically linked (i.e., they influence each other's displacements, as can be recognised on displacement-distance profiles; e.g., Peacock and Sanderson, 1991) but are not geometrically linked (i.e., they are not physically connected at an intersection point), at least not in the plane in which they are observed (Peacock et al., 2017).

#### 2.2.2. Intersection damage zone

The area of deformation around the intersection point (or intersection line) of two or more faults (Fig. 5). The faults are therefore geometrically-linked, although they need not be kinematically-linked. The faults can mutually cross-cut each other (e.g., Fig. 5a; Horsfield, 1980; Watterson et al., 1998; Ferrill et al., 2009), both abut at a point (Fig. 5b), one can abut the other (Fig. 6), or the later fault may displace the older fault. High displacement gradients may occur near the intersection between faults (Fig. 5c), accommodated by the structures in the damage zone.

*Interaction* damage zones therefore include the *linking* damage zones of Kim et al. (2004) as a sub-class that occurs between sub-parallel synchronously active faults (e.g., within relay ramps). Linking damage zones of Kim et al. (2004) could be approaching damage zones if the faults are kinematically-linked but not geometrically-linked (e.g., a stage 2 relay ramp of Peacock and Sanderson, 1991), but would be intersection damage zones if the faults are geometrically-linked (e.g., a stage 3 relay ramp of Peacock and Sanderson, 1991).

Note that some caution is needed in distinguishing between approaching and intersection damage zones because it might be difficult to define the low displacement tip areas of faults (e.g., Pickering et al., 1997). Similarly, apparently unconnected faults may be linked by damage that is below the scale of observation (e.g., Rotevatn and Fossen, 2011). Thus, apparently unconnected faults may actually meet within the network of structures that form the damage zone. Also, faults are three-dimensional structures, so although two approaching faults may not be geometrically-linked on the surface on which they are being observed (e.g., the exposure surface), they may share an intersection line elsewhere in the rock volume. This is discussed in more detail below.

The inclusion of structures between non-parallel and non-

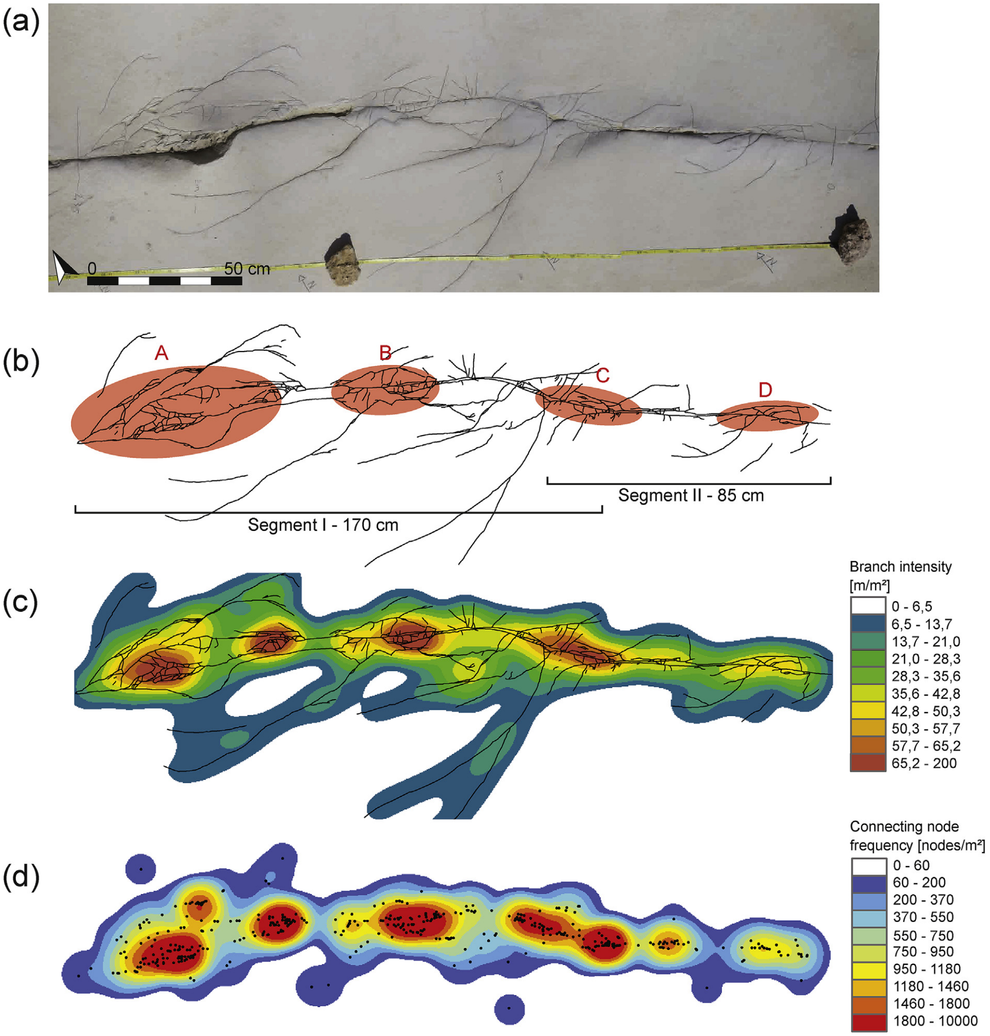

**Fig. 3.** Data for a fault zone and related fractures in Miocene limestones, western Malta (from Dimmen, 2016): The fault zone has a throw of several centimetres. (a) Photomosaic of the fault zone. (b) Map of the fracture network and normal fault zone. The more structurally complex zones are marked in red and labelled A-D. We use the same definition of "complex zone" as used by Dimmen et al. (2017), i.e., a zone in which fracture frequencies are particularly high, and where a wide variation of fracture orientations occurs. (c) Density map, showing the topological parameter "branch intensity", presenting the total branch length per square metre, and hence a measure of the network complexity. (d) Density map showing the topological parameter "connecting node frequency", presenting the number of connecting nodes per square metre, and hence the connectivity of the network.

synchronous faults within the category of *interaction* damage zones broadens the Kim et al. (2004) classification to include a much wider range of structures. For example, a later fault may interact with an earlier fault that represents a mechanical barrier to the propagation of the later fault, and thereby create a damage zone. Fig. 6 shows damage associate with the intersection of the Courthouse Fault and the earlier Moab Fault (Fossen et al., 2005), this damage zone being characterised by a network of deformation bands. Maerten (2000) presents numerical modelling and field data from the Courthouse Rock area (Fig. 6) to illustrate the mechanics of intersecting faults. Maerten (2000) shows that slickenside lineation orientations near fault intersection lines need not be in the direction of the remote maximum shear stress as resolved on the fault plane because of fault interaction, and suggests that care is therefore needed when using standard inverse methods to compute palaeostresses from slickenside data around interacting faults.

Whilst we divide *interaction* damage zones into those that are *linking*, *approaching* and *intersecting*, it may be possible to further sub-divide these damage zones, for example to differentiate between intersecting faults that abut, splay, cross-cut coevally or cross-cut sequentially. Such further sub-classification is, however, likely to add to confusion rather than clarity (e.g., Endersby, 2009),

**Table 1**
Types of damage zone defined here, with examples.

| Damage zone type | | Description | Figure in this paper | Outcrop-scale example | Larger example |
|---|---|---|---|---|---|
| Distributed | | Area of precursory damage spread throughout the rock mass, where deformation is more intense than the region "background" level | 8 | Mollema and Antonellini (1999, Fig. 13) | Ross et al. (2017, Fig. 1) |
| Tip | | Area of deformation because of stress concentration at a fault tip | 2a | McGrath and Davison (1995, Fig. 5) | Kim et al. (2004, Fig. 3) |
| Wall | | Area of deformation resulting from the propagation of a fault through rock, or from damage associated with the increase in slip on a fault | 2b | Srivastava et al. (2016, Fig. 8) | Kim et al. (2004, Fig. 7) |
| Interaction | Linking | Area of deformation at a step between two sub-parallel coeval faults | 2c | Cook et al. (2006, Fig. 2) | Karakhanian et al. (2002, Fig. 2) |
| | Approaching | Area of deformation related to interaction between two or more faults that do not intersect | 4 | Kelly et al. (1998, Fig. 6a) | Mouslopoulou et al. (2007, Fig. 3) |
| | Intersecting | Area of deformation around the intersection point (or intersection line) of two or more faults | 5, 6 | Delogkos et al. (2017, Fig. 1) | Shalaby et al. (2005, Fig. 2) |
| Fault bend | | Area of deformation accommodating deformation along or around a bend on a fault | 7 | Jackson et al. (2006, Fig. 9) | Harris et al. (2002, Fig. 6a) |

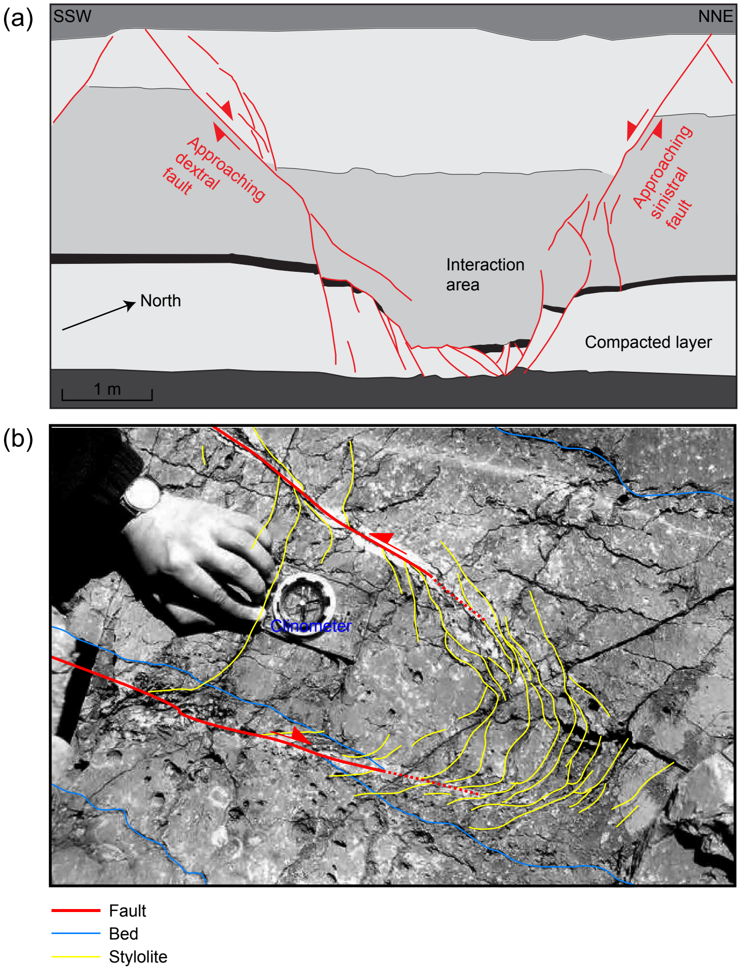

**Fig. 4.** Examples of *approaching* damage zones. (a) Interaction between conjugate normal faults in Eocene turbidites, Myanmar (Morley, 2014, Fig. 13). High displacement gradients along the faults in the interaction area are accommodated by compaction of one of the sandstone beds. Four different sandstone units are illustrated using different grey fills. (b) Stylolites between conjugate thrusts in the Carboniferous Limestone at Tutt Head, Mumbles, UK (Hyett, 1990; Crider and Peacock, 2004, Fig. 6a). The lower thrust has the geometry of a normal fault (i.e., the hanging-wall is displaced downwards) its current orientation.

and we therefore recommend simply that the interacting faults are characterised according to the scheme presented by Peacock et al. (2017), which shows that interacting faults may be characterised using the following criteria: 1) geometry and topology, e.g., the orientations of the faults, and if or how they link to each other; 2) kinematics, i.e., the displacement distributions of the interacting faults and whether the displacement directions are parallel, perpendicular or oblique to the intersection line; 3) displacement and strain in the interaction zone, i.e., whether the interacting faults have the same or opposite displacement directions, and if extension or contraction dominates in the acute bisector between the faults; 4) chronology, i.e., whether the interacting faults are the same or different ages.

The form of damage that occurs will be influenced by the rheology of the host rock (e.g., Windarto et al., 2011) and by the style of interaction. It is possible that the scheme of Peacock et al. (2017) may be used to characterise interaction damage zones, for example to help predict whether extension or contraction will

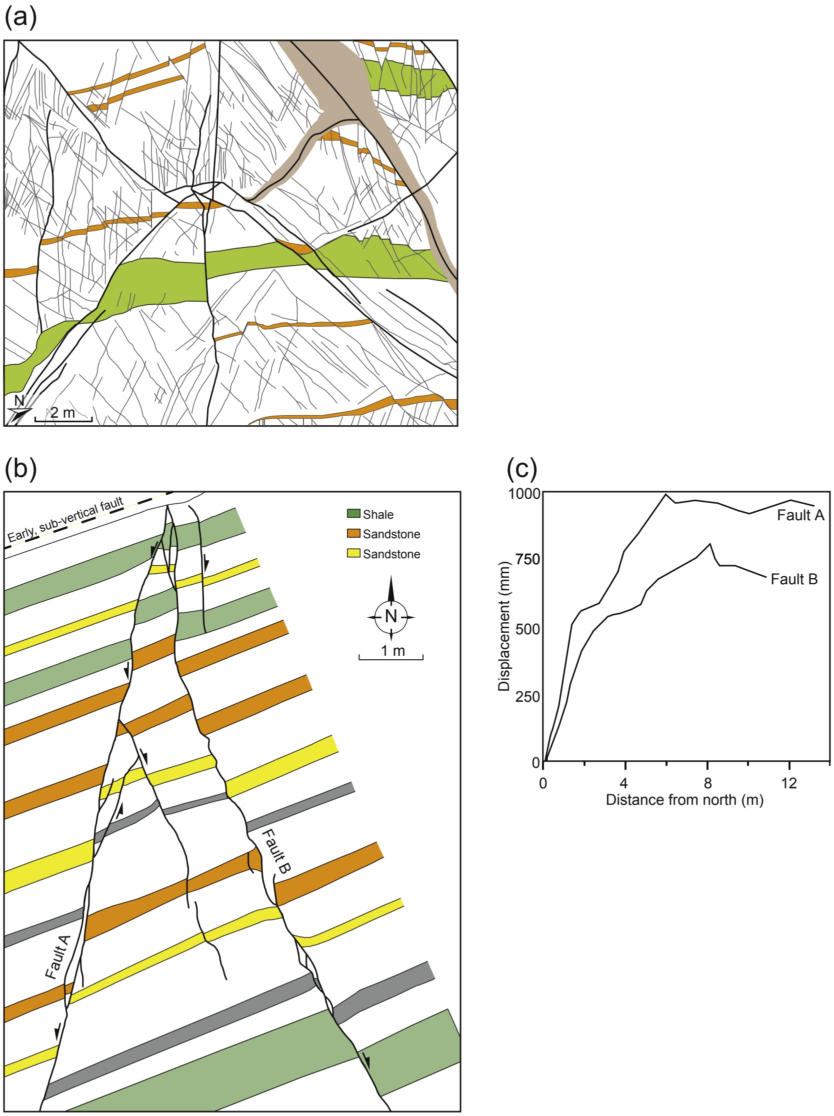

**Fig. 5.** Examples of *intersecting* damage zones where the faults are the same age. (a) Interaction between mutually cross-cutting conjugate normal faults in Eocene turbidites, Myanmar (Morley, 2014, Fig. 20). (b) Conjugate strike-slip faults in sub-vertical Lower Palaeozoic turbidites, Gipsy Point, Kirkcudbright, UK (Peacock, 1991, Fig. 8a). The faults die out at a point in the north of the area. Some representative beds are shown to illustrate displacements. (c) Displacement-distance graph for Fig. 5(b). The faults have high displacement gradients towards their tips at the intersection point.

dominate within a damage zone. In this context, the contraction represented by the compaction of a rock layer in the acute bisector between the two approaching faults illustrated in Fig. 4(a) is predictable. Such contraction is related to the decrease in displacement related to the kinematic interaction between the faults.

### *2.3. Fault bend damage zones*

Faults are rarely perfectly planar, but commonly show bends both along-strike (e.g., Bozkurt and Sözbilir, 2006, Fig. 5) and down-dip (e.g., Fagereng et al., 2014). Fault bends can be broadly divided into two groups. Firstly, a double bend occurs along a relatively short portion of the fault to link two relatively straight portions (Fig. 7a–c). Secondly, the fault may have a single bend away from a relatively long and straight portion of a fault (Fig. 7d), with commonly described examples of these being listric normal faults (e.g., McClay et al., 1991; Rotevatn and Jackson, 2014), upwards splaying thrusts (e.g., Butler, 1982; Bonini et al., 2000; Amos et al., 2007, Fig. 9), and along-strike splays along strike-slip faults (Cunningham et al., 1996; Karakhanian et al., 2002, Fig. 11).

Bends along faults in the displacement direction can be either contractional (Fig. 7a; e.g., Janecke et al., 2010) or extensional (Fig. 7b; e.g., Kurt et al., 2013). Contractional bends create space problems of displacing the wall-rocks around the bends, with fault networks (Fig. 7a), folds or cleavage (e.g., Legg et al., 2007) commonly developed. Extensional bends can create pull-aparts (e.g., Gürbüz and Gürer, 2009; Peacock and Anderson, 2012) or other zones of dilation. Neutral bends and steps occur perpendicular to the displacement direction (Fig. 7c). Commonly described examples of bends along faults perpendicular to the displacement direction include bends along the strike of normal faults (Peacock and Sanderson, 1994) and lateral ramps along thrusts (Boyer and Elliott, 1982). Such bends do not create the space problems typical of extensional and contractional bends.

Note that bends along faults may represent old linkage points (e.g., Peacock and Sanderson, 1991), so fault bend damage zones may have evolved from linking damage zones. It may be difficult to determine whether or not the bend formed by linkage if there is extensive damage.

### *2.4. Distributed damage zones*

The term *distributed damage zone* has been used in the seismology (e.g., Lyakhovsky et al., 1997; Finzi et al., 2009) and rock mechanics (e.g., Le and Bažant, 2014) literature to refer to the system of fractures that develop as a precursor to an earthquake event or to fault development (e.g., Reches and Lockner, 1994). We suggest that *distributed* damage zone can also be used in the discipline of structural geology to refer to an area or region in which precursory fault damage is spread throughout the rock mass and where deformation is more intense (i.e., higher fracture frequencies and greater strain) than the region background level (Fig. 8). For example, Mollema and Antonellini (1999, Fig. 13) show the development of localised joints that evolve into a through-going involving the rotation and disruption of the joint-bound blocks (also see Fig. 8b–e). At a larger scale, extension in a region may initiate as widely distributed normal faults, with the deformation becoming localised on the largest structures (e.g., Hardacre and Cowie, 2003; Soliva and Schultz, 2008).

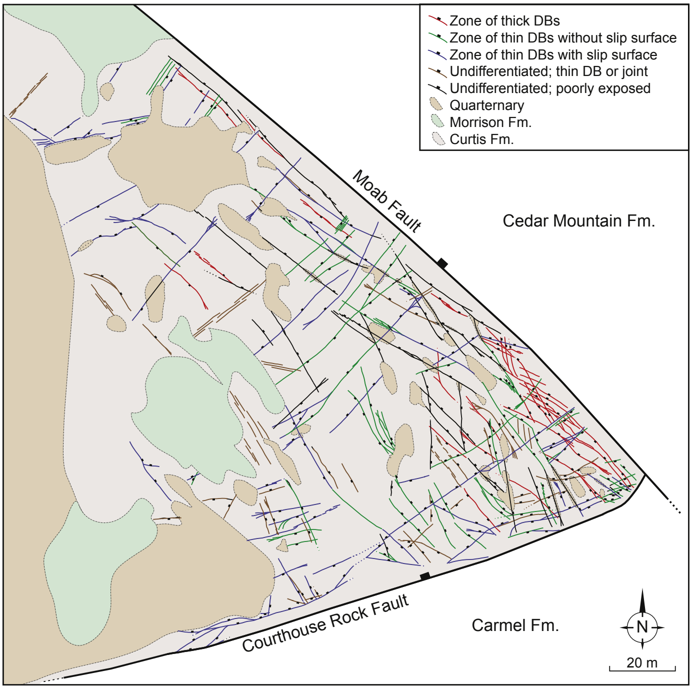

**Fig. 6.** Example of an *intersecting* damage zones where the faults are different ages. The intersection damage zone between the older Moab Fault and the younger Courthouse Rock Fault is dominated by a network of deformation bands in the Jurassic Entrada Sandstone (Fossen et al., 2005, Fig. 10; Johansen et al., 2005, Fig. 4).

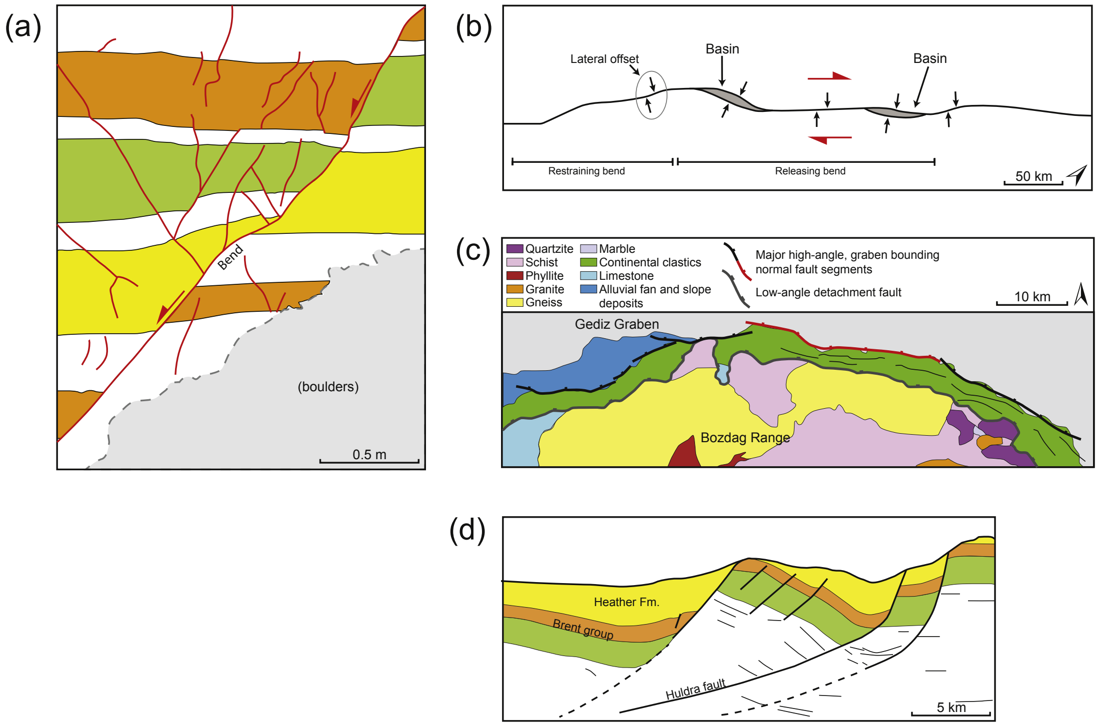

**Fig. 7.** Examples of *fault bend* damage zones. (a) Contractional bend along a normal fault in the Cretaceous Chalk at Flamborough Head, Yorkshire, UK (Peacock and Zhang, 1994, Fig. 5b). A network of synthetic and antithetic faults in the hanging-wall accommodate displacement around the fault bend. (b) Large-scale extensional bends along the dextral strike-slip Bocono fault zone of Venezuela, accommodated by pull-apart basins, with the lateral offset representing the amount of displacement on the fault system (Mann, 2007, Fig. 35). (c) Neutral bends and steps along normal faults in map view, from the Gediz Graben of western Turkey (Kent et al., 2016, Fig. 2). (d) Synthetic faults and rollover in the hanging-wall of a listric normal fault, from the Huldra-Brage area of the northern North Sea (Fossen et al., 2003, Fig. 18b).

## 3. Discussion

### 3.1. Damage zones in three-dimensions

When analysed in the field, interpretation of faults and damage zones has to be made on the exposure surface. The field examples we present (e.g., Figs. 2–8) are exposed on gently- or steeply-dipping rock exposures. Usually, inferences have to be made about the 3D geometries of the faults, and this can be problematic. For example, various models have been published for the three-dimensional geometries of relay ramps and the stepping normal faults between which they occur (Fig. 9). Larsen (1988) suggests that relay ramps develop between stepping listric normal faults that curve off a common detachment. Peacock and Sanderson (1991) suggest the stepping normal faults can be more planar and may be connected or unconnected at depth. Huggins et al. (1995) suggest the stepping normal faults may splay upwards off a common fault with a similar displacement direction and orientation. Freitag et al. (in press) show that normal faults can be disconnected and have relatively large displacements at depth, but connect upwards where displacements are lower. These different models suggest that an individual exposure surface cannot be used to infer the 3D geometries of a pair of stepping normal faults or of the damage within relay ramps between them. For example, an approaching damage zone identified at a field locality (e.g., Fig. 9) *may* be an intersecting damage zone elsewhere on the fault planes (Fig. 10). Such a damage zone must be referred to as an approaching damage zone because it cannot be determined what happens elsewhere.

Some inferences can be made, however, about the likely 3D geometries of faults and damage zones based on analysis of a series of exposed fault systems. For example, Peacock and Sanderson (1991, 1994) use different field examples of relay ramps to develop a four-stage evolutionary model. Similarly, Kim et al. (2003, 2004) show how damage zones may vary around a fault in 3D based on observations and interpretations of a range of examples exposed on gently- and steeply-dipping exposure surfaces. When considering the evolution of faults and damage zones based on field observations, inferences have to be made based on abutting and cross-cutting relationships (e.g., Peacock et al., 2017) and upon interpreting different examples as being at different evolutionary stages. Analogue models can also be used to show how damage zones may evolve (e.g., Cembrano et al., 2005, Fig. 11).

Opportunities to analyse faults, and therefore damage zones, in 3D is commonly limited to mines or sequential opencast mine faces (e.g., Barnett et al., 1987), and to 3D seismic data (e.g., Freitag et al., in press), although many of the sort of structures typical in damage zones would not be detectable on seismic data.

### 3.2. Fault growth and scaling

Damage will tend to be moved from on location around a fault to

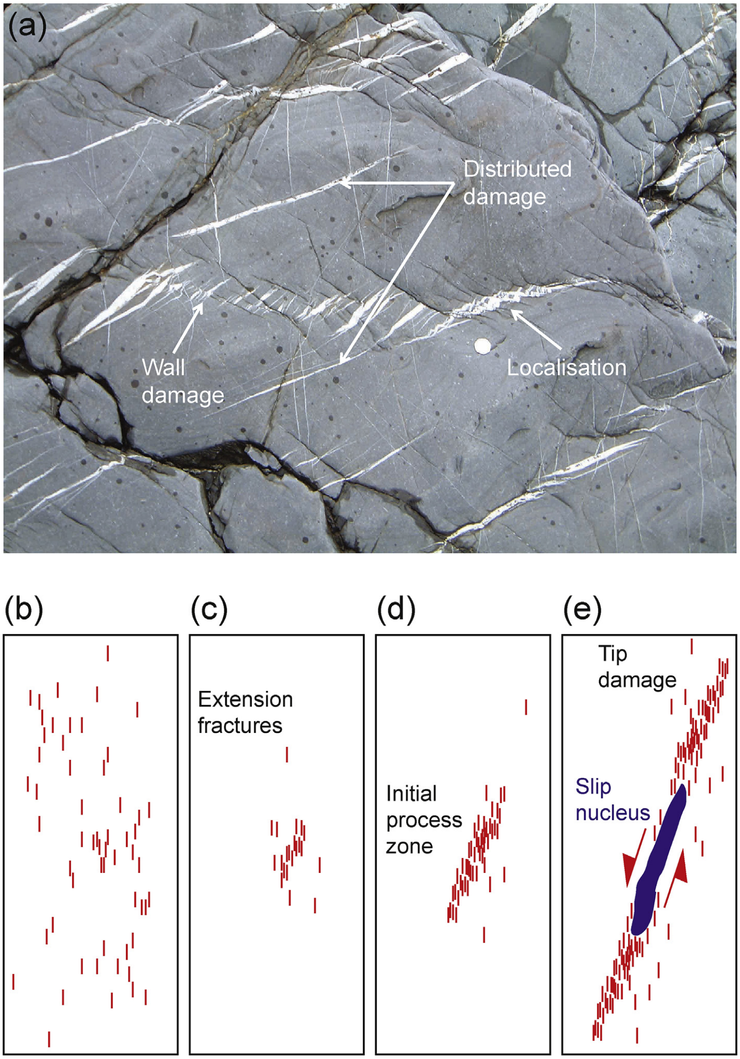

**Fig. 8.** Examples of *distributed* damage zones. (a) Veins in Carboniferous sandstones at Crackington Haven, Cornwall. Some localisation of the deformation has occurred in insipient fault zones, as marked by en echelon veins linked by stylolites. More isolated veins represent distributed damage. A thinner set of veins at a high angle to those highlighted also appear to represent distributed damage. (b)–(e) Four-stage model for the localisation of deformation, from distributed damage (Fig. 8b) to a fault with a slip nucleus and tip damage (Fig. 8e). From Reches and Lockner (1994). Red lines show the fractures active during that evolutionary stage. We suggest that the example presented in Fig. 8(a) has evolved by the stages shown in Fig. 8(b)–(e).

another location as displacement increases, so the origins of the damage may be obscured. For example, structures initially developed at the tip of a fault will occur in the wall of that fault as to propagates, and may be displaced around a fault bend as fault growth continues. Structures at a particular location may therefore have various origins, e.g., having components of tip-, wall- and bend-damage zones. Similarly, different damage zone types may merge as displacement continues to increase.

Faults have been shown to have scale-invariant geometries (e.g., Tchalenko, 1970), with damage zones occurring at a wide range of scales (Kim and Sanderson, 2006). The damage zones classified in this paper also probably occur at a wide range of scales. The ambiguities caused by the movement and merger of damage zones as displacement continues is, however, likely to increase for faults with larger displacements.

Faults typical grow through multiple seismic slip events (e.g., Sibson, 1989). Various papers have attempted to link damage zones to seismic events (e.g., Dor et al., 2009; Gratier et al., 2013; Smeraglia et al., 2016). Whilst it may be possible to use information about the different types of damage zones described here to gain insights into earthquake events, this is beyond the scope of this paper.

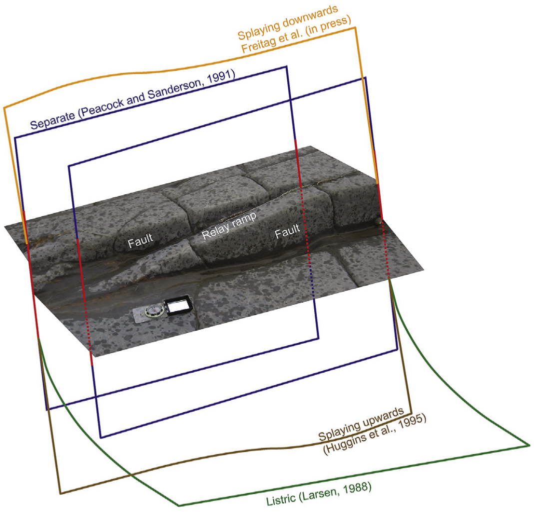

**Fig. 9.** Photograph of a relay ramp exposed on a Liassic limestone bedding plane at Kilve, Somerset, UK (e.g., Peacock and Sanderson, 1994). Four different models of the extrapolation of the three-dimensional geometries of the faults are shown. Larsen (1988) predicts listric faults connected at depth, Peacock and Sanderson (1991) suggests the faults may have originally been separate, Huggins et al. (1995) predicts the faults splay off a single fault at depth, while the model of Freitag et al. (in press) suggests that the fault could merge upwards. This illustrates the difficulties in predicting three-dimensional geometries and connectivity of faults based on an exposure.

### 3.3. Fault reactivation and damage zones

Some damage zones can be created or enhanced by fault reactivation. For example, relay ramps can be modified if the bounding normal faults are reactivated as reverse faults (e.g., Barton et al., 1998) or as strike-slip (e.g., Zampieri and Massironi, 2007) faults. Fig. 11 shows a schematic model for a transfer between stepping normal faults in Liassic sedimentary rocks at East Quantoxhead, Somerset, UK. The stepping normal faults were reactivated in dextral transpression, modifying the transfer zone between them and creating a network of strike-slip faults (Kelly et al., 1999).

Such reactivation may be important in the development of damage zones in rift systems subjected to multiple phases of deformation. For example, Henza et al. (2011) show analogue models and natural examples of normal fault systems that developed with one extension direction that became linked when subjected to a different extension direction. Similarly, Henstra et al. (2015, Fig. 9) show the development of networks of relatively small faults developed in area of interaction between relatively large faults subjected to a series of different extension directions on the Norwegian continental shelf. Similar structures are also illustrated by Giba et al. (2012).

### 3.4. Post-faulting mineralisation and fluid flow

Damage zones are *generally* areas of increased fracture frequency and linkage (Fig. 3). Such concentrations of fractures tend to be fluid flow conduits if the fractures are open (e.g., Berkowitz, 1995; Davatzes and Aydin, 2003; Walker et al., 2013; Rotevatn and Bastesen, 2014; Dimmen et al., 2017). Relay ramps and the linking damage zones between normal faults that step in map view have been shown to control fluid flow (e.g., Fossen and Rotevatn, 2016). Similarly, column heights in hydrocarbon fields can be controlled by fault intersections (e.g., Gartrell et al., 2004; Hermanrud et al., 2014). We propose that interaction damage zones between faults (e.g., Fig. 3), especially dilational structures, may control fluid migration. Fracturing generally involves dilation (e.g., Sibson et al., 1975), so there will be a tendency for enhanced secondary porosity within damage zones, unless they are dominated by such compactional structures as deformation bands (e.g., Fossen and Rotevatn, 2012) or stylolites (e.g., Ehrenberg, 2006).

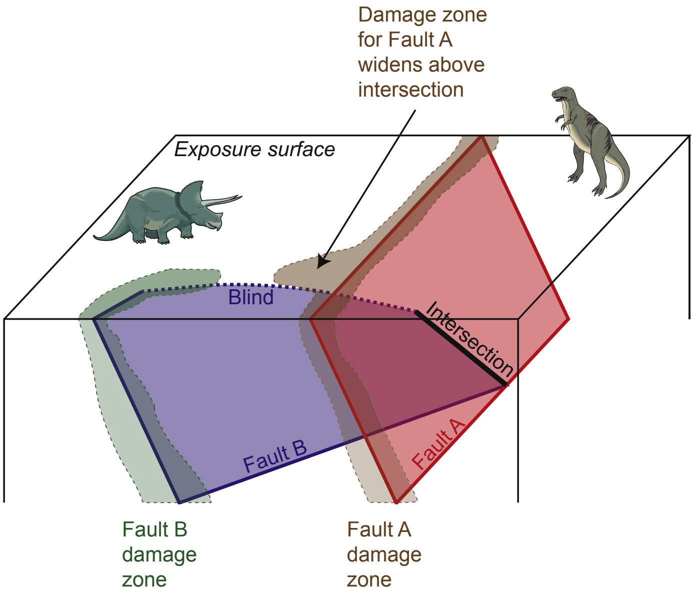

**Fig. 10.** Schematic diagram to show that the width of a wall damage zone may be influenced by interaction with a blind fault. Faults A and B intersect at depth but are approaching on the exposure surface. Interaction between the faults widens the damage zone of Fault A above the intersection line.

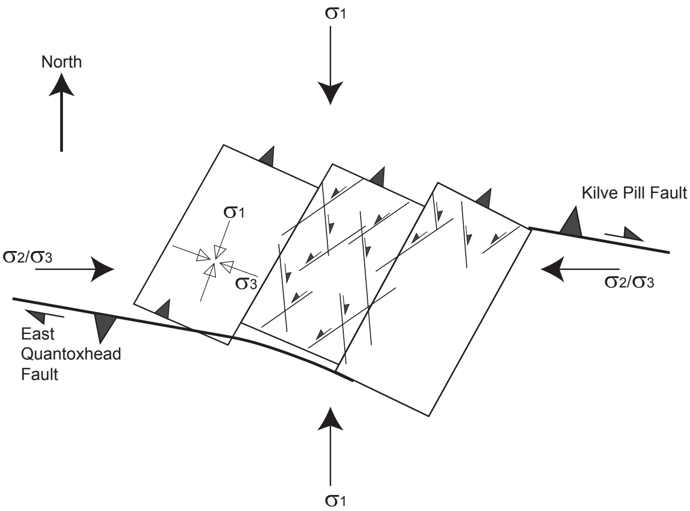

**Fig. 11.** Schematic diagram to illustrate a model for the formation of the strike-slip network in the step between the East Quantoxhead and Kilve Pill faults in the Liassic sedimentary rocks of Somerset, UK, as an example of a damage zone related to fault reactivation (modified from Kelly et al., 1999, Fig. 11). A transfer zone developed between the south-dipping East Quantoxhead Fault and the north-dipping Kilve Pill Fault during Mesozoic extension. These faults were reverse-reactivated during Tertiary contraction. A component of dextral transpression occurred, causing the transfer zone to become a contractional step, in which stress perturbation occurred and a network of strike-slip faults developed. Shortening was accommodated by the formation of thrusts at the southern end of the blocks. Unfilled arrows show the local stress axes, and filled arrows show the "regional" stress axes.

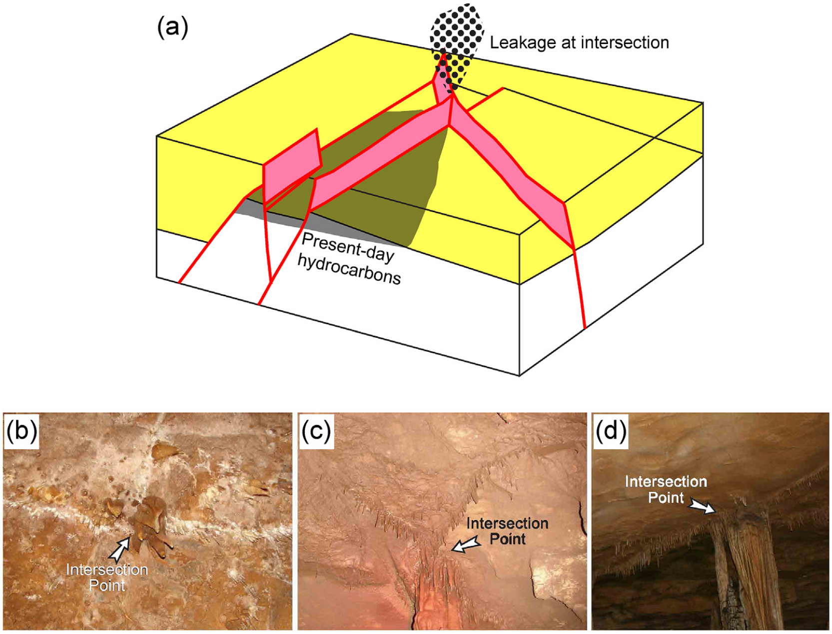

**Fig. 12.** Evidence for fluid flow at fault intersections. (a) Example of a hydrocarbon field with evidence of column height controlled by an interaction damage zone (Gartrell et al., 2004, Fig. 9). (b) to (d) Stalactites at fault intersections exposed in the roofs of caves, indicating enhanced fluid flow at the intersections (Kim and Sanderson, 2010).

Dilation and enhanced secondary porosity would, however, tend to be especially increased in such settings as extensional steps between, or extensional bends along, faults (e.g., Fig. 7b; Sibson, 1987). Characterising such intersections in the way proposed by

Peacock et al. (2017) will help predict which fault intersections may control column heights.

Understanding of the likely deformation with damage zones caused by particular fault patterns will help prediction of which structures are likely to have developed, e.g., in a sub-surface example based on seismic interpretation. For example, knowledge of typical damage and strain distributions between and around field examples of approaching conjugate strike-slip faults will give insights into likely structures and possible permeabilities in remotely-sensed examples.

Stress perturbation may occur within damage zones (e.g., Kattenhorn et al., 2000; Tamagawa and Pollard, 2008), and this may create a wider range of fracture orientations and greater connectivity (Fig. 3). For any given present-day stress field, therefore, there is more chance that some of the fractures are optimally orientated to be open in that stress field. Also, stresses can be higher within damage zones (e.g., Crider and Pollard, 1998; Imber et al., 2004). Faults can influence the orientations of stresses after faulting has ceased, for example with post-fault joints following perturbed stress trajectories (e.g., Bourne and Willemse, 2001; Peacock, 2001).

Syn- or post-deformation mineralisation may, however reduce porosity within damage zones (e.g., Sibson, 1987; Kristensen et al., 2016), and this may be of economic significance. For example, Sakran et al. (2009) illustrate gold mineralisation in the damage zone of an extensional fault bend.

Figure 12 shows a fault system that was active until the Miocene but that shows gas chimneys that indicate that it is currently controlling fluid migration (Gartrell et al., 2004). It is possible that the relationship between *in situ* stresses and the fault are enabling this migration. Person et al. (2012) illustrate how fault intersections can control the migration of hydrothermal fluids, while Jung et al. (2014, Fig. 2) illustrate that fault intersections can control $CO_2$ migration.

## 4. Conclusions

*Tip*, *wall*, and *linking* damage zones have been defined by Kim et al. (2004) and are useful in describing the distribution of damage around segmented faults. In this paper we define a new class of *interaction* damage zones that accommodate displacement variations along, and strain between, two faults of any relative orientation, displacement and age. These are sub-divided into *approaching* damage zones, where the faults show kinematic linkage but not geometric linkage, and *intersection* damage zones, where the faults are geometrically-linked. Interaction damage zones would incorporate the linking damage zones of Kim et al. (2004), where the interacting faults are sub-parallel and synchronous. Extending the definition of damage zones, it is also possible to give other categories based on the location at which they form, including *fault bend* and *distributed* damage zones. We therefore suggest that a descriptive prefix be added to *damage zone* to describe the origin or location at which it formed.

Fault zones and related damage are commonly analysed on outcrop surfaces, from which it is often difficult to make inferences about the 3D geometry. The definition of damage zone type for a particular example will therefore apply to that outcrop surface only. For example, approaching faults observed on an outcrop surface may intersect elsewhere within the rock mass. Inferences about the 3D geometries of faults and their damage zones, and about their evolution, can, however, be made by analysing a range of examples (e.g., Kim et al., 2004).

Improved characterisation of fault development and interaction may help make predictions about the structures present in damage zones, which may therefore help understand fluid migration and the likelihood of seal breach. Dilation in damage zones can represent narrow and localised channels for fluid flow within a reservoir. Care is needed, however, because post-fault stresses and mineralisation can influence permeability, so post-faulting deformation, fluid flow and *in situ* stresses must be considered when making predictions about reservoir and seal behaviour.

## Acknowledgements

Andrea Billi and Rich Walker are thanked for their helpful reviews. Casey Nixon is thanked for useful discussions.

## References

Amos, C.B., Burbank, D.W., Nobes, D.C., Read, S.A.L., 2007. Geomorphic constraints on listric thrust faulting: implications for active deformation in the Mackenzie Basin, South Island, New Zealand. J. Geophys. Res. 112, B03S11. http://dx.doi.org/10.1029/2006JB004291.

Barnett, J.A.M., Mortimer, J., Rippon, J.H., Walsh, J.J., Watterson, J., 1987. Displacement geometry in the volume containing a single normal fault. Am. Assoc. Pet. Geol. Bull. 71, 925–937.

Barton, C.M., Evans, D.J., Bristow, C.R., Freshney, E.C., Kirby, G.A., 1998. Reactivation of relay ramps and structural evolution of the mere Fault and wardour monocline, northern Wessex Basin. Geol. Mag. 135, 383–395.

Bastesen, E., Rotevatn, A., 2012. Evolution and structural style of relay zones in layered limestone–shale sequences: insights from the Hammam Faraun Fault Block, Suez rift, Egypt. J. Geol. Soc. 169, 477–488.

Berkowitz, B., 1995. Analysis of fracture network connectivity using percolation theory. Math. Geol. 27, 467–483.

Billi, A., 2005. Grain size distribution and thickness of breccia and gouge zones from thin (<1 m) strike-slip fault cores in limestone. J. Struct. Geol. 27, 1823–1837.

Billi, A., Salvini, F., Storti, F., 2003. The damage zone-fault core transition in carbonate rocks: implications for fault growth, structure and permeability. J. Struct. Geol. 25, 1779–1794.

Bonini, M., Sokoutis, D., Mulugeta, G., Katrivanos, E., 2000. Modelling hanging wall accommodation above rigid thrust ramps. J. Struct. Geol. 22, 1165–1179.

Bourne, S.J., Willemse, E.J.M., 2001. Elastic stress control on the pattern of tensile fracturing around a small fault network at Nash Point. J. Struct. Geol. 23, 1753–1770.

Boyer, S.E., Elliott, D., 1982. Thrust systems. Am. Assoc. Pet. Geol. Bull. 66, 1196–1230.

Bozkurt, E., Sözbilir, H., 2006. Evolution of the large-scale active Manisa fault, southwest Turkey: implications on fault development and regional tectonics. Geodin. Acta 19, 427–453.

Braathen, A., Tveranger, J., Fossen, H., Skar, T., Cardozo, N., Semshaug, S.E., Bastesen, E., Sverdrup, E., 2009. Fault facies and its application to sandstone reservoir. Am. Assoc. Pet. Geol. Bull. 93, 891–917.

Butler, R.W.H., 1982. Terminology of structures in thrust belts. J. Struct. Geol. 4, 239–245.

Caine, J.S., Evans, J.P., Forster, C.B., 1996. Fault zone architecture and permeability structure. Geology 24, 1025–1028.

Cembrano, J., González, G., Arancibia, G., Ahumada, I., Olivares, V., Herrera, V., 2005. Fault zone development and strain partitioning in an extensional strike-slip duplex: a case study from the Mesozoic Atacama fault system, Northern Chile. Tectonophysics 400, 105–125.

Childs, C., Manzocchi, T., Walsh, J.J., Bonson, C.G., Nicol, A., Schöpfer, M.P.J., 2009. A geometric model of fault zone and fault rock thickness variations. J. Struct. Geol. 31, 117–127.

Choi, J.H., Edwards, P., Ko, K., Kim, Y.S., 2016. Definition and classification of fault damage zones: a review and a new methodological approach. Earth-Sci. Rev. 152, 70–87.

Cook, J.E., Dunne, W.M., Onasch, C.M., 2006. Development of a dilatant damage zone along a thrust relay in a low-porosity quartz arenite. J. Struct. Geol. 28, 776–792.

Cowie, P.A., Scholz, C.H., 1992. Growth of faults by accumulation of seismic slip. J. Geophys. Res. 97, 11085–11095.

Crider, J.G., Peacock, D.C.P., 2004. Initiation of brittle faults in the upper crust: a review of field observations. J. Struct. Geol. 26, 691–707.

Crider, J.G., Pollard, D.D., 1998. Fault linkage: three-dimensional mechanical interaction between echelon normal faults. J. Geophys. Res. 103, 24373–24391.

Cunningham, W.D., Windley, B.F., Dorjnamjaa, D., Badamgarov, J., Saandar, M., 1996. Late cenozoic transpression in southwestern Mongolia and the Gobi Altai-Tien Shan connection. Earth Planet. Sci. Lett. 140, 67–81.

de Joussineau, G., Mutlu, O., Aydin, A., Pollard, D.D., 2007. Characterization of strike-slip fault-splay relationships in sandstone. J. Struct. Geol. 29, 1831–1842.

Davatzes, N.C., Aydin, A., 2003. Overprinting faulting mechanisms in high porosity sandstones of SE Utah. J. Struct. Geol. 25, 1795–1813.

Delogkos, E., Childs, C., Manzocchi, T., Walsh, J.J., Pavlides, S., 2017. The role of bed-parallel slip in the development of complex normal fault zones. J. Struct. Geol. 97, 199–211.

Dimmen, V., 2016. Structural Controls on Fluid Flow in Carbonate Rocks: Quantitative Insights from the Maltese Islands. MSc thesis. University of Bergen.

Dimmen, V., Rotevatn, A., Nixon, C.W., Peacock, D.C.P., Nærland, K., 2017. Quantifying structural controls on fluid flow: insights from carbonate-hosted fault damage zones on the Maltese Islands. J. Struct. Geol. 101, 43–57.

Dor, O., Chester, J.S., Ben-Zion, Y., Brune, J.N., Rockwell, T.K., 2009. Characterization of damage in sandstones along the Mojave Section of the San Andreas Fault: implications for the shallow extent of damage generation. Pure Appl. Geophys. 166, 1747–1773.

Ehrenberg, S.N., 2006. Porosity destruction in carbonate platforms. J. Pet. Geol. 29, 41–52.

Endersby, J., 2009. Lumpers and splitters: Darwin, Hooker, and the search for order. Science 326, 1496–1499.

Fagereng, Å., Smith, Z., Rowe, C.D., Makhubu, B., Sylvester, F.Y.G., 2014. Stress, strain, and fault behavior at a thrust ramp: insights from the Naukluft thrust, Namibia. J. Struct. Geol. 58, 95–107.

Ferrill, D.A., Morris, A.P., McGinnis, R.N., 2009. Crossing conjugate normal faults in field exposures and seismic data. Am. Assoc. Pet. Geol. Bull. 93, 1471–1488.

Finzi, Y., Hearn, E.H., Ben-Zion, Y., Lyakhovsky, V., 2009. Structural properties and deformation patterns of evolving strike-slip faults: numerical simulations incorporating damage rheology. Pure Appl. Geophys. 166, 1537–1573.

Fossen, H., Rotevatn, A., 2012. Characterization of deformation bands associated with normal and reverse stress states in the Navajo Sandstone, Utah: discussion. Am. Assoc. Pet. Geol. Bull. 96, 869–876.

Fossen, H., Rotevatn, A., 2016. Fault linkage and relay structures in extensional settings - a review. Earth-Sci. Rev. 154, 14–28.

Fossen, H., Hesthammer, J., Johansen, T.E.S., Sygnabere, T.O., 2003. Structural geology of the Huldra Field, northern North Sea – a major tilted fault block at the eastern edge of the Horda Platform. Mar. Pet. Geol. 20, 1105–1118.

Fossen, H., Johansen, T.E.S., Hesthammer, J., Rotevatn, A., 2005. Fault interaction in porous sandstone and implications for reservoir management; examples from southern Utah. Am. Assoc. Pet. Geol. Bull. 89, 1593–1606.

Freitag, U.A., Sanderson, D.J., Lonergan, L., Bevan, T.G., 2017. Comparison of upwards splaying and upwards merging segmented normal growth faults. J. Struct. Geol. 100, 1–11.

Gartrell, A., Zhang, Y., Lisk, M., Dewhurst, D., 2004. Fault intersections as critical hydrocarbon leakage zones: integrated field study and numerical modelling of an example from the Timor Sea, Australia. Mar. Pet. Geol. 21, 1165–1179.

Giba, M., Walsh, J.J., Nicol, A., 2012. Segmentation and growth of an obliquely reactivated normal fault. J. Struct. Geol. 39, 253–267.

Gratier, J.P., Thouvenot, F., Jenatton, L., Tourette, A., Doan, M.L., Renard, F., 2013. Geological control of the partitioning between seismic and aseismic sliding behaviours in active faults: evidence from the Western Alps, France. Tectonophysics 600, 226–242.

Gürbüz, A., Gürer, Ö.F., 2009. Middle Pleistocene extinction process of pull-apart basins along the North Anatolian fault zone. Phys. Earth Planet. Inter. 173, 177–180.

Hardacre, K.M., Cowie, P.A., 2003. Controls on strain localization in a two-dimensional elastoplastic layer: insights into size-frequency scaling of extensional fault populations. J. Geophys. Res. 108 http://dx.doi.org/10.1029/2001JB001712.

Harris, L.B., Koyi, H.A., Fossen, H., 2002. Mechanisms for folding of high-grade rocks in extensional tectonic settings. Earth-Sci. Rev. 59, 163–210.

Hayman, N.W., Karson, J.A., 2007. Faults and damage zones in fast-spread crust exposed on the north wall of the Hess Deep Rift: conduits and seals in seafloor hydrothermal systems. Geochem. Geophys. Geosyst. 8 http://dx.doi.org/10.1029/2007GC001623.

Henstra, G.A., Rotevatn, A., Gawthorpe, R.L., Ravnås, R., 2015. Evolution of a major segmented normal fault during multiphase rifting: the origin of plan-view zigzag geometry. J. Struct. Geol. 74, 45–63.

Henza, A.A., Withjack, M.O., Schlische, R.W., 2011. How do the properties of a pre-existing normal-fault population influence fault development during a subsequent phase of extension? J. Struct. Geol. 33, 1312–1324.

Hermanrud, C., Halkjelsvik, M.E., Kristiansen, K., Bernal, A., Strömbäck, A.C., 2014. Petroleum column-height controls in the western Hammerfest Basin, Barents Sea. Pet. Geosci. 20, 227–240.

Horsfield, W.T., 1980. Contemporaneous movement along crossing conjugate normal faults. J. Struct. Geol. 2, 305–310.

Huggins, P., Watterson, J., Walsh, J.J., Childs, C., 1995. Relay zone geometry and displacement transfer between normal faults recorded in coal-mine plans. J. Struct. Geol. 17, 1741–1755.

Hyett, A.J., 1990. Deformation around a thrust tip in carboniferous limestone at Tutt Head, near Swansea, south Wales. J. Struct. Geol. 12, 47–58.

Imber, J., Tuckwell, G.W., Childs, C., Walsh, J.J., Manzocchi, T., Heath, A.E., Strand, J., 2004. Three-dimensional distinct element modelling of relay growth and breaching along normal faults. J. Struct. Geol. 26, 1897–1911.

Ishii, E., 2016. Far-field stress dependency of the failure mode of damage-zone fractures in fault zones: results from laboratory tests and field observations of siliceous mudstone. J. Geophys. Res. 121, 70–91.

Jackson, C.A.L., Gawthorpe, R.L., Sharp, I.R., 2006. Style and sequence of deformation during extensional fault-propagation folding: examples from the Hammam Faraun and El-Qaa fault blocks, Suez Rift, Egypt. J. Struct. Geol. 28, 519–535.

Janecke, S.U., Dorsey, R.J., Forand, D., Steely, A.N., Kirby, S.M., Lutz, A.T., Housen, B.A., Belgarde, B., Langenheim, V.E., Rittenour, T.M., 2010. High Geologic Slip Rates since Early Pleistocene Initiation of the San Jacinto and San Felipe Fault Zones in the San Andreas Fault System: Southern California, USA. Geological Society of America, Special Paper 475, p. 48.

Johansen, T.E.S., Fossen, H., Kluge, R., 2005. The impact of syn-faulting porosity reduction on damage zone architecture in porous sandstone: an outcrop example from the Moab Fault, Utah. J. Struct. Geol. 27, 1469–1485.

Jung, N.H., Han, W.S., Watson, Z.T., Graham, J.P., Kim, K.Y., 2014. Fault-controlled $CO_2$ leakage from natural reservoirs in the Colorado Plateau, East-Central Utah. Earth Planet. Sci. Lett. 403, 358–367.

Karakhanian, A., Djrbashian, R., Trifonov, V., Philip, H., Arakelian, S., Avagian, A., 2002. Holocene-historical volcanism and active faults as natural risk factors for Armenia and adjacent countries. J. Volcanol. Geotherm. Res. 113, 319–344.

Kattenhorn, S.A., Aydin, A., Pollard, D.D., 2000. Joints at high angles to normal fault strike: an explanation using 3-D numerical models of fault-perturbed stress fields. J. Struct. Geol. 22, 1–23.

Kelly, P.G., Sanderson, D.J., Peacock, D.C.P., 1998. Damage, linkage and evolution of strike-slip fault zones. J. Struct. Geol. 20, 1477–1493.

Kelly, P.G., McGurk, A., Peacock, D.C.P., Sanderson, D.J., 1999. Reactivated normal faults in the Mesozoic of the Somerset coast, and the role of fault scale in reactivation. J. Struct. Geol. 21, 493–509.

Kent, E., Boulton, S.J., Stewart, I.S., Whittaker, A.C., Alçiçek, M.C., 2016. Geomorphic and geological constraints on the active normal faulting of the Gediz (Alasehir) Graben, Western Turkey. J. Geol. Soc. Lond. 173, 666–678.

Kim, Y.S., Sanderson, D.J., 2006. Structural similarity and variety at the tips in a wide range of strike-slip faults: a review. Terra Nova 18, 330–344.

Kim, Y.S., Sanderson, D.J., 2010. Inferred fluid flow through fault damage zones based on the observation of stalactites in carbonate caves. J. Struct. Geol. 32, 1305–1316.

Kim, Y.S., Peacock, D.C.P., Sanderson, D.J., 2003. Strike-slip faults and damage zones at marsalforn, Gozo Island, Malta. J. Struct. Geol. 25, 793–812.

Kim, Y.S., Peacock, D.C.P., Sanderson, D.J., 2004. Fault damage zones. J. Struct. Geol. 26, 503–517.

Kristensen, T.B., Rotevatn, A., Peacock, D.C.P., Henstra, G.A., Midtkandal, I., Grundvåg, S.A., 2016. Structure and flow properties of syn-rift border faults: the interplay between fault damage and fault-related chemical alteration (Dombjerg Fault, Wollaston Forland, NE Greenland). J. Struct. Geol. 92, 99–115.

Kurt, H., Sorlien, C.C., Seeber, L., Steckler, M.S., Shillington, D.J., Cifci, G., Cormier, M.H., Dessa, J.X., Atgin, O., Dondurur, D., Demirbag, E., Okay, S., Imren, C., Gurcay, S., Carton, H., 2013. Steady late Quaternary slip rate on the Cinarcik section of the North Anatolian fault near Istanbul, Turkey. Geophys. Res. Lett. 40, 1–5.

Larsen, P.-H., 1988. Relay structures in a Lower Permian basement-involved extension system, East Greenland. J. Struct. Geol. 10, 3–8.

Le, J.L., Bažant, Z.P., 2014. Finite weakest-link model of lifetime distribution of quasibrittle structures under fatigue loading. Math. Mech. Solids 19, 56–70.

Legg, M.R., Goldfinger, C., Kamerling, M.J., Chaytor, J.D., Einstein, D.E., 2007. Morphology, structure and evolution of California Continental Borderland restraining bends. In: Cunningham, W.D., Mann, P. (Eds.), Tectonics of Strike-slip Restraining and Releasing Bends. Geological Society, London, Special Publications, 290, pp. 143–168.

Lyakhovsky, V., Ben-Zion, Y., Agnon, A., 1997. Distributed damage, faulting, and friction. J. Geophys. Res. 102, 27635–27649.

Maerten, L., 2000. Variation in slip on intersecting normal faults: implications for paleostress inversion. J. Geophys. Res. 105, 25553–25565.

Mann, P., 2007. Global catalogue, classification and tectonic origins of restraining- and releasing bends on active and ancient strike-slip fault systems. In: Cunningham, W.D., Mann, P. (Eds.), Tectonics of Strike-slip Restraining and Releasing Bends. Geological Society, London, Special Publications 290, pp. 1–142.

McClay, K.R., Waltham, D.A., Scott, A.D., Abousetta, A., 1991. Physical and seismic modelling of listric normal fault geometries. In: Roberts, A.M., Yielding, G., Freeman, B. (Eds.), The Geometry of Normal Faults. Geological Society of London Special Publications 56, pp. 231–240.

McGrath, A.G., Davison, I., 1995. Damage zone geometry around fault tips. J. Struct. Geol. 17, 1011–1024.

Michie, E.A.H., Haines, T.J., Healy, D., Neilson, J.E., Timms, N.E., Wibberley, C.A.J., 2014. Influence of carbonate facies on fault zone architecture. J. Struct. Geol. 65, 82–99.

Mitchell, T.M., Faulkner, D.R., 2009. The nature and origin of off-fault damage surrounding strike-slip fault zones with a wide range of displacements: a field study from the Atacama fault system, northern Chile. J. Struct. Geol. 31, 802–816.

Mollema, P.N., Antonellini, M., 1999. Development of strike-slip faults in the dolomites of the Sella group, Northern Italy. J. Struct. Geol. 21, 273–292.

Morley, C.K., 2014. Outcrop examples of soft-sediment deformation associated with normal fault terminations in deepwater, Eocene turbidites: a previously undescribed conjugate fault termination style? J. Struct. Geol. 69, 189–208.

Morley, C.K., Nixon, C.W., 2016. Topological characteristics of simple and complex normal fault networks. J. Struct. Geol. 84, 68–84.

Mouslopoulou, V., Nicol, A., Little, T.A., Walsh, J.J., 2007. Terminations of large strike-slip faults: an alternative model from New Zealand. In: Cunningham, W.D., Mann, P. (Eds.), Tectonics of Strike-slip Restraining and Releasing Bends. Geological Society, London, Special Publications, 290, pp. 387–415.

Peacock, D.C.P., 1991. Displacements and segment linkage in strike-slip fault zones. J. Struct. Geol. 13, 1025–1035.

Peacock, D.C.P., 2001. The temporal relationship between joints and faults. J. Struct.

Geol. 23, 329–341.

Peacock, D.C.P., Anderson, M.W., 2012. The scaling of pull-aparts and implications for fluid flow in areas with strike-slip faults. J. Pet. Geol. 35, 389–400.

Peacock, D.C.P., Sanderson, D.J., 1991. Displacements, segment linkage and relay ramps in normal fault zones. J. Struct. Geol. 13, 721–733.

Peacock, D.C.P., Sanderson, D.J., 1994. Geometry and development of relay ramps in normal fault systems. Am. Assoc. Pet. Geol. Bull. 78, 147–165.

Peacock, D.C.P., Sanderson, D.J., 1999. Deformation history and basin-controlling faults in the Mesozoic sedimentary rocks of the Somerset coast. Proc. Geol. Assoc. 110, 41–52.

Peacock, D.C.P., Zhang, X., 1994. Field examples and numerical modelling of oversteps and bends along normal faults in cross-section. Tectonophysics 234, 147–167.

Peacock, D.C.P., Nixon, C.W., Rotevatn, A., Sanderson, D.J., Zuluaga, L.F., 2016. Glossary of fault and other fracture networks. J. Struct. Geol. 92, 12–29.

Peacock, D.C.P., Nixon, C.W., Rotevatn, A., Sanderson, D.J., Zuluaga, L.F., 2017. Interacting faults. J. Struct. Geol. 97, 1–22.

Pedley, H.M., House, M.R., Waugh, B., 1976. The geology of Malta and Gozo. Proc. Geol. Assoc. 87, 325–341.

Person, M., Hofstra, A., Sweetkind, D., Stone, W., Cohen, D., Gable, C.W., Banerjee, A., 2012. Analytical and numerical models of hydrothermal fluid flow at fault intersections. Geofluids 12, 312–326.

Pickering, G., Peacock, D.C.P., Sanderson, D.J., Bull, J.M., 1997. Modelling tip zones to predict the displacement and length characteristics of faults. Am. Assoc. Pet. Geol. Bull. 81, 82–99.

Qu, D., Tveranger, J., 2016. Incorporation of deformation band fault damage zones in reservoir models. Am. Assoc. Pet. Geol. Bull. 100, 423–443.

Reches, Z., Lockner, D.A., 1994. Nucleation and growth of faults in brittle rock. J. Geophys. Res. 99, 18159–18173.

Ross, Z.E., Hauksson, E., Ben-Zion, Y., 2017. Abundant off-fault seismicity and orthogonal structures in the San Jacinto fault zone. Sci. Adv. 3 http://dx.doi.org/10.1126/sciadv.1601946.

Rotevatn, A., Bastesen, E., 2014. Fault linkage and damage zone architecture in tight carbonate rocks in the Suez Rift (Egypt): implications for permeability structure along segmented normal faults. In: Spence, G.H., Redfern, J., Aguilera, R., Bevan, T.G., Cosgrove, J.W., Couples, G.D., Daniel, J.M. (Eds.), Advances in the Study of Fractured Reservoirs. Geological Society of London, Special Publications 374, pp. 79–95.

Rotevatn, A., Fossen, H., 2011. Simulating the effect of subseismic fault tails and process zones in a siliciclastic reservoir analogue: implications for aquifer support and trap definition. Mar. Pet. Geol. 28, 1648–1662.

Rotevatn, A., Jackson, C.A.L., 2014. 3D structure and evolution of folds during normal fault dip linkage. J. Geol. Soc. Lond. 171, 821–829.

Rotevatn, A., Fossen, H., Hesthammer, J., Aas, T.E., Howell, J.A., 2007. Are relay ramps conduits for fluid flow? Structural analysis of a relay ramp in Arches National Park, Utah. In: Lonergan, L., Jolly, R.J.H., Rawnsley, K., Sanderson, D.J. (Eds.), Fractured Reservoirs. Geological Society, London, Special Publications, 270, pp. 55–71.

Rotevatn, A., Thorsheim, E., Bastesen, E., Fossmark, H.S., Torabi, A., Sælen, G., 2016. Sequential growth of deformation bands in carbonate grainstones in the hangingwall of an active growth fault: implications for deformation mechanisms in different tectonic regimes. J. Struct. Geol. 90, 27–47.

Sakran, S.M., Said, A., El Alfy, Z., El Sharkawi, M.A., 2009. Hammash releasing bend and its control of gold mineralization, Hammash gold mine area, South Eastern desert, Egypt. Egypt. J. Geol. 53, 87–99.

Scholz, C.H., Cowie, P.A., 1990. Determination of total strain from faulting using slip measurements. Nature 346, 837–839.

Shalaby, A., Stüwe, K., Makroum, F., Fritz, H., Kebede, T., Klötzli, U., 2005. The Wadi mubarak belt, eastern desert of Egypt: a neoproterozoic conjugate shear system in the Arabian-Nubian shield. Precambrian Res. 136, 27–50.

Shipton, Z.K., Cowie, P.A., 2003. A conceptual model for the origin of fault damage zone structures in high-porosity sandstone. J. Struct. Geol. 25, 333–344.

Sibson, R.H., 1987. Earthquake rupturing as a mineralizing agent in hydrothermal systems. Geology 15, 701–704.

Sibson, R.H., 1989. Earthquake faulting as a structural process. J. Struct. Geol. 11, 1–14.

Sibson, R.H., Moore, J.M.M., Rankin, A.H., 1975. Seismic pumping - a hydrothermal fluid transport mechanism. J. Geol. Soc. 131, 653–659.

Simmenes, T.H., Hermanrud, C., Remi Ersland, R., Georgescu, L., Sollie, O.C.E., 2016. Relationships between bright amplitudes in overburden rocks and leakage from underlying reservoirs on the Norwegian Continental Shelf. Pet. Geosci. 23, 10–16.

Smeraglia, L., Berra, F., Billi, A., Boschi, C., Carminati, E., Doglioni, C., 2016. Origin and role of fluids involved in the seismic cycle of extensional faults in carbonate rocks. Earth Planet. Sci. Lett. 450, 292–305.

Soliva, R., Schultz, R.A., 2008. Distributed and localized faulting in extensional settings: insight from the North Ethiopian Rift – Afar transition area. Tectonics 27, TC2003,. http://dx.doi.org/10.1029/2007TC002148.

Srivastava, V., Mukul, M., Barnes, J.B., 2016. Main Frontal thrust deformation and topographic growth of the Mohand Range, northwest Himalaya. J. Struct. Geol. 93, 131–148.

Storti, F., Balsamo, F., Clemenzi, L., Mozafari, M., Al-Kindy, M.H.N., Solum, J., Swennen, R., Taberner, C., Tueckmantel, C., 2015. Complex fault-fold interactions during the growth of the Jabal Qusaybah anticline at the western tip of the Salakh Arch, Oman. Tectonics 34, 488–509.

Tamagawa, T., Pollard, D.D., 2008. Fracture permeability created by perturbed stress fields around active faults in a fractured basement reservoir. Am. Assoc. Pet. Geol. Bull. 92, 743–764.

Tchalenko, J.S., 1970. Similarities between shear zones of different magnitudes. Bull. Geol. Soc. Am. 81, 1625–1640.

Tondi, E., Antonellini, M., Aydin, A., Marchegiani, L., Cello, G., 2006. The role of deformation bands, stylolites and sheared stylolites in fault development in carbonate grainstones of Majella Mountain, Italy. J. Struct. Geol. 28, 376–391.

Walker, R.J., Holdsworth, R.E., Armitage, P.J., Faulkner, D.R., 2013. Fault zone permeability structure evolution in basalts. Geology 41, 59–62.

Watterson, J., Nicol, A., Walsh, J.J., Meier, D., 1998. Strains at the intersections of synchronous conjugate normal faults. J. Struct. Geol. 17, 847–862.

Whittaker, A., Green, G.W., 1983. Geology of the Country Around Weston-super-mare. Memoir of the Geological Survey of Great Britain, Sheet 279 and parts of 263 and 295.

Wibberley, C.A.J., Shimamoto, T., 2003. Internal structure and permeability of major strike-slip fault zones: the median tectonic line in Mie Prefecture, southwest Japan. J. Struct. Geol. 25, 59–78.

Willemse, E.J.M., Peacock, D.C.P., Aydin, A., 1997. Nucleation and growth of strike-slip faults in limestone. J. Struct. Geol. 19, 1461–1477.

Windarto, W., Gunawan, A.Y., Sukarno, P., Soewono, E., 2011. Modeling of mud filtrate invasion and damage zone formation. J. Pet. Sci. Eng. 77, 359–364.

Zampieri, D., Massironi, M., 2007. Evolution of a poly-deformed relay zone between fault segments in the eastern Southern Alps, Italy. In: Cunningham, W.D., Mann, P. (Eds.), Tectonics of Strike-slip Restraining and Releasing Bends. Geological Society, London, Special Publications, 290, pp. 351–366.

B

# Appendix B: Connectivity and network development of carbonate-hosted fault damage zones from western Malta.

Casey W. Nixon, Kari Nærland, Atle Rotevatn, Vilde Dimmen, David J. Sanderson, Thomas B. Kristensen

*Published in Journal of Structural Geology, 141 (2020) 104212*

https://doi.org/10.1016/j.jsg.2020.104212

Journal of Structural Geology 141 (2020) 104212

Contents lists available at ScienceDirect

Journal of Structural Geology

journal homepage: http://www.elsevier.com/locate/jsg

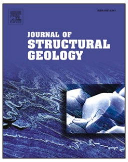

# Connectivity and network development of carbonate-hosted fault damage zones from western Malta

Casey W. Nixon[a,*], Kari Nærland[a,1], Atle Rotevatn[a], Vilde Dimmen[a], David J. Sanderson[b], Thomas B. Kristensen[a,2]

[a] *Department of Earth Science, University of Bergen, Allegaten 41, 5007, Bergen, Norway*
[b] *Ocean and Earth Sciences, University of Southampton, Southampton, SO14 3ZH, UK*

ARTICLE INFO

*Keywords:*
Connectivity
Fault damage zone
Topology
Fracture network
Graph theory

ABSTRACT

Using outcrop-based examples, we investigate the topological and graph characteristics of various fault damage zones in carbonate rocks on Malta. The damage zone fracture networks are analysed as a series of nodes (isolated *I*-nodes; connected *Y*/*X*-nodes) and branches (*II*-, *IC*-, *CC*-branches), which may link to form connected components and fracture-bounded regions. We compare the metrics of the different nodes, branches, regions and components that make-up each damage zone fracture network, calculating parameters that assess their connectivity. Results identify distinct topological signatures and graph metrics for different tip-, relay- and splay-damage zones, providing a new classification that describes and quantifies their arrangement and connectivity. Placing the studied damage zones in a fault evolutionary model highlights topological pathways whereby tip-damage zones, dominated by *I*-nodes and *II*-branches, give way to relay-damage zones, dominated by *Y*-nodes and *CC*-branches. During this process, tree-like components link to form larger interconnected components with many regions. This systematically changes the graph metrics of the network increasing the number of branches and regions relative to nodes and components. The topological pathways and graph metrics provide important insights into how damages zones might develop as faults propagate, interact and link and could have implications when assessing their importance for fluid-flow.

## 1. Introduction

Fault damage zones represent the volume of deformed rock surrounding a fault as a result of fault initiation, propagation, interaction and slip accumulation (e.g. Cowie and Scholz, 1992; McGrath and Davison, 1995; Kim et al., 2004; Choi et al., 2016; Peacock et al., 2017). A variety of different fault damage zones have been identified and classified in the literature depending on their location relevant to the parent fault(s), including but not limited to: tip, wall, linkage, interaction and fault bend damage zones (i.e. Kim et al., 2004; Choi et al., 2016; Peacock et al., 2017). Such damage zones form due to local stress concentrations or perturbations along or between faults, often accommodating variations in the distribution of strain and displacement (e.g. Kim et al., 2000, 2001; Nixon et al., 2019). They commonly consist of numerous fractures (e.g. veins, joints, small faults, deformation bands, stylolites etc.) of different scales, types and orientations, forming networks that contribute to the overall deformation of the rock.

A detailed understanding of the development of the different structures within fault damage zones can provide valuable insights on processes of fault growth and development (Cowie and Shipton, 1998; Kim et al., 2003; Shipton and Cowie, 2003; Fossen et al., 2005; Childs et al., 2009; Faulkner et al., 2011) as well as earthquake initiation and rupture patterns (King, 1986; Sibson, 1989; Kim and Sanderson, 2008; Soliva et al., 2008; Choi et al., 2012; Johri et al., 2014; Perrin et al., 2016). Of particular economic significance is the control of fault damage on fluid flow and rock permeability in the upper crust (Caine et al., 1996; Shipton et al., 2002; Leckenby et al., 2005; Kim and Sanderson, 2010; Mitchell and Faulkner, 2012; Ogata et al., 2014; Dimmen et al., 2017, 2020). Thus damage zones can be crucial factors when exploring for water aquifers (e.g. Huyakorn et al., 1983), ore mineral deposits (e.g. Curewitz and Karson, 1997), hydrocarbon reservoirs (e.g. Gartrell et al., 2004; Fossen et al., 2005; Rotevatn et al., 2007) and storage sites for $CO_2$

---

[*] Corresponding author.
*E-mail address:* casey.nixon@uib.no (C.W. Nixon).
[1] Now at: ConocoPhillips, Ekofiskvegen 35, 4056 Tananger, Norway.
[2] Now at: Statoil, Sandslivegen 90, 5254 Sandsli, Norway.

https://doi.org/10.1016/j.jsg.2020.104212
Received 9 March 2020; Received in revised form 15 September 2020; Accepted 2 October 2020
Available online 7 October 2020
0191-8141/© 2020 The Author(s). Published by Elsevier Ltd. This is an open access article under the CC BY license (http://creativecommons.org/licenses/by/4.0/).

(e.g. Shipton et al., 2004; Dockrill and Shipton, 2010).

A plethora of literature, therefore, exists on fault damage zones with studies mainly focusing on characterising damage zone architectures and geometries (e.g. McGrath and Davison, 1995; Kim et al., 2001, 2004; Berg and Skar, 2005; Johansen and Fossen, 2008; Gudmundsson et al., 2010; Rotevatn and Bastesen, 2014; Choi et al., 2016; Peacock et al., 2017), geometric dimensions of damage zones and subsequent scaling relationships with fault displacement/length (e.g. Hull, 1988; Knott et al., 1996; Vermilye and Scholz, 1998; Beach et al., 1999; Shipton and Cowie, 2001; Mitchell and Faulkner, 2009; Faulkner et al., 2011), fracture abundances and distributions within damage zones (e.g. Micarelli et al., 2003, 2006; Berg and Skar, 2005; Savage and Brodsky, 2011) and the effects of damage on physical rock properties such as permeability (e.g. Caine et al., 1996; Shipton et al., 2002; Mitchell and Faulkner, 2012). Less attention, however, has been given to characterising the arrangement (topology) and connectivity of the fractures within fault damage zones. This is important as fracture connectivity is crucial for assessing percolation potential and thus fluid flow through a rock body (Adler and Thovert, 1999; Manzocchi, 2002; Sanderson and Nixon, 2018). This is especially the case in low permeability rocks, such as the carbonate rocks used in this study, where permeability is often solely reliant on fractures and their connectivity (Faulkner et al., 2010).

The aim of this paper is to investigate the topological characteristics of different fault damage zones, with a focus on quantifying the development of fracture connectivity. The study applies a topological analysis based on graph theory (i.e. Sanderson et al., 2019) to examples of damage zones associated with metre-scale extensional faults observed in carbonate rocks along the western coast of Malta (Fig. 1). A topological analysis provides a description of the geometrical relationships between the fractures within a network and is essential for assessing fracture network connectivity (Jing and Stephansson, 1997; Sanderson and Nixon, 2015, 2018). The topological character of a fracture network is important as two fracture networks can have similar geometries (trace lengths, orientations and fracture intensities) but different topologies and thus connectivity, which could result in very different fluid flow properties (e.g. Sanderson and Nixon, 2015, 2018). Therefore, this study focuses on constraining the potential variations in topology and connectivity of fracture networks within different fault damage zones. We explore the differences and similarities between the different types of damage zone, producing a topology-based classification scheme that describes both the connectivity and complexity of their fracture networks. Finally, we extrapolate the results to discuss how fracture networks develop within damage zones by using the different studied examples, with varying degrees of structural complexity, as proxies for damage zone maturity.

## 2. Damage zone terminology

Numerous studies have proposed different classification and nomenclature schemes for describing fault damage zones. Kim et al. (2004) define *tip*, *wall* and *linkage* damage zones based on their location around subparallel segmented faults. Peacock et al. (2017) broaden this classification to include *interaction damage zones* around non-parallel and non-synchronous faults including *intersection* and *approaching* damage zones. Choi et al. (2016) use *along-fault*, *around-tip* and *cross-fault* damage, an approach that describes a damage zone based on the plane of observation and the damage zone position around an exposed fault. In this paper we follow the recommendation of Peacock et al. (2017) and use a prefix based on the damage zones' location in order to distinguish the three different types of studied damage zone (Fig. 2):

- *Tip-damage zones* refer to damage around the lateral tips of an extensional fault, observed in plan-view. The damage in these zones is related to increased stresses at the tips of faults as they grow and propagate (e.g. Cowie and Scholz, 1992; Vermilye and Scholz, 1998). These are the same as tip damage zones described by Kim et al. (2004) and could either be mixed mode or mode III tip damage according to the around-tip damage zone classification of Choi et al. (2016).

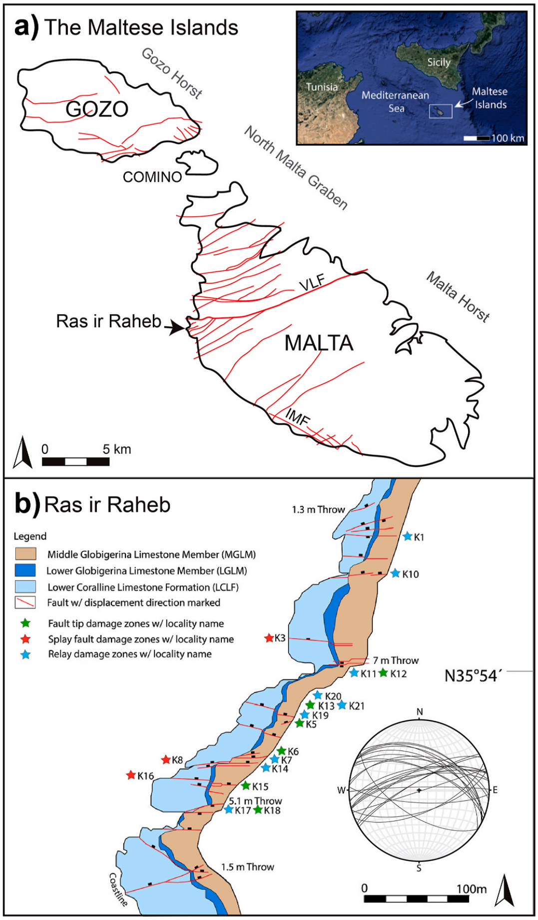

**Fig. 1.** a) Map of the Maltese Islands, showing the location of the largest faults in red (VLF = Victoria Lines Fault; IMF = Il Maghlaq Fault), and the location of the study area at the western coast of Malta (After Pedley et al., 1976; Michie et al., 2014; Dimmen et al., 2017). Inset image shows the regional location of the Maltese Islands within the Mediterranean Sea – attribution given to Google Earth (Data: SIO, NOAA, U.S. Navy, NGA, GEBCO; Image: Landsat/Copernicus). b) Map of the study area at Ras ir Raheb (After Michie et al., 2014). The stereoplot shows the trends of the normal faults found along the wave-cut platform on which the studied networks are situated (After Dimmen et al., 2017). The locations and names of the damage zones presented within this paper are marked by stars. (For interpretation of the references to colour in this figure legend, the reader is referred to the Web version of this article.)

- *Relay-damage zones* refer to damage around geometrically or kinematically linked, synchronous, sub-parallel and overlapping extensional faults, observed in plan-view. These damage zones can be associated with different stages of fault segment linkage from relay ramp structures between soft-linked faults to fully breached relays of hard-linked faults. The damage in these zones is related to fault interaction often accommodating the transfer of strain or displacement between two fault segments (e.g. Peacock and Sanderson, 1991, 1994; Huggins et al., 1995). These damage zones are

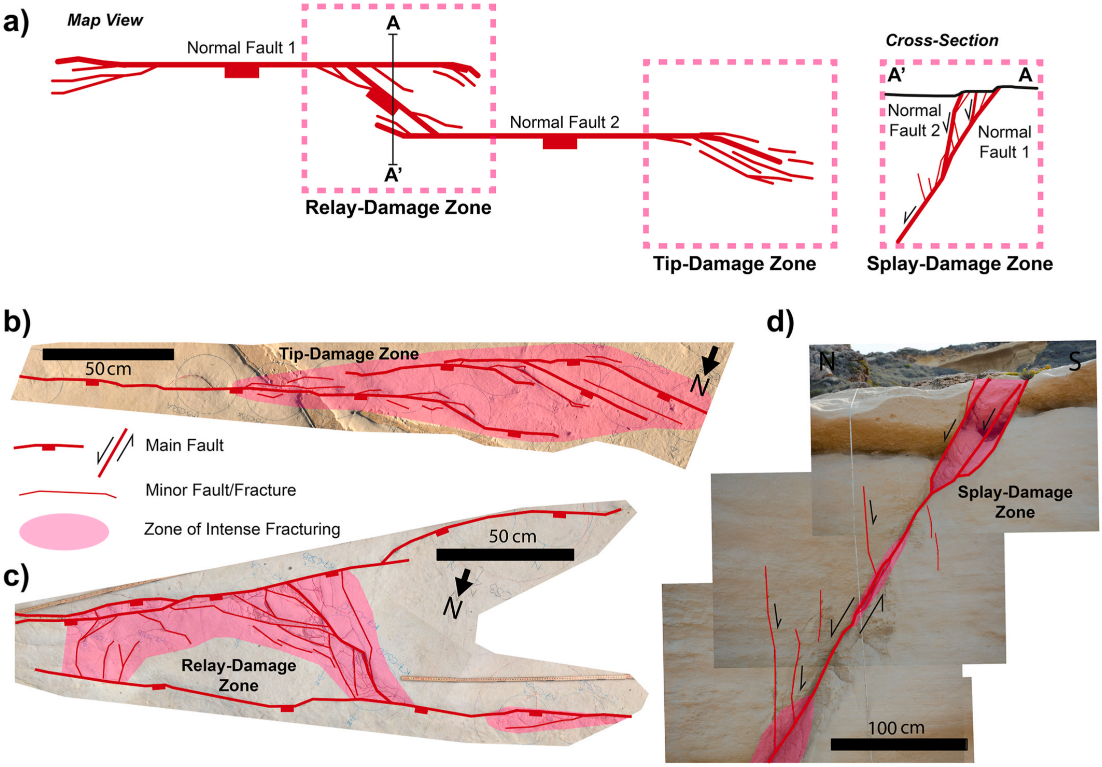

**Fig. 2.** a) Illustration of the different types of damage zone (tip-, relay-, splay-) according to where they are placed in relation to the overall geometry of the fault(s). These terms are used for normal fault damage zones in this study. b), c) and d) are interpreted photographs of localities K5, K7 and K3 respectively, showing field examples of the different types of damage zone. See Fig. 1b for locations of the three field examples.

equivalent to along-fault linkage damage zones (Kim et al., 2004; Choi et al., 2016).

- *Splay-damage zones* represent damage associated with upward splaying or bifurcating, synthetic faults that are observed in cross-section. These may be cross-sectional views of either a relay-damage zone or a mode III tip-damage zone, which could be considered as cross-fault damage or an around-tip damage, respectively (Choi et al., 2016).

These different damage zones are associated with local stresses during the propagation and linkage of faults as they grow and develop. We use several examples of each damage zone type to cover a range of structural complexities and as proxies for evolutionary stages of damage zone development during fault growth. The term *structural complexity* refers to the fracture abundance and range of orientations exhibited in a damage zone. We use the terms *simple* and *complex* as relative descriptions of the structural complexity of each damage zone, with complex indicating greater fracture abundances often displaying a wider range of orientations.

## 3. Geological setting

The Maltese Islands (Malta, Gozo, and Comino; Fig. 1a) are situated on the Malta Platform, which forms the NNE shoulder of the Late Miocene-Early Pliocene Pantelleria Rift (Reuther and Eisbacher, 1985; Dart et al., 1993; Jolivet and Faccenna, 2000). The archipelago is dominated by an ENE-WSW trending horst and graben system, comprising of the North Gozo and North Malta grabens (Dart et al., 1993; Putz-Perrier and Sanderson, 2010), that was activated during the Miocene before reaching a peak in activity during the Pliocene-Quaternary (Illies, 1981; Bosence and Pedley, 1982; Finetti, 1984; Jongsma et al., 1985). Major and minor extensional faults on the islands generally follow the trend of the horst and graben system with the exception of the ESE-WNW trending Il Maghlaq Fault (IMF; Fig. 1a), located on the southern coast of Malta, which has a similar trend to the Pantelleria Rift (Pedley et al., 1976; Illies, 1981; Reuther and Eisbacher, 1985; Bonson et al., 2007; Rotevatn et al., 2016). The Victoria Lines Fault (VLF) is a large graben-bounding fault (up to 195 m displacement) that separates the North Malta Graben from the Malta Horst to the south (Fig. 1a). The small extensional faults (<10 m displacement) that form the basis of this study are located at Ras ir Raheb, about 500–1000 m into the footwall of the VLF on the Malta Horst (Dart et al., 1993; Putz-Perrier and Sanderson, 2010; Michie et al., 2014; Dimmen et al., 2017). These small extensional faults may be considered as part of a >2 km wide footwall damage zone associated with the VLF, which includes several large splay faults distributing the displacement of the VLF (Putz-Perrier and Sanderson, 2010, Fig. 1a).

The islands comprise a sequence of Oligocene and Miocene carbonates that have a well-defined stratigraphy (Pedley et al., 1976; Dart et al., 1993). Along the coast at Ras ir Raheb (Fig. 1b), the stratigraphy can be divided into the Oligocene platform carbonates of the Lower Coralline Limestone Formation (LCLF) and the Miocene pelagic carbonates of the Globigerina Limestone Formation (Dart et al., 1993), which provide excellent outcrops for detailed studies of damage zones of small-scale extensional faults (e.g. Putz-Perrier and Sanderson, 2010; Dimmen et al., 2017). The Globigerina Limestone Formation can be divided into the Lower Globigerina Limestone Member (LGLM) and the Middle Globigerina Limestone Member (MGLM). The LGLM consists of fossiliferous packstones and wackestones and is marked at the top by a 50 cm thick phosphoritic conglomerate with an abundance of bivalve-, bryozoan-, solitary coral-, and echinoid-fossils (Pedley, 1987). The MGLM consists of highly bioturbated mudstones interbedded with thin layers (50–100 cm thick) of phosphoritc conglomerate (Pedley et al., 1976; Bennett, 1979). The studied fault damage zones described in this study include relay- and tip-damage zones observed in plan-view on pavement outcrops of the MGLM and splay-damage zones observed in cross-section in cliff outcrops of both the LGLM and MGLM (Fig. 1b).

## 4. Methodology

### 4.1. Mapping of damage zones

Field outcrops of 6 tip-damage zones, 9 relay-damage zones and 3 splay-damage zones were identified and documented in detail along sub-horizontal pavements and cliffs of the Globigerina Limestone Formation at Ras ir Raheb (Nærland, 2016) (Fig. 1b). All fault damage zones were photographed, mapped and structurally characterised allowing them to be classified depending on their structural complexity. Structural data were collected for faults exposed along the coast, including fault plane orientations and measured fault displacements. The high-resolution outcrop images were then merged, imported and georeferenced in ArcGIS where the fracture networks associated with each fault damage zone were then digitised for further geospatial and topological analysis (e.g. Nyberg et al., 2018).

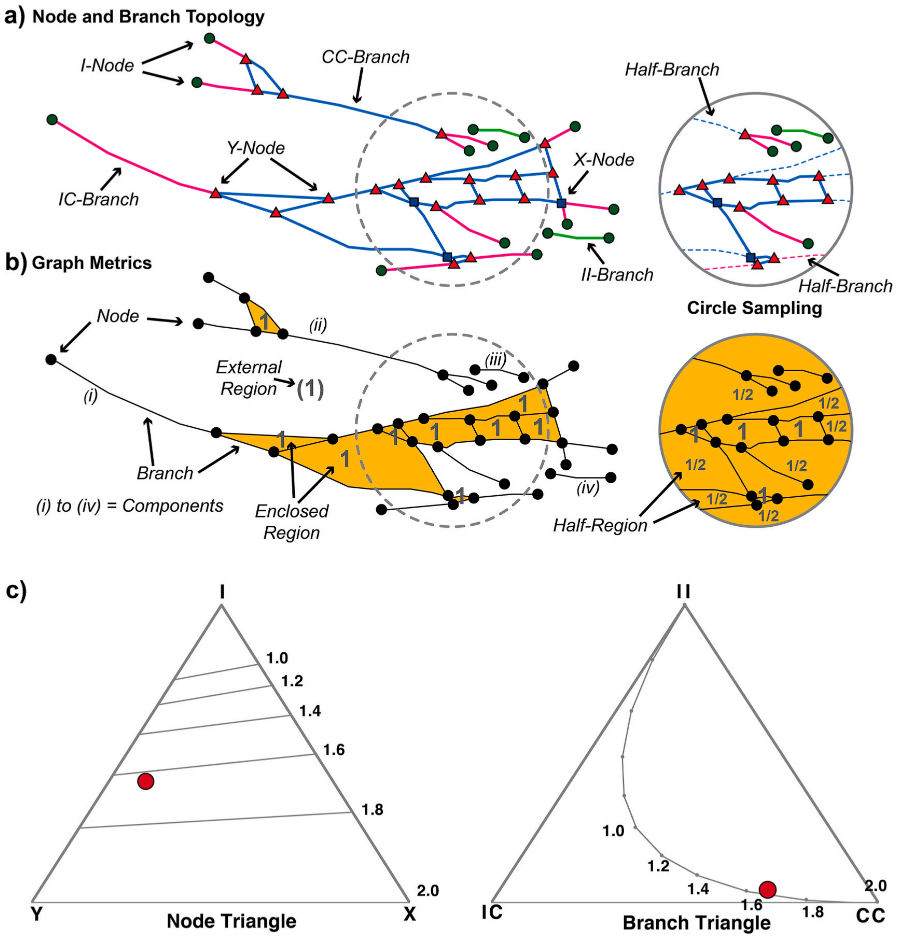

**Fig. 3.** a) Trace map of a fracture network illustrating different node and branch types. b) Graph representation of the same fracture network showing nodes (dots), branches (lines), regions (shaded) and components (i-iv). The circles to the right of the trace maps illustrate circle sampling of the different nodes, branches and regions. c) ternary diagrams of the different node and branch types with red dots representing the topology of the fracture network trace map in Fig. 3a. The contours represent the connections per branch and how this changes relative to the topology. (For interpretation of the references to colour in this figure legend, the reader is referred to the Web version of this article.)

### 4.2. Network topology and assessing connectivity

A topological analysis was applied to each digitised fault damage zone in order to characterise the networks within them and to constrain their connectivity. In topology, each two-dimensional fracture network is considered as a planar graph consisting of nodes and branches between nodes (Manzocchi, 2002; Sanderson and Nixon, 2015; Sanderson et al., 2019). Based on the relationships between the fractures we can identify 3 types of node: *I*-nodes representing the tip of a fracture; *Y*-nodes representing the point of splaying or abutting fractures; and *X*-nodes representing the intersection point between two crossing fractures. Therefore, *Y*- and *X*-nodes are connecting nodes whereas *I*-nodes are isolated (Fig. 3a). As branches have one node at each end they can be classified into three types, based on whether the nodes are connecting (*C*) or isolated (*I*): isolated branches (*II*), singly connected branches (*IC*) and doubly connected branches (*CC*) (Sanderson and Nixon, 2015) (Fig. 3a). The number counts of each node type ($N_I$, $N_Y$, $N_X$) and branch type ($B_{II}$, $B_{IC}$, $B_{CC}$) can be used to plot their proportions on ternary diagrams, topologically characterising the fracture networks. The number of branches (*B*) and number of nodes (*N*) are related to each other by:

$$B = (N_I + 3N_Y + 4N_X) / 2 \qquad (1)$$

It should be noted that when sampling topological elements, that branches extending beyond the sample area are counted as half-branches in this relationship as only one end node is visible.

Where a network plots in a ternary diagram is representative of the network's connectivity. Isolated and poorly connected networks will plot towards the *I*-node and *II*-branch corners of each ternary diagrams, whereas well connected networks will plot towards the *Y*-*X* axis and *CC* corner (Fig. 3). Furthermore, the number counts of the different node types can be used to calculate parameters that directly describe the degree of connectivity within a network such as *connections per branch* ($C_B$), which describes the degree of connectivity between branches:

$$C_B = (3N_Y + 4N_X) / B \qquad (2)$$

As branches only have two nodes associated with them (i.e. *I* or *C*) values of $C_B$ range from 0 to 2 and can also be contoured onto both the node and branch ternary diagrams (Fig. 3) (Sanderson and Nixon, 2015, 2018).

Another parameter is the *average degree* ($<D>$), which describes the degree to which nodes are connected to branches (Sanderson et al., 2019). It is defined by the ratio between the number of branches (*B*) and the number of nodes (*N*), whereby:

$$B / N = <D> / 2 \qquad (3)$$

Thus $<D>$ provides an important link between the nodes and branches of the network. Within a fracture network an *I*-node has a degree of 1, a *Y*-node has a degree of 3 and an *X*-node has a degree of 4. Thus the average degree will vary from $<D> = 1$ (for poorly connected networks dominated by *I*-nodes and isolated branches) to $<D> = 4$ (for a completely connected network dominated by crossing fractures forming only *X*-nodes and *CC*-branches) (Fig. 3). Many natural fracture networks, particularly joint systems and fault networks, are often dominated by abutting relationships and Y-nodes (e.g. Nixon et al., 2012; Morley and Nixon, 2016; Duffy et al., 2017) and expected values of $<D>$ will likely lie between 1 and 3.

### 4.3. Euler's theorem, regions and components

In graph theory the arrangement of the different nodes and branches within each fracture network forms a planar graph (Sanderson et al., 2019). As well as nodes and branches each planar graph contains components and regions bounded by cycles (Fig. 3b). The simplest component is an isolated branch (i.e. components *iii* and *iv* in Fig. 3b) but numerous connected nodes and branches will produce a connected component (i.e. components *i* and *ii* in Fig. 3b). Connected components represent clusters of fractures and can form anything from finite tree-like clusters to infinite networks. Regions, on the other hand, are the enclosed spaces within connected components representing the blocks of rock between fractures (Sanderson et al., 2019).

Equation (3) shows that the number of branches (*B*) and number of nodes (*N*) can be linked to one another through the average degree ($<D>$). However, they can also be related to the number of components (*K*) and number of regions (*R*) through a generalisation of Euler's theorem (Euler, 1758; Sanderson et al., 2019), where by:

$$R = B - N + K \qquad (4)$$

This indicates specific relationships between the different metrics (*R, B, N* and *K*) for a given network. In this paper we focus on comparing these different graph metrics to identify any relationships that could be useful for further classifying or describing the damage zones.

In addition, equation (4) is useful for extracting further metrics about a network. In particular, it can be used to extract the number of regions (or blocks between fractures) within each fracture network, simply calculated from the number of nodes, branches and connected components. If the area (*A*) of the extent of the sampled fracture network is known then we can also calculate an average block area (*A/R*) for the network (Sanderson et al., 2019). Furthermore, dividing the average block area by the total sample area will give the dimensionless block intensity ($R_{22}$), which can be simplified to:

$$R_{22} = A^{-1}. (A / R) = 1 / R \qquad (5a)$$

As *R* represents the number of enclosed regions, we can modify Equation (5a) to include an external infinite region representing the surrounding rock mass:

$$R_{22} = 1 / (R + 1) \qquad (5b)$$

Thus, from equation (5b), values for $R_{22}$ will range from 0 to 1, with 1 representing an intact rock mass that becomes more broken up as $R_{22}$ tends to 0. Therefore, as well as characterising the topology and connectivity of each damage zone we can also constrain how broken up the rock mass is within each damage zone, hence, quantifying the amount of damage. It is worth noting that this measure is highly influenced by the observed extent of a network and thus should only be used when comparing entire networks or sample areas of the same size.

### 4.4. Sampling and assessing spatial variability

As well as collecting geometric and topological data for the damage zone as a whole, we also subsampled each damage zone to assess spatial variability. Circle samples that eliminate orientation bias (Mauldon et al., 2001; Sanderson and Nixon, 2015) were used to subsample along-strike and dip of the main faults associated with each damage zone. Within each circle sample the area, total trace-length, and the number of different topological elements (nodes, branches, components and regions) were recorded.

The sampling of nodes is straight forward as you simply count the number of nodes that lie within each circle sample (Fig. 3a). However, a branch may go beyond the boundary of a sample area, which means that: a) the length of such a branch is unknown or censored; and b) only one node associated with the branch lies within the sample area. Such branches can only be counted as half-branches. If topological information for the surrounding network is known, then the topology of the half-branch can still be determined. However, if this information is unknown then the topology of the branch cannot be determined and is classified as unknown. If a branch passes through a circle sample area then its associated nodes do not lie within the sample, thus the branch is not included in the branch count. This approach ensures that the branch count is consistent with the number of branches (*B*) calculated from the node count in equation *1*. When calculating the number of regions (*R*) for each circle sample, using equation *4,* we assume that the network is part of one connected component (after excluding isolated branches) as the components may be connected outside the sample area. Thus $R = B - N + 1$, resulting in a minimum value for the number of regions within each circle. Furthermore, a consequence of counting half-branches is that the value of $R$ will include complete regions, within the circle sample, as well as half-regions which leave the sample area (Sanderson et al., 2019).

The recorded circle sample data were used to calculate subsequent along-strike/along-dip profiles of different parameters including: i) fracture intensity, defined as total fracture trace-length per unit area ($m^{-1}$ or $m/m^2$); ii) connecting node frequency, defined as the number of connections per unit area ($N_C/m^2$); and iii) the dimensionless block intensity ($R_{22}$). In addition, contour plots of fracture intensity and connecting node frequency are used to illustrate variations within each damage zone.

## 5. Results

### 5.1. Structural description of the damage zones

All of the studied damage zones are associated with normal faults, with less than 1.5 m of displacement, and consist of smaller faults (displacements up to a few cm) and opening-mode fractures. The faults generally have steep dips (up to 85°) and form a bimodal fault population with conjugate sets trending NNE-WSW and ESE-WNW (Fig. 1b). The examples of each type of fault damage zone (tip-, relay-, splay-) show varying degrees of structural complexity and can be further classified based on their structural style (Figs. 4–6).

We identify three different tip-damage zones with the simplest en echelon tips comprising overlapping and stepping fractures (e.g. Fig. 4a and b). More structurally complex tips include horsetail tips (e.g. Fig. 4c and f) that form several obliquely splaying fractures along-strike of the fault tip, and bifurcating tips (e.g. Fig. 4d and e) that include numerous splaying and intersecting fault strands and fractures. Local fracture intensities range spatially from 10 $m^{-1}$ to 120 $m^{-1}$ with the more complex tip damage zones exhibiting the highest intensities, often located at splays or areas of intense bifurcation, whereas the simplest tip damage zones only exhibit intensities <80 $m^{-1}$ (e.g. Fig. 4a–c).

The relay-damage zones are divided into intact relays, singly-breached relays and multiply-breached relays (Fig. 5). Intact relays comprise overlapping fault segments that may be interacting but have no physical linkage between the segments across the entire relay ramp. In the singly-breached relays, the fault segments are overlapping and interacting with a single linking fault/fracture crossing the relay ramp between the two segments. Multiply-breached relays are where the two fault segments are linked by two or more faults/fractures, thus breaking up the relay ramp creating a more complex damage zone. Local fracture intensities range spatially from 10 $m^{-1}$ to 200 $m^{-1}$ with the intact relay damage zones exhibiting the lowest intensities of <80 $m^{-1}$ and the singly-breached relays containing intensities up to 100 $m^{-1}$ (Fig. 5d and e). The highest intensity values are exhibited by the more complex multiply-breached relays (Fig. 5f–i), with greatest intensities restricted to linkage areas where faults/fractures are either splaying from or abutting the main fault segments.

Splay-damage zones can range in complexity from a main fault with one or two synthetic splay faults (Fig. 6a and b) to a main fault with several synthetic splay faults interconnected by numerous antithetic faults/fractures (Fig. 6c). The examples in this study show local fracture intensities ranging from 10 to 180 $m^{-1}$, with K16 being the least structurally complex and exhibiting the lowest fracture intensities. In general local fracture intensities are less than 100 $m^{-1}$, however, much higher values are observed at lenses and around splay intersections as shown for examples K3 and K8 (Fig. 6).

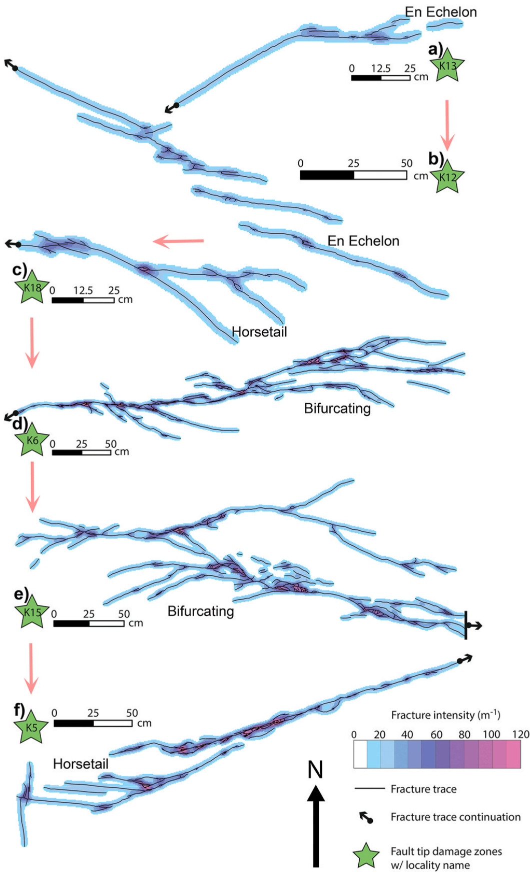

**Fig. 4.** Fracture trace maps of different fault tip-damage zones with their locality name and structural style labelled. The documented damage zones are all exposed in the MGLM. The damage zones are arranged according to the red arrows, which correspond to a relative increase in fracture intensity and connections per branch. These match the red arrows in the node and branch triangular plots in Fig. 7. (For interpretation of the references to colour in this figure legend, the reader is referred to the Web version of this article.)

### 5.2. Damage zone topology and connectivity

In the next sections, we will explore the topology and graph metrics of the three main types of fault damage zone (tip-, relay- and splay-). The triangular plots in Fig. 7, along with Table 1, illustrate the proportions of the different node and branch types of each studied damage zone. The damage zones are mostly dominated by *I*- or *Y*-nodes, but show a broad variation plotting close to the *I–Y* axis. Furthermore, almost all the damage zones are dominated by *IC*- or *CC*-branches, so plotting close to the *IC-CC* axis of the branch triangle.

The fault tip-damage zones (Fig. 4) plot closer to the *I*-node corner of the node triangle than relay- and splay-damage zones (Fig. 7a). Example K13, an en echelon tip, exhibits the greatest proportion of *I*-nodes at ~95% and is one of three tip-damage zones with no *X*-nodes (i.e. K13, K12, K18; Fig. 7a and Table 1). Whereas example K5, a horsetail tip, has the highest proportion of *Y*-nodes (~55%) and *X*-nodes (~3%) of all six fault tip-damage zones (Fig. 7a and Table 1). The branch triangle shows that most of the fault tip-damage zones plot along the *IC-CC* axis with low proportions of *II*-branches, between 4% and 8% (Fig. 7b and

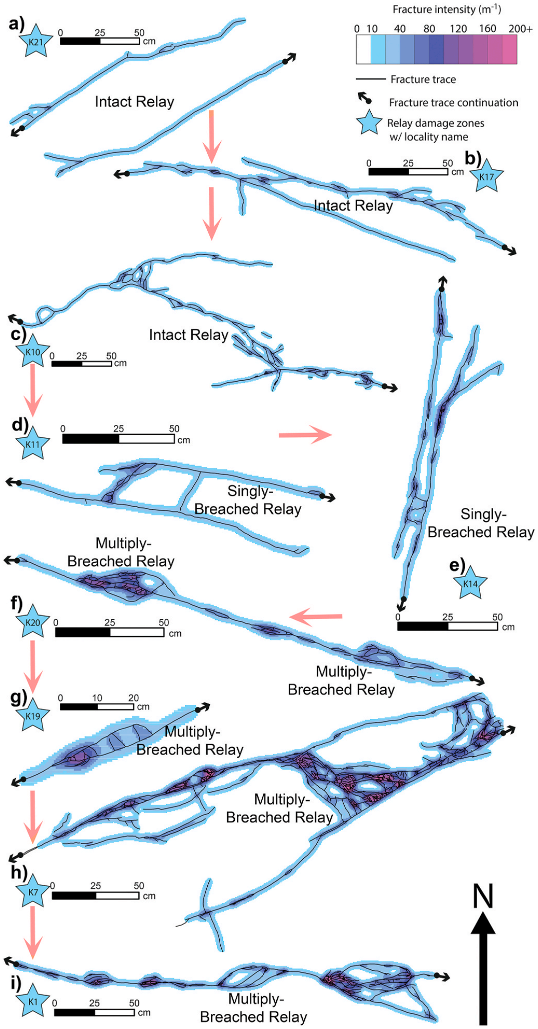

**Fig. 5.** Fracture trace maps of different fault relay-damage zones with their locality name and structural style labelled. The documented damage zones are all exposed in the MGLM. The damage zones are arranged according to the red arrows, which correspond to a relative increase in fracture intensity and connections per branch. These match the red arrows in the node and branch triangular plots in Fig. 7. (For interpretation of the references to colour in this figure legend, the reader is referred to the Web version of this article.)

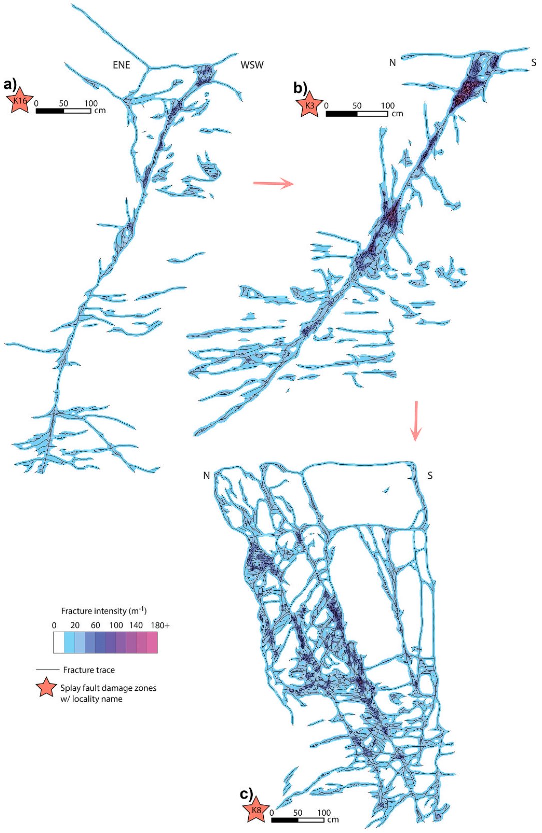

**Fig. 6.** Fracture trace maps of different fault splay-damage zones with their locality name and structural style labelled. These splay fault damage zones are all exposed in vertical outcrops of the LGLM and MGLM. The damage zones are arranged according to the red arrows, which correspond to a relative increase in fracture intensity and connections per branch. These match the red arrows in the node and branch triangular plots in Fig. 7. (For interpretation of the references to colour in this figure legend, the reader is referred to the Web version of this article.)

Table 1). The en echelon tip, K13, is the only fault damage zone dominated by *II*-branches with a proportion of >70%, thus plotting in the *II*-branch corner of the triangle. The en echelon tips produce the most isolated branches and nodes due to their unlinked and stepping fracture arrays. The nature of the bifurcating and horsetail tips, with numerous splaying and branching fractures, mean they have greater potential for creating *Y*-nodes and *IC*- or *CC*-branches.

The relay-damage zones (Fig. 5) plot closer to the *Y*-node corner of the triangle than both tip- and splay-damage zones (Fig. 7c). However, the examples show a large spread in node topology with examples K17 and K21, both intact relays, dominated by *I*-nodes with proportions of 57% and 67%, respectively. In contrast, the singly- (K11, K14) and multiply-breached relays (K1, K7, K19, K20) are all dominated by *Y*-nodes, with the latter showing the greatest proportion of connecting nodes (>80% *Y*- and *X*-nodes; Fig. 7c and Table 1) than any of the studied damage zones. Note that the multiply-breached relays also have greater proportions of *X*-nodes (between 8% and 11%) than any other damage zones. The relay-damage zones are dominated by *IC*- and *CC*-branches, with proportions of *II*-branches at <10%. The intact relays (K10, K17, K21; Fig. 7d and Table 1) exhibit more *IC*-branches (>30%) than the other relay-damage zones, with multiply-breached relays exhibiting up to 91% *CC*-branches, which is much greater than the other types of damage zone. The results indicate a progressive increase in both the proportion of connecting nodes (*Y*- and *X*-nodes) and *CC*-branches from intact relays to singly-breached relays to multiply-breached relays. These differences are a result of differences in their structural style with intact relays displaying more bifurcating fractures producing more *IC*-branches. Whereas the singly- and multiply-breached relays produce linking fractures between the two fault segments thus creating more *CC*-branches and less *I*-nodes.

Splay-damage zones are clustered in both the node and the branch

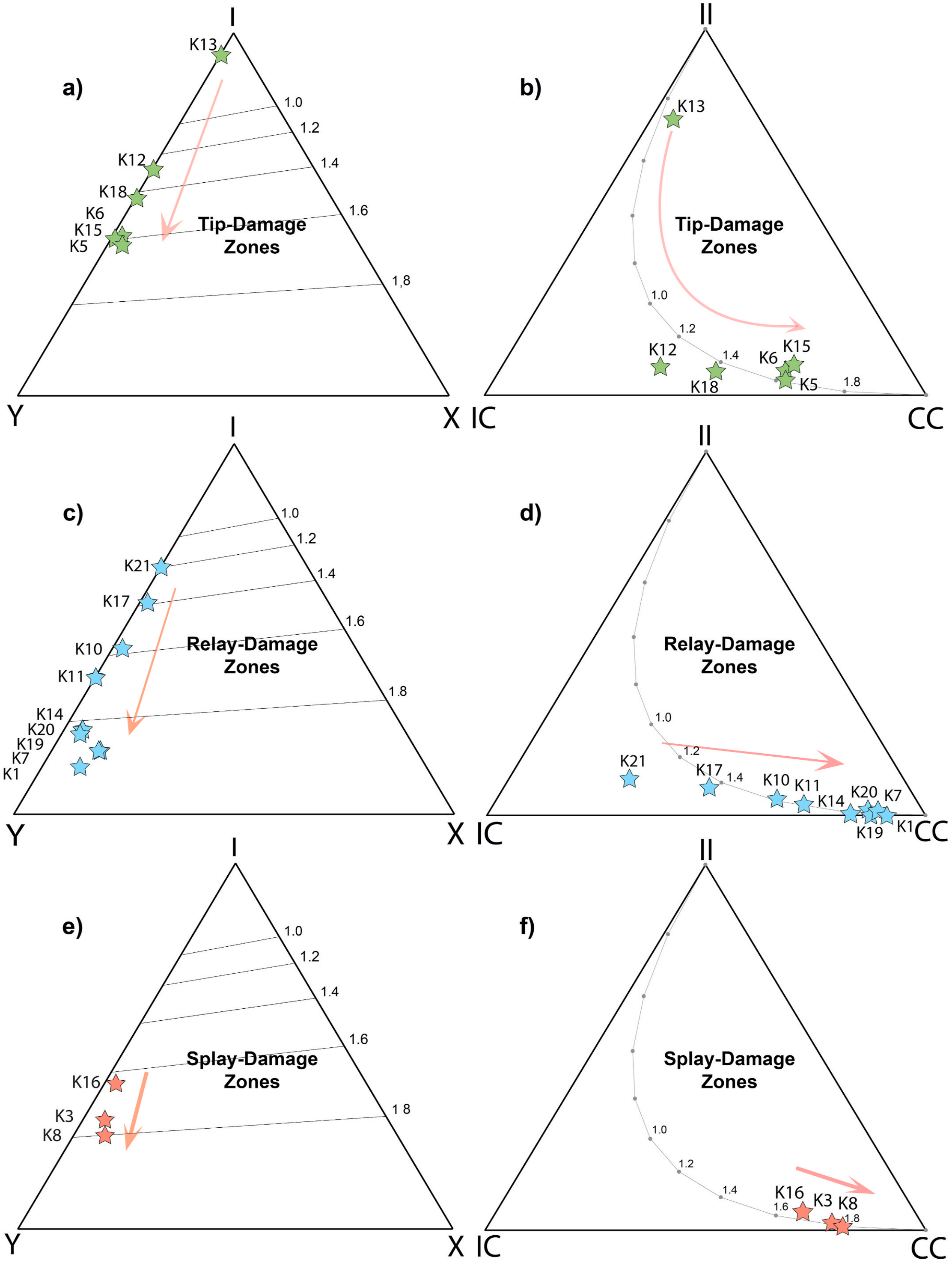

(caption on next page)

**Fig. 7.** Node and branch triangular plots of each damage zone example. Fault tip-damage zones are presented in a) and b); Relay-damage zones are presented in c) and d); and splay-damage zones are presented in e) and f). The node triangles (left) illustrate the proportions of *I*-, *Y*- and *X*-nodes mapped for each damage zone. The branch triangles (right) illustrate the proportions of *II*-, *IC*-, and *CC*-branches mapped for each damage zone. The locality name of each damage zone is indicated and the red arrows correspond with the arrangement of the fracture trace maps in Figs. 4–6. (For interpretation of the references to colour in this figure legend, the reader is referred to the Web version of this article.)

**Table 1**
Topology and graph data for each fault damage zone example including: node and branch type proportions; graph metrics, i.e. number of nodes (*N*), branches (*B*), components (*K*) and regions (*R*); average degree ($<D>$); connections per branch ($C_B$). See text for definitions and derivation.

| Field Example | Damage Zone Type | Node Proportions | | | Branch Proportions | | | Graph Metrics | | | | Degree of Connectivity | |
|---|---|---|---|---|---|---|---|---|---|---|---|---|---|
| | | I | Y | X | II | IC | CC | N | B | K | R | <D> | $C_B$ |
| K12 | Tip - En Echelon | 63% | 37% | 0% | 8% | 56% | 36% | 51.5 | 47.5 | 4 | 0 | 1.8 | 1.3 |
| K13 | Tip - En Echelon | 89% | 11% | 0% | 70% | 9% | 22% | 3.5 | 3.5 | 1 | 1 | 2.0 | 0.5 |
| K5 | Tip - Horsetail | 42% | 55% | 3% | 4% | 30% | 66% | 218 | 251 | 4 | 37 | 2.3 | 1.6 |
| K6 | Tip - Bifurcating | 44% | 55% | 2% | 6% | 28% | 65% | 306 | 356 | 6 | 56 | 2.3 | 1.6 |
| K15 | Tip - Bifurcating | 45% | 53% | 2% | 8% | 26% | 66% | 209.5 | 244.5 | 3 | 38 | 2.3 | 1.6 |
| K18 | Tip - Horsetail | 55% | 45% | 0% | 6% | 44% | 49% | 29.5 | 29.5 | 2 | 2 | 2,0 | 1.4 |
| K10 | Relay - Intact | 44% | 55% | 1% | 5% | 31% | 64% | 108 | 121 | 3 | 16 | 2.2 | 1.6 |
| K17 | Relay - Intact | 57% | 41% | 2% | 8% | 46% | 47% | 48.5 | 48.5 | 4 | 4 | 2.0 | 1.4 |
| K21 | Relay - Intact | 67% | 33% | 0% | 10% | 60% | 30% | 21 | 18 | 3 | 0 | 1.7 | 1.2 |
| K11 | Relay - Singly Breached | 38% | 63% | 0% | 3% | 26% | 71% | 32 | 35 | 1 | 4 | 2.2 | 1.7 |
| K14 | Relay - Singly Breached | 23% | 73% | 4% | 1% | 17% | 83% | 106.5 | 136.5 | 2 | 32 | 2.6 | 1.8 |
| K20 | Relay - Multiply Breached | 22% | 74% | 4% | 2% | 12% | 86% | 151.5 | 202.5 | 2 | 53 | 2.7 | 1.8 |
| K1 | Relay - Multiply Breached | 13% | 79% | 9% | 0% | 9% | 91% | 294.5 | 413.5 | 2 | 121 | 2.8 | 1.9 |
| K7 | Relay - Multiply Breached | 17% | 72% | 11% | 1% | 10% | 89% | 888 | 1242.5 | 3 | 357.5 | 2.8 | 1.9 |
| K19 | Relay - Multiply Breached | 17% | 72% | 10% | 0% | 13% | 88% | 30 | 40 | 1 | 11 | 2.7 | 1.9 |
| K3 | Splay | 30% | 65% | 5% | 2% | 20% | 78% | 2665 | 3352 | 33 | 720 | 2.5 | 1.8 |
| K8 | Splay | 26% | 67% | 7% | 1% | 18% | 81% | 2851.5 | 3696.5 | 11 | 856 | 2.6 | 1.8 |
| K16 | Splay | 40% | 58% | 2% | 5% | 25% | 70% | 715 | 848.5 | 22 | 155.5 | 2.4 | 1.6 |

plots, reflecting a low variability in topology (Fig. 7e and f). They generally have topologies more similar to the relay-damage zones than the tip-damage zones (Fig. 7). The node plot shows that the splay-damage zones have large proportions of connecting nodes, ranging from ~60% to ~74% (Table 1). There are also very few *II*-branches (<6%) within the splay-damage zones with the largest proportion of their branches being fully connected *CC*-branches (>70%; Fig. 7f and Table 1).

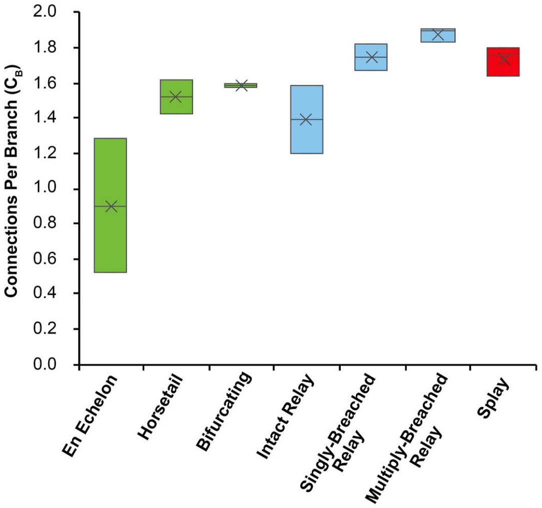

**Fig. 8.** Box plots illustrating the range (box), mean (cross) and median (line) in connections per branch for each type and style of damage zone. Green, blue and red boxes correspond to tip-, relay- and splay-damage zones respectively with different structural styles are listed along the x-axis. (For interpretation of the references to colour in this figure legend, the reader is referred to the Web version of this article.)

The differences in topology between the three types of fault damage zone are reflected in the number of connections per branch ($C_B$; Fig. 8 and Table 1), with tip-damage zones having the lowest range of $C_B$ (0.52–1.62), with en echelon tips forming the least connected fracture networks ($C_B < 1.30$; Fig. 8). Horsetail and bifurcating tips produce better connected tip-damage zones with values of $C_B > 1.40$. In the relay-damage zones $C_B$ increases from less connected intact relays to very connected multiply-breached relays (Fig. 8). Intact relays display a similar range of $C_B$ to the tip-damage zones as they comprise two overlapping but soft linked fault tips. In contrast, multiply-breached relays are the most connected damage zone examples with values of $C_B > 1.85$, which can be expected from hard linked fault segments. Splay-damage zones also produce well connected fracture networks with values of $C_B > 1.60$, similar to singly-breached relays (Fig. 8).

### 5.3. Graph metrics

The plots in Fig. 9 compare various graph metrics (i.e. number of nodes, branches, regions and compartments; Table 1) of the different damage zone fracture networks. Fig. 9a and b compare the number of branches (*B*) to the number of regions (*R*) and components (*K*), respectively. These metrics are normalised to the total number of nodes (*N*), which accounts for different sizes of network (i.e. larger networks produce greater numbers of nodes). Furthermore, this produces the parameter $B/N$ (number of branches per node or branch to node ratio) on the y-axis, which is the equivalent of $<D>/2$, thus linking to the degree of connectivity. The plots indicate clear relationships where an increase in the branch to node ratio ($B/N$) results in an increase in the number of regions (Fig. 9a) and a decrease in the number of components (Fig. 9b). The combined effect of these relationships means that the number of regions per component ($R/K$) within each damage zone increases with the ratio of branches to nodes ($B/N$) (Fig. 9c). This increase

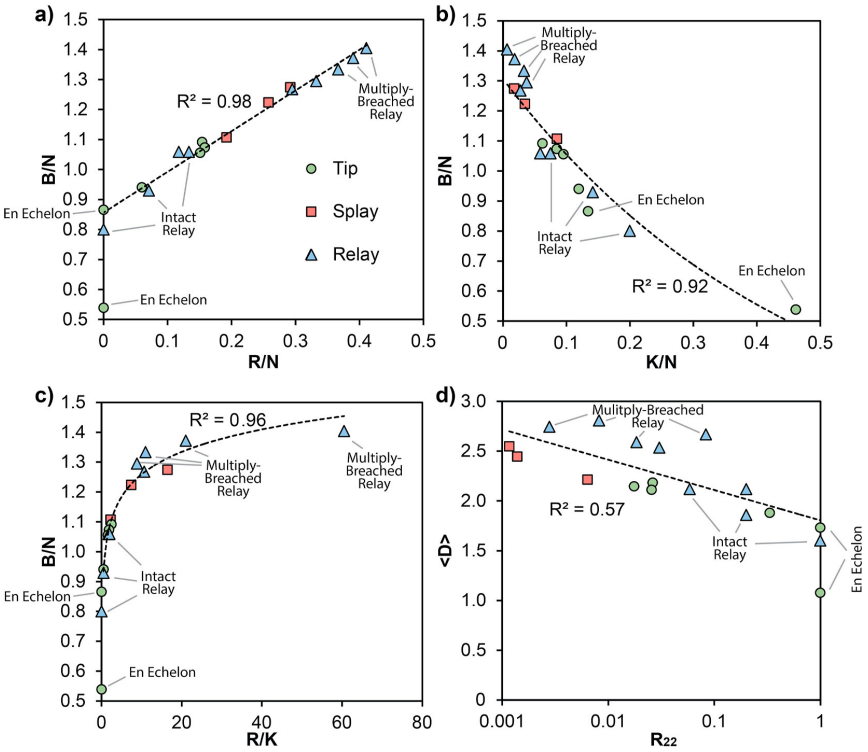

**Fig. 9.** Scatter plots comparing different graph metrics for each tip-damage zone (green circles), relay-damage zone (blue triangles) and splay-damage zone (red squares). a) Plot of the ratio of branches to nodes ($B/N$) against the ratio of regions to nodes ($R/N$); b) Plot of the ratio of branches to nodes ($B/N$) against the ratio of components to nodes ($K/N$); c) Plot of the ratio of branches to nodes ($B/N$) against the ratio of regions to components ($R/K$); d) Plot of the average degree ($<D>$) against the dimensionless block intensity ($R_{22}$). Note that values for $B/N$ correspond to $<D>/2$. (For interpretation of the references to colour in this figure legend, the reader is referred to the Web version of this article.)

in the regions per component does not begin until the fracture networks reach a branch to node ratio of 0.9 (Fig. 9c), equivalent to an average degree ($<D>$) of 1.8, as no regions form below this degree of connectivity (Fig. 9a).

The tip-damage zones form fracture networks with low numbers of regions (Fig. 9a) but have high numbers of components (Fig. 9b). This is particularly the case for en echelon tips which form no regions (Fig. 9a) but have large proportions of isolated ($II$) and singly connected ($IC$) branches (e.g. Figs. 4 and 7b). As a result, they produce the lowest branch to node ratios ($B/N < 0.9$). The relay-damage zones show a large spread in graph metrics with intact relays overlapping with tip-damage zones, so producing less regions but more components in comparison to the singly-breached and multiply-breached relays (Fig. 9a and b). The multiply-breached relays produce the most number of regions and least number of components of all the studied damage zones, resulting in the highest number of regions per component (Fig. 9c). Splay-damage zones show the least spread in graph metrics with relatively moderate numbers of regions and low numbers of components (Fig. 9a and b), thus displaying similar characteristics to the singly- and multiply-breached relays.

Overall there appears to be a trend where, relative to the size of their networks, the more structurally complex damage zones (i.e. singly- and multiply-breached relays) produce more regions per component than for simple damage zones (i.e. en echelon tips and intact relays). This relationship is reflected in Fig. 9d, which illustrates influence of the degree of connectivity, with the dimensionless block intensity ($R_{22}$) tending to 1 as the average degree ($<D>$) decreases towards 1.8. This suggests simple en echelon tips leave the rock mass relatively intact ($R_{22} = 1$), as they produce no blocks, whereas the more complex multiply-breached relays break it into many blocks ($R_{22} \ll 1$). The fracture networks of splay-damage zones show the lowest values of $R_{22}$ ($<0.01$), suggesting they produce the most amount of damage in comparison to the other damage zones.

### 5.4. Spatial variations in topology and damage

One example of each type of damage zone (tip-, relay-, splay-) is selected for full presentation to explore the spatial distribution of different topological parameters and fracture abundances. Specifically, we use contour maps in combination with circle samples (CS) that record along-strike/along-dip profiles in fracture intensity, connecting node frequency, average degree ($<D>$) and the dimensionless block intensity ($R_{22}$) (Figs. 10–12). We focus on describing the locations of structurally complex areas, with high fracture intensities and a range of fracture orientations, within each type of damage zone and their relationship with topological and graph measures.

#### 5.4.1. Fault tip damage zone: example K5

Example K5 is a small (max. throw: 1 cm) NNW-dipping normal fault exposed in a pavement outcrop within the MGLM (Fig. 1b). The normal fault tip comprises two main fault segments, that are soft linked, and splays into a set of WNW-trending wing-cracks (Fig. 10a). The fracture

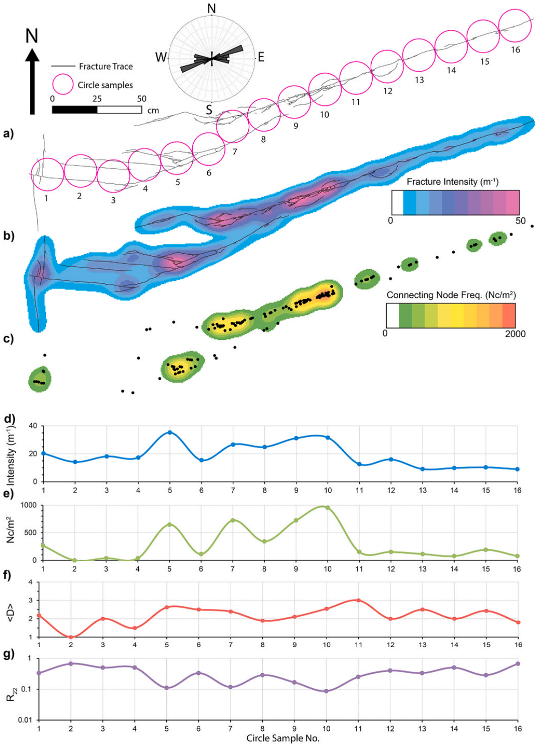

**Fig. 10.** a) Digitised fracture trace map of the tip-damage zone at locality K5 showing the position of 16 circle samples and a length-weighted rose diagram of the fracture trends. b) Contour map, showing the fracture abundance measure "fracture intensity". c) Contour map showing the topological parameter "connecting node frequency". d) Along strike profile of fracture intensity measured in each circle sample in Fig. 10a e) Along strike profile of connecting node frequency ($Nc/cm^2$) measured in each circle sample in Fig. 10a f) Along strike profile of average degree ($<D>$) measured in each circle sample in Fig. 10a g) Along strike profile of the dimensionless bock intensity ($R_{22}$) measured in each circle sample in Fig. 10a.

intensity map (Fig. 10b) shows values mostly below 20 $m^{-1}$, with bullseyes of higher values restricted to bifurcation points (e.g. CS5, CS7 and CS8; Fig. 10a) or areas of lensing (e.g. CS9 to CS10; Fig. 10a) within the main part of the tip-damage zone. Bullseyes in the connecting node frequency map are also restricted to areas of bifurcation and lensing (Fig. 10c). This relationship is reflected on along-strike profiles of fracture intensity (Fig. 10d) and connecting node frequency (Fig. 10e) with corresponding peaks at CS5, CS7 and CS10.

Values of $R_{22}$ are $>0.1$, indicating a low to moderate amount of damage, but show a clear inverse relationship to connecting node frequency and fracture intensity with lows at CS5, CS7 and CS10. This indicates that these areas of bifurcation and lensing within the damage zone are sites of increased damage where high fracture abundances and numbers of connections break the rock mass into numerous blocks. Values for $<D>$ vary from 1 to 3, forming a broadly undulating but consistent profile with a decrease towards end of the tip zone from CS4 to CS1. They do not appear to correlate directly with the other profiled measures suggesting that the degree of connectivity is spatially less variable and not directly related to local increases in fracture intensity and connecting node frequency.

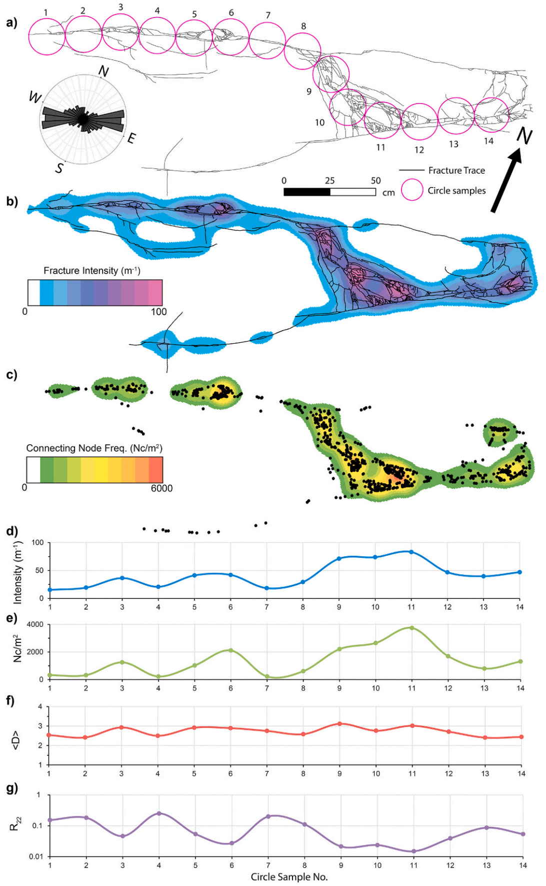

**Fig. 11.** a) Digitised fracture trace map of the relay-damage zone at locality K7, showing the position of 14 circle samples and a length-weighted rose diagram of the fracture trends. b) Contour map, showing the fracture abundance measure "fracture intensity". c) Contour map showing the topological parameter "connecting node frequency". d) Along strike profile of fracture intensity measured in each circle sample in Fig. 11a e) Along strike profile of connecting node frequency ($Nc/cm^2$) measured in each circle sample in Fig. 11a f) Along strike profile of average degree ($<D>$) measured in each circle sample in Fig. 11a g) Along strike profile of the dimensionless bock intensity ($R_{22}$) measured in each circle sample in Fig. 11a.

### 5.4.2. Relay damage zone: example K7

Example K7 is a small (max. throw: 8 cm) multiply-breached relay, exposed in a pavement outcrop within the MGLM (Fig. 1b), between two right-stepping ENE-trending normal faults that dip towards NNW. Within the relay-damage zone, a wide range of fracture orientations are observed with ~NW-trending faults/fractures breaching across the relay (Fig. 11a). Fracture intensities are generally less than 50 $m^{-1}$ along the relay bounding faults with minor bullseyes and peaks associated with lensing (i.e. CS3, CS5 and CS6; Fig. 11b and d). The highest intensity values ($>50$ $m^{-1}$) are observed along the relay breach with bullseyes where breaching fractures splay from or abut the ENE-trending relay bounding faults (i.e. CS8 to CS9 and CS11 to CS12; Fig. 11b and d). The highest connecting frequencies ($>2000$ $N_c/m^2$) also occur along the relay breach (i.e. CS8-CS12), with a major bullseye and maximum profile peak in sample CS11 where breaching fractures splay and abut

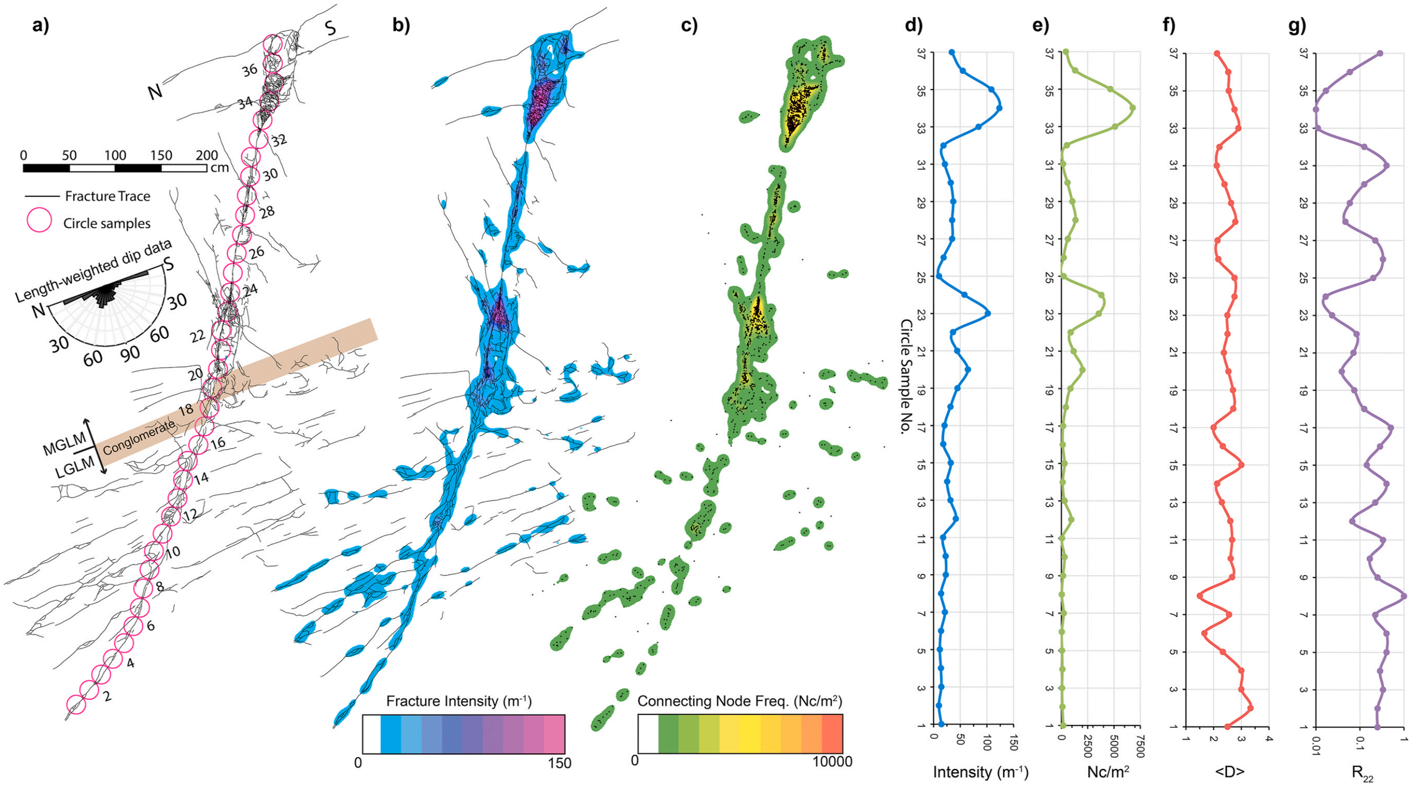

**Fig. 12.** a) Digitised fracture trace map of the splay-damage zone at locality K3, showing the position of 37 circle samples and a length-weighted rose diagram of the fracture dip trends. Note that the boundary between the MGLM and LGLM is indicated as well as the position of a phosphoritic conglomerate. b) Contour map, showing the fracture abundance measure "fracture intensity". c) Contour map showing the topological parameter "connecting node frequency". d) Along-dip profile of fracture intensity measured in each circle sample in Fig. 12a e) Along-dip profile of connecting node frequency ($Nc/cm^2$) measured in each circle sample in Fig. 12a f) Along-dip profile of average degree ($<D>$) measured in each circle sample in Fig. 12a g) Along-dip profile of the dimensionless bock intensity ($R_{22}$) measured in each circle sample in Fig. 12a.

the southern relay bounding fault (Fig. 11c and e). Minor bullseyes and peaks in connecting node frequency also occur in areas of lensing along the relay bounding faults (i.e. CS3 and CS6).

The $R_{22}$ values in example K7 again show an inverse relationship with intensity and connecting node frequency and are considerably lower on average ($<0.1$) than example K5, indicating a moderate to high level of damage. The increased fracture abundance along with higher numbers of intersections in the breached area produce the lowest $R_{22}$ values, tending towards 0.01 (Fig. 11g). Unlike the other parameters the average degree ($<D>$) is relatively constant along-strike of the damage zone, ranging from ~2.5 to ~3 (Fig. 11f). Slightly higher values of $<D>$ coincide with areas of lensing along the relay bounding faults and the breached relay area, matching patterns in fracture intensity and connecting node frequency.

### 5.4.3. *Splay fault damage zone: example K3*

Example K3 is a NNW-dipping normal fault observed in a cliff section offsetting the LGLM and MGLM with a maximum throw of ~40 cm (Fig. 1b). The fault is planar in the MGLM, with a dip of ~60°, whereas in the LGLM the fault has a more listric character (Fig. 12a). Within the LGLM fracturing around the fault is dominated by long layer-parallel fractures, whereas within the MGLM there are numerous steeply dipping antithetic and synthetic faults/fractures. Key features include a lens stretching in and above a phosphoritic conglomerate at the top of the LGLM and a footwall splay zone located in the upper part of the outcrop within the MGLM (Fig. 12a).

Within the LGLM (CS1 to CS16) the splay damage zone shows relatively low fracture intensities ($<50\ m^{-1}$; Fig. 12b and d) and connecting node frequencies ($<1000\ N_c/m^2$; Fig. 12c and e). Furthermore, along this interval $R_{22}$ values undulate around an average of ~0.3, a relatively low amount of damage. The transition from the LGLM through the phosphoritic conglomerate to the MGLM (CS17 to CS21) shows an increase in both fracture intensity and connecting node frequency, with peaks at CS20 immediately above the conglomerate. This spatial pattern is mirrored by the $R_{22}$ profile, which decreases to values $< 0.1$ representing an increase in damage (Fig. 12g). Values of $<D>$ are highly variable within the LGLM, ranging from 1.5 to 3.5 (Fig. 12f), which contrasts with the relatively low and stable profiles of fracture intensity and connecting node frequency. The high variability in connectivity within the LGLM could be related to the numerous layer-parallel fractures obliquely cross-cutting the main fault and its subsidiary faults and fractures.

In the MGLM, discrete bullseyes and peaks in both fracture intensity (Fig. 12b and d) and connecting node frequency (Fig. 12c and e) occur where the largest antithetic fault/fracture intersects the main fault (CS22 to CS24). At this intersection point there is also a significant decrease in $R_{22}$, which tends towards 0.01 (Fig. 12g), indicating a high amount of damage with the rock mass very broken up at this location. The highest fracture intensities and connecting node frequencies along K3 occur within the footwall splay zone (CS32 to CS37), where broad bullseyes and peaks occur immediately above the main splay bifurcation point (Fig. 12a–e). The peaks in fracture intensity and the number of connections measured in these circle samples coincide with the lowest $R_{22}$ values (0.01; Fig. 12g), highlighting that these samples represent a highly damaged zone. Within the MGLM, highs in $<D>$ broadly coincide with highs in fracture intensity and connecting node frequency as well as lows in $R_{22}$. This shows that the degree of connectivity can be influenced spatially by large changes in the fracture abundance and the number of connections.

## 6. Discussion

### 6.1. *New characteristics of damage zones from topology and graph metrics*

The application of topology and graph metrics to damage zones adds information to their characterisation based on the underlying relationships between the fractures within their fracture networks. The node and branch topological model (Figs. 3a and 13a) describes the different types of connections between the fractures and how fracture traces are connected to others within the network (Sanderson and Nixon, 2015, 2018). In addition, graph metrics provide a generalisation of the constitutive elements (nodes, branches, regions and components) that make-up each fracture network (Figs. 3b and 13b; Sanderson et al., 2019) and how those elements relate to one another. Thus, these two approaches provide a means to classify networks based on their arrangement and connectivity, complementing traditional studies that focus on describing their architecture and geometry (e.g. McGrath and Davison, 1995; Kim et al., 2004; Choi et al., 2016; Peacock et al., 2017). Our results indicate that different types of damage zone are characterised by distinct topological signatures and graph metrics, with differences and similarities between each type (as summarised by Fig. 13):

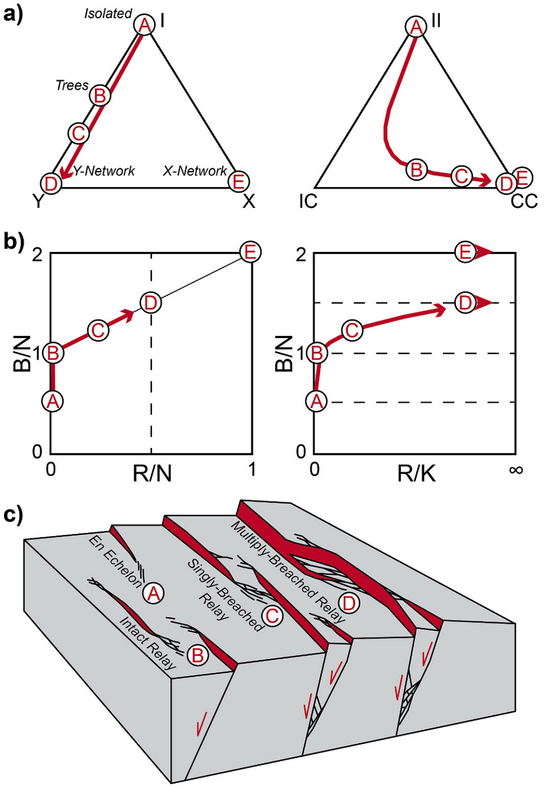

**Fig. 13.** Schematic diagram illustrating the topological and graph characteristics of fault damage zones. a) Node (left) and branch (right) triangles. b) Plots of different graph metrics with the ratio of branches to nodes ($B/N$) plotted against the ratio of regions to nodes ($R/N$) and the ratio of regions to components ($R/K$) on the left and right, respectively. Positions A to E represent fracture networks with different topological and graph characteristics. The red arrows illustrate potential topological pathways for an evolving damage zone, as illustrated by the block diagram in c).

- *Tip-damage zones (Positions A-C)* – En echelon tips have simple networks consisting of numerous isolated fractures, thus they plot between positions A and B on Fig. 13 as unconnected fracture networks (i.e. $C_B < 1.3$; Fig. 8) with high proportions of *I*-nodes and *II*-branches

(Fig. 7). These networks comprise numerous components with very low branch to node ratios ($B/N < 1$) and no regions (Fig. 9). At position B, complex tip-damage zones (e.g. horsetail tips, bifurcating tips) form, producing more connected fracture networks (i.e. $C_B =$ 1.3–1.6; Fig. 8) with increased proportions of $Y$-nodes and high proportions of $IC$-branches (Fig. 7). These networks begin to form numerous small tree-like components with low branch to node ratios ($B/N = 1$) and very few regions (Fig. 9).

- *Relay-damage zones (Positions B-D)* – Intact relays consist of two overlapping fault tips that are approach one another but do not link, resulting in characteristics similar to tip-damage zones, generally plotting between positions B and C on Fig. 13. Singly-breach relays plot close to C, forming complex and moderately connected networks (i.e. $C_B > 1.6$; Fig. 8) with greater proportions of $Y$-nodes and $CC$-branches (Fig. 7b). Thus, their networks produce large tree-like components with high branch to node ratios ($B/N$ up to $\sim$1.3) and moderate numbers of regions (Fig. 9). Finally, multiply-breached relays tend to plot closer to D, representing well-connected networks (with $C_B > 1.8$; Fig. 8) dominated by $Y$-nodes and high proportions of $CC$-branches. These consist of a few large interconnected components with very high branch:node ratios ($B/N > 1.3$) and high numbers of regions (Fig. 9).
- *Splay-damage zones (Positions C-D)* – Although these fault damage zones are observed in cross-section they show similar characteristics to singly- and multiply-breached relays, plotting between positions C and D on Fig. 13. The fracture networks display a moderate degree of connectivity (i.e. $C_B > 1.6$; Fig. 8), due to high proportions of $Y$-nodes and $CC$-branches (Fig. 7). They also produce large tree-like components with high branch to node ratios, the same as singly-breached relays, but generally have fewer components with more regions (i.e. Fig. 9).

The topological characteristics and graph metrics of the studied damage zones indicate a clear link to their structural style and complexity (i.e. high fracture abundances, range of orientations), with tip-damage zones forming the simplest networks and relay-damage zones forming the most complex. Tip-damage zones accommodate decreases in displacement at fault tips and are generated by stress concentrations, which are enhanced by larger displacement gradients (e.g. Cowie and Scholz, 1992; Cowie and Shipton, 1998; Shipton and Cowie, 2003). However, relay-damage zones involve the interacting stress fields of two fault tips, which inhibits tip propagation and increases displacement gradients as well as causes local rotations in the stress field between the two faults (c.f. Willemse et al., 1996; Crider and Pollard, 1998; Gupta and Scholz, 2000; Kattenhorn et al., 2000). Thus, the resultant damage zones will exhibit greater fracture intensities and varied fracture orientations in comparison to isolated fault tip-damage zones (e.g. Peacock and Sanderson, 1994; Bastesen and Rotevatn, 2012; Fossen and Rotevatn, 2016). Such increases in fracture intensity and variations in fracture orientation will increase connectivity (e.g. Sanderson and Nixon, 2018). Thus, more structurally complex damage zones are generally better connected, with greater proportions of connecting nodes and $CC$-branches that form larger components with more regions. Similar relationships between structural complexity and topological character have been described for rift fault networks, where complex multiphase rifts form more connected networks with higher proportions of $Y$-nodes and $CC$-branches in comparison to simple single-phase rifts (Morley and Nixon, 2016; Duffy et al., 2017).

Overall these topological and graph characteristics provide new quantitative descriptions of network arrangement and connectivity, allowing a more meaningful comparison of the different damage zone types. An additional advantage of using topology and graph theory is that they are dimensionless and therefore the topology of damage zones and their fracture networks can be used and compared on a range of scales. Furthermore, the distinct topologies and trends in their graph metrics make it possible to predict the properties of the different damage zones. This can be useful when estimating deformation around fault tips and fault linkage in the subsurface, where small-scale structures in damage zones are not easily observed due to data resolution limitations (e.g. seismic reflection data; Enge et al., 2007) Thus this can have implications when assessing fluid-flow conduits and barriers (e.g. Leveille et al., 1997), the integrity of structural traps (e.g. Gartrell et al., 2006) and the structural configuration and compartmentalization of reservoirs in large-scale fault tips and relay damage zones (e.g. Pickering et al., 1997; Rotevatn et al., 2009; Rotevatn and Fossen, 2011; Richards et al., 2015).

### 6.2. Damage zone development and topological pathways

When faults grow they propagate, interact and accumulate slip to increase in both length and displacement, allowing them to accommodate greater strains and become more linked (e.g. Cowie and Scholz, 1992; Peacock and Sanderson, 1994; Cartwright et al., 1995; Cowie et al., 2000; Walsh et al., 2001; Childs et al., 2003; Bull et al., 2006; Duffy et al., 2017; Rotevatn et al., 2019). During these processes of fault evolution, damage zones will generally increase in size and become more complex (Shipton and Cowie, 2001, 2003; e.g. Kim et al., 2003; Fossen et al., 2005; Childs et al., 2009; Bastesen and Rotevatn, 2012). For example, slip accumulation on a fault will enhance stress concentrations at the fault tip, producing a wider and more intense tip-damage zone (c.f. Shipton and Cowie, 2003). Furthermore, if the fault tip propagates and interacts with another fault then the tip-damage zone will evolve into a relay-damage zone, adding more damage structures to or overprinting the existing damage zone (Kim et al., 2003, 2004).

The variety of structural styles and complexities of the tip- and relay-damage zones observed in the study area illustrate this spectrum of damage zone development, as presented in the evolutionary model shown in Fig. 13c (i.e. A-D). Firstly, we infer that en echelon tips (A) might evolve into more complex horsetail and bifurcating tips (B) with increased slip and tip propagation, similar to the tip-damage zone evolution suggested by Kim et al. (2003) for strike-slip faults. Secondly, the three types of relay-damage zone clearly represent different stages of fault linkage (e.g. Peacock and Sanderson, 1991, 1994; Walsh and Watterson, 1991; Huggins et al., 1995; Childs et al., 2009; Bastesen and Rotevatn, 2012; Fossen and Rotevatn, 2016), with intact relays (B) expected to evolve into singly-breached relays (C) and finally multiply-breached relays (D) as the faults progressively interact and link. Using this evolutionary model, we discuss how the topology and graph characteristics of the damage zones might develop and how their arrangement and connectivity potentially evolves.

The topological and graph characteristics of the tip- and relay-damage zones (Figs. 7 and 9) indicate that they evolve along well-constrained topological pathways, as illustrated by the red arrows between positions A and D on Fig. 13a and b. The tip-damage zones only evolve part way along these pathways, initially dominated by I-nodes and II-branches before forming more $Y$-nodes and $IC$-branches and eventually $CC$-branches (Fig. 13a). This represents fractures splaying and bifurcating as horsetail/bifurcating tip-damage zones develop. The node to branch ratios of the damage zones increase (particularly between positions A and B) as components increase in size and begin to link to form trees. After position B the components are connected enough to start forming regions (Fig. 13b).

Relay-damage zones evolve further along the topological pathways, becoming dominated by $Y$-nodes and $CC$-branches (Fig. 13b; positions B-D) as across-fault fractures develop within the relay and abut/cross-cut each other. Once the relays start to breach at position C, the number of components decreases as the two tip-damage zones of the interacting faults link to form larger interconnected networks. The number of regions per component substantially increases as more and more regions form within these interconnected damage zones.

These topological pathways provide important insights into how networks develop in damage zones during fault evolution. The node and branch topologies evolve along similar pathways predicted for rift fault networks as shown by Duffy et al. (2017). They apply node and branch topology to physical clay analogue models, showing how topology changes in fault networks with increasing finite strain. Their results are compared with natural examples of rift fault networks and also highlight the importance of across-strike faulting in reaching more evolved topologies. The similarities between the damage zone fracture networks and rift fault networks suggest that the pathways highlighted in this study could be more widely applied to larger scale fault networks.

### 6.3. *Controls on spatial variability along fault damage zones*

All the studied damage zones show spatial variability in their complexity along-strike/dip. More simple zones consist of a fault segment and damage with low fracture intensities and connecting node frequencies, which leave the rock mass relatively intact. These separate more complex parts consist of higher fracture intensities and connecting node frequencies that break up the rock mass into numerous blocks. These complex zones are often located around irregularities along the faults/fractures, such as bends that create lenses or intersections associated with bifurcations/abutments. As faults accrue displacement, these irregularities can locally perturb or concentrate stress, enhancing the development of fractures within the damage zone (e.g. Segall and Pollard, 1980; Rawnsley et al., 1992; Willemse and Pollard, 1998; Maerten et al., 2002; Berg and Skar, 2005; Fossen et al., 2005; Childs et al., 2009).

The fault splay-damage zones also show variations in damage between the different limestone members observed in the study area. In the Lower Globergerina Limestone Member (LGLM) a simple damage zone is observed, whereas in the Middle Globergerina Limestone Member (MGLM) more complex zones develop around intersections with splay faults and numerous antithetic faults. Studies have shown how changes in the mechanical and compositional properties of limestones can affect fracturing and faulting (e.g. Wennberg et al., 2006; Ortega et al., 2010; Michie et al., 2014; Korneva et al., 2018). Ortega et al. (2010) and Korneva et al. (2018) highlight how the level of dolomitization can control fracture intensity, but the limestones in the study area do not appear dolomitized. Wennberg et al. (2006) and Michie et al. (2014) illustrate the influence of texture and grainsize on fracturing and fault zone development, respectively. Both indicate that more fine-grained mud-supported limestones are likely to develop more fractures and large fracture networks than more coarse-grained, grain-supported limestones. As the MGLM consists of mudstones and the LGLM is composed of packstones and wackestones (Pedley et al., 1976; Pedley, 1987), we suggest the difference in damage zone development is caused by contrasts in grain size and mud composition of the limestones. This highlights the importance of considering the lithology when considering the character of damage zones and fault related deformation.

The presence of structurally complex zones highlights that deformation is not evenly distributed within a damage zone. It has been shown that such zones of increased fracturing and complexity can accommodate greater strains within the damage zone and help maintain strain compatibility (Nixon et al., 2019). Furthermore, such zones of complexity can have an impact on the behaviour of fluids within a damage zone. If the fractures are open, then these zones of high fracture abundance can enhance and localise flow (e.g. Davatzes et al., 2003; Kim and Sanderson, 2010; Dimmen et al., 2017, 2020). The variety in fracture orientations and the increased number of intersections helps maintain flow pathways, due to a greater probability that fractures are optimally orientated to remain open in any given stress-field (Sanderson and Zhang, 2004). Thus, in tight carbonate rocks with low matrix permeability the structurally complex zones can represent highly-permeable conduits for fluid flow (e.g. Tamagawa and Pollard, 2008; Rotevatn and Bastesen, 2014).

### 6.4. *Insights into the three-dimensional connectivity of faults tips and relay zones*

Traditionally many of the descriptions of fault tip- and relay-damage zones have been acquired from two-dimensional outcrop surfaces (e.g. McGrath and Davison, 1995; Kim et al., 2003; Peacock et al., 2017; Nixon et al., 2019; this study), and there have been less observations of their three-dimensional character. Multiple sections through a fracture network can be used for providing more representative measurements of the network in three-dimensions – for example, one could apply stereology and average results from the different sections (e.g. Sanderson et al., 2019). The splay-damage zones in this study represent cross sections through either a relay- or tip-damage zone, providing an opportunity to compare their plan-view and cross-sectional characteristics in topology and connectivity. In plan-view there is much variability in topology (i.e. Fig. 7) and connectivity (i.e. Fig. 8) of the different tip- (i.e. $C_B = \sim 0.5$ to $\sim 1.6$) and relay-damage zones (i.e. $C_B = \sim 1.2$ to $\sim 1.9$). In contrast, the splay-damage zones produce more consistent topologies and connectivity (i.e. $C_B = \sim 1.65$ to $\sim 1.8$), despite variations in style and complexity (i.e. Figs. 7 and 8). This suggests that even if fractures are not well connected along-strike (i.e. $C_B < 1.5$; Sanderson and Nixon, 2015, 2018), it is likely that they are connected along-dip in cross-section (i.e. $C_B > 1.5$; Sanderson and Nixon, 2015, 2018). This is due to the formation of both synthetic and antithetic fractures within the damage zones and their opposing dip directions (i.e. Fig. 6). In low-permeability carbonate rocks, where the fractures provide permeability, such variations in fracture connectivity increases the potential for anisotropy in the rocks permeability (e.g. Balberg and Binenbaum, 1983; Long and Witherspoon, 1985; Zhang and Sanderson, 1995) as it impacts the percolation threshold of the fracture network (e.g. Manzocchi, 2002; Saevik and Nixon, 2017; Sanderson and Nixon, 2018). For example, if the fractures act as fluid conduits then tip-damage zones are likely to have greater along-dip permeabilities due to their low along-strike (i.e. plan view) connectivity, whereas singly-breached and multiply-breached relays are likely to have a more isotropic permeability as the degree of connectivity is similar in both sections of observation.

## 7. Conclusion

Field-examples of different tip-, relay- and splay-damage zones, associated with small-scale normal faults in carbonate rocks from Malta, have been mapped in detail and analysed in terms of their geometry, topology and graph characteristics. This has allowed us to document and quantify the arrangement and connectivity of the damage zone fracture networks and how they vary spatially. In addition, placing the damage zones in the context of a fault evolutionary model has allowed us to explore the potential network development of fault damage zones. Key findings include:

- Different tip-, relay- and splay-damage zones show distinct topological and graph characteristics, which are closely related to the structural style and complexity of the damage zones.
- Tip-damage zones produce the simplest networks with higher proportions of *I*-nodes and *II-*/*IC*-branches, resulting in low to moderate degrees of connectivity (i.e. $C_B = \sim 0.5$ to $\sim 1.6$). Their networks include many isolated and small tree-like components that have few regions.
- Relay- and splay-damage zones produce more complex networks with higher proportions of *Y*-nodes and *CC*-branches, with moderate to high degrees of connectivity (i.e. $C_B = \sim 1.2$ to $\sim 1.9$). Their networks include large tree-like or interconnected components with the potential to develop numerous regions.
- Combining information from plan-view (tip- and relay-damage zones) and cross-section (splay-damage zones) examples can provide a more representative pseudo 3-D evaluation of a damage zones

topology and connectivity. Connectivity can vary considerably in plan-view but is more consistent in cross-section, which can be important for assessing permeability anisotropy.

- Locations of stress perturbations and concentrations (i.e. fault bends and fault intersection points) produce complex zones within each damage zone. These consist of higher fracture intensities and higher connecting node frequencies. Thus these complex zones exhibit greater amounts of damage, breaking the rock mass up into numerous blocks.
- As faults propagate, interact and accumulate slip their damage zones evolve along well constrained topological pathways. Networks are initially dominated by *I*-nodes and *II*-branches and evolve towards networks dominated by *Y*-nodes and *CC*-branches. Thus damage zone connectivity increases substantially as more and more fractures form in the damage zone. The components within the network will grow and link, evolving from many tree-like components to a few large interconnected components. In addition, the regions per component significantly increases as more regions form and components link.

The application of topology and graph theory to these different damage zones provides new information that complements traditional characterisations based on descriptions of their geometry and architecture. Furthermore, the topological and graph characterisation provides an important link to the fluid-flow behaviour of the damage zones by quantifying the arrangement and connectivity of their fracture networks. The distinct characteristics of the different damage zones in this study could provide useful insights when assessing flow properties of identified damage zones in the subsurface.

## CRediT authorship contribution statement

**Casey W. Nixon:** Writing - original draft, Formal analysis, Data curation, led the writing with input, All authors contributed to the collection and analysis of data, KN led the writing with input, All authors contributed to the collection and analysis of data. **Kari Nærland:** Writing - original draft, Formal analysis, Data curation, led the writing with input, All authors contributed to the collection and analysis of data. **Atle Rotevatn:** Formal analysis, Data curation, also helped with figures, All authors contributed to the collection and analysis of data. **Vilde Dimmen:** Writing - original draft, Formal analysis, Data curation, led the writing with input, All authors contributed to the collection and analysis of data. **David J. Sanderson:** Formal analysis, Data curation, All authors contributed to the collection and analysis of data.

## Declaration of competing interest

The authors declare that they have no known competing financial interests or personal relationships that could have appeared to influence the work reported in this paper.

## Acknowledgements

This research was funded by a VISTA scholarship (Project Number: 6257) – a basic research program in collaboration between The Norwegian Academy of Science and Letters, and Statoil (now Equinor). Sanderson acknowledges support from a Leverhulme Emeritus Fellowship. David Peacock is thanked for useful discussions.

## References

Adler, P.M., Thovert, J.F., 1999. Fractures and Fracture Networks. Kluwer Academic Publishers, Dordrecht.

Balberg, I., Binenbaum, N., 1983. Computer study of the percolation threshold in a two-dimensional anisotropic system of conducting sticks. Phys. Rev. B 28, 3799–3812. https://doi.org/10.1103/PhysRevB.28.3799.

Bastesen, E., Rotevatn, A., 2012. Evolution and structural style of relay zones in layered limestone-shale sequences: insights from the Hammam Faraun Fault Block, Suez rift, Egypt. J. Geol. Soc. 169, 477–488. https://doi.org/10.1144/0016-76492011-100.

Beach, A., Welbon, A.I., Brockbank, P.J., McCallum, J.E., 1999. Reservoir damage around faults; outcrop examples from the Suez Rift. Petrol. Geosci. 5, 109–116. https://doi.org/10.1144/petgeo.5.2.109.

Bennett, S., 1979. A Transgressive Carbonate Sequence Spanning the Paleogene Neogene Boundary on the Maltese Islands. Annales Geologiques Des Pays Helleniques, pp. 71–80.

Berg, S.S., Skar, T., 2005. Controls on damage zone asymmetry of a normal fault zone: outcrop analyses of a segment of the Moab fault, SE Utah. J. Struct. Geol. 27, 1803–1822. https://doi.org/10.1016/j.jsg.2005.04.012.

Bonson, C.G., Childs, C., Walsh, J.J., Schöpfer, M.P.J., Carboni, V., 2007. Geometric and kinematic controls on the internal structure of a large normal fault in massive limestones: the Maghlaq Fault, Malta. J. Struct. Geol. 29, 336–354. https://doi.org/10.1016/j.jsg.2006.06.016.

Bosence, D.W.J., Pedley, H.M., 1982. Sedimentology and palaeoecology of a Miocene coralline algal biostrome from the Maltese Islands. Palaeogeogr. Palaeoclimatol. Palaeoecol. 38, 9–43. https://doi.org/10.1016/0031-0182(82)90062-1.

Bull, J.M., Barnes, P.M., Lamarche, G., Sanderson, D.J., Cowie, P.A., Taylor, S.K., Dix, J. K., 2006. High-resolution record of displacement accumulation on an active normal fault: implications for models of slip accumulation during repeated earthquakes. J. Struct. Geol. 28, 1146–1166. https://doi.org/10.1016/j.jsg.2006.03.006.

Caine, J.S., Evans, J.P., Forster, C.B., 1996. Fault zone architecture and permeability structure. Geology 24, 1025–1028. https://doi.org/10.1130/0091-7613(1996)024<1025:FZAAPS>2.3.CO;2.

Cartwright, J., Trudgill, B., Mansfield, C., 1995. Fault growth by segment linkage: an explanation for scatter in maximum displacement and trace length data from the Canyonlands Grabens of SE Utah. J. Struct. Geol. 17, 1319–1326.

Childs, C., Manzocchi, T., Walsh, J.J., Bonson, C.G., Nicol, A., Schöpfer, M.P.J., 2009. A geometric model of fault zone and fault rock thickness variations. J. Struct. Geol. 31, 117–127. https://doi.org/10.1016/J.JSG.2008.08.009.

Childs, C., Nicol, A., Walsh, J.J., Watterson, J., 2003. The growth and propagation of synsedimentary faults. J. Struct. Geol. 25, 633–648.

Choi, J.-H., Edwards, P., Ko, K., Kim, Y.-S., 2016. Definition and classification of fault damage zones: a review and a new methodological approach. Earth Sci. Rev. 152, 70–87. https://doi.org/10.1016/J.EARSCIREV.2015.11.006.

Choi, J.H., Jin, K., Enkhbayar, D., Davvasambuu, B., Bayasgalan, A., Kim, Y.S., 2012. Rupture propagation inferred from damage patterns, slip distribution, and segmentation of the 1957 MW 8.1 Gobi-Altay earthquake rupture along the Bogd fault, Mongolia. Journal of Geophysical Research B: Solid Earth 117. https://doi.org/10.1029/2011JB008676.

Cowie, P.A., Gupta, S., Dawers, N.H., 2000. Implications of fault array evolution for synrift depocentre development: insights from a numerical fault growth model. Basin Res. 12, 241–261.

Cowie, P.A., Scholz, C.H., 1992. Growth of faults by accumulation of seismic slip. J. Geophys. Res. 97, 11085–11095.

Cowie, P.A., Shipton, Z.K., 1998. Fault tip displacement gradients and process zone dimensions. J. Struct. Geol. 20, 983–997. https://doi.org/10.1016/S0191-8141(98)00029-7.

Crider, J.G., Pollard, D.D., 1998. Fault linkage: three-dimensional mechanical interaction between echelon normal faults. J. Geophys. Res.: Solid Earth 103, 24373–24391. https://doi.org/10.1029/98jb01353.

Curewitz, D., Karson, J.A., 1997. Structural settings of hydrothermal outflow: fracture permeability maintained by fault propagation and interaction. J. Volcanol. Geoth. Res. 79, 149–168. https://doi.org/10.1016/S0377-0273(97)00027-9.

Dart, C.J., Bosence, D.W.J., McClay, K.R., 1993. Stratigraphy and structure of the Maltese Graben system. J. Geol. Soc. 150, 1153–1166. https://doi.org/10.1144/gsjgs.150.6.1153.

Davatzes, N.C., Aydin, A., Eichhubl, P., 2003. Overprinting faulting mechanisms during the development of multiple fault sets in sandstone, Chimney Rock fault array, Utah, USA. Tectonophysics 363, 1–18. https://doi.org/10.1016/S0040-1951(02)00647-9.

Dimmen, V., Rotevatn, A., Nixon, C.W., 2020. The relationship between fluid flow, structures, and depositional architecture in sedimentary rocks: an example-based overview. Geofluids 2020, 1–19. https://doi.org/10.1155/2020/3506743. Article ID 3506743.

Dimmen, V., Rotevatn, A., Peacock, D.C.P., Nixon, C.W., Nærland, K., 2017. Quantifying structural controls on fluid flow: insights from carbonate-hosted fault damage zones on the Maltese Islands. J. Struct. Geol. 101, 43–57. https://doi.org/10.1016/J.JSG.2017.05.012.

Dockrill, B., Shipton, Z.K., 2010. Structural controls on leakage from a natural CO2 geologic storage site: central Utah. U.S.A. Journal of Structural Geology 32, 1768–1782. https://doi.org/10.1016/j.jsg.2010.01.007.

Duffy, O.B., Nixon, C.W., Bell, R.E., Jackson, C.A.L., Gawthorpe, R.L., Sanderson, D.J., Whipp, P.S., 2017. The topology of evolving rift fault networks: single-phase vs multi-phase rifts. J. Struct. Geol. 96, 192–202. https://doi.org/10.1016/J.JSG.2017.02.001.

Enge, H.D., Buckley, S.J., Rotevatn, A., Howell, J.A., 2007. From outcrop to reservoir simulation model: workflow and procedures. Geosphere 3, 469–490. https://doi.org/10.1130/GES00099.1.

Euler, L., 1758. Elementa doctrinae solidorum. Novi Commentarii Academiae Scientiarum Petropolitanae 4, 109–140.

Faulkner, D.R., Jackson, C.A.L., Lunn, R.J., Schlische, R.W., Shipton, Z.K., Wibberley, C.A.J., Withjack, M.O., 2010. A review of recent developments concerning the structure, mechanics and fluid flow properties of fault zones. J. Struct. Geol. 32, 1557–1575. https://doi.org/10.1016/j.jsg.2010.06.009.

Faulkner, D.R., Mitchell, T.M., Jensen, E., Cembrano, J., 2011. Scaling of fault damage zones with displacement and the implications for fault growth processes. J. Geophys. Res. 116, 1–11. https://doi.org/10.1029/2010JB007788.

Finetti, I., 1984. Geophysical study of the Sicily Channel rift zone. Boll. Geofis. Teor. Appl. 26, 3–28.

Fossen, H., Johansen, T.E.S., Hesthammer, J., Rotevatn, A., 2005. Fault interaction in porous sandstone and implications for reservoir management; examples from southern Utah. AAPG (Am. Assoc. Pet. Geol.) Bull. 89, 1593–1606. https://doi.org/10.1306/07290505041.

Fossen, H., Rotevatn, A., 2016. Fault linkage and relay structures in extensional settings—a review. Earth Sci. Rev. 154, 14–28. https://doi.org/10.1016/J.EARSCIREV.2015.11.014.

Gartrell, A., Bailey, W.R., Brincat, M., 2006. A new model for assessing trap integrity and oil preservation risks associated with postrift fault reactivation in the Timor Sea. AAPG (Am. Assoc. Pet. Geol.) Bull. 90, 1921–1944. https://doi.org/10.1306/06200605195.

Gartrell, A., Zhang, Y., Lisk, M., Dewhurst, D., 2004. Fault intersections as critical hydrocarbon leakage zones: integrated field study and numerical modelling of an example from the Timor Sea, Australia. Mar. Petrol. Geol. 21, 1165–1179. https://doi.org/10.1016/J.MARPETGEO.2004.08.001.

Gudmundsson, A., Simmenes, T.H., Larsen, B., Philipp, S.L., 2010. Effects of internal structure and local stresses on fracture propagation, deflection, and arrest in fault zones. J. Struct. Geol. 32, 1643–1655. https://doi.org/10.1016/j.jsg.2009.08.013.

Gupta, A., Scholz, C.H., 2000. A model of normal fault interaction based on observations and theory. J. Struct. Geol. 22, 865–879. https://doi.org/10.1016/S0191-8141(00)00011-0.

Huggins, P., Watterson, J., Walsh, J.J., Childs, C., 1995. Relay zone geometry and displacement transfer between normal faults recorded in coal-mine plans. J. Struct. Geol. 17, 1741–1755. https://doi.org/10.1016/0191-8141(95)00071-K.

Hull, J., 1988. Thickness-displacement relationships for deformation zones. J. Struct. Geol. 10, 431–435. https://doi.org/10.1016/0191-8141(88)90020-X.

Huyakorn, P.S., Lester, B.H., Faust, C.R., 1983. Finite element techniques for modeling groundwater flow in fractured aquifers. Water Resour. Res. 19, 1019–1035. https://doi.org/10.1029/WR019i004p01019.

Illies, J.H., 1981. Graben Formation — the Maltese Islands — a Case History. Developments in Geotectonics. Elsevier, pp. 151–168. https://doi.org/10.1016/B978-0-444-41956-9.50018-6.

Jing, L., Stephansson, O., 1997. Network topology and homogenization of fractured rocks. In: Jamtveit, B., Yardley, B.W. (Eds.), Fluid Flow and Transport in Rocks. Mechanisms and Effects. Chapman & Hall, Oxford, pp. 191–202.

Johansen, T.E.S., Fossen, H., 2008. Internal geometry of fault damage zones in interbedded siliciclastic sediments. Geological Society, London, Special Publications 299, 35–56. https://doi.org/10.1144/SP299.3.

Johri, M., Dunham, E.M., Zoback, M.D., Fang, Z., 2014. Predicting fault damage zones by modeling dynamic rupture propagation and comparison with field observations. J. Geophys. Res.: Solid Earth 119, 1251–1272. https://doi.org/10.1002/2013JB010335.

Jolivet, L., Faccenna, C., 2000. Mediterranean extension and the Africa-Eurasia collision. Tectonics 19, 1095–1106. https://doi.org/10.1029/2000TC900018.

Jongsma, D., van Hinte, J.E., Woodside, J.M., 1985. Geologic structure and neotectonics of the North African continental Margin south of sicily. Mar. Petrol. Geol. 2, 156–179. https://doi.org/10.1016/0264-8172(85)90005-4.

Kattenhorn, S.A., Aydin, A., Pollard, D.D., 2000. Joints at high angles to normal fault strike: an explanation using 3-D numerical models of fault-perturbed stress fields. J. Struct. Geol. 22, 1–23. https://doi.org/10.1016/S0191-8141(99)00130-3.

Kim, Y.-S., Andrews, J.R., Sanderson, D.J., 2000. Damage zones around strike-slip fault systems and strike-slip fault evolution, Crackington Haven, southwest England. Geosci. J. 4, 53–72.

Kim, Y.-S., Andrews, J.R., Sanderson, D.J., 2001. Reactivated strike–slip faults: examples from north Cornwall, UK. Tectonophysics 340, 173–194. https://doi.org/10.1016/S0040-1951(01)00146-9.

Kim, Y.-S., Peacock, D.C.P., Sanderson, D.J., 2004. Fault damage zones. J. Struct. Geol. 26, 503–517. https://doi.org/10.1016/j.jsg.2003.08.002.

Kim, Y.-S., Peacock, D.C.P., Sanderson, D.J., 2003. Mesoscale strike-slip faults and damage zones at Marsalforn, Gozo Island, Malta. J. Struct. Geol. 25, 793–812. https://doi.org/10.1016/S0191-8141(02)00200-6.

Kim, Y.-S., Sanderson, D.J., 2010. Inferred fluid flow through fault damage zones based on the observation of stalactites in carbonate caves. J. Struct. Geol. 32, 1305–1316. https://doi.org/10.1016/j.jsg.2009.04.017.

Kim, Y.S., Sanderson, D.J., 2008. Earthquake and fault propagation, displacement and damage zones. Structural Geology: New Research 99–118.

King, G., 1986. Speculations on the geometry of the initiation and termination processes of earthquake rupture and its relation to morphology and geological structure. Pure Appl. Geophys. 124, 567–585.

Knott, S.D., Beach, Alastair, Brockbank, P.J., Lawson, J., Mccallum, J.E., Welbon, A.I., Beach, Alastalr, Square, R.E., Glasgow, G., 1996. Spatial and mechanical controls on normal fault populations. J. Struct. Geol. 18, 359–372.

Korneva, I., Bastesen, E., Corlett, H., Eker, A., Hirani, J., Hollis, C., Gawthorpe, R.L., Rotevatn, A., Taylor, R., 2018. The effects of dolomitization on petrophysical properties and fracture distribution within rift-related carbonates (Hammam Faraun Fault Block, Suez Rift, Egypt). J. Struct. Geol. 108, 108–120. https://doi.org/10.1016/j.jsg.2017.06.005.

Leckenby, R.J., Sanderson, D.J., Lonergan, L., 2005. Estimating flow heterogeneity in natural fracture systems. J. Volcanol. Geoth. Res. 148, 116–129. https://doi.org/10.1016/j.jvolgeores.2005.03.017.

Leveille, G., Knipe, R., More, C., Ellis, D., Dudley, G., Jones, G., Fisher, Q.J., Allinson, G., 1997. Compartmentalization of Rotliegendes Gas Reservoirs by Sealing Faults, Jupiter Fields Area, Southern North Sea, vol. 123. Geological Society, London, Special Publications, pp. 87–104.

Long, J.C.S., Witherspoon, P.A., 1985. The relationship of the degree of interconnection to permeability in fracture networks. J. Geophys. Res. 90, 3087. https://doi.org/10.1029/JB090iB04p03087.

Maerten, L., Gillespie, P., Pollard, D.D., 2002. Effects of local stress perturbation on secondary fault development. J. Struct. Geol. 24, 145–153. https://doi.org/10.1016/S0191-8141(01)00054-2.

Manzocchi, T., 2002. The connectivity of two-dimensional networks of spatially correlated fractures. Water Resour. Res. 38, 1162. https://doi.org/10.1029/2000WR000180.

Mauldon, M., Dunne, W.M., Rohrbaugh, M.B., 2001. Circular scanlines and circular windows: new tools for characterizing the geometry of fracture traces. J. Struct. Geol. 23, 247–258. https://doi.org/10.1016/S0191-8141(00)00094-8.

McGrath, A., Davison, I., 1995. Damage zone geometry around fault tips. J. Struct. Geol. 17, 1011–1024.

Micarelli, L., Moretti, I., Daniel, J.M., 2003. Structural properties of rift-related normal faults: the case study of the Gulf of Corinth, Greece. J. Geodyn. 36, 275–303. https://doi.org/10.1016/S0264-3707(03)00051-6.

Micarelli, L., Moretti, I., Jaubert, M., Moulouel, H., 2006. Fracture analysis in the south-western Corinth rift (Greece) and implications on fault hydraulic behavior. Tectonophysics 426, 31–59. https://doi.org/10.1016/j.tecto.2006.02.022.

Michie, E.A.H., Haines, T.J., Healy, D., Neilson, J.E., Timms, N.E., Wibberley, C.A.J., 2014. Influence of carbonate facies on fault zone architecture. J. Struct. Geol. 65, 82–99. https://doi.org/10.1016/j.jsg.2014.04.007.

Mitchell, T.M., Faulkner, D.R., 2012. Towards quantifying the matrix permeability of fault damage zones in low porosity rocks. Earth Planet Sci. Lett. 339–340, 24–31. https://doi.org/10.1016/j.epsl.2012.05.014.

Mitchell, T.M., Faulkner, D.R., 2009. The nature and origin of off-fault damage surrounding strike-slip fault zones with a wide range of displacements: a field study from the Atacama fault system, northern Chile. J. Struct. Geol. 31, 802–816. https://doi.org/10.1016/j.jsg.2009.05.002.

Morley, C.K., Nixon, C.W., 2016. Topological characteristics of simple and complex normal fault networks. J. Struct. Geol. 84, 68–84. https://doi.org/10.1016/j.jsg.2016.01.005.

Nærland, K., 2016. Topology of Normal Fault Damage Zones in Carbonate Rocks, Malta-implications for the Development of Connectivity in Evolving Fault Networks. MSc. thesis. Department of Earth Science. University of Bergen, unpublished.

Nixon, C.W., Sanderson, D.J., Bull, J.M., 2012. Analysis of a strike-slip fault network using high resolution multibeam bathymetry, offshore NW Devon U.K. Tectonophysics 541–543, 69–80. https://doi.org/10.1016/j.tecto.2012.03.021.

Nixon, C.W., Vaagan, S., Sanderson, D.J., Gawthorpe, R.L., 2019. Spatial distribution of damage and strain within a normal fault relay at Kilve, U.K. J. Struct. Geol. 118, 194–209. https://doi.org/10.1016/J.JSG.2018.10.016.

Nyberg, B., Nixon, C.W., Sanderson, D.J., 2018. NetworkGT: a GIS tool for geometric and topological analysis of two-dimensional fracture networks. Geosphere 14, 1618–1634. https://doi.org/10.1130/GES01595.1.

Ogata, K., Senger, K., Braathen, A., Tveranger, J., 2014. Fracture corridors as seal-bypass systems in siliciclastic reservoir-cap rock successions: field-based insights from the Jurassic Entrada Formation (SE Utah, USA). J. Struct. Geol. 66, 162–187. https://doi.org/10.1016/j.jsg.2014.05.005.

Ortega, O.J., Gale, J.F.W., Marrett, R., 2010. Quantifying diagenetic and stratigraphic controls on fracture intensity in platform carbonates: an example from the Sierra Madre Oriental, northeast Mexico. J. Struct. Geol. 32, 1943–1959. https://doi.org/10.1016/J.JSG.2010.07.004.

Peacock, D.C.P., Dimmen, V., Rotevatn, A., Sanderson, D.J., 2017. A broader classification of damage zones. J. Struct. Geol. 102, 179–192. https://doi.org/10.1016/J.JSG.2017.08.004.

Peacock, D.C.P., Sanderson, D.J., 1994. Geometry and development of relay ramps in normal fault systems. AAPG (Am. Assoc. Pet. Geol.) Bull. 78, 147–165.

Peacock, D.C.P., Sanderson, D.J., 1991. Displacements, segment linkage and relay ramps in normal fault zones. J. Struct. Geol. 13, 721–733. https://doi.org/10.1016/0191-8141(91)90033-F.

Pedley, H., 1987. Controls on Cenozoic carbonate deposition in the Maltese Islands: review and reinterpretation. Memor. Soc. Geol. Ital. 38, 81–94.

Pedley, H.M., House, M.R., Waugh, B., 1976. The geology of Malta and Gozo. PGA (Proc. Geol. Assoc.) 87, 325–341. https://doi.org/10.1016/S0016-7878(76)80005-3.

Perrin, C., Manighetti, I., Ampuero, J.P., Cappa, F., Gaudemer, Y., 2016. Location of largest earthquake slip and fast rupture controlled by along-strike change in fault structural maturity due to fault growth. J. Geophys. Res.: Solid Earth 121, 3666–3685. https://doi.org/10.1002/2015JB012671.

Pickering, G., Peacock, D.C.P., Sanderson, D.J., Bull, J.M., 1997. Modeling tip zones to predict the throw and length characteristics of faults. AAPG (Am. Assoc. Pet. Geol.) Bull. 81, 82–99.

Putz-Perrier, M.W., Sanderson, D.J., 2010. Distribution of faults and extensional strain in fractured carbonates of the North Malta Graben. AAPG (Am. Assoc. Pet. Geol.) Bull. 94, 435–456. https://doi.org/10.1306/08260909063.

Rawnsley, K.D., Rives, T., Petti, J.P., Hencher, S.R., Lumsden, A.C., 1992. Joint development in perturbed stress fields near faults. J. Struct. Geol. 14, 939–951. https://doi.org/10.1016/0191-8141(92)90025-R.

Reuther, C.D., Eisbacher, G.H., 1985. Pantelleria Rift - crustal extension in a convergent intraplate setting. Geol. Rundsch. 74, 585–597. https://doi.org/10.1007/BF01821214.

Richards, F.L., Richardson, N.J., Bond, C.E., Cowgill, M., 2015. Interpretational variability of structural traps: implications for exploration risk and volume uncertainty. Geological Society, London, Special Publications 421, 7–27. https://doi.org/10.1144/SP421.13.

Rotevatn, A., Bastesen, E., 2014. Fault linkage and damage zone architecture in tight carbonate rocks in the Suez Rift (Egypt): implications for permeability structure along segmented normal faults. Geological Society, London, Special Publications 374, 79–95. https://doi.org/10.1144/SP374.12.

Rotevatn, A., Fossen, H., 2011. Simulating the effect of subseismic fault tails and process zones in a siliciclastic reservoir analogue: implications for aquifer support and trap definition. Mar. Petrol. Geol. 28, 1648–1662. https://doi.org/10.1016/j.marpetgeo.2011.07.005.

Rotevatn, A., Fossen, H., Hesthammer, J., Aas, T.E., Howell, J.A., 2007. Are relay ramps conduits for fluid flow? Structural analysis of a relay ramp in Arches National Park, Utah. Geological Society, London, Special Publications 270, 55–71. https://doi.org/10.1144/GSL.SP.2007.270.01.04.

Rotevatn, A., Jackson, C.A.L., Tvedt, A.B.M., Bell, R.E., Blækkan, I., 2019. How do normal faults grow? J. Struct. Geol. 125, 174–184. https://doi.org/10.1016/j.jsg.2018.08.005.

Rotevatn, A., Thorsheim, E., Bastesen, E., Fossmark, H.S.S., Torabi, A., Sælen, G., 2016. Sequential growth of deformation bands in carbonate grainstones in the hangingwall of an active growth fault: implications for deformation mechanisms in different tectonic regimes. J. Struct. Geol. 90, 27–47. https://doi.org/10.1016/j.jsg.2016.07.003.

Rotevatn, A., Tveranger, J., Howell, J.A., Fossen, H., 2009. Dynamic investigation of the effect of a relay ramp on simulated fluid flow: geocellular modelling of the Delicate Arch Ramp, Utah. Petrol. Geosci. 15, 45–58. https://doi.org/10.1144/1354-079309-779.

Saevik, P.N., Nixon, C.W., 2017. Inclusion of topological measurements into Analytic estimates of effective permeability in fractured Media. Water Resour. Res. 53, 9424–9443. https://doi.org/10.1002/2017WR020943.

Sanderson, D.J., Nixon, C.W., 2018. Topology, connectivity and percolation in fracture networks. J. Struct. Geol. 115, 167–177. https://doi.org/10.1016/J.JSG.2018.07.011.

Sanderson, D.J., Nixon, C.W., 2015. The use of topology in fracture network characterization. J. Struct. Geol. 72, 55–66.

Sanderson, D.J., Peacock, D.C.P., Nixon, C.W., Rotevatn, A., 2019. Graph theory and the analysis of fracture networks. J. Struct. Geol. 125, 155–165. https://doi.org/10.1016/j.jsg.2018.04.011.

Sanderson, D.J., Zhang, X., 2004. Stress-controlled localization of deformation and fluid flow in fractured rocks. Geological Society, London, Special Publications 231, 299–314.

Savage, H.M., Brodsky, E.E., 2011. Collateral damage: evolution with displacement of fracture distribution and secondary fault strands in fault damage zones. J. Geophys. Res. 116, B03405. https://doi.org/10.1029/2010JB007665.

Segall, P., Pollard, D.D., 1980. Mechanics of discontinuous faults. J. Geophys. Res.: Solid Earth 85, 4337–4350. https://doi.org/10.1029/JB085IB08P04337.

Shipton, Z.K., Cowie, P.A., 2003. A conceptual model for the origin of fault damage zone structures in high-porosity sandstone. J. Struct. Geol. 25, 333–344. https://doi.org/10.1016/S0191-8141(02)00037-8.

Shipton, Z.K., Cowie, P.A., 2001. Damage zone and slip-surface evolution over μm to km scales in high-porosity Navajo sandstone, Utah. J. Struct. Geol. 23, 1825–1844. https://doi.org/10.1016/S0191-8141(01)00035-9.

Shipton, Z.K., Evans, J.P., Kirschner, D., Kolesar, P.T., Williams, A.P., Heath, J., 2004. Analysis of CO2 leakage through "low-permeability" faults from natural reservoirs in the Colorado Plateau, east-central Utah. Geological Society, London, Special Publication 233, 43–58. https://doi.org/10.1144/GSL.SP.2004.233.01.05.

Shipton, Z.K., Evans, J.P., Robeson, K.R., Forster, C.B., Snelgrove, S., 2002. Structural heterogeneity and permeability in faulted eolian sandstone: implications for subsurface modeling of faults. AAPG (Am. Assoc. Pet. Geol.) Bull. 86, 863–883. https://doi.org/10.1306/61eedbc0-173e-11d7-8645000102c1865d.

Sibson, R.H., 1989. Earthquake faulting as a structural process. J. Struct. Geol. 11, 1–14. https://doi.org/10.1016/0191-8141(89)90032-1.

Soliva, R., Benedicto, A., Schultz, R.A., Maerten, L., Micarelli, L., 2008. Displacement and interaction of normal fault segments branched at depth: implications for fault growth and potential earthquake rupture size. J. Struct. Geol. 30, 1288–1299. https://doi.org/10.1016/j.jsg.2008.07.005.

Tamagawa, T., Pollard, D.D., 2008. Fracture permeability created by perturbed stress fields around active faults in a fractured basement reservoir. AAPG (Am. Assoc. Pet. Geol.) Bull. 92, 743–764. https://doi.org/10.1306/02050807013.

Vermilye, J.M., Scholz, C.H., 1998. The process zone: a microstructural view of fault growth. J. Geophys. Res.: Solid Earth 103, 12223–12237. https://doi.org/10.1029/98JB00957.

Walsh, J.J., Childs, C., Meyer, V., Manzocchi, T., Imber, J., Nicol, A., Tuckwell, G., Bailey, W.R., Bonson, C.G., Watterson, J., Nell, P.A., Strand, J., 2001. Geometric controls on the evolution of normal fault systems. Geological Society, London, Special Publications 186, 157–170. https://doi.org/10.1144/GSL.SP.2001.186.01.10.

Walsh, J.J., Watterson, J., 1991. Geometric and kinematic coherence and scale effects in normal fault systems. In: Roberts, A.M., Yielding, G., Freeman, B. (Eds.), Geological Society, vol. 59. Special Publications, London, pp. 193–203.

Wennberg, O.P., Svana, T., Azizzadeh, M., Aqrawi, A.M.M., Brockbank, P., Lyslo, K.B., Ogilvie, S., 2006. Fracture intensity vs. mechanical stratigraphy in platform top carbonates: the Aquitanian of the Asmari formation, Khaviz anticline, Zagros, SW Iran. Petrol. Geosci. 12, 235–246. https://doi.org/10.1144/1354-079305-675.

Willemse, E.J.M., Pollard, D.D., 1998. On the orientation and patterns of wing cracks and solution surfaces at the tips of a sliding flaw or fault. J. Geophys. Res.: Solid Earth 103, 2427–2438. https://doi.org/10.1029/97jb01587.

Willemse, E.J.M., Pollard, D.D., Aydin, A., 1996. Three-dimensional analyses of slip distributions on normal fault arrays with consequences for fault scaling. J. Struct. Geol. 18, 295–309. https://doi.org/10.1016/S0191-8141(96)80051-4.

Zhang, X., Sanderson, D.J., 1995. Anisotropic features of geometry and permeability in fractured rock masses. Eng. Geol. 40, 65–75. https://doi.org/10.1016/0013-7952(95)00040-2.

NORDIC ECOLABEL
241 PRINTED MATTER 731

Graphic design: Communication Division, UiB / Print: Skipnes Kommunikasjon AS

UNIVERSITAS BERGENSIS

uib.no

ISBN: 9788230858707 (print)
9788230860045 (PDF)